AIX-MARSEILLE UNIVERSITÉ
Institut **U**niversitaire des **S**ystèmes **T**hermiques **I**ndustriels
— UMR CNRS 7343 —

SIMULATION DE L'ATOMISATION D'UNE GOUTTE PAR UN ÉCOULEMENT À GRANDE VITESSE

présentée et soutenue publiquement
pour obtenir le grade de

Docteur de Aix-Marseille Université
Spécialité : Mécanique et Physique des Fluides
École Doctorale 353, Sciences pour l'Ingénieur

par
Kevin SCHMIDMAYER
le 12 Octobre 2017

Directeur de thèse :	Professeur Éric Daniel – IUSTI – Aix-Marseille Université
Co-encadrant de thèse :	Docteur Fabien Petitpas – IUSTI – Aix-Marseille Université

JURY

Rapporteurs :	
Professeur Rémi Abgrall,	Universität Zürich, Switzerland
Professeur Tim Colonius,	California Institute of Technology, USA
Examinateurs :	
Professeur Éric Daniel,	Aix-Marseille Université, France
Professeur Michaël Dumbser,	University of Trento, Italy
Professeur Sergey Gavrilyuk,	Aix-Marseille Université, France
Professeur Henri Gouin,	Aix-Marseille Université, France
Docteur Ludovic Hallo,	CEA-CESTA, France

Remerciements

Je tiens tout d'abord à remercier Éric Daniel qui aura été un formidable directeur de thèse, autant sur le plan scientifique que sur le plan humain. Il aura su m'accompagner du début à la fin et je n'aurais pu demander mieux comme directeur. La deuxième personne à qui je pense est bien entendu mon co-encadrant de thèse Fabien Petitpas avec qui j'aurais passé de longues heures de travail dans une atmosphère des plus appréciables grâce à son humour détonnant. Ensuite, je tiens à remercier le soutien et la précision scientifique qu'aura apporter l'admirable mathématicien Sergey Gavrilyuk, puis le débordant d'idées qu'est Nicolas Favrie, ainsi que l'entière équipe SHOC qui m'auront permis de travailler dans un environnement idéal. Ces personnes auront été sans équivoque des éléments clés de la réussite de cette thèse, ils ont ma profonde reconnaissance et ma sincère amitié.

Je tiens également à remercier Tim Colonius et Rémi Abgrall qui m'ont fait l'honneur d'être les rapporteurs de cette thèse, ainsi qu'Henri Gouin, Michaël Dumbser, Sergey Gavrilyuk, Ludovic Hallo et Éric Daniel d'avoir accepté d'être membre de mon jury de thèse.

Une pensée ira également vers ceux qui ont partagé mon quotidien au laboratoire, je pense notamment aux multiples doctorants et post-doctorants qui auront croisés mon chemin avec une mention spécial au futur docteur Anthony Castillo qui m'aura suivi après l'école d'ingénieur dans cette aventure.

Un grand merci aussi au personnel administratif et scientifique de l'IUSTI, et notamment au directeur du laboratoire Lounès Tadrist, qui auront su maintenir un environnement favorable à l'exercice de mes travaux.

Ce travail n'aurait pas été le même sans les encouragements et le soutien de mes amis. Je pense tout particulièrement à Régis Recoules qui ne m'aura jamais lâché et m'aura permis de me changer complétement les idées afin que je traverse au mieux les différentes épreuves parcourues tout au long de ma thèse. Il en va de même à ma famille et ma belle-famille sans qui, non seulement la thèse, mais mon cursus complet et mon apprentissage personnel n'auraient été aussi satisfaisant et enrichissant.

Enfin viens mes remerciements les plus profonds à ma mère et à ma femme à qui je dédie ce travail, je les remercie infiniment pour leurs écoutes, leurs soutiens et leurs encouragements tout au long de mon parcours. Les deux personnes sans qui je n'aurais pu réussir aussi bien cette fin de cursus. Les deux personnes qui me poussent et me donnent toujours l'envie de donner le meilleur de moi. Tout simplement, les deux personnes à qui je tiens le plus au monde.

Avant-propos / Foreword

En raison du large public auquel ce manuscrit s'adresse, sa structure est partagée entre la langue française et la langue anglaise. Le premier chapitre, écrit en français, fait office d'introduction sur l'atomisation d'une goutte et de résumé étendu du contenu complet du manuscrit. Il est présenté sous une forme autonome où des renvois aux chapitres correspondants sont faits pour le lecteur souhaitant obtenir des détails. Le manuscrit est divisé en trois autres chapitres. Les deux premiers traitent de l'établissement d'un nouveau modèle et d'une nouvelle méthode numérique pour les écoulements compressibles multiphasiques avec effets capillaires, et de la construction d'une nouvelle méthode de raffinement adaptatif du maillage utilisant des arbres des bords des cellules en plus de celui sur les cellules. Ils ont vocation à étudier au mieux la simulation numérique de l'atomisation d'une goutte. Ainsi, le dernier chapitre présente une étude sur l'atomisation d'une goutte. Le contenu de ces trois chapitres a été publié ou est en cours de publication à la date de la rédaction, ils sont donc écrits en anglais. Une liste des publications réalisées ou soumises est fournie ci-dessous.

By virtue of the wide public to whom this manuscript is addressed, its structure is shared between the French language and the English language. The first chapter, written in French, serves as an introduction to the atomization of droplet and an extended summary of the complete contents of the manuscript. It is presented in an autonomous form where references to the corresponding chapters are made for the reader wishing to obtain more details. The manuscript is divided into three other chapters. The first two deal with the establishment of a new model and a new numerical method for multiphase compressibles flows with capillary effects, and with a construction of a new method of adaptive mesh refinement using trees of cells edges in addition to that on cells. Thus, the last chapter presents a study on the droplet atomization. The content of these three chapters has been published or is being published at the date of writing, so they are written in English. A list of the publications produced or submitted is provided below.

Publications

- K. Schmidmayer, F. Petitpas, E. Daniel, N. Favrie, S.L. Gavrilyuk. A model and numerical method for compressible flows with capillary effects. *Journal of Computational Physics*, 334:468-496, 2017.

- K. Schmidmayer, F. Petitpas, E. Daniel. Adaptive mesh refinement method based on cells boundaries trees for compressible multiphase flows. *Submitted*, 2017.

- K. Schmidmayer, E. Daniel, F. Petitpas. A model and numerical method for high speed flows with capillary, viscous and heat conduction effects. *The American Institute of Aeronautics and Astronautics, Aviation 2016, 46th AIAA Fluid Dynamics Conference*, Washington, D.C.

Table des matières / Contents

Nomenclature

Quantités physiques / Physical quantities

	Français	English	Unité / unity
a	Vitesse du son	Speed of sound	$m.s^{-1}$
c	Fonction couleur	Color function	(-)
E	Energie totale	Total energy	$J.kg^{-1}$
e	Energie interne	Internal energy	$J.kg^{-1}$
$\mathbf{F}$	Vecteur des variables de flux, ou Vecteur force		
	Vector of fluxes variables, or Force vector		
$\mathbf{G}$	Vecteur des variables de gradient		
	Vector of gradient variables		
$\mathbf{H}$	Vecteur de quantités non-conservatives ou de relaxation		
	Vector of non-convervative or relaxation quantities		
$\overline{\overline{I}}$	Tenseur identité	Identity tensor	
K	Coefficient acoustique	Acoustic coefficient	
P	Pression	Pressure	Pa
Re	Nombre de Reynolds	Reynolds number	(-)
$\mathbf{S}$	Vecteur de termes sources		
	Source terms vector		
s	Entropie	Entropy	$J.kg^{-1}.K^{-1}$
$\mathbf{n}$	Vecteur normal à l'interface	Interface normal vector	(-)
$\mathbf{t}$	Vecteur tangentiel à l'interface	Interface tangential vector	(-)
T	Température	Temperature	K
t	Temps	Time	s
$\mathbf{U}$	Vecteur de variables conservatives		
	Vector of conservative variables		
$\mathbf{u}$	Vecteur vitesse	Velocity vector	
u	Vitesse dans la direction x	Velocity in the x-direction	$m.s^{-1}$
v	Vitesse dans la direction y	Velocity in the y-direction	$m.s^{-1}$
$\mathbf{W}$	Vecteur de variables primitives	Vector of primitive variables	
$\mathbf{w}$	Gradient de la fonction couleur	Color function gradient	m^{-1}
w	Vitesse dans la direction z	Velocity in the z-direction	$m.s^{-1}$
w_i	Gradient de la fonction couleur dans la i-ème direction		

	Color function gradient in the i-th direction		m^{-1}
We	Nombre de Weber	Weber number	(-)
$\mathbf{x}$	Vecteur d'espace	Space vector	
x	Variable spatiale dans la direction x		
	Spatial variable in the x-direction		
Y	Fraction massique	Mass fraction	
y	Variable spatiale dans la direction y		
	Spatial variable in the y-direction		
Z	Impédance acoustique	Acoustic impedance	$kg.m^{-2}.s^{-1}$
z	Variable spatiale dans la direction z		
	Spatial variable in the z-direction		
α	Fraction volumique	Volume fraction	(-)
γ	Coefficient polytropique	Polytropic coefficient	(-)
ε_σ	Energie potentielle capillaire	Capillary potential energy	$J.m^{-3}$
κ	Courbure	Curvature	m^{-1}
μ	Coefficient de relaxation de la pression, ou Viscosité dynamique		
	Pressure relaxation coefficient, or Dynamic viscosity		(-), $kg.s^{-1}.m^{-1}$
ρ	Densité	Density	$kg.m^{-3}$
σ	Coefficient capillaire	Capillary coefficient	$N.m^{-1}$
$\overline{\overline{\tau}}$	Tenseur de contraintes	Stress tensor	$N.m^{-2}$
$\overline{\overline{\Omega}}$	Tenseur capillaire	Capillary tensor	$N.m^{-2}$
Subscript			
c	Capillarité	Capillary	
f	Vitesse du son de mélange gelée		
	Frozen mixture sound speed		
h	Hyperbolique	Hyperbolic	
I	Interface	Interface	
k	Numéro de la phase	Phase number	
n	Normale	Normal	
nc	Non-conservatif	Non-conservative	
num	Numérique	Numerical	
t	Tangente	Tangent	
th	Théorique	Theoretical	
∞	Condition d'écoulement libre externe		
	External free stream condition		
Superscript			
(n)	Porté par la normale x	Normal carrying	
(t)	Porté par la tangente x	Tangent carrying	
x	Direction x	x-direction	
y	Direction y	y-direction	
z	Direction z	z-direction	

Quantités algorithmiques / Algorithmic quantities

	Français	English	Unité / unity
A	Procédure d'avancement	Advancing procedure	
cfl	Critére de Courant-Friedrichs-Lewy		
	Courant-Friedrichs-Lewy criterion		(-)
G	Procédure de gradient	Gradient procedure	
I	Procédure d'intégration	Integration procedure	
l	Niveau dans un arbre	Level in a tree	
Nb	Cellule voisine	Neighboring cell	
R	Procédure de raffinement	Refinement procedure	
Δt	Pas de temps	Time-step	s
ϵ	Paramètre de détection de gradient		
	Gradient detection parameter		(-)
ξ	Indicateur de raffinement adaptatif du maillage		
	Adaptive mesh refinement indicator		(-)
Subscript			
B	Cellule voisine côté bas	Bottom neighbouring cell	
i	Numéro de la cellule du maillage	Mesh cell number	
j	Numéro de la cellule du maillage	Mesh cell number	
L	Cellule voisine côté gauche	Left neighbouring cell	
R	Cellule voisine côté droite	Right neighbouring cell	
s	Numéro du bord de cellule du maillage		
	Mesh cell boundary number		
T	Cellule voisine côté haut	Top neighbouring cell	
Superscript			
0	Temps avant l'application du pas de temps		
	Time before the time-step application		
n	Temps après l'application du pas de temps		
	Time after the time-step application		
$*$	Solution du problème de Riemann		
	Solution of the Riemann problem		

Acronymes / Acronyms

	Français	English
$1D$	Une dimension	One-dimensional
$2D$	Deux dimensions	Two-dimensional
$3D$	Trois dimensions	Three-dimensional
AMR	Raffinement adaptatif du maillage Adaptive mesh refinement	
CFL	Courant-Friedrichs-Lewy	Courant-Friedrichs-Lewy
DNS	Simulation numérique direct	Direct numerical simulation
EOS	Equation d'état	Equation of state
$HLLC$	Harten-Lax-van Leer-contact	Harten-Lax-van Leer-contact

Chapitre 1

Introduction générale

1.1 Contexte et motivations

L'étude de l'atomisation de gouttes de liquides par des écoulements à grande vitesse a été et est toujours motivée par trois principales applications : l'endommagement lors de l'impact des gouttes de pluie sur les avions durant les vols supersoniques causant l'érosion de leur surface (Engel [17], Joseph et al. [42], Igra and Takayama [37, 38]), la dissémination d'agents liquides (Theofanous [89], Chauvin et al. [9, 10]), et la seconde phase de l'atomisation de jets de liquide pouvant intervenir par exemple dans des chambres de combustion ou dans des moteurs Diesel (Welch et Boyle [96], Meng et Colonius [59], Devassy et al. [15]).

Historiquement, Taylor [88] réalisa des travaux expérimentaux dans le but d'investiguer l'éclatement aérodynamique d'une goutte isolée à l'aide d'un canon à air comprimé, ouvrant ainsi la voie à une multitude de travaux dédiés à ce phénomène. Les expériences de Taylor sont rapidement suivies d'autres travaux comme ceux de Engel [17], Hanson et al. [31], Lane [50], Ranger et Nicholls [75], et Simpkins et Bales [86], où le phénomène d'éclatement aérodynamique peut cette fois-ci être provoqué par l'écoulement engendré par une onde de choc. La figure 1.1 présente une expérience, réalisée plus récemment par Theofanous et al. [90], d'atomisation d'une goutte d'eau dans un écoulement à Mach $= 0,16$. La compréhension de l'atomisation d'une goutte isolée est conduite par le désir de prédire et de contrôler la distribution finale des tailles des gouttes. Une compréhension détaillée des mécanismes physiques de l'éclatement et finalement de la taille des fragments est donc cruciale pour l'ingénierie lors de l'amélioration du design et des performances. Par exemple, pour des applications avec combustion, l'atomisation des gouttes de fuel joue un rôle important dans l'augmentation de la surface et donc des transferts de chaleur et de masse entre le fuel et le gaz ambiant. Cependant, contrairement aux intuitions, les plus petites tailles de gouttes ne sont pas nécessairement produites par les plus grandes vitesses du gaz ambient (Guildenbecher et al. [26]), elles dépendent de la dynamique d'éclatement de la goutte initiale et donc des différents processus physiques mises en jeu. C'est pourquoi, l'amélioration de cette compréhension est impérative pour prédire au mieux et ainsi contrôler la taille finale des gouttes. En conséquence, la littérature sur l'éclatement aérodynamique d'une goutte s'est focalisée sur la caractérisation et la cartographie des différents régimes d'éclatement (Engel [17], Hanson et al. [31], Hsiang et Faeth [34], Lane [50], Ranger et Nicholls [75], Wierzba et Takayama [97]), sur le calcul des temps caractéristiques de ce dernier (Hsiang et Faeth [34], Ranger et Nicholls [75]), sur la dépendance vis-à-vis des différents paramètres comme la densité ou la viscosité (Hanson et al. [31], Theofanous et al. [90]), sur la prédiction des tailles des gouttes finales (Pilch et Erdman [71], Ranger et Nicholls [75]), et sur les propriétés instationnaires de la traînée (Engel [17], Joseph et al. [42], Simpkins et Bales [86]). En revanche, ces recherches expérimentales et théoriques ont mené à de nombreux résultats souvent en désaccord, et en définitive la compréhension complète des phénomènes ayant lieu demeure évasive (Khosla et al. [47]).

En effet, une goutte isolée dans un écoulement de gaz est un système physique relativement simple. Cependant, les processus physiques mises en jeu lors de l'éclatement révèlent une complexité importante. Ceux-ci relient étroitement les petites échelles en espace et en temps, la dynamique des fluides compressibles et instationnaires, la dynamique de l'interface, les instabilités hydrodynamiques et le transfert de chaleur et de masse. De

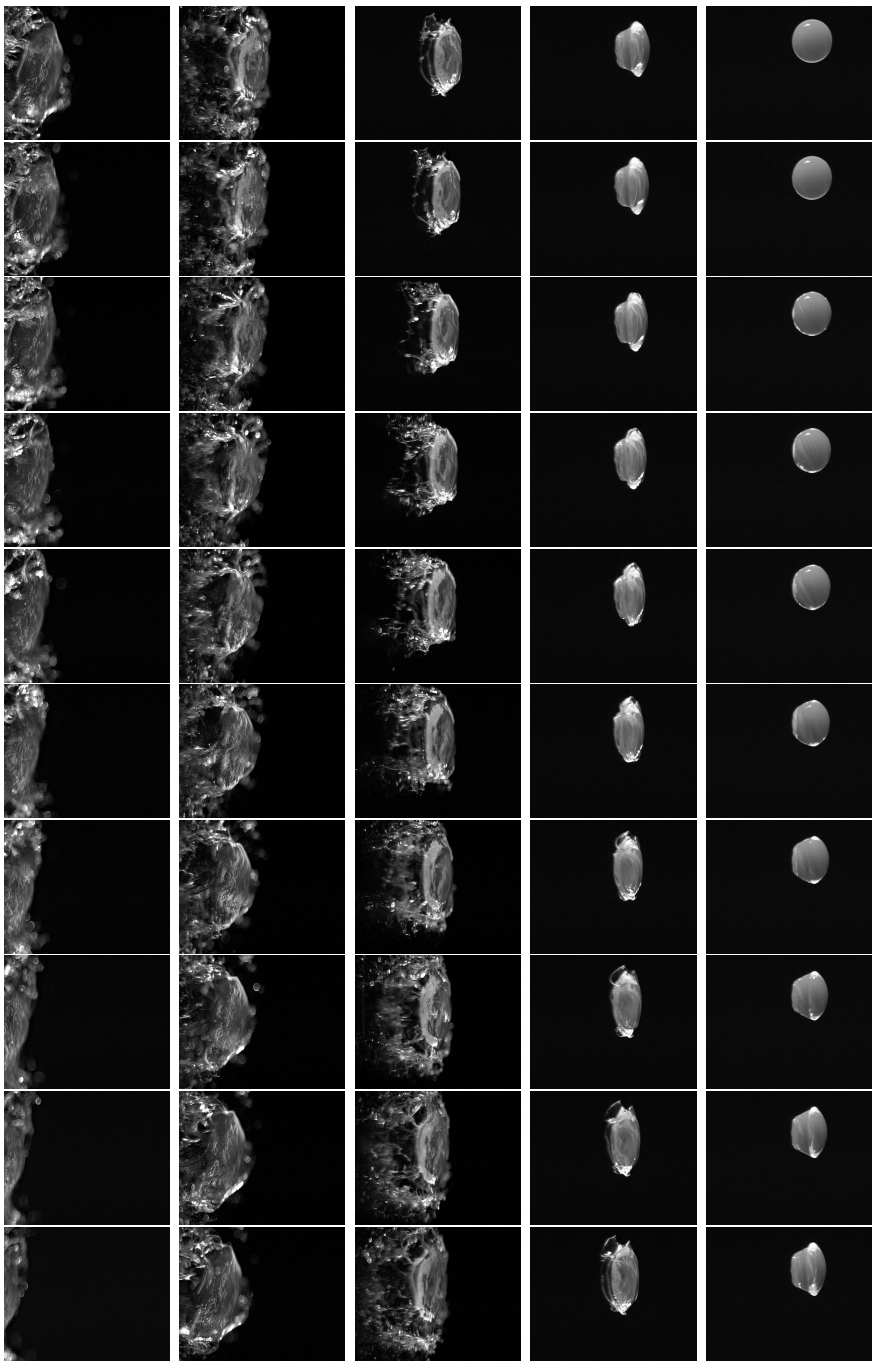

Figure 1.1: Réimprimé de Theofanous et al. [90]. Visualisation expérimentale de l'aérodynamisme d'une goutte d'eau dans un écoulement à Mach $= 0,16$. L'écoulement se dirige de la droite vers la gauche, et les images sont ordonnées de haut en bas, de droite à gauche. Les images individuelles sont reproduites à partir de la vidéo stockée en ligne (URL: http://dx.doi.org/10.1063/1.3680867.6). © 2012, American Institute of Physics.

plus, les études expérimentales sur l'atomisation d'une goutte sont mises en difficulté par le formidable défi de réaliser des visualisations avec des résolutions spatiales et temporelles suffisantes pour étudier précisément les processus physiques prenant place. Tandis que les travaux théoriques complets sont presque impossibles du fait de la liste des phénomènes physiques interconnectés précédemment cités.

Depuis le début du siècle seulement, la simulation numérique directe (DNS) est apparue comme un outil précieux capable d'étudier l'éclatement de goutte isolée. Malheureusement, en raison des coûts de calcul élevés des simulations entièrement tridimensionnelles, les études numériques d'aérodynamisme ont souvent été réalisées en deux dimensions (Chen [11], Igra et Takayama [36, 38, 39]) ou avec des approximations d'axi-symétrie (Aalburg et al. [1], Han et Tryggvason [28], Wadhwa et al. [95]). De plus, les rapports de densité de fluide sont souvent supposés petits, ou les fluides sont considérés comme incompressibles (Aalburg et al. [1], Han et Tryggvason [28], Jalaal et Mehravaran [41], Quan et Schmidt [73]). Par la suite, les études étaient focalisées sur les premiers instants de l'éclatement de fluides compressibles avec faible rapport de densité, quand les instabilités de Richtmyer-Meshkov et/ou de Rayleigh-Taylor apparaissent (Yang et al. [99], Quirk et Karni [74], Layes et Le Metayer [51]). C'est seulement récemment qu'une étude approfondie pour élucider les mécanismes physiques responsables de l'éclatement a été réalisée par Meng et Colonius [59, 58] avec des fluides à fort rapport de densité et pour des simulations numériques directes à deux et à trois dimensions. Ils ont ainsi commencé à combler une lacune dans la description phénoménologique et l'identification des processus intervenant lors des premiers instants de l'éclatement. Toutefois, ni les effets capillaires ni les effets visqueux n'ont été pris en compte, ce qui constitue une première barrière à l'étude des instants plus longs, là où ces effets deviennent significatifs et où la formation de nouvelles gouttes apparaît. Il sera notamment présenté dans les travaux de cette présente thèse l'impact de la prise en compte ou non des effets capillaires sur des temps longs. Une seconde barrière intervient et correspond toujours au coût en calcul pour obtenir une résolution spatiale suffisante afin d'observer finement la physique s'opérant sur ces temps longs. Ces coûts étant trop important si l'utilisation d'une méthode numérique appropriée n'est pas entreprise.

L'atomisation d'une goutte par un écoulement à grande vitesse peut être divisée en deux phases distinctes : l'éclatement se produit d'abord sous la forme d'aplatissement de la goutte (compressions dans la direction longitudinale de l'écoulement et étirements dans la direction transversale), comprenant également des filaments, puis il se poursuit *via* l'obtention d'une multitude de gouttes de tailles réduites (voir figure 1.2). Au cours de cette seconde phase de l'éclatement aérodynamique d'une goutte isolée, des calculs adimensionnés montrent que les effets capillaires semblent avoir un impact plus important que ceux visqueux. Les principaux objectifs pour le présent travail sont donc de combler une partie des déficits précédemment cités. Le premier concerne le manque de physique pris en compte dans les modèles simplifiés et notamment les effets capillaires. En effet, le nombre de Weber nous indique que l'amplitude des forces de tension de surface tend au même ordre de grandeur que celle des forces inertielles. Les effets capillaires semblent donc avoir un impact important sur le comportement de l'éclatement aux temps longs et a assurément un impact important sur la formation des gouttes de tailles réduites. Ainsi, il est introduit dans ces travaux un nouveau modèle capable de traiter correctement

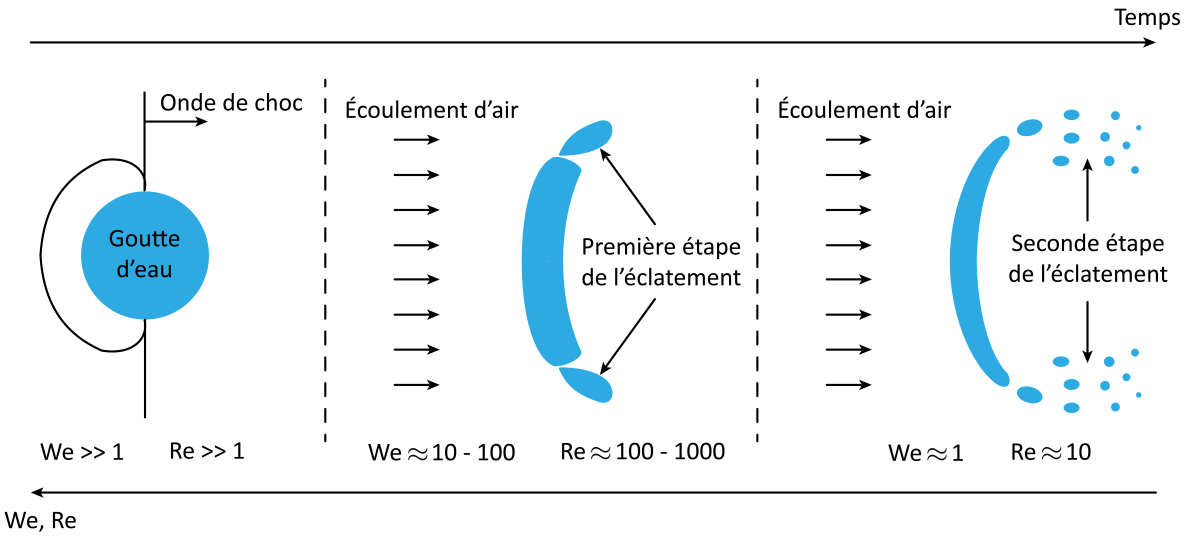

Figure 1.2: Schéma des 3 principales étapes de l'atomisation d'une goutte isolée par un écoulement à grande vitesse, écoulement ici initié par une onde de choc. La première étape correspond au passage de l'onde de choc sur la goutte, avec notamment une onde de choc réfléchie. Les deuxième et troisième étapes représentent, respectivement, la première et la seconde phase de l'atomisation. Une échelle des nombres de Weber et de Reynolds est donnée (We = forces inertielles/forces capillaires, et Re = forces internielles/forces visqueuses). L'objectif ici étant d'atteindre cette seconde phase avec la formation de plus petites gouttes.

des écoulements compressibles multiphasiques avec effets capillaires. A noter que l'aspect compressible pour chacun des fluides est un élément important pour le traitement des ondes et des dynamiques rapides lors de l'éclatement par écoulement à grande vitesse. Puis, le deuxième principal objectif étant la mise en place d'une méthode numérique appropriée à la résolution de ce modèle et utilisant une méthode de remaillage adaptatif (AMR) permettant d'obtenir une résolution spatiale suffisante pour des coûts en calculs raisonnables.

La suite de ce chapitre est donc organisée comme suit : une introduction à la capillarité pour les modèles multiphasiques et pour les méthodes numériques utilisant la notion de volume (section 1.2), suivie d'une présentation des principales contributions de cette thèse, c'est-à-dire l'établissement du nouveau modèle précédemment cité et de la nouvelle méthode numérique appropriée à sa résolution (section 1.3), ainsi que la construction de la nouvelle méthode de raffinement adaptatif du maillage (section 1.4). Ces derniers étant précédées quand nécessaire d'un état de l'art sur le sujet en question. Puis d'une dernière partie synthétisant les principaux résultats sur l'atomisation (section 1.5).

1.2 Capillarité, de sa description physique à sa modélisation

La capillarité est un phénomène d'interaction qui se produit aux interfaces entre deux milieux non miscibles. Une force appliquée sur l'interface apparaît et est donc couramment nommée tension capillaire ou tension de surface. Ce phénomène, qui peut être décrit à l'échelle moléculaire comme des interactions inter-moléculaires (attractions et répulsions), peut aussi être décrit d'un point de vue plus macroscopique à l'échelle de l'interface entre ces deux milieux. Ce second point de vue est rappelé dans la section suivante en référence aux travaux de Landau et Lifshitz [49]. La physique liée à la tension de surface y est décrite au travers de notions, non seulement physiques, mais aussi géométriques. Cet aspect est un point important à retenir pour la construction du modèle présenté dans le chapitre 2. Ensuite, la méthode de Brackbill et al. [8] est présentée, laquelle a un impact majeur sur la modélisation des effets capillaires. En effet, cette méthode permet d'exprimer la tension de surface comme une force, non plus surfacique, mais volumique, pouvant ainsi être introduite dans les modèles multiphasiques et les méthodes numériques utilisant la notion de volume. Les travaux réalisés par Brackbill et al. représentent donc une étude fondamentale pour la mise en place du nouveau modèle developpé par la suite (chapitre 2).

1.2.1 Description physique des effets capillaires

1.2.1.1 Loi de Laplace

Landau et Lifshitz exposent le problème de la tension de surface par une observation des phénomènes visibles et en déduisent une représentation liant à la fois la physique et la géométrie. Ils retrouvent ainsi la loi de Laplace sur le saut de pression prenant place au travers d'un interface courbe entre deux fluides. En effet, lors de l'observation d'un volume de contrôle avec deux milieux de natures différentes séparés par une interface S (voir figure 1.3), la mesure du travail nécessaire pour provoquer une variation de volume due au déplacement infinitésimal de l'interface $\delta\zeta$ peut s'écrire comme une intégration surfacique des variations de pressions :

$$\text{Travail} = -\int\int \left(P_1 - P_2\right) \delta\zeta dS.$$

Cependant, pour écrire le travail δR du déplacement total de la surface, le travail lié à la variation d'aire de la surface de séparation $\sigma\delta S$ doit être ajouté, où σ est la tension superficielle et δS est la variation de l'aire de la surface.

$$\delta R = \sigma\delta S - \int\int \left(P_1 - P_2\right) \delta\zeta dS.$$

À noter que la condition d'équilibre mécanique est vérifiée pour $\delta R = 0$.

Définissons maintenant R_1 et R_2 les rayons de courbure en un point de la surface, définis positifs si orientés vers le milieu 1 (voir figure 1.4). Lors du déplacement infinitésimal, les

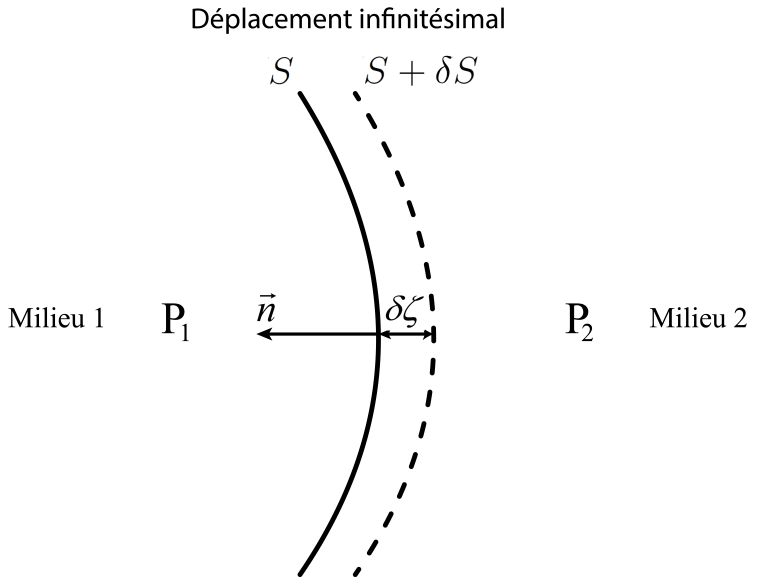

Figure 1.3: Représentation du déplacement infinitésimal d'une interface.

éléments de longueur dl_1 et dl_2, qui sont ici des éléments de la circonférence du cercle de rayon R_1 et du cercle de rayon R_2 formant eux-mêmes une ellipsoïde, subissent des accroissements égaux à :

$$\frac{\delta\zeta}{R_1}dl_1, \frac{\delta\zeta}{R_2}dl_2.$$

Après déplacement, l'élément de surface $dS' = dl_1 dl_2$ devient :

$$dS' = dl_1\left(1+\frac{\delta\zeta}{R_1}\right)dl_2\left(1+\frac{\delta\zeta}{R_2}\right) \approx dl_1 dl_2\left(1+\frac{\delta\zeta}{R_1}+\frac{\delta\zeta}{R_2}\right),$$

soit une variation de :

$$\delta S' = dl_1 dl_2 \delta\zeta\left(\frac{1}{R_1}+\frac{1}{R_2}\right).$$

Ainsi la variation totale de l'aire de la surface de séparation est :

$$\delta S = \int\int \delta\zeta\left(\frac{1}{R_1}+\frac{1}{R_2}\right)dS.$$

Donc la condition d'équilibre est respectée si :

$$\int\int \delta\zeta\left((P_1-P_2)-\sigma\left(\frac{1}{R_1}+\frac{1}{R_2}\right)\right)dS = 0,$$

or ceci doit être vrai pour tous les déplacements infinitésimaux arbitraires, donc $\forall\delta\zeta$, et ainsi la loi de Laplace est obtenu sous l'hypothèse que le coefficient de tension superficielle soit constant le long de la surface ($\sigma = \text{cst}$) :

$$P_1 - P_2 = \sigma\left(\frac{1}{R_1}+\frac{1}{R_2}\right). \tag{1.1}$$

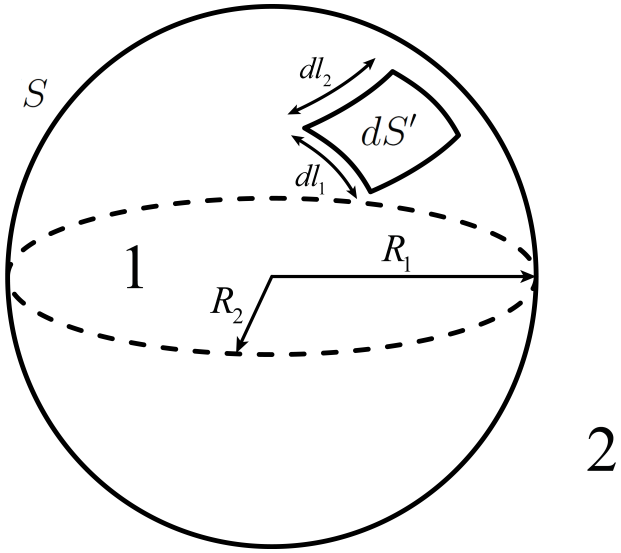

Figure 1.4: Représentation des rayons de courbure d'une surface entre deux milieux.

À noter qu'à l'état d'équilibre, la tension de surface tend vers un minimum d'énergie et donc tend à réduire au minimum la surface de l'interface, ce qui indique donc que cet interface sera dans un état stable sous une forme sphérique ($R_1 = R_2$). De plus, comme annoncé précédemment, il est important de noter ici que la description physique des effets capillaires passe par une description géométrique. En effet, l'expression du saut de pression de Laplace dépend d'une partie physique, ici exprimée par le coefficient de tension de surface σ, et d'une partie géométrique, ici décrite par les rayons de courbures, R_1 et R_2, qui représentent donc l'agencement des deux milieux séparés par une interface. Ainsi, pour traiter correctement les problèmes faisant intervenir la capillarité, il est important de bien distinguer ce qui dépend de la physique et ce qui dépend de la géométrie (point qui est utilisé et détaillé lors de l'établissement du nouveau modèle section 1.3 et chapitre 2).

Prenons un exemple pour illustrer ce que représente le saut de pression de Laplace. On sait que pour chaque couple possible de fluides il existe une tension de surface s'exercant au niveau de l'interface entre ces deux fluides. Cette tension est proportionelle au coefficient de tension de surface qui lui-même dépend principalement du couple en question mais aussi de la température de l'interface. Quelques valeurs de ces coefficients pour différents couples de fluides (liquide-gaz) à température ambiante de 20°C sont :

- Eau-Air : $\sigma = 72,8 \cdot 10^{-3} N.m^{-1}$,
- Éthanol-Air : $\sigma = 22,27 \cdot 10^{-3} N.m^{-1}$,
- Mercure-Air : $\sigma = 436 \cdot 10^{-3} N.m^{-1}$,

et un dernier exemple peut-être la valeur du couple eau-air mais cette fois-ci dans une condition de température de 100°C (eau liquide) : $\sigma = 58,85 \cdot 10^{-3} N.m^{-1}$. On remarque ainsi que les valeurs de ces coefficients peuvent varier considérablement en fonction des deux variables précédemment cités (couple et température). Considérons donc une goutte

d'eau dans un environnement composé d'air et à température ambiante de 20°C. Donnons nous une taille de goutte de rayon $R = 1mm$. Finalement, l'application de la loi de Laplace (1.1) nous permet de déterminer le saut de pression présent entre l'intérieur de la goutte (pression P_1) et l'air ambiant (pression P_2) :

$$P_1 - P_2 = \frac{2\sigma}{R} = 145,6Pa.$$

A noter que pour un couple et une température données, plus la goutte est de taille réduite, plus le saut de pression est important.

1.2.1.2 Ajout des forces visqueuses et des forces tangentielles de la tension de surface

Positionnons-nous dans un cas où nous n'avons pas de tension de surface. À la frontière de séparation de deux fluides une égalité des forces de frottements s'exerce sur la surface des deux fluides, cette égalité s'exprime :

$$\left(\overline{\overline{\tau}}_2 - \overline{\overline{\tau}}_1\right) \cdot \mathbf{n} = 0,$$

avec $\overline{\overline{\tau}}$ tenseurs de contraintes et $\mathbf{n}$ la normale à la surface.

Si l'on tient compte maintenant de la tension superficielle, on doit faire figurer dans cette équation une force supplémentaire dont la valeur est donnée par la loi de Laplace (1.1) dirigée suivant la normale à la surface :

$$\left(\overline{\overline{\tau}}_2 - \overline{\overline{\tau}}_1\right) \cdot \mathbf{n} = \sigma \left(\frac{1}{R_1} + \frac{1}{R_2}\right) \mathbf{n}.$$

Que l'on peut réécrire sous une autre forme en décomposant les tenseurs de contraintes $\overline{\overline{\tau}}$ en une somme de tenseurs de pression $P\overline{\overline{I}}$ et de contraintes visqueuses $\overline{\overline{\tau}}_{vis}$:

$$\left(P_1 - P_2\right) \mathbf{n} = \left(\overline{\overline{\tau}}_{vis,1} - \overline{\overline{\tau}}_{vis,2}\right) \cdot \mathbf{n} + \sigma \left(\frac{1}{R_1} + \frac{1}{R_2}\right) \mathbf{n}.$$

Il est à noter que dans le cadre précédent nous n'étions pas dans le cas général. En effet, le coefficient de tension superficielle σ n'est pas nécessairement constant le long de la surface et ainsi l'intégration au long de celle-ci engendre une force supplémentaire dirigée suivant la tangente à cette surface. Or nous savons que la variabilité de la pression donne naissance à une force volumique. En effet, s'il n'y a aucune différence de pression, cette force volumique est nulle, cependant, dès lors qu'une différence existe, cette force volumique s'exprime comme $-\boldsymbol{\nabla} P$. Par analogie, il existe une force due à la variabilité de la tension de surface au niveau de l'interface seule puisque c'est seulement en ce lieu qu'il existe une tension de surface. Cette force sera donc une force tangentielle s'exerçant sur l'unité d'aire de la surface de séparation (interface) et est donnée par $\boldsymbol{\nabla}_t \sigma$. Le gradient est défini comme la somme du gradient tangentiel et normal à l'interface $\boldsymbol{\nabla} = \boldsymbol{\nabla}_n + \boldsymbol{\nabla}_t$. Un signe positif

est appliqué car les forces de tension cherchent à réduire l'aire de la surface alors que les forces de pression cherchent à accroître le volume. On a donc :

$$\left(P_1 - P_2 - \sigma\left(\frac{1}{R_1} + \frac{1}{R_2}\right)\right)\mathbf{n} = \left(\overline{\overline{\tau}}_{vis,1} - \overline{\overline{\tau}}_{vis,2}\right)\cdot\mathbf{n} + \boldsymbol{\nabla}_t\sigma. \tag{1.2}$$

On notera que cette condition ne peut être satisfaite que dans le cas d'un fluide visqueux. En effet, pour un fluide parfait $\overline{\overline{\tau}}_{vis} = \overline{\overline{0}}$, et donc le membre de gauche de l'égalité représente un vecteur dirigé suivant la normale, tandis que le membre restant de droite représente un vecteur dirigé suivant la tangente à la surface. Il est évident qu'une telle égalité est irréalisable (à l'exclusion du cas trivial où ces quantités sont chacune nulles). Ainsi, Landau et Lifshitz expriment ici le fait que les forces capillaires tangentielles, qui induisent l'effet Marangoni, n'ont lieu d'être que dans le seul cas où les forces visqueuses existent.

L'équation (1.2) exprime donc l'équilibre qu'il y a entre les différentes forces mises en jeu au niveau de l'interface. Cependant, il n'est pas si aisé de formuler à partir de cette équation des expressions des termes capillaires dans une équation de quantité de mouvement et/ou dans une équation d'énergie utilisées dans les modèles multiphasiques. En effet, les modèles s'énoncent sous une forme volumique, il y a donc une contradiction avec la forme surfacique exprimée précédemment. Ainsi, l'objectif de la prochaine section est de déterminer une forme permettant d'introduire ces termes capillaires dans un modèle basé sur une notion volumique.

1.2.2 Modélisation volumique de la capillarité pour les modèles multiphasiques

Au cours des dernières décennies, plusieurs études théoriques ont été réalisées pour traiter les effets capillaires dans les écoulements multiphasiques. Les travaux de Brackbill et al. [8] ont permis d'écrire une force surfacique en une force volumique, relativement simple à traiter comme terme source dans un modèle à écoulements multiphasiques. Cette force volumique de la tension de surface est exprimée grâce à une fonction couleur $\tilde{c}(\mathbf{x})$ et l'obtention de cette force fait donc l'objet de cette section. Cette approche a été utilisée dans de nombreuses simulations numériques (Chen et Doolen [12], Sussman et al. [87], Gueyffier et al. [25], Osher et Fedkiw [62, 63], Tryggvason et al. [94], Périgaud et Saurel [66], Le Martelot et al. [52]) où les effets capillaires sont ajoutés aux équations de quantité de mouvement et d'énergie.

1.2.2.1 Cas général

Réécrivons dans un premier temps l'équation générale (1.2) établie par Landau et Lifshitz avec une projection sur la normale et sur la tangente à l'interface, et où les tenseurs visqueux pour des fluides Newtoniens peuvent être réecrit de la manière suivante :

$$\overline{\overline{\tau}}_{vis,\gamma,\alpha\beta} = \mu_\gamma\left(\frac{\partial u_\alpha}{\partial x_\beta} + \frac{\partial u_\beta}{\partial x_\alpha}\right)_\gamma.$$

où μ est la viscosité dynamique, et γ, α et β sont les indices correspondant respectivement au fluide en question et aux deux sommations.

La projection de l'équation (1.2) sur la normale $\mathbf{n}$ à l'interface s'exprime alors :

$$P_1 - P_2 + \sigma\left(\frac{1}{R_1} + \frac{1}{R_2}\right) = 2\sum_{\alpha} \mu_1 n_\alpha \left(\frac{\partial u_\alpha}{\partial n}\right)_1 - \mu_2 n_\alpha \left(\frac{\partial u_\alpha}{\partial n}\right)_2, \tag{1.3}$$

où :

$$\frac{\partial}{\partial n} = \mathbf{n} \cdot \boldsymbol{\nabla},$$

et la projection sur la tangente $\mathbf{t}$ à l'interface s'exprime :

$$\sum_{\alpha\beta} \mu_2 \left(t_\alpha \frac{\partial u_\alpha}{\partial n} + n_\beta \frac{\partial u_\beta}{\partial t}\right)_2 - \mu_1 \left(t_\alpha \frac{\partial u_\alpha}{\partial n} + n_\beta \frac{\partial u_\beta}{\partial t}\right)_1 = \frac{\partial \sigma}{\partial t}, \tag{1.4}$$

où :

$$\frac{\partial}{\partial t} = \mathbf{t} \cdot \boldsymbol{\nabla}.$$

Pour traiter correctement la suite, on doit tout d'abord définir les gradients normal et tangentiel, ainsi que la courbure.

1.2.2.2 Définitions des gradients et courbures

Le gradient normal s'exprime :

$$\boldsymbol{\nabla}_n = \mathbf{n}\left(\mathbf{n} \cdot \boldsymbol{\nabla}\right),$$

et donc indirectement le gradient tangentiel :

$$\boldsymbol{\nabla}_t = \boldsymbol{\nabla} - \boldsymbol{\nabla}_n.$$

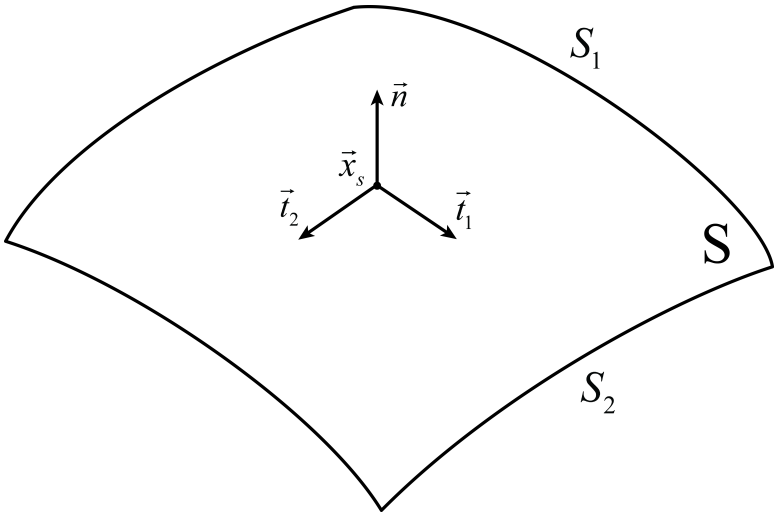

Figure 1.5: Représentation d'une surface quelconque.

Pour définir la courbure, considérons une interface S en trois dimensions (figure 1.5). À chaque point $\mathbf{x}_S$, sur S, on peut définir un ensemble de vecteurs de base orthonormée $(\mathbf{t}_1, \mathbf{t}_2, \mathbf{n})$, où $\mathbf{t}_1$ et $\mathbf{t}_2$ sont dans le plan tangent et $\mathbf{n}$ est l'unité normale à S. Deux courbes sur S, S_1 et S_2, peuvent être associés à ce système de coordonnées, avec S_1 le long de $\mathbf{t}_1$ et S_2 le long de $\mathbf{t}_2$. Ainsi on peut définir les vecteurs de courbure $\boldsymbol{\kappa}_1$ et $\boldsymbol{\kappa}_2$ comme :

$$\boldsymbol{\kappa}_1 \equiv \frac{d\mathbf{t}_1}{dS_1} = (\mathbf{t}_1 \cdot \boldsymbol{\nabla})\,\mathbf{t}_1, \boldsymbol{\kappa}_2 \equiv \frac{d\mathbf{t}_2}{dS_2} = (\mathbf{t}_2 \cdot \boldsymbol{\nabla})\,\mathbf{t}_2.$$

La courbure, κ, est alors définie comme la somme géométrique des deux courbures $\kappa_1 = \|\boldsymbol{\kappa}_1\|$ et $\kappa_2 = \|\boldsymbol{\kappa}_2\|$:

$$\kappa\left(\mathbf{x}_S\right) = \kappa_1\left(\mathbf{x}_S\right) + \kappa_2\left(\mathbf{x}_S\right),$$

On remarque que :

$$\kappa \neq \sqrt{\kappa_1^2 + \kappa_2^2},$$

et donc que le vecteur de courbure $\boldsymbol{\kappa}$ n'est pas la somme vectorielle de $\boldsymbol{\kappa}_1$ et $\boldsymbol{\kappa}_2$:

$$\boldsymbol{\kappa} \neq \boldsymbol{\kappa}_1 + \boldsymbol{\kappa}_2.$$

1.2.2.3 Force surfacique de la tension de surface

La courbure κ est définie, cependant, l'utilisation sous cette expression reste difficile en raison de la nécessité de connaître S_1 et S_2. C'est pourquoi une autre formulation est nécessaire. Pour cela, un élément d'aire $\delta\mathbf{A} = \mathbf{n}\delta A$ au point $\mathbf{x}_S$ sur S est défini (figure 1.6). C représente une courbe incluant cet élément et a une longueur d'arc élémentaire dl. La force surfacique exercée sur l'élément δA par ce qui l'entoure et qui traverse la ligne élémentaire dl est égale à $\sigma\mathbf{t}dl$, où $\mathbf{t}$ est la tangente unitaire à S perpendiculaire au vecteur arc élémentaire $\mathbf{dl}$.

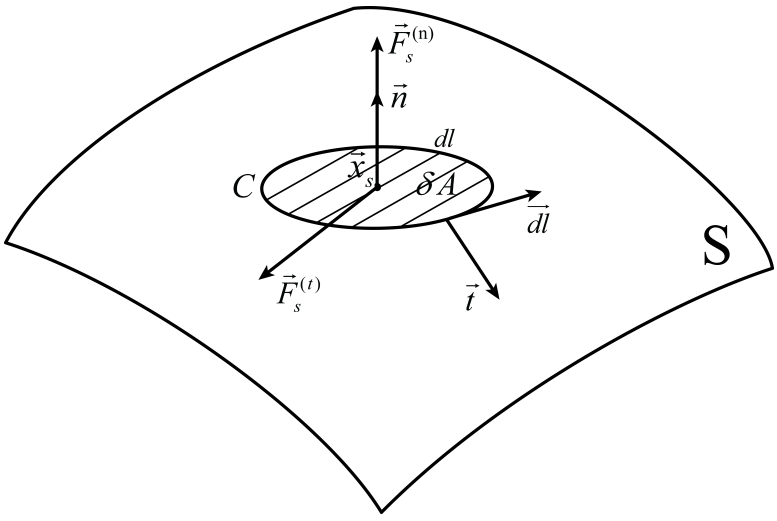

Figure 1.6: Représentation d'une surface quelconque avec les différentes forces opérant sur un élément d'aire de cette surface.

La force surfacique nette s'appliquant sur l'élément δA, $\mathbf{F}_{SA}\delta A$ correspond à la somme de toutes les forces $\sigma\mathbf{t}dl$ exercées sur chaque élément de la longueur d'arc dl et s'exprime donc :

$$\mathbf{F}_{SA}\delta A = \oint_C \mathbf{F}_S dl = \oint_C \sigma\mathbf{t}dl.$$

Or $\mathbf{t}dl = \mathbf{dl} \times \mathbf{n}$ donc :

$$\mathbf{F}_{SA}\delta A = \oint_C \mathbf{dl} \times \mathbf{n}\sigma.$$

En utilisant le théorème de Stokes on obtient :

$$\mathbf{F}_{SA}\delta A = \int\int_S (\mathbf{n} \times \boldsymbol{\nabla}) \times \mathbf{n}\sigma dA,$$

et pour $\delta A \to 0$:

$$\mathbf{F}_{SA}\delta A = \delta A \left((\mathbf{n} \times \boldsymbol{\nabla}) \times \mathbf{n}\sigma\right).$$

Ainsi, toujours dans la limite où $\delta A \to 0$ et en appliquant l'opérateur différentiel à la fois sur $\mathbf{n}$ et σ, la force surfacique s'exprime :

$$\mathbf{F}_{SA} = (\mathbf{n} \times \boldsymbol{\nabla}) \times \mathbf{n}\sigma = \sigma (\mathbf{n} \times \boldsymbol{\nabla}) \times \mathbf{n} + (\mathbf{n} \times \boldsymbol{\nabla}\sigma) \times \mathbf{n}. \tag{1.5}$$

En utilisant l'opérateur différentiel précédemment exprimé comme étant la somme des opérateurs normal et surfacique (tangentiel) et du fait que par définition $\mathbf{n} \times \boldsymbol{\nabla}_n = 0$, on peut écrire que $\mathbf{n} \times \boldsymbol{\nabla} = \mathbf{n} \times \boldsymbol{\nabla}_t$. Couplé aux relations d'identités, le premier terme quasi-complet (sans σ) du membre de droite de l'équation (1.5) peut s'exprimer comme :

$$(\mathbf{n} \times \boldsymbol{\nabla}_t) \times \mathbf{n} = \mathbf{n} \times (\boldsymbol{\nabla}_t \times \mathbf{n}) = \boldsymbol{\nabla}_t \left(\frac{\mathbf{n}^2}{2}\right) - (\mathbf{n} \cdot \boldsymbol{\nabla}_t)\,\mathbf{n} = -\mathbf{n}\,(\boldsymbol{\nabla}_t \cdot \mathbf{n}),$$

et le second terme comme :

$$(\mathbf{n} \times \boldsymbol{\nabla}\sigma) \times \mathbf{n} = (\mathbf{n} \cdot \mathbf{n})\,\boldsymbol{\nabla}\sigma - \mathbf{n}\,(\mathbf{n} \cdot \boldsymbol{\nabla})\,\sigma = \boldsymbol{\nabla}\sigma - \boldsymbol{\nabla}_n\sigma = \boldsymbol{\nabla}_t\sigma.$$

Finalement, la force surfacique sur l'élément s'exprime :

$$\mathbf{F}_{SA}(\mathbf{x}_S) = \mathbf{F}_{SA}^{(n)}(\mathbf{x}_S) + \mathbf{F}_{SA}^{(t)}(\mathbf{x}_S), \tag{1.6}$$

où $\mathbf{F}_{SA}^{(n)}(\mathbf{x}_S) = -\sigma\mathbf{n}\,(\boldsymbol{\nabla}_t \cdot \mathbf{n})$ et $\mathbf{F}_{SA}^{(t)}(\mathbf{x}_S) = \boldsymbol{\nabla}_t\sigma$. La courbure peut maintenant être identifiée à travers $\mathbf{F}_{SA}^{(n)}(\mathbf{x}_S)$:

$$\mathbf{F}_{SA}^{(n)}(\mathbf{x}_S) = \sigma\mathbf{n}\kappa,$$

où $\kappa = -(\boldsymbol{\nabla}_t \cdot \mathbf{n})$. Donc le vecteur de courbure est donné par $\kappa = \mathbf{n}\kappa$, et puisque $\boldsymbol{\nabla}_n \cdot \mathbf{n} = 0$, la courbure peut se réécrire :

$$\kappa = -(\boldsymbol{\nabla} \cdot \mathbf{n}). \tag{1.7}$$

De cette manière, la courbure peut aisément être calculée puisque le vecteur unitaire normal à l'interface, $\mathbf{n}$, est obtenu à partir de la fonction couleur $\tilde{c}$, qui est définie dans la section suivante (1.2.2.4), et $\mathbf{n}$ est défini par :

$$\mathbf{n}(\mathbf{x}) = \frac{\boldsymbol{\nabla}\tilde{c}(\mathbf{x})}{\|\boldsymbol{\nabla}\tilde{c}(\mathbf{x})\|}. \tag{1.8}$$

1.2.2.4 Fonction couleur

Pour déterminer la valeur de κ en tout point d'un système, il est nécessaire de calculer la normale à l'interface d'après (1.8). Celle-ci étant elle-même calculée par le biais d'une fonction couleur qui permet de situer l'interface.

Brackbill et al. définissent la fonction couleur comme une fonction caractéristique discontinue qui prend donc des valeurs différentes dans chacun des fluides et au niveau de l'interface :

$$\tilde{c}(\mathbf{x}) = \begin{cases} c_1 & \text{dans le fluide 1,} \\ c_2 & \text{dans le fluide 2,} \\ \langle c \rangle = \frac{c_1+c_2}{2} & \text{à l'interface.} \end{cases} \tag{1.9}$$

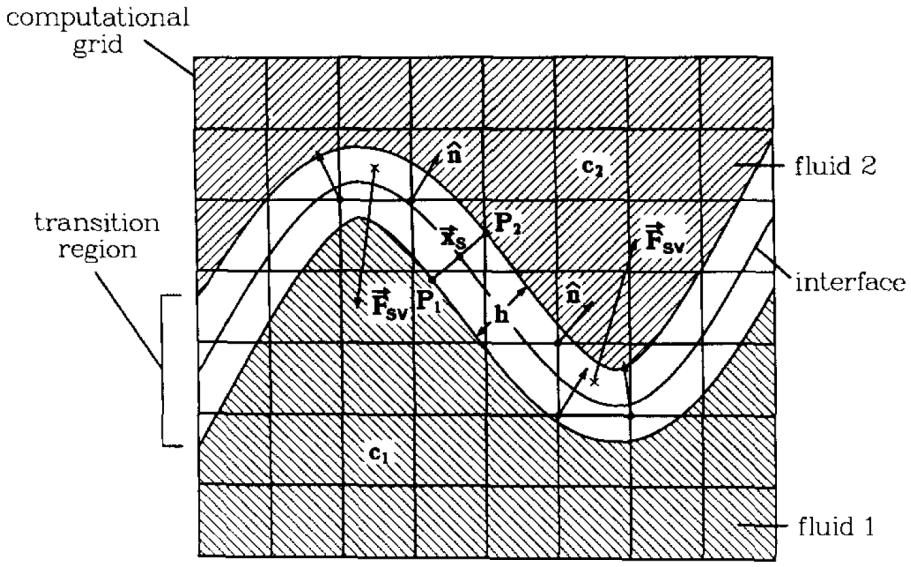

Figure 1.7: Réimprimé de Brackbill et al. [8]. Schéma représentant les coutours de la fonction couleur $\tilde{c}$ qui séparent les fluides avec une valeur c_1 pour l'un des deux fluides et c_2 pour l'autre. La zone de transition (claire) a une épaisseur h. Les normales et les forces de tension de surface sont aussi apparentes. © 1992, Academic Press, Inc.

Cependant, un interface n'est jamais physiquement discontinue et a donc une certaine épaisseur. Ainsi, pour respecter la notion de continuité, la fonction caractéristique discontinue de la fonction couleur est ainsi remplacée par une variation lissée de la couleur du mélange $\tilde{c}(\mathbf{x})$, passant donc d'une valeur c_1 dans un fluide à une valeur c_2 dans un autre, sur une distance $O(h)$, où h est une longueur comparable à l'épaisseur d'un interface. On considère ainsi une zone de transition entre les deux fluides (figure 1.7). La valeur de $\tilde{c}$ est donnée par une interpolation avec cette zone de transition qui remplace l'interface : $c_1 \leqslant \tilde{c}(\mathbf{x}) \leqslant c_2$. Ainsi la courbure varie continuement d'un contour à l'autre quand $Kh < 1$.

Puisque la fonction couleur localise l'interface, elle obéit à une équation de transport :

$$\frac{\partial \tilde{c}(\mathbf{x})}{\partial t} + \mathbf{u}_I \cdot \boldsymbol{\nabla} \tilde{c}(\mathbf{x}) = 0,$$

où $\mathbf{u}_I$ est la vitesse de l'interface.

À noter que Brackbill et al. proposent de considérer la densité dans le rôle de fonction caractéristique pour des écoulements de fluides incompressibles. Une notion que nous voulons écarter puisque l'idée première que nous proposons est de complétement distinguer ce qui dépend de la géométrie de ce qui dépend de la physique.

1.2.2.5 Simplification du problème

Dans le cadre général, la modélisation des effets capillaires pose de nombreuses complications. En effet, la prise en compte des termes visqueux complexifient l'expression sur la normale, voir équation (1.3), et donc par la suite la modélisation des forces capillaires s'y appliquant. Puis, la prise en compte de la variabilité du coefficient de tension de surface le long de l'interface, traduit par des termes tangentielles dans l'équation (1.4), est un point difficile car il est nécessaire de correctement comprendre et donc modéliser cette variation qui dépend de multiples effets comme par exemple la différence de température entre deux positions de l'interface.

Brackbill et al. proposent donc de réaliser une simplification du problème pour modéliser les effets capillaires. Les hypothèses sont les suivantes :

- Le coefficient de tension de surface est considéré constant $\sigma = cste$, ce qui élimine les termes tangentiels,
- Les fluides sont considérés comme non visqueux ($\mu = 0$).

Ainsi l'expression du saut de pression de Laplace décrit par Landau et Lifshitz, équation (1.1), est retrouvée :

$$[P] \equiv P_2 - P_1 = \sigma\kappa,$$

où $\kappa = 1/R_1 + 1/R_2$, et une analogie peut être opérée avec la force surfacique précédemment décrite. Cette force étant désormais seulement portée par la normale, l'équation (1.6) devient :

$$\mathbf{F}_{SA}(\mathbf{x}_S) = \mathbf{F}_{SA}^{(n)}(\mathbf{x}_S) = \sigma\kappa(\mathbf{x}_S)\,\mathbf{n}(\mathbf{x}_S), \tag{1.10}$$

où $\sigma\kappa$ représente la tension de surface portée par la normale $\mathbf{n}(\mathbf{x}_S)$ par unité d'aire interfaciale A au point $(\mathbf{x}_S)$ sur A.

1.2.2.6 Établissement de la force volumique de la tension de surface

Rappelons que l'objectif est d'obtenir une expression sous forme volumique de la force de tension de surface. Cette force volumique permet de traiter relativement simplement les effets capillaires dans un modèle à écoulements multiphasiques et où elle est introduite sous forme de terme source.

Considérons donc une force volumique $\mathbf{F}_v(\mathbf{x})$ donnant la correcte force de tension de surface par unité d'aire interfaciale $\mathbf{F}_{SA}(\mathbf{x}_S)$ quand $h \to 0$:

$$\lim_{h\to 0} \int\int\int_{\Delta V} \mathbf{F}_v(\mathbf{x})\, d^3x = \int\int_{\Delta A} \mathbf{F}_{SA}(\mathbf{x}_S)\, dA, \tag{1.11}$$

où l'aire intégrée correspond à une portion ΔA de l'interface étendue sur un volume réduit de l'intégration ΔV. Ce volume est donc construit de manière à ce que ses bords soient normaux à la surface et que son épaisseur h soit petite comparée au rayon de courbure de l'interface A. De plus, il est nécessaire que $\mathbf{F}_v(\mathbf{x})$ soit une force localisée au niveau de l'interface et donc que sa valeur soit nulle en dehors de la région associée à cette interface :

$$\mathbf{F}_v(\mathbf{x}) = \mathbf{0} \text{ pour } \mathbf{n}(\mathbf{x}_S) \cdot (\mathbf{x} - \mathbf{x}_S) \geqslant h.$$

Brackbill et al. réalisent ensuite une étude à la limite au niveau de l'interface A quand l'épaisseur de celui-ci h tend vers 0 et en utilisant une fonction d'interpolation ϕ pour la variation de la fonction couleur sur la zone de transition. Ils expriment ainsi le gradient de la fonction couleur $\boldsymbol{\nabla}\tilde{c}(\mathbf{x})$ sous forme d'intégrale surfacique sur l'interface :

$$\boldsymbol{\nabla}\tilde{c}(\mathbf{x}) = \frac{[c]}{h^3} \int\int_A \mathbf{n}(\mathbf{x}_S)\, \phi(\mathbf{x} - \mathbf{x}_S)\, dA,$$

où le saut de couleur s'exprime comme $[c] = c_2 - c_1$. Par la suite, ils expriment sous une forme d'intégrale volumique sur un volume V l'intégrale surfacique de $\mathbf{F}_{SA}$ sur l'interface (détails dans [8]) :

$$\int\int_A \mathbf{F}_{SA}(\mathbf{x}_S)\, dA = \lim_{h\to 0} \int\int\int_V \sigma\kappa(\mathbf{x}) \frac{\boldsymbol{\nabla}\tilde{c}(\mathbf{x})}{[c]} d^3x.$$

Par identification entre ce résultat et l'égalité posée au départ (équation (1.11)), nous déterminons l'expression de la force volumique de tension de surface $\mathbf{F}_v(\mathbf{x})$:

$$\lim_{h\to 0} \int\int\int_V \mathbf{F}_v(\mathbf{x})\, d^3x = \lim_{h\to 0} \int\int\int_V \sigma\kappa(\mathbf{x}) \frac{\boldsymbol{\nabla}\tilde{c}(\mathbf{x})}{[c]} d^3x,$$

$$\mathbf{F}_v(\mathbf{x}) = \sigma\kappa(\mathbf{x}) \frac{\boldsymbol{\nabla}\tilde{c}(\mathbf{x})}{[c]}, \tag{1.12}$$

où l'on rappelle que la courbure s'exprime, équation (1.7) :

$$\kappa = -(\boldsymbol{\nabla} \cdot \mathbf{n}),$$

et la normale à l'interface, équation (1.8) :

$$\mathbf{n} = \frac{\boldsymbol{\nabla}\tilde{c}(\mathbf{x})}{\|\boldsymbol{\nabla}\tilde{c}(\mathbf{x})\|}.$$

Cette force volumique peut ainsi être introduite dans divers modèles compressibles ou incompressibles. Elle apparait donc sous cette forme, c'est-à-dire comme terme source, dans l'équation de quantité de mouvement du mélange et son travail $\mathbf{F}_v \cdot \mathbf{u}$, toujours comme terme source, apparait lui dans l'équation d'énergie du mélange. Le problème de cette formulation est donc le fait qu'elle soit un terme source, ce qui engendre évidemment la perte de la conservation de la quantité de mouvement et de l'énergie. Ainsi, le premier objectif de cette thèse est d'introduire cette force sous une forme conservative dans un nouveau modèle pour traiter les écoulements compressibles avec effets capillaires, cela fait l'object de la prochaine section et du chapitre 2.

1.3 Un nouveau modèle et une nouvelle méthode numérique pour les écoulements compressibles avec effets capillaires

Cette section est une introduction du chapitre 2 correspondant à l'article [82] et donc seulement les principales contributions sont présentées ici. Un nouveau modèle pour les problèmes d'interface avec effets capillaires dans les fluides compressibles est présenté avec une nouvelle méthode numérique spécifique pour traiter les écoulements capillaires et la propagation des ondes acoustiques. Ce nouveau modèle multiphasique est en accord avec les principes physiques de conservation et respecte la seconde loi de la thermodynamique. Dans la nouvelle méthode numérique, le système global d'équations est divisé en plusieurs sous-modèles. Chaque sous-modèle est hyperbolique ou faiblement hyperbolique et peut être résolu avec une méthode numérique adéquate. Cette méthode est testée et validée grâce à des comparaisons avec des solutions analytiques (loi de Laplace) et à des résultats expérimentaux sur l'éclatement d'une goutte par une onde de choc.

1.3.1 Méthode à interface raide ou méthode à interface diffuse

Faisons tout d'abord un point rapide sur les deux grandes familles de méthodes numériques pour traiter les problèmes à interface :

- La première famille de méthodes considère les interfaces comme raides. Les interfaces raides peuvent être obtenues en utilisant des méthodes de suivi d'interface, où habituellement une fonction, dite de "level-set", suit l'interface (Osher et Sethian [64]). Cependant, de telles formulations impliquent souvent des modifications des systèmes d'équations. Par exemple, une équation d'évolution de la pression peut remplacer l'équation d'énergie autour des interfaces (Karni [44, 45]). Dans la méthode "Ghost Fluid" (Fedkiw et al. [21]) et sa version simplifiée (Koren et al. [48]), des variables thermodynamiquement similaires sont ajoutées dans les interfaces. Ces méthodes ne génèrent pas d'oscillations parasites dans les interfaces, mais fondamentalement elles ne sont pas conservatives (Liu et al. [54]). Des progrès ont été réalisés récemment concernant cet aspect (Hu et al. [35], Luo et al. [55], Han et al. [29], Schranner et al. [83]). Cependant, du fait de leur nature non conservative, ces méthodes ne sont pas très fiables lorsque apparaissent des problèmes faisant intervenir des ondes de choc. En effet, on ne garantit pas le traitement correct de propagation des ondes dans le milieu, tout particulièrement au niveau de l'interface.

- La seconde famille de méthodes s'appelle méthodes d'interface diffuse. Dans cette classe de méthodes, les interfaces ne sont pas explicitement suivies et sont autorisées à se diffuser numériquement (Abgrall et Karni [2], Saurel et Abgrall [76]). Ces méthodes sont particulièrement intéressantes car elles sont capables de faire face à l'apparition et à la disparition dynamique des interfaces. En outre, c'est aussi la seule classe de modèles où la thermodynamique des cellules de mélange est bien définie, grâce à une équation d'état spécifique pour chaque phase (liquide ou gaz).

La seconde famille de méthodes dite d'interface diffuse est donc celle utilisée dans la suite de ce manuscrit. Ainsi, plus de précisions concernant cette famille sont données ci-dessous (section 1.3.2) et dans le chapitre 2. De plus, une revue plus complète sur chacune de ces deux familles est accessible dans la thèse de Petitpas [67].

1.3.2 Écoulements compressibles capillaires : l'état de l'art

L'étude des effets capillaires dans le cadre des méthodes à interfaces diffuses repose sur la généralisation du modèle Allaire et al. [4] qui n'inclut pas initialement les effets capillaires. Périgaud et Saurel [66] ont étendu ce modèle en les incluant et où la force volumique de tension de surface, équation (1.12), apparaît comme un terme de flux dans l'équation de quantité de mouvement. Il est de même pour le travail de cette force $\mathbf{F}_v(\mathbf{x}) \cdot \mathbf{u}$ dans l'équation d'énergie totale. Dans cette référence, comme dans Gueyffier et al. [25] dans le cadre des écoulements incompressibles, une formulation conservative a été obtenue :

$$\begin{cases} \frac{\partial \alpha_1}{\partial t} + \mathbf{u} \cdot \boldsymbol{\nabla} \alpha_1 & = 0, \\ \frac{\partial \alpha_k \rho_k}{\partial t} + \boldsymbol{\nabla} \cdot (\alpha_k \rho_k \mathbf{u}) & = 0, \\ \frac{\partial \rho \mathbf{u}}{\partial t} + \boldsymbol{\nabla} \cdot \left(\rho \mathbf{u} \otimes \mathbf{u} + P \overline{\overline{I}} - \sigma \left(\|\boldsymbol{\nabla} \alpha_1\| \overline{\overline{I}} - \frac{\boldsymbol{\nabla} \alpha_1 \otimes \boldsymbol{\nabla} \alpha_1}{\|\boldsymbol{\nabla} \alpha_1\|} \right) \right) & = 0, \\ \frac{\partial \rho E + \varepsilon_\sigma}{\partial t} + \boldsymbol{\nabla} \cdot \left(\mathbf{u} \left(\rho E + \varepsilon_\sigma + P \right) - \sigma \left(\|\boldsymbol{\nabla} \alpha_1\| \overline{\overline{I}} - \frac{\boldsymbol{\nabla} \alpha_1 \otimes \boldsymbol{\nabla} \alpha_1}{\|\boldsymbol{\nabla} \alpha_1\|} \right) \cdot \mathbf{u} \right) & = 0, \end{cases}$$

où α_k et ρ_k sont la fraction volumique et la densité de la phase k. ρ, $\mathbf{u}$, P, $E = e + \frac{1}{2}\|\mathbf{u}\|^2$ et e sont respectivement les variables de mélange pour la densité, la vitesse, la pression, l'énergie totale et l'énergie interne. L'énergie interne du mélange est définie comme $e = \sum_k Y_k e_k(\rho_k, P)$ et chaque fluide est régi par sa propre équation d'état $e_k = e_k(\rho_k, P)$. L'introduction des effets capillaires dans les flux (formulation conservative) conduit à un nouveau terme dans l'équation d'énergie totale du mélange, $\varepsilon_\sigma = \sigma \|\boldsymbol{\nabla} \alpha_1\|$ qui est défini comme une énergie potentielle capillaire. Notez que α_1 obéit à une équation de transport et joue dans ce modèle le rôle de la fonction couleur (1.9) puisque que la vitesse de l'interface est égal à celle du fluide ($\mathbf{u}_I = \mathbf{u}$) lorsque l'équilibre des vitesses est considéré. Dans [66], les auteurs ont utilisé une fermeture d'équilibre de pression, permettant la résolution de problèmes d'interface dédiés aux écoulements à grande vitesse. Cependant, comme pour le modèle d'Allaire et al. [4], la seconde loi de la thermodynamique n'est vérifiée que si la condition d'équilibre thermique $T = T_k$, avec $k = \{1, 2\}$, est aussi retenue. Pour ce modèle, la fermeture d'équilibre de pression seule ne permet donc pas de respecter la deuxième loi de la thermodynamique pour le mélange.

Le Martelot et al. [52] ont corrigé cet inconvénient en incluant les effets capillaires dans un système d'équations d'équilibre des vitesses, des pressions et des températures en considérant la fraction de masse comme la fonction de couleur : la seconde loi de la thermodynamique est alors respectée. Cependant, les vitesses caractéristiques ont été estimées sous l'hypothèse que la courbure locale est fixée. Même si une telle approche est physiquement raisonnable, elle ne nous permet pas d'estimer rigoureusement les vitesses de propagation. En outre, la fermeture de l'équilibre thermique est raisonnable pour la description du phénomène d'ébullition, mais elle est trop forte pour l'étude de l'éclatement d'une goutte par un écoulement à grande vitesse. En effet, rien ne nous garantit que

l'équilibre thermique soit physiquement présent lors d'études sur des dynamiques rapides, notamment avec des ondes de choc.

Il apparait alors évident que l'introduction d'un nouveau modèle ayant des vitesses d'ondes clairement définies avec les effets capillaires sous une forme conservative, et qui peut encore être compatible avec l'augmentation de l'entropie du mélange sans l'hypothèse d'équilibre des températures, est nécessaire.

1.3.3 Le nouveau modèle

Le nouveau modèle que nous proposons est basé sur celui de Kapila et al. [43]. Ce dernier modèle s'est révélé approprié pour traiter les problèmes à interfaces entre fluides compressibles. Plusieurs extensions de ce modèle ont été développées pour résoudre plusieurs problèmes concrets liés à la transition de phase (Massoni et al. [56], Saurel et al. [79]), à la cavitation (Petitpas et al. [69]), à la détonation dans des matériaux hautements énergétiques (Petitpas et al. [70]), à l'interaction solide-fluide et la compaction des milieux granulaires (Favrie et Gavrilyuk [19, 18]) et aux écoulements à faible nombre de Mach (Murrone et Guillard [60]). Il considère les écoulements compressibles à deux phases en équilibre mécanique (équilibre des pressions et des vitesses). Dans ce modèle, la fraction volumique obéit à l'équation suivante provenant de la condition d'équilibre de la pression :

$$\frac{\partial \alpha_1}{\partial t} + \mathbf{u} \cdot \boldsymbol{\nabla} \alpha_1 = K \boldsymbol{\nabla} \cdot \mathbf{u},$$

où le terme $K\boldsymbol{\nabla} \cdot \mathbf{u}$ représente les différences dans le comportement acoustique des deux phases. K est donné par :

$$K = \frac{\rho_2 a_2^2 - \rho_1 a_1^2}{\frac{\rho_2 a_2^2}{\alpha_2} + \frac{\rho_1 a_1^2}{\alpha_1}},$$

a_k étant la vitesse du son de la phase k.

Les effets capillaires sont ensuite ajoutés sous une forme conservative. Comme expliqué précédemment dans la section 1.2, ces effets capillaires doivent faire intervenir deux notions que nous tenons à distinguer et qui sont la physique et la géométrie. Ainsi, nous choisissons de conserver le fait que la fonction couleur soit une variable purement géométrique et donc une équation supplémentaire pour celle-ci est ajoutée. On montrera par la suite que l'introduction de cette équation supplémentaire est un ingrédient important pour l'étude d'hyperbolicité. Deux méthodologies s'offrent à nous pour l'obtention du nouveau modèle. La première méthode est d'ajouter la force de tension de surface de Brackbill et al. et son travail au modèle de Kapila et al., puis de les modifier sous une forme conservative. La seconde consiste à se donner une énergie, prenant bien entendu en compte l'énergie capillaire, et à appliquer le principe de Hamilton pour la dérivation du modèle. Le modèle

final est donc le suivant :

$$\begin{cases} \frac{\partial \alpha_1}{\partial t} + \mathbf{u}\cdot\boldsymbol{\nabla}\alpha_1 - K\boldsymbol{\nabla}\cdot\mathbf{u} & = 0, \\ \frac{\partial \alpha_k\rho_k}{\partial t} + \boldsymbol{\nabla}\cdot(\alpha_k\rho_k\mathbf{u}) & = 0, \\ \frac{\partial \rho\mathbf{u}}{\partial t} + \boldsymbol{\nabla}\cdot\left(\rho\mathbf{u}\otimes\mathbf{u} + P\overline{\overline{I}} + \overline{\overline{\Omega}}\right) & = 0, \\ \frac{\partial \rho E+\varepsilon_\sigma}{\partial t} + \boldsymbol{\nabla}\cdot\left((\rho E + \varepsilon_\sigma + P)\,\mathbf{u} + \overline{\overline{\Omega}}\cdot\mathbf{u}\right) & = 0, \\ \frac{\partial c}{\partial t} + \mathbf{u}\cdot\boldsymbol{\nabla}c & = 0, \end{cases} \tag{1.13}$$

avec $\overline{\overline{\Omega}}$ étant le tenseur capillaire donné par :

$$\overline{\overline{\Omega}} = -\sigma\left(\|\boldsymbol{\nabla}c\|\overline{\overline{I}} - \frac{\boldsymbol{\nabla}c\otimes\boldsymbol{\nabla}c}{\|\boldsymbol{\nabla}c\|}\right).$$

L'énergie capillaire est égale à $\varepsilon_\sigma = \sigma\|\boldsymbol{\nabla}c\|$ et la fonction couleur est normalisée par son saut : $c = \tilde{c}/[\tilde{c}]$. On peut noter que les termes capillaires sont similaires à ceux présentés dans [66] à la différence près que la fonction couleur c est conservée à la place de la fraction volumique α. Ce point sera fondamental pour la suite.

Les termes de tension de surface n'affectent pas la pression ni les équations d'entropie. L'évolution de l'équation de pression s'écrit donc :

$$\frac{dP}{dt} + \rho a^2\boldsymbol{\nabla}\cdot(\mathbf{u}) = 0.$$

où a est la vitesse du son du mélange de Wood [98] :

$$a^2 = \left(\rho\sum_k \frac{\alpha_k}{\rho_k a_k^2}\right)^{-1}.$$

Comme dans Kapila et al. [43], les équations d'entropie restent inchangées lors de mouvement continu :

$$\frac{ds_k}{dt} = 0,$$

L'équation d'entropie du mélange est assurée :

$$\frac{ds}{dt} = \sum_k \frac{dY_k s_k}{dt} = 0.$$

Le modèle est démontré faiblement hyperbolique et admet 5 ondes différentes :

$$\lambda_1 = u,$$

$$\lambda_{2,3} = u \pm a_s, \tag{1.14}$$

$$\lambda_{4,5} = u \pm a_c, \tag{1.15}$$

où :

$$a_s^2 = \frac{a^2 + b + \sqrt{(a^2+b)^2 - 4a^2 b\,(n_2^2 + n_3^2)}}{2},$$

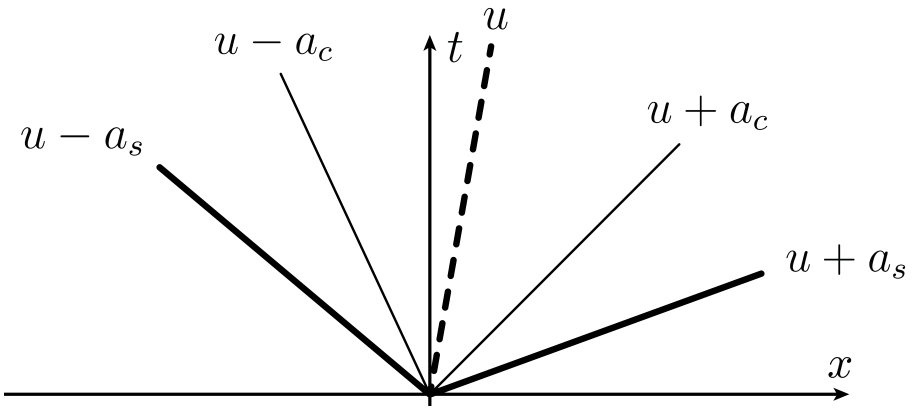

Figure 1.8: Le nouveau modèle (1.13) admet deux types d'ondes acoustiques.

$$a_c^2 = \frac{a^2 + b - \sqrt{\left(a^2+b\right)^2 - 4a^2 b\left(n_2^2 + n_3^2\right)}}{2},$$
$$b = \frac{\sigma \|\mathbf{w}\|}{\rho}\left(n_2^2 + n_3^2\right).$$

et (1.14) correspond aux ondes acoustiques tandis que (1.15) correspond aux ondes capillaires (voir figure 1.8).

Cependant, du fait de sa faible hyperbolicité, ce système d'équilibre ne sera pas résolu numériquement sous cette forme (voir la section suivante pour la discussion sur la méthode numérique).

1.3.4 Résolution du modèle : une méthode numérique appropriée

La résolution numérique du modèle (1.13) représente un défi concernant les deux points suivants :

- La première difficulté est due au terme $K\boldsymbol{\nabla} \cdot \mathbf{u}$ dans l'équation d'évolution de la fraction volumique. C'est l'ingrédient précieux qui mène au respect de l'équation d'entropie du mélange lorsqu'une hypothèse d'équilibre de pression est retenue. Néanmoins, la présence de ce terme non conservatif complique considérablement la méthode numérique qui dépend crucialement du choix des relations appropriées de Rankine-Hugoniot (voir [23] et [80] pour plus de détails). C'est la raison pour laquelle un modèle de pression sans équilibre est préféré. Il contient un terme de relaxation des pressions au lieu du terme non conservateur $K\boldsymbol{\nabla} \cdot \mathbf{u}$ dans l'équation de fraction volumique. Ce modèle est présenté ci-dessous.

- La seconde difficulté concerne le traitement simultané des 5 ondes qui sont présentes dans le modèle. Cette difficulté est contournée par l'utilisation de modèles fractionnés qui se révèlent, respectivement, hyperbolique et faiblement hyperbolique.

1.3.4.1 Modèle de relaxation des pressions avec effets capillaires

Parce que l'équation de la fraction volumique, qui est non conservative, présente un problème majeur concernant la résolution numérique, on propose le modèle en déséquilibre de pression faiblement hyperbolique suivant :

$$\begin{cases} \frac{\partial \alpha_1}{\partial t} + \mathbf{u}\cdot\nabla\alpha_1 & = \mu\left(P_1 - P_2\right), \\ \frac{\partial \alpha_1\rho_1}{\partial t} + \boldsymbol{\nabla}\cdot\left(\alpha_1\rho_1\mathbf{u}\right) & = 0, \\ \frac{\partial \alpha_2\rho_2}{\partial t} + \boldsymbol{\nabla}\cdot\left(\alpha_2\rho_2\mathbf{u}\right) & = 0, \\ \frac{\partial \rho\mathbf{u}}{\partial t} + \boldsymbol{\nabla}\cdot\left(\rho\mathbf{u}\otimes\mathbf{u} + P\overline{\overline{I}} + \overline{\overline{\Omega}}\right) & = \mathbf{0}, \\ \frac{\partial \alpha_1\rho_1 e_1}{\partial t} + \boldsymbol{\nabla}\cdot\left(\alpha_1\rho_1 e_1\mathbf{u}\right) + \alpha_1 P_1\boldsymbol{\nabla}\cdot\mathbf{u} & = -\mu P_I\left(P_1 - P_2\right), \\ \frac{\partial \alpha_2\rho_2 e_2}{\partial t} + \boldsymbol{\nabla}\cdot\left(\alpha_2\rho_2 e_2\mathbf{u}\right) + \alpha_2 P_2\boldsymbol{\nabla}\cdot\mathbf{u} & = \mu P_I\left(P_1 - P_2\right), \\ \frac{\partial c}{\partial t} + \mathbf{u}\cdot\boldsymbol{\nabla}c & = 0, \end{cases} \tag{1.16}$$

où μ est le coefficient de relaxation des pressions, $P_I = \frac{Z_2P_1 + Z_1P_2}{Z_1+Z_2}$ (voir [77] pour plus de détails) et $Z_k = \rho_k a_k$ est l'impédance acoustique de la phase k. La pression du mélange est donnée par :

$$P = \alpha_1 P_1 + \alpha_2 P_2.$$

En raison de la condition $P_1 \neq P_2$ dans ce modèle, l'équation d'énergie totale du mélange est remplacée par l'équation d'énergie interne pour chaque phase. On peut remarquer que les effets de tension de surface sont manquants dans les équations d'énergie phasique. En effet, il ne s'agit que d'une caractéristique du mélange intervenant aux interfaces entre fluides. Dans ce sens, l'équation d'énergie totale du mélange du système peut être écrite sous la forme donnée dans 1.13 :

$$\frac{\partial \rho E + \varepsilon_\sigma}{\partial t} + \boldsymbol{\nabla}\cdot\left(\left(\rho E + \varepsilon_\sigma + P\right)\mathbf{u} + \overline{\overline{\Omega}}\cdot\mathbf{u}\right) = 0. \tag{1.17}$$

L'équation (1.17) est redondante lorsque les deux équations d'énergie interne phasique sont résolues, mais il apparaîtra qu'elle est un ingrédient important pour la méthode numérique afin d'assurer la conservation de l'énergie, et pour préserver un traitement correct des ondes de choc. Elle est ainsi ajoutée au système lors de sa résolution.

Les équations d'entropie pour le système (1.16) peuvent également être écrites :

$$\alpha_1\rho_1 T_1\frac{ds_1}{dt} = \mu(P_1 - P_2)^2\frac{Z_1}{Z_1 + Z_2},$$

$$\alpha_2\rho_2 T_2\frac{ds_2}{dt} = \mu(P_1 - P_2)^2\frac{Z_2}{Z_1 + Z_2},$$

qui assure que l'entropie du mélange ($s = Y_1 s_1 + Y_2 s_2$) augmente.

Le modèle (1.13) peut être retrouvé comme limite asymptotique du modèle (1.16) lorsque la pression de chaque phase tend à être égale.

Cependant, pour répondre à la seconde difficulté concernant le traitement simultané des 5 ondes du modèle, une procédure spéciale de fractionnement sera effectuée pour la résolution numérique du modèle (1.16).

1.3.4.2 Procédure de fractionnement

La résolution du modèle (1.16) se déroule en 3 étapes : traitement des ondes acoustiques du système, traitement de la capillarité et enfin relaxation de la pression. Le modèle (1.16) sans les termes de relaxation est donc divisé en deux sous-modèles. Le premier sous-modèle ne tient pas compte des termes de tension de surface et le second ne contient que ceux-ci. Les sous-modèles ne sont présentés ci-dessous que dans la direction x.

Sous-modèle hyperbolique 1

Le premier sous-modèle est similaire à celui présenté dans [80] avec des équations découplées supplémentaires pour le gradient de la fonction couleur :

$$\begin{cases} \dfrac{\partial \alpha_1}{\partial t} + u\dfrac{\partial \alpha_1}{\partial x} & = 0, \\ \dfrac{\partial \alpha_1\rho_1}{\partial t} + \dfrac{\partial \alpha_1\rho_1 u}{\partial x} & = 0, \\ \dfrac{\partial \alpha_2\rho_2}{\partial t} + \dfrac{\partial \alpha_2\rho_2 u}{\partial x} & = 0, \\ \dfrac{\partial \rho u}{\partial t} + \dfrac{\partial \rho u^2 + \alpha_1 P_1 + \alpha_2 P_2}{\partial x} & = 0, \\ \dfrac{\partial \rho v}{\partial t} + \dfrac{\partial \rho u v}{\partial x} & = 0, \\ \dfrac{\partial \rho w}{\partial t} + \dfrac{\partial \rho u w}{\partial x} & = 0, \\ \dfrac{\partial \alpha_1\rho_1 e_1}{\partial t} + \dfrac{\partial \alpha_1\rho_1 e_1 u}{\partial x} + \alpha_1 P_1 \dfrac{\partial u}{\partial x} & = 0, \\ \dfrac{\partial \alpha_2\rho_2 e_2}{\partial t} + \dfrac{\partial \alpha_2\rho_2 e_2 u}{\partial x} + \alpha_2 P_2 \dfrac{\partial u}{\partial x} & = 0, \\ \dfrac{\partial w_1}{\partial t} + \dfrac{\partial w_1 u}{\partial x} & = 0, \\ \dfrac{\partial w_2}{\partial t} + u\dfrac{\partial w_2}{\partial x} & = 0, \\ \dfrac{\partial w_3}{\partial t} + u\dfrac{\partial w_3}{\partial x} & = 0. \end{cases} \tag{1.18}$$

Ce système décrit uniquement le transport et les ondes de compression. L'équation de w_1 est prise sous une forme conservative pour permettre la possibilité de considérer des solutions faibles. Les autres termes de cette équation seront traités dans le deuxième sous-modèle.

Les valeurs propres du système sont :

$$\lambda_{1,2,3,4,5,6,7,8,9} = u,$$
$$\lambda_{10} = u - a_f,$$
$$\lambda_{11} = u + a_f,$$

où a_f est la vitesse du son du mélange dite de "figée" :

$$a_f^2 = Y_1 a_1^2 + Y_2 a_2^2.$$

L'hyperbolicité de ce premier sous-modèle est prouvée dans [80].

Sous-modèle faiblement hyperbolique 2

Le second sous-modèle est :

$$\begin{cases} \frac{\partial \alpha_1}{\partial t} & = 0, \\ \frac{\partial \alpha_1 \rho_1}{\partial t} & = 0, \\ \frac{\partial \alpha_2 \rho_2}{\partial t} & = 0, \\ \frac{\partial \rho u}{\partial t} + \left(\frac{\partial \Omega_{11}}{\partial w_1}\frac{\partial w_1}{\partial x} + \frac{\partial \Omega_{11}}{\partial w_2}\frac{\partial w_2}{\partial x} + \frac{\partial \Omega_{11}}{\partial w_3}\frac{\partial w_3}{\partial x} \right) & = 0, \\ \frac{\partial \rho v}{\partial t} + \left(\frac{\partial \Omega_{12}}{\partial w_1}\frac{\partial w_1}{\partial x} + \frac{\partial \Omega_{12}}{\partial w_2}\frac{\partial w_2}{\partial x} + \frac{\partial \Omega_{12}}{\partial w_3}\frac{\partial w_3}{\partial x} \right) & = 0, \\ \frac{\partial \rho w}{\partial t} + \left(\frac{\partial \Omega_{13}}{\partial w_1}\frac{\partial w_1}{\partial x} + \frac{\partial \Omega_{13}}{\partial w_2}\frac{\partial w_2}{\partial x} + \frac{\partial \Omega_{13}}{\partial w_3}\frac{\partial w_3}{\partial x} \right) & = 0, \\ \frac{\partial \alpha_1 \rho_1 e_1}{\partial t} & = 0, \\ \frac{\partial \alpha_2 \rho_2 e_2}{\partial t} & = 0, \\ \frac{\partial w_1}{\partial t} + w_2 \frac{\partial v}{\partial x} + w_3 \frac{\partial w}{\partial x} & = 0, \\ \frac{\partial w_2}{\partial t} & = 0, \\ \frac{\partial w_3}{\partial t} & = 0. \end{cases} \tag{1.19}$$

Ce second système décrit les effets capillaires. De plus, le produit non-conservatif dans l'équation de w_1 est bien défini parce que w_2 et w_3 sont continus au travers d'un choc.

1.3.5 Une nouvelle méthode numérique

La nouvelle méthode numérique est présentée comme une méthode à 3 étapes. Chaque étape est effectuée successivement afin de contourner des problèmes numériques spécifiques :

- Premièrement, le modèle hyperbolique en déséquilibre de pression (1.18) est résolu à l'aide d'une méthode de type Godunov.
- Deuxièmement, le modèle (1.19) est résolu. Une attention particulière est accordée au choix des termes de flux afin d'assurer la conservation de la quantité de mouvement et de l'énergie.
- Troisièmement, une procédure de relaxation conduit à l'équilibre de la pression.

La chaîne de ces trois étapes équivaut à résoudre le modèle (1.13). Le vecteur inconnu $\mathbf{U}^{n+1}$ est obtenu à partir de la condition initiale $\mathbf{U}^n$ par l'application des trois opérateurs successifs selon la séquence :

$$\mathbf{U}^{n+1} = L_{relax} L_{cap} L_{hyper} \left(\mathbf{U}^n \right),$$

où le vecteur $\mathbf{U}$ contient les quantités inconnues définies dans le système :

$$\mathbf{U} = \left[\alpha_1, \alpha_1\rho_1, \alpha_2\rho_2, \rho u, \rho v, \rho w, \alpha_1\rho_1 e_1, \alpha_2\rho_2 e_2, c, \rho E + \varepsilon_\sigma \right]^T$$

Chaque étape de la méthode numérique est entièrement détaillée dans le chapitre 2. Il est important de noter que, pour les différents termes capillaires, le vecteur $\mathbf{w}$ est calculé *via* les dérivations de la fonction couleur qui sont calculées en utilisant des approximations

de différences finies de second ordre. De plus, pour parcourir la chaîne des opérateurs, la solution au temps $n+1$ est obtenue par un algorithme de relaxation de la pression qui corrige les composantes de $\mathbf{U}^{cap}$:

$$\mathbf{U}^{n+1} = L_{relax}\left(\mathbf{U}^{cap}\right).$$

Les détails sur l'algorithme de relaxation de la pression ainsi que sur la procédure de correction utilisée pour garantir la conservation de l'énergie totale se trouvent dans Saurel et al. [80].

1.3.6 Résultats et conclusion

Une multitude de résultats représentatifs des capacités de la méthode sont présentés dans le chapitre 2 mais ici seulement les fondamentaux, concernant le saut de pression de Laplace pour les effets capillaires seuls et l'éclatement d'une colonne d'eau par un écoulement à grande vitesse pour le couplage des effets capillaires avec les ondes acoustiques, sont donnés ici.

Le premier exemple de résultat utilisant ce modèle et cette méthode est présenté dans la figure 1.9 et concerne donc le saut de pression de Laplace. La solution utilisant les termes sources de Brackbill et al. et la solution théorique suivant la loi de Laplace sont aussi présentées. On peut voir ici que des meilleurs résultats sont obtenus sur les valeurs du saut en comparaison à ceux de l'intégration de termes sources. Il est aussi présenté dans le chapitre 2 que la rapidité de convergence et la stabilité ont été améliorées.

Le second résultat concerne l'intéraction d'une onde de choc et d'une colonne d'eau (voir figure 1.10 pour schéma de la configuration de départ). L'onde de choc se propage dans un milieux composé d'air à conditions atmosphériques, de la gauche vers la droite et avec une vitesse de Mach $= 1,3$. Un écoulement à grande vitesse est donc produit en aval du choc et va procéder à l'éclatement de la colonne. La colonne d'eau a un diamètre de $6,4mm$. La figure 1.11 montre le résultat de l'éclatement de la colonne 1 $600\mu s$ après le passage du choc (étant déjà sorti du champ de visualisation). On observe ainsi que la colonne a une forme aplatie avec des filaments s'en détachant pour ensuite former un début de gouttes de tailles réduites.

En conclusion, ce nouveau modèle et cette nouvelle méthode numérique garantissent la conservation de la masse, de la quantité de mouvement et de l'énergie et le respect de la seconde loi de la thermodynamique est préservé. La comparaison avec la "méthode d'intégration des termes sources" et les expériences ont montré les avantages du nouveau modèle et de la méthode numérique. La simulation de l'éclatement aérodynamique d'une colonne d'eau induite par une onde de choc a montré que la méthode est capable de traiter avec précision l'interaction entre les ondes de pression et les effets capillaires dans la même formulation.

Dans le but de simuler l'atomisation d'une seule goutte par un écoulement à grande vitesse, c'est-à-dire, obtenir de petites gouttelettes, une étape supplémentaire est nécessaire pour réaliser cette simulation avec un temps de calcul raisonnable. En effet, la résolution spatiale demandée pour cette simulation est fine et le domaine à simuler doit être large par rapport à la taille de la goutte initiale, ce qui induit directement des temps de calculs

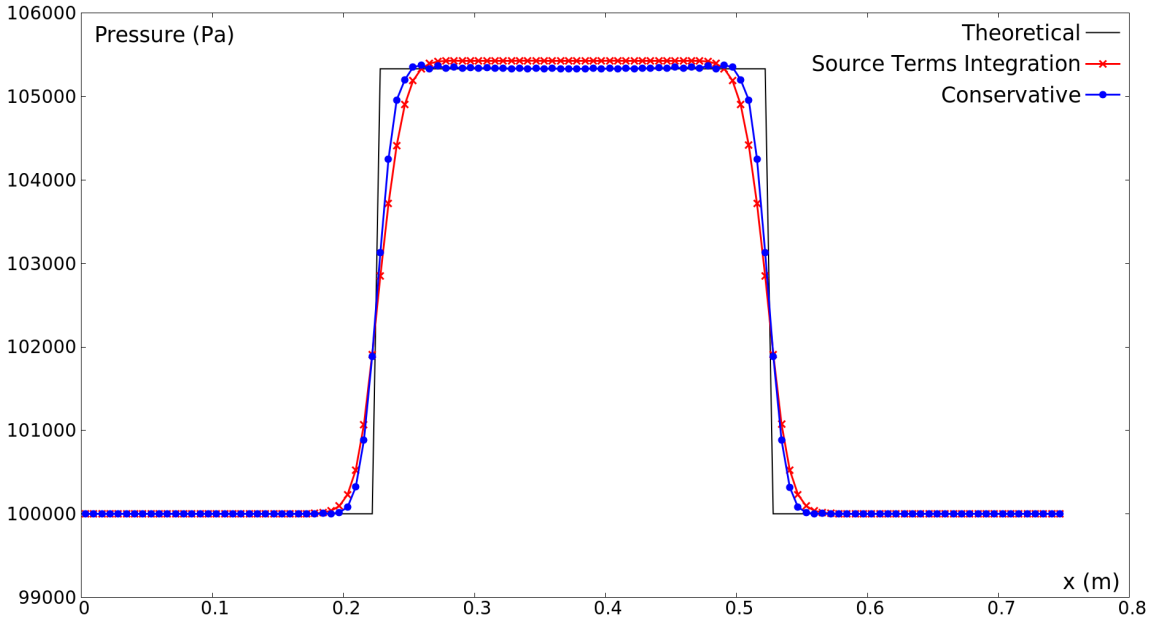

Figure 1.9: Saut de pression dans une une colonne de liquide (2D) dans de l'air. $\sigma = 800N.m^{-1}$, $R = 0,1496m$ et donc $[P] = 5\ 347Pa$. Les résultats théorique (ligne noire) et des simulations convergées avec la méthode d'intégration du terme source (croix rouges) et la méthode conservative (points bleus) sont affichés respectivement à $6,68s$ et $2,07s$.

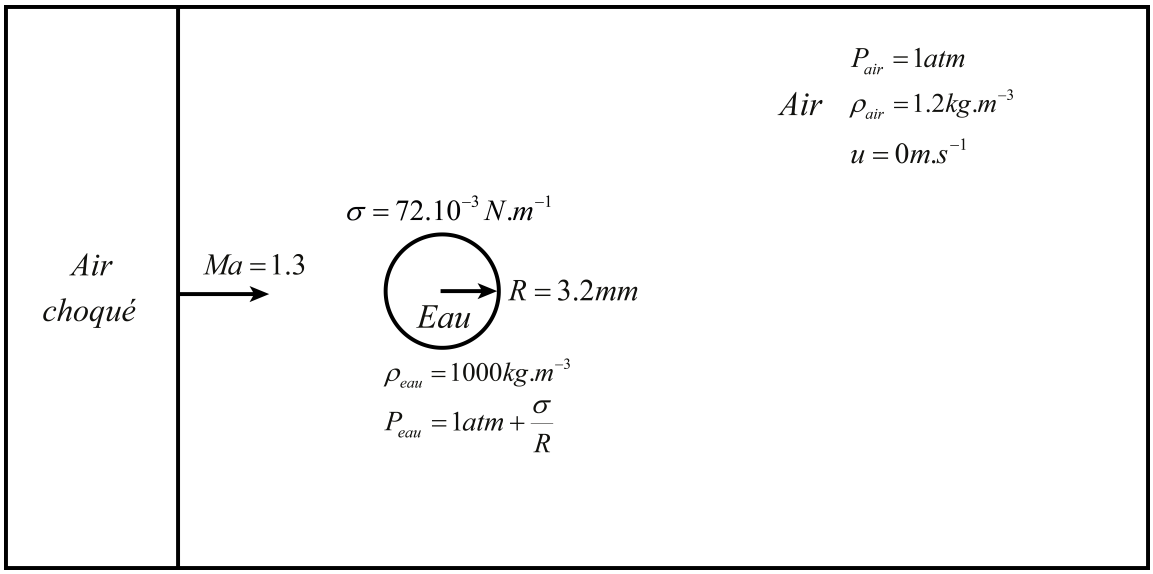

Figure 1.10: Schéma de l'initialisation pour l'interaction d'une onde de choc avec une colonne d'eau.

pouvant être extrêmement grands. C'est pourquoi, une méthode de raffinement adaptatif du maillage (AMR) est entreprise et présentée dans la section suivante, celle-ci résume donc le chapitre 3.

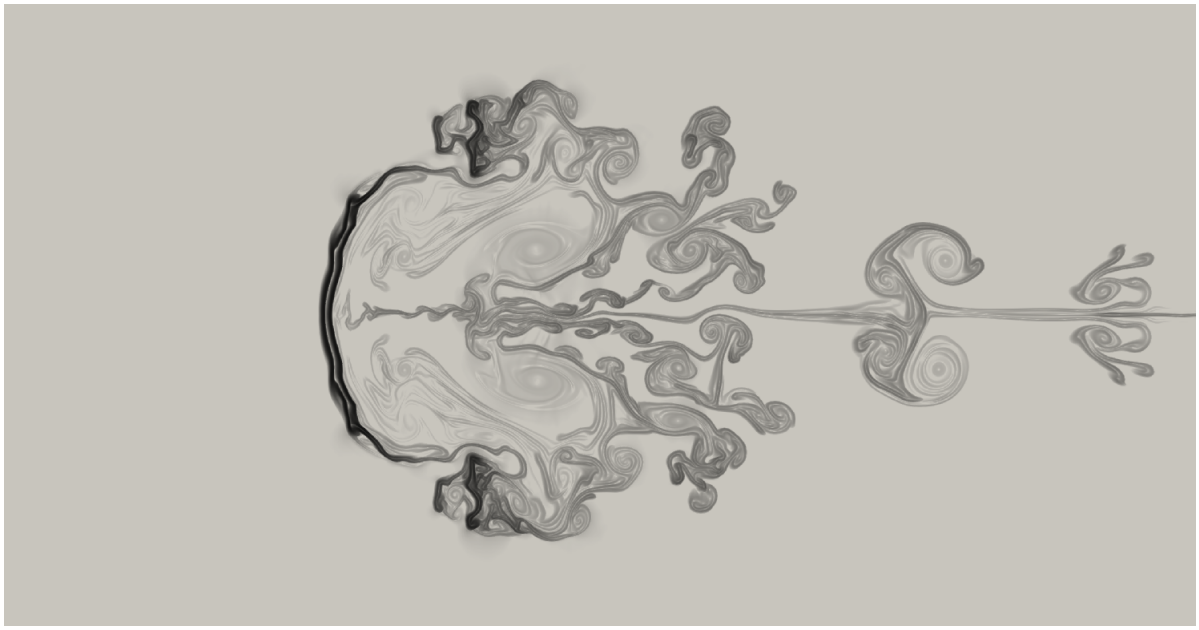

Figure 1.11: Visualisation au travers d'un schlieren (fonction proportionnelle au gradient de densité du mélange) de la simulation numérique de l'éclatement d'une colonne d'eau 1 600μs après le passage du choc, choc se déplaçant de gauche à droite avec une vitesse de Mach $= 1,3$ dans l'air atmosphérique et étant déjà sorti du champ de visualisation.

1.4 Méthode de raffinement adaptatif du maillage (AMR) basée sur des arbres de bords de cellules pour les écoulements compressibles multiphasiques

Cette section est une introduction du chapitre 3 et reflète donc les principales idées qui y sont développées. Elles concernent notamment la construction d'une nouvelle méthode de raffinement adaptatif du maillage utilisant, non seulement un arbre de cellules, mais aussi des arbres de bords de cellules dans le but d'optimiser le temps de calcul et donc de permettre une résolution optimale pour la simulation de l'atomisation tout en conservant des temps de calcul raisonnables.

1.4.1 Contexte

Lors de simulations de la dynamique des fluides, la précision des résultats est conditionnée par le niveau de raffinement de la grille de calcul. Néanmoins, plus la grille est fine, plus le coût en calcul concernant le temps CPU et plus le coût en mémoire sont importants. Pour les calculs d'écoulements stationnaires, l'utilisation de maillages non-structurés et de techniques de raffinement de grilles à des emplacements bien définis peut conduire à des résultats très précis (voir par exemple des simulations autour d'hydrofoils [33]). Pour les

calculs d'écoulements fortement instationnaires et où des ondes de choc ou des interfaces interviennent, la réalisation de résultats précis est conditionnée par l'utilisation d'une très petite taille de cellule. Ainsi, une grande quantité de temps de calcul est gaspillée pour calculer des solutions dans des cellules où très peu de variations se produisent (exemple dans la figure 1.12).

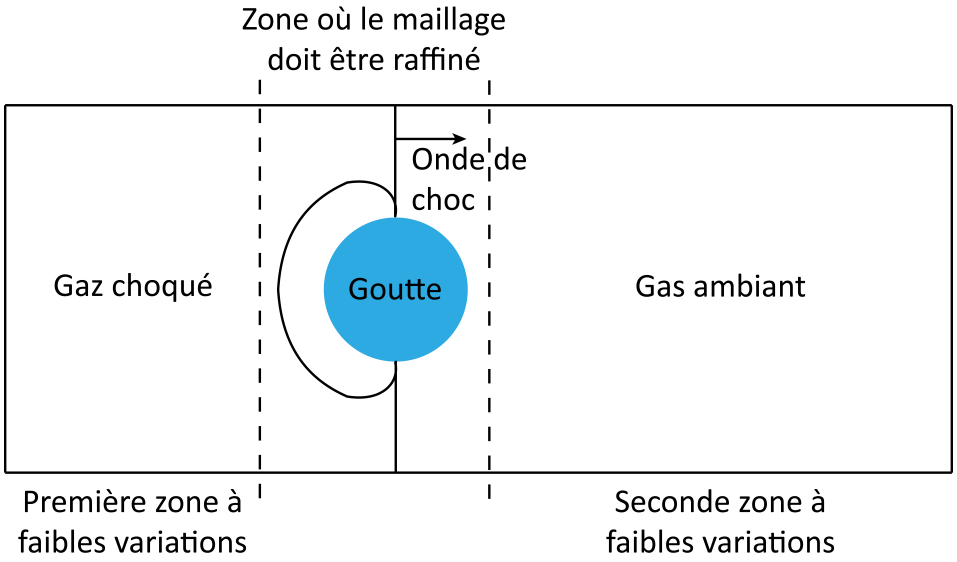

Figure 1.12: Schéma d'une interaction choc-goutte où se distinguent deux parties : l'une où le maillage doit être raffiné et l'autre où ce n'est pas nécessaire.

En ce qui concerne les écoulements multiphasiques, en particulier dans le cadre de méthodes à interface diffuse [78], la remarque précédente est amplifiée par la complexité du modèle :

- un nombre important d'équations d'évolution peut être résolu (Hank et al. [30], Petitpas et al. [70]),
- des solveurs itératifs pour une procédure de relaxation peuvent également être nécessaires (Saurel et al. [80], Han et al. [27]),
- des solveurs de Riemann coûteux sont parfois nécessaires pour tenir compte de la physique mise en jeu (Le Métayer et al. [53]).

Sur la base de ces observations, l'utilisation de raffinement adaptatif du maillage (AMR) représente une option intéressante pour réduire les coûts en temps CPU et en mémoire lors du traitement d'écoulements compressibles multiphasiques complexes. Ce type de technique fait donc l'object de cette étude.

1.4.2 Méthode AMR : l'état de l'art

Lorsqu'une méthode AMR est intégrée dans un code de calcul traitant la dynamique des fluides, la grille de calcul est adaptée dynamiquement afin d'être raffinée là où il est nécessaire

et de maintenir une grille grossière ailleurs. Ces méthodes AMR sont adaptées et sont déjà utilisées de manière massive pour de nombreuses applications :

- magnetohydrodynamiques (Anderson et al. [5], Dumbser et al. [16]),
- écoulements multiphasiques incompressibles comme pour les mouvements de gouttes dans un microcanal ou l'atomisation de jets de liquide (Chen et Yang [13], Popinet et Rickard [72]),
- écoulements compressibles dans les milieux poreux (Pau et al.[65]).

L'analyse de la littérature montre que l'on peut remarquer qu'il existe principalement deux approches dans le contexte de schéma de volumes finis :

- La première est une approche où les cellules sont organisées en grilles cartésiennes (Berger et Oliger [7], Berger et Colella [6]). L'ensemble du domaine de calcul est représenté par une grille de base grossière et, lorsqu'une plus grande résolution est nécessaire, des grilles plus fines sont placées sur des grilles plus grossières. Cela définit une hiérarchie de grille, de la grille la plus grossière à la plus raffinée, qui peut être organisée comme un "arbre de grille". La génération ou la destruction d'une grille se produit lorsque l'erreur relative locale entre les calculs effectués sur la grille actuelle et respectivement la grille plus fine ou plus grossière, passe un critère donné. L'avantage principal de cette approche est le fait que le schéma numérique pour la physique traitée est indépendant de la grille, de sorte que le même schéma puisse être appliqué quelle que soit la grille considérée. Cela signifie également que tout schéma pour une grille unique peut être utilisé sans modifications importantes pour l'AMR. En revanche, les inconvénients de cette approche sont dus à la structure rigide de la grille. Elle induit que la simulation d'écoulements complexes nécessite le recouvrement avec un nombre important de grilles et plusieurs grilles de même niveau de raffinement peuvent alors se chevaucher. Une duplication des cellules est héritée de ce chevauchement et un nombre important de nouvelles cellules de calcul peut être gaspillé dans des régions à écoulement régulier. De plus, la reconstruction périodique de l'ensemble de la hiérarchie de la grille est nécessaire lorsque l'écoulement évolue avec le temps.

- Dans la seconde approche, le raffinement se produit sur une cellule individuelle et cela définit directement un arbre de cellules (méthode d'arbre de cellules) (Young et al. [100]). Chaque cellule peut être raffinée ou déraffinée indépendamment des autres. En outre, le raffinement du maillage se produit localement là où il est nécessaire, puis à chaque niveau de l'arbre, le maillage peut donc avoir une forme non uniforme. Le principal avantage de l'approche des arbres de cellules est la flexibilité dans le raffinement et le déraffinement. Cette flexibilité est payée par le fait que les schémas numériques standard basés sur des grilles ne peuvent pas être utilisés directement sur un arbre. Le calcul des flux et la stratégie liée au pas de temps sur un arbre sont différent de ceux d'une grille, cela signifie que le schéma numérique dépend légèrement du niveau calculé. De plus, un accès aux cellules voisines est plus difficile dans un

arbre que dans un tableau et le balayage de l'arborescence pour accéder aux voisins les plus proches est une procédure difficile à vectoriser et à paralléliser. En outre, le coût en mémoire oscille entre un coût supérieur ou inférieur à celui de la première approche du fait qu'il y ait moins de cellules à stocker mais qu'un arbre engendre un surcoût pour être maintenu.

Dans Khokhlov [46], l'utilisation d'une structure de données différente permet de contourner ces deux derniers problèmes. La structure de Khokhlov implique un arbre complétement interconnecté où les cellules ont à la fois connaissance de leurs cellules enfants, de leurs cellules parents et de leurs cellules voisines. Cette interconnexion offre un accès efficace à l'information sur un arbre. Khokhlov améliore également le coût en mémoire pour la conservation de l'arbre en regroupant les cellules dans une structure dite d'"oct". En outre, le critère de raffinement repose sur des variations physiques entre cellules voisines. Ce raffinement dynamique est généralement assuré par le suivi des discontinuités (comme des ondes de choc ou des discontinuités de contact). Le raffinement évolue donc avec les caractéristiques de l'écoulement ce qui le rend plus adapté à la résolution d'écoulements fortement dynamiques.

1.4.3 Une nouvelle méthode AMR

Dans ce travail, nous conservons la seconde approche pour sa capacité à facilement adapter le maillage pour des écoulements instationnaires. Ainsi, une version modifiée de la méthode de Khokhlov est présentée. Il est important de mentionner que la méthode originale a été développée à la fin des années 90 et l'objectif était de simuler des écoulements compressibles monophasiques utlisant une méthode AMR avec les meilleures performances concernant l'efficacité et la mémoire. Même si le développement d'un algorithme efficace est toujours un problème clé de nos jours, les contraintes sur la mémoire ne sont plus aussi cruciales qu'elles l'étaient. Les problèmes d'aujourd'hui sont liés aux écoulements complexes multiphysiques (comprenant plusieurs phases, solides, transition de phase, réactions chimiques, viscosité, capillarité ...) qui sont décrits par des modèles mathématiques complexes pour lesquels le coût en calcul représente la limitation, bien plus que la mémoire. C'est pourquoi deux spécificités de la méthode de Khokhlov doivent être soulignées :

- La première est que, l'arbre complètement interconnecté implique beaucoup d'opérations pour trouver les cellules voisines. Cela devient un point critique lorsque l'algorithme est utilisé pour résoudre un modèle complexe couplé à une méthode à ordre élevé où la procédure pour trouver les voisins se produit de nombreuses fois (calculs de flux à chaque étape de la méthode à ordre élevé, calculs des gradients pour l'exécution de la méthode AMR ou pour l'application d'un phénomène physique donné, etc.).

- La seconde est que si la méthode AMR est implémentée dans un code où le maillage peut être cartésien ou non, trouver les voisins pourrait impliquer de nombreuses opérations complexes.

La nouvelle méthode que nous proposons présente deux avantages : l'algorithme AMR général est d'abord simple et la recherche des cellules voisines est améliorée. Le point clé

est le rôle joué par les bords des cellules (contours géométriques) : évidemment pour les calculs de flux et aussi parce que ces bords définissent naturellement le lien entre deux cellules. Cette nouvelle méthode étend l'approche de Khovhlov sur deux points : la structure de l'arbre de cellule est légèrement modifiée et un second arbre est utilisé pour stocker certaines informations des bords des cellules. L'ajout de cette seconde structure d'arbre de bords présente les avantages de réduire le nombre d'opérations pendant l'intégration du pas de temps et de simplifier l'algorithme. L'inconvénient est d'augmenter raisonnablement la mémoire impliquée. Raisonnablement parce que le nombre d'informations supplémentaires stockées pour chaque bord de cellule est relativement faible par rapport à ce qui est nécessaire dans une cellule.

1.4.4 Description de la structure de données AMR

Rappelons d'abord la structure de données de méthode AMR basée sur les arbres de cellules. Une cellule de calcul est représentée par un nœud à un niveau donné dans un arbre. Chaque nœud d'un arbre est lié à :

- Un nœud parent représentant une cellule de calcul au niveau inférieur. La racine d'un arbre est un nœud particulier sans parent.
- Un nombre donné de nœuds enfants représentant des cellules de calcul au niveau supérieur. Le nombre de nœuds enfants dépend de la géométrie et de la dimension du problème. Une feuille d'un arbre est un nœud particulier sans enfant et les calculs liés aux quantités physiques (non liés à l'AMR) ne se produisent que sur un nœud qui est une feuille.

Chaque cellule dans la méthode AMR peut être divisée en un nombre donné de cellules enfants. Un exemple de fractionnement possible dans la grille cartésienne 1D/2D/3D est présenté sur la partie droite de la figure 1.13 et un exemple d'arbre représentant les données pour une méthode AMR 1D est présenté sur sa partie gauche.

1.4.4.1 Rappel de la méthode de Khokhlov [46] : FTT

La structure en arbre est la structure la plus évidente pour définir et optimiser le stockage des données des cellules dans une méthode AMR. Sa flexibilité permet le raffinement et le déraffinement *via* la destruction et la reconstruction des nœuds choisis dans l'arbre. La pierre angulaire d'une telle méthode réside dans la manière choisie de parcourir les cellules dans l'arbre qui peut être une opération complexe et coûteuse selon les liens entre les cellules. Dans sa version la plus simple, un nœud ne peut être accédé que par la navigation de l'arbre à partir de sa racine. On comprend facilement que l'opération simple consistant à localiser les voisins d'une cellule donnée (par exemple pour calculer les flux inter-cellules) devient rapidement une source de temps de calcul gaspillé. Une autre solution est l'utilisation d'un arbre nommé Fully Threaded Tree (FTT, arbre complétement fileté) où chaque nœud a la connaissance de son nœud parent, de ses nœuds enfants et de ses nœuds voisins. Cette amélioration facilite la navigation de l'arbre dans toutes les directions

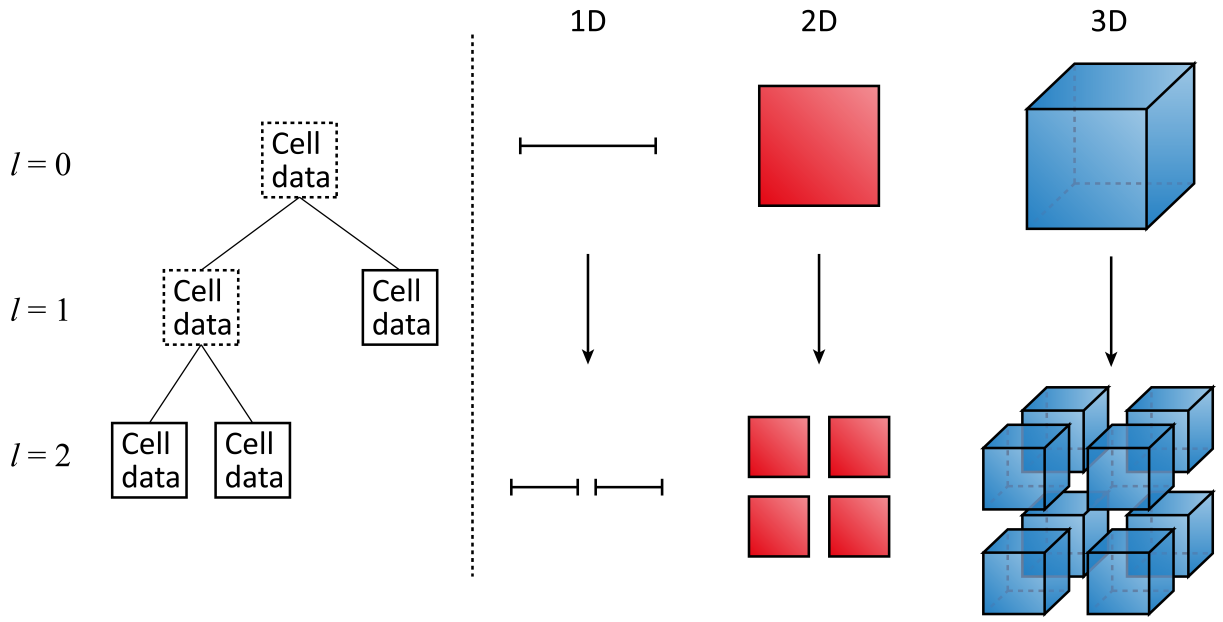

Figure 1.13: Figure divisée en deux parties. À gauche, un exemple d'arbre représentant la structure de données pour une méthode AMD 1D. "l" correspond au niveau dans l'arbre. À droite, le fractionnement possible d'une cellule. Une cellule 1D/2D/3D donnera naissance dans la grille cartésienne à respectivement 2/4/8 cellules enfants.

(du parent aux enfants, de l'enfant au parent et même entre les voisins). Cette possibilité de parcourir l'arbre dans toutes les directions présente néanmoins l'inconvénient d'augmenter considérablement la mémoire utilisée (en ajoutant plusieurs pointeurs agissant comme des fils). Il rend également les opérations de maintenance sur l'arbre plus compliquées lorsque le raffinement et le déraffinement se produisent.

Khokhlov propose de regrouper les cellules en "octs" afin de limiter le stockage supplémentaire en raison des liaisons entre les nœuds et de limiter les coûts des opérations de maintenance. Chaque oct contient 8 cellules ordonnées (en 3D), un pointeur vers sa cellule parent au niveau inférieur et 6 pointeurs vers les cellules parents des octs voisins. Chaque cellule contient des variables d'écoulement et un pointeur vers un oct enfant de niveau supérieur. La majorité des pointeurs, tout comme les propriétés géométriques (niveau, position, taille, etc.), sont donc regroupés pour être stockées en octs plutôt que dans les cellules. En conséquence, les coûts en mémoire sont considérablement réduits (en particulier en 3D) par rapport à une version simple de FTT sans structure en oct.

L'économie du coût en mémoire est indéniable lorsqu'on traite les équations d'Euler, cela est plus discutable lorsqu'il s'agit de modèles complexes traduisant des problèmes multiphysiques. Dans de telles applications de méthode AMR, le rapport entre les variables d'écoulement et les variables géométriques/AMR augmente considérablement. Khokhlov explique que le coût de sa version AMR avec oct-FTT est de 2 mots en mémoire par cellule au lieu de 17 mots/cellule pour une version non oct de FTT. Ces coûts en mémoire supplémentaires doivent être comparés aux variables d'écoulement nécessaires à stocker (5 mots/cellule pour les équations d'Euler, mais 6N mots/cellules pour un écoulement à

N-phase sans physique supplémentaire).

En plus du ratio sur l'économie du coût en mémoire qui diminue quand le modèle, et donc la physique, se complique, un autre inconvénient des arbres structurés en oct est que le temps de calcul associé aux passages oct à cellule et cellule à oct, ou en d'autres termes le temps supplémentaire nécessaire pour rechercher les cellules voisines, est estimé à environ 20% lors de la simulation d'écoulement monophasique avec une méthode du premier ordre. Ici encore, lorsque des modèles complexes couplés à des schémas numériques à ordre élevé sont les centres d'interêt (fait intervenir une recherche des voisins pour chaque calcul de flux du schéma à ordre élevé, pour chaque calcul de gradient, etc.), ce temps supplémentaire de calcul impliqué par la structure peut ne plus être négligeable.

1.4.4.2 Idée de base de la nouvelle structure de données AMR : L'ajout d'arbres de bords de cellules

Un moyen efficace d'éviter d'augmenter le temps CPU et la difficulté à rechercher des voisins dans des calculs parallèles est de profiter des informations relatives aux bords de cellules. Dans le cadre des volumes finis, un bord de cellule peut être défini comme un contour géométrique entre deux cellules de calcul qui est le siège des calculs de flux. Un bord peut être défini comme un objet qui stocke deux pointeurs, un pour une cellule "gauche" et un autre pour une cellule "droite". La disponibilité de tels objets évite la recherche des voisins lors de la résolution de flux inter-cellules. Dans un contexte plus général de maillages non-structurés, elle évite également d'utiliser un tableau de connectivité. Cela implique que les algorithmes des volumes finis utilisant cette structure de données peuvent être facilement utilisés quelle que soit la structure du maillage.

En plus des arbres de cellules, nous proposons ainsi de définir des arbres de bords. Dans ces arbres de bords, les bords des cellules sont représentés par des nœuds qui sont liés à d'autres nœuds de bords par des arêtes. La dualité de l'arbre des cellules et des arbres de bords représente une structure de données complexe qui simplifie grandement l'algorithme et réduit les coûts en calcul. Suite à cette remarque, la nouvelle structure de données se compose de :

- Cellules organisées en arborescence (arbre en oct ou non). Ils peuvent également être liés aux bords.
- Bords également organisées dans des structures en arbres. Ils peuvent aussi être regroupés dans un arbre en quad pour imiter les structures d'arbres cellulaires en oct de Khokhlov (un bord sera divisé en 4 bords enfants en 3D).

L'ajout des arbres de bords dans la méthode AMR implique des coûts en mémoire supplémentaires. Néanmoins, avec cette nouvelle structure de données, les calculs aux bords (flux, gradients, etc.) sont naturellement accessibles sans recherches des voisins. Ce point important rend la méthode facilement extensible aux maillages non-structurés. En outre, la structure en oct utilisée dans le travail de Khokhlov peut être maintenue pour regrouper les informations concernant les propriétés géométriques dans le cadre cartésien.

1.4.4.3 Quelques détails sur la structure des arbres

Pour plus de commodité lors de la présentation, la structure de données est présentée pour des arbres non-oct.

L'arbre principal de la méthode est assez similaire à celui d'une méthode classique FTT. Les cellules de calcul constituent les nœuds de l'arbre des cellules. En particulier, ils contiennent les propriétés de l'écoulement (fonction du modèle) ainsi que des données géométriques. Ces nœuds de cellules comprennent également des données supplémentaires spécifiques à la méthode AMR :

* Un nombre entier pour son niveau (0 pour la racine, > 0 sinon),
* Un pointeur pour chacun de ses nœuds de cellules enfants (jusqu'à 8 en 3D cartésien),
* Un pointeur supplémentaire pour chacun de ses bords (jusqu'à 6 en 3D cartésien),
* Un pointeur pour la racine de chaque nouveau bord interne (jusqu'à 12 en 3D cartésien). Le cas particulier des bords internes est présenté dans la suite.

En comparaison à une méthode FTT classique, la nouveauté réside dans les pointeurs vers des bords qui représentent un coût additionel en mémoire d'un maximum de 11 pointeurs/cellule en 3D (12 nouveaux pointeurs pour les bords internes, 1 de moins parce que le pointeur vers la cellule parent n'est plus nécessaire dans la méthode). À noter qu'une cellule donnée peut être fractionnée ou non (si ses pointeurs sur les nœuds des cellules enfants sont nuls).

La seconde et nouvelle structure de données est représentée par de nouveaux arbres de bords. Un bord de cellule est un nouvel objet qui comprend deux pointeurs de cellules (un pour la cellule de gauche et un pour la cellule de droite). L'intérêt de la présence de tels objets dans une méthode de volumes finis réside dans un meilleur accès au calcul des flux entre deux cellules de calcul. En effet, avec de tels objets, aucune table de connectivité ne doit être spécifiée, ce qui rend la méthode non restrictive du cadre cartésien. Dans la présente méthode AMR, les bords des cellules constituent des nœuds de nouveaux arbres de bords. Ces nœuds de bords incluent ensuite des données supplémentaires spécifiques à la méthode AMR :

* Un nombre entier pour son niveau,
* Un pointeur vers chacun de ses nœuds de bords enfants (jusqu'à 4 en 3D).

Cette nouvelle structure de données possède une spécificité particulière. En effet, considérons l'exemple d'une cellule cartésienne 2D représentée dans la figure 1.14. Cette cellule est entourée de 4 bords (arêtes bleus). Le raffinement de cette cellule donnera naissance à 4 nouvelles cellules de calcul et à 12 nouveaux bords. Parmi ces 12 bords, 8 d'entre eux proviennent du fractionnement des bords de la cellule parent (arêtes rouges pointillées) et apparaissent naturellement comme des enfants des nœuds des bords parents. De plus, 4 nouveaux bords apparaissent à l'intérieur de la cellule parent à la suite de son fractionnement et sont considérées comme des racines de nouveaux arbres de bords (arêtes vertes pointillées avec points et traits). Par conséquent, le fractionnement d'une cellule donnée agira sur les arbres des bords de deux façons :

- Cela augmentera la profondeur des arbres déjà existants. Les bords “externes” de la cellule parent, qui étaient des feuilles avant le fractionnement, deviennent parents de nouveaux bords (jusqu’à 4 en 3D), ces derniers sont donc des feuilles.
- Dans le même temps, il générera également de nouveaux bords “internes” qui sont des racines (et des feuilles) de nouveaux arbres de bords.

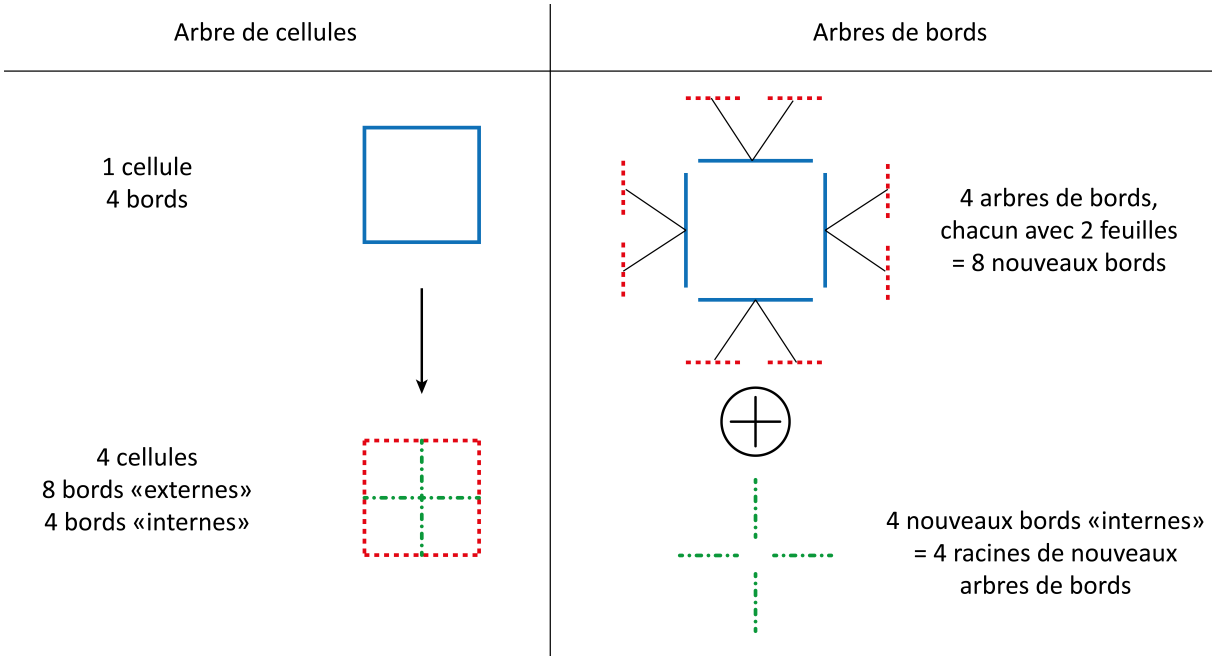

Figure 1.14: Exemple 2D de la dualité des arbres de cellules et de bords.

Le nombre de bords peut être important. Néanmoins, les arbres de bords augmentent raisonnablement la mémoire impliquée puisqu’ils n’ont besoin que de quelques pointeurs supplémentaires pour chaque bord. Une comparaison complète en termes de mémoire requise par rapport à la structure FTT classique (en oct ou non) est présentée dans le chapitre 3.

1.4.5 Contenu complet du chapitre 3

La principale nouveauté, concernant les bords de cellules, vient d’être développée et du fait des nombreuses définitions et inter-connections entre les différentes parties du chapitre 3, il est donné ici seulement une liste des points qui y sont abordés :

- La structure de données AMR étendue est décrite.
- L’algorithme AMR général dans le contexte de schéma de volumes finis (couplé avec les solveurs de Riemann pour les calculs de flux) est présenté. La stratégie liée au pas de temps, les procédures d’avancement et de raffinement du maillage sont détaillées.

- L'extension de la méthode AMR au modèle d'écoulement multiphasique du chapitre 2 est présentée avec notamment les particularités liées au calcul des gradients, pour le traitement des termes capillaires, mais aussi à la procédure de relaxation qui s'applique notamment lors du déraffinement des cellules.

1.4.6 Résultats et conclusion

Une nouvelle méthode de raffinement adaptatif du maillage utilisant des arbres de bords des cellules a été présentée et une extension pour les écoulements multiphasiques est présentée dans le chapitre 3. L'addition de cette seconde structure en arbre de bords présente les avantages de réduire le nombre d'opérations pendant l'intégration du pas de temps (la recherche des cellules voisines est améliorée) et de simplifier l'algorithme général. L'inconvénient est d'augmenter raisonnablement la mémoire impliquée. Raisonnablement parce que le nombre d'informations supplémentaires stockées pour chaque bord de cellule est relativement faible par rapport à ce qui est nécessaire dans une cellule.

L'application de la nouvelle méthode AMR sur différents cas test - transport, tube à choc et écoulements capillaires en 1D, 2D et 3D - est présentée dans le chapitre 3 avec des comparaisons quantitatives concernant des solutions exactes ou des résultats utilisant une méthode non-AMR afin d'analyser le bénéfice de cette nouvelle méthode. L'efficacité du temps de calcul et le coût raisonnable en mémoire y sont montrés.

Un rapide exemple de résultat sur l'interaction choc-goutte présenté dans la section 1.3.6 avec la configuration exprimé dans la figure 1.10 est donné ici et où 4 niveau de raffinement, en plus du maillage initial (niveau 0), sont testé (voir figure 1.15 et 1.16). On peut ainsi voir que le maillage raffiné au niveau maximum suit correctement les discontinuités (chocs et interfaces) et les gradients de densité relativement important (ici visible dans l'écoulement d'air à l'arrière de la goutte, droite sur les images) aux cours de leurs évolutions. Les résultats sont alors très satisfaisant et une étude complète sur l'interaction choc-goutte utilisant le modèle et les méthodes présentés, dans le but d'obtenir des gouttes de tailles réduites sur des temps plus longs, est alors le but du chapitre suivant.

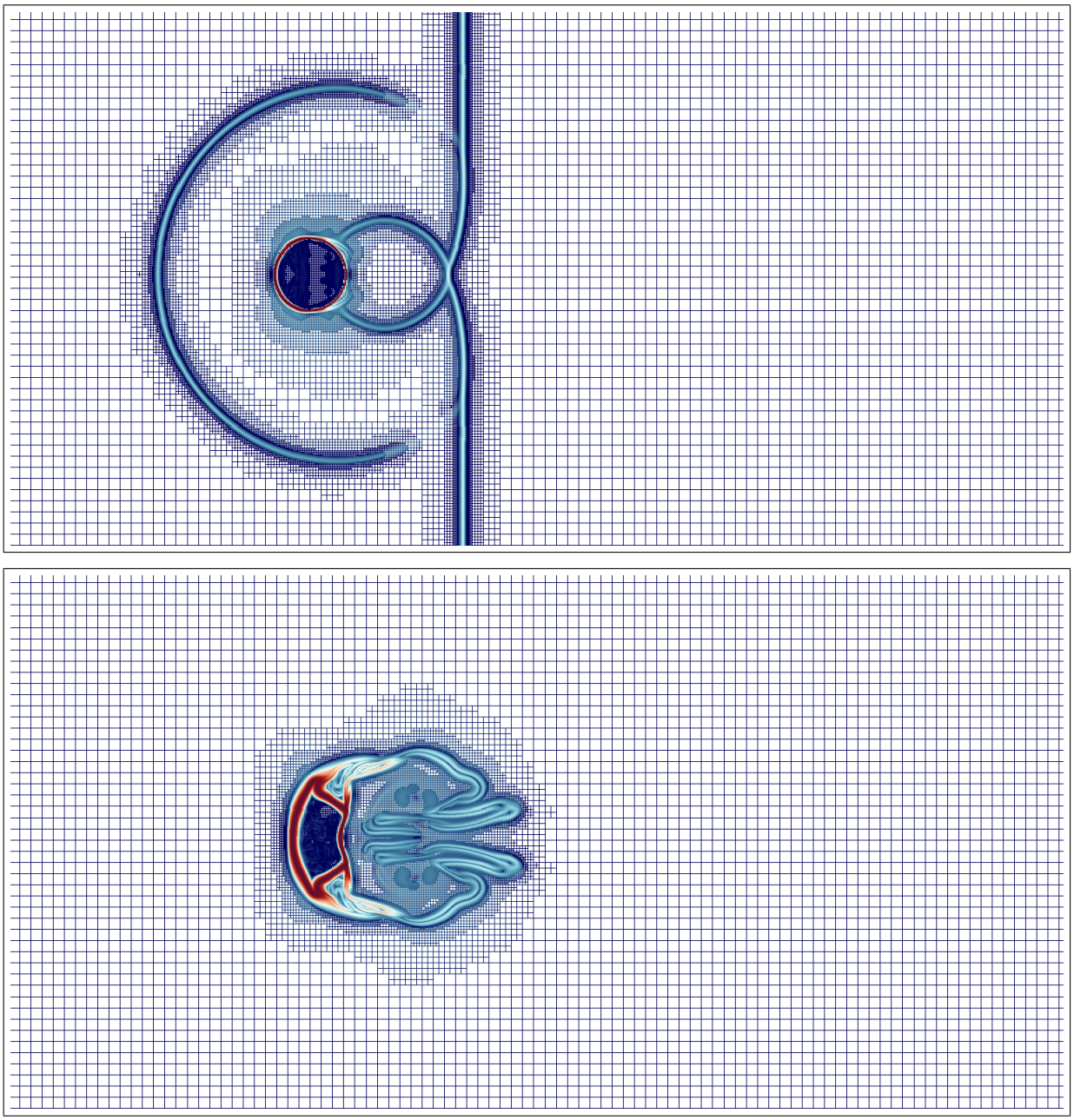

Figure 1.15: Visualisation du maillage au travers d'un schlieren (fonction proportionnelle au gradient de densité du mélange, en rouge les forts gradients et en bleu ceux faibles ou nuls) de la simulation numérique de l'éclatement d'une colonne d'eau $38\mu s$ (haut) et $400\mu s$ (bas) après le passage du choc, choc se déplaçant de gauche à droite avec une vitesse de Mach $= 1,3$ dans l'air atmosphérique.

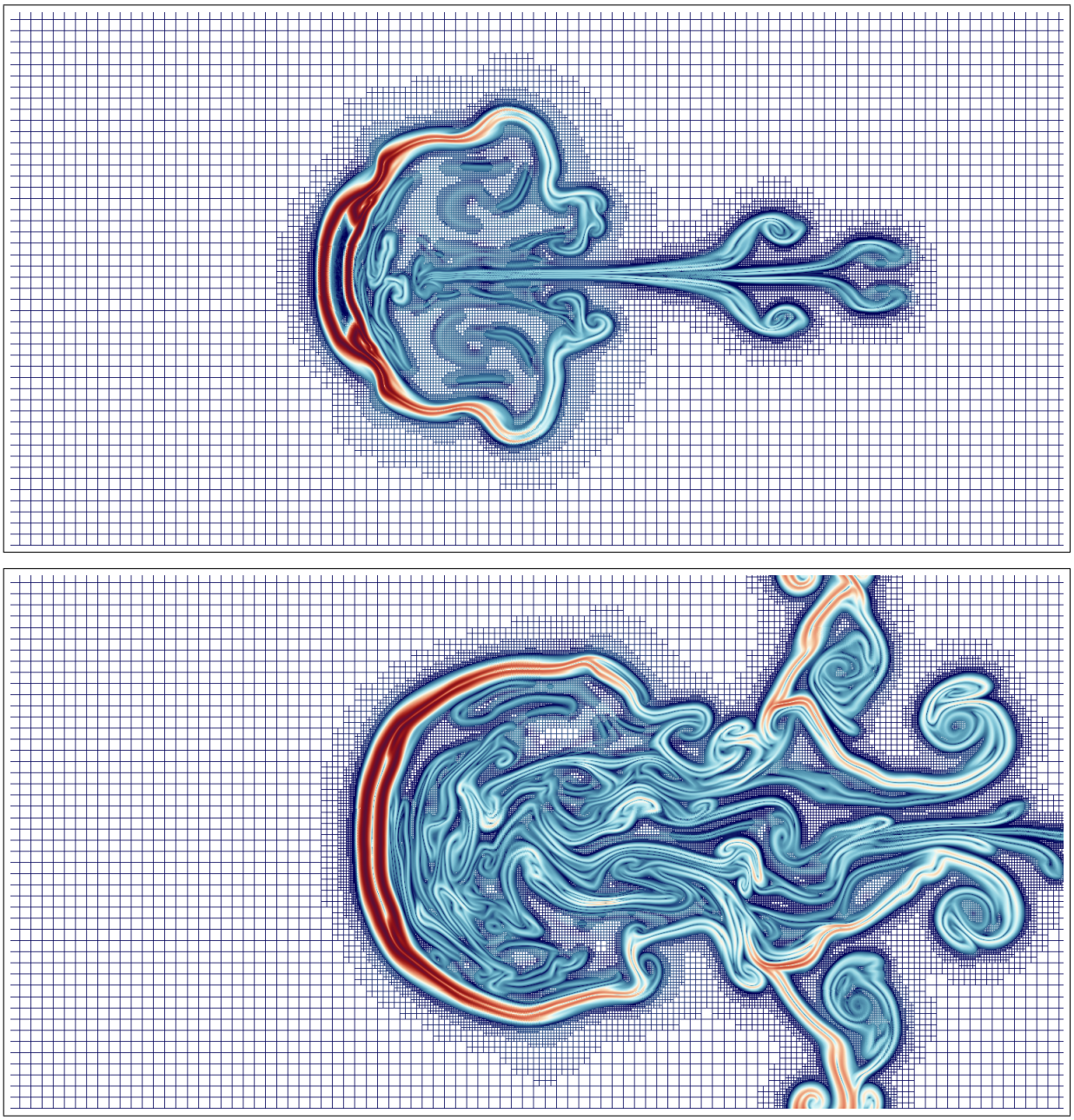

Figure 1.16: Visualisation du maillage au travers d'un schlieren (fonction proportionnelle au gradient de densité du mélange, en rouge les forts gradients et en bleu ceux faibles ou nuls) de la simulation numérique de l'éclatement d'une colonne d'eau $800\mu s$ (haut) et $1\ 200\mu s$ (bas) après le passage du choc, choc se déplaçant de gauche à droite avec une vitesse de Mach $= 1,3$ dans l'air atmosphérique.

1.5 L'atomisation

Cette section est un court résumé du chapitre 4 sur l'atomisation d'une colonne d'eau, pour le cas 2D, et d'une goutte d'eau, pour le cas 3D, par un écoulement à grande vitesse. Dans ce chapitre est développé une étude sur l'impact des différents paramètres dans le but de réaliser au mieux la simulation complète de l'atomisation. Cette étude s'articule autour des points suivants :

- Le choix du limiteur des pentes pour les méthodes numériques à ordre élevé. La méthode du deuxième ordre MUSCL-Hancock sera finalement utilisée avec le limiteur MC pour les variables d'interface et le limiteur Minmod pour les autres.
- Le choix des variables physiques utilisées pour la procédure de raffinement lors de l'utilisation de la méthode AMR.
- L'approximation d'une condition de symétrie.
- L'influence des effets capillaires sur l'atomisation.

Ainsi, ne sont présentés dans ce résumé que les deux principaux résultats de l'atomisation, c'est-à-dire, les résultats finaux pour la simulation en 2D puis en 3D.

1.5.1 2D: l'atomisation d'une colonne d'eau

La simulation est effectuée jusqu'à 3 000μs après la première interaction entre le choc et la colonne d'eau. La figure 1.17 présente sur l'image supérieure le résultat de la simulation au temps 2 200μs avec en rouge un seuil sur la fraction volumique de l'eau pour des valeurs égales ou supérieures à $0,1$ ($\alpha \geqslant 0,1$). En raison de la variation de densité élevée entre l'eau et l'air, on suppose que ce critère permet de représenter l'eau. À cet instant, il se produit un éclatement dit de "sac" car la colonne initiale est séparée en deux morceaux par le processus suivant : la partie avant centrale de la colonne se déplace vers l'arrière avec une vitesse plus grande que celle de ses parties latérales. De plus, en regardant les expériences, comme celle de Igra et Takayama [40], un brouillard de gouttelettes d'eau micrométriques est observable. Ces gouttelettes micrométriques ne sont pas directement obtenues dans les simulations en raison de la résolution du maillage qui doit être effectuée, en particulier avec l'effet de la diffusion numérique. Dans la simulation présentée, la fraction volumique de l'eau est diffusée et suit l'écoulement à l'arrière de la colonne comme le ferait le brouillard. La visualisation du brouillard dans la simulation est donc réalisée en représentant la fonction $\alpha^{\frac{1}{3}}$ qui permet d'observer plus nettement les petites valeurs de la fraction volumique d'eau sans amplifier les grandes. Le résultat de cette fonction est représenté avec une couleur bleue sur cette image supérieure.

L'atomisation complète de la colonne d'eau est présentée dans le chapitre 4 et pendant cette atomisation, trois phases principales sont déterminées :

- La première phase concerne la compression et l'étirement de la colonne initiale jusqu'à des temps autour de 800μs. Des filaments apparaissent également lentement au

niveau des parties latérales de la colonne. Dans le chapitre, les processus d'éclatement sont aussi présentés au travers de la vorticité. Des vortex à l'arrière de la colonne et à l'arrière des filaments sont montrés, en particulier pour les premiers instants de l'éclatement.

- Ensuite, pour la deuxième phase, la compression et l'étirement continuent jusqu'à ce que les vortex à l'arrière de la colonne, en tirant les parties latérales loin du centre et avec le couplage des effets capillaires, casse la colonne initiale en deux morceaux (apparaît aux environ de 1 500μs) . L'éclatement de sac a donc lieu. Pendant ce temps, les filaments sont créés et expulsés hors de la colonne. Une fois détachés, certains de ces filaments convergent vers des gouttelettes. On peut noter que des phénomènes similaires d'éclatement, comme celui de la colonne initiale, se produisent sur les filaments et sur les nouvelles gouttelettes formées. Des petits vortex à l'arrière de ces derniers sont ainsi remarqués. Pour faire office d'exemple, il est aussi présenté le champ de vorticité au temps 2 200μs sur l'image inférieure de la figure 1.17.

- Finalement, la troisième phase correspond à l'éclatement de chaque petite gouttelette d'eau en encore plus petites gouttelettes. Il convient de noter que, même si les plus petites gouttelettes disparaissent en raison de la diffusion numérique et de la résolution maximum du maillage, des gouttelettes de forme semblable à un rond sont observables. Ce dernier point est synonyme des nombres locaux de Weber relativement faibles. Les diamètres caractéristiques d des gouttelettes de tailles réduites observées ayant une forme semblable à un rond sont d'environ $0,2mm \leq d \leq 0,8mm$.

L'atomisation d'une colonne d'eau a donc été accomplie et celle d'une goutte d'eau (3D) est donc entreprise dans la suite.

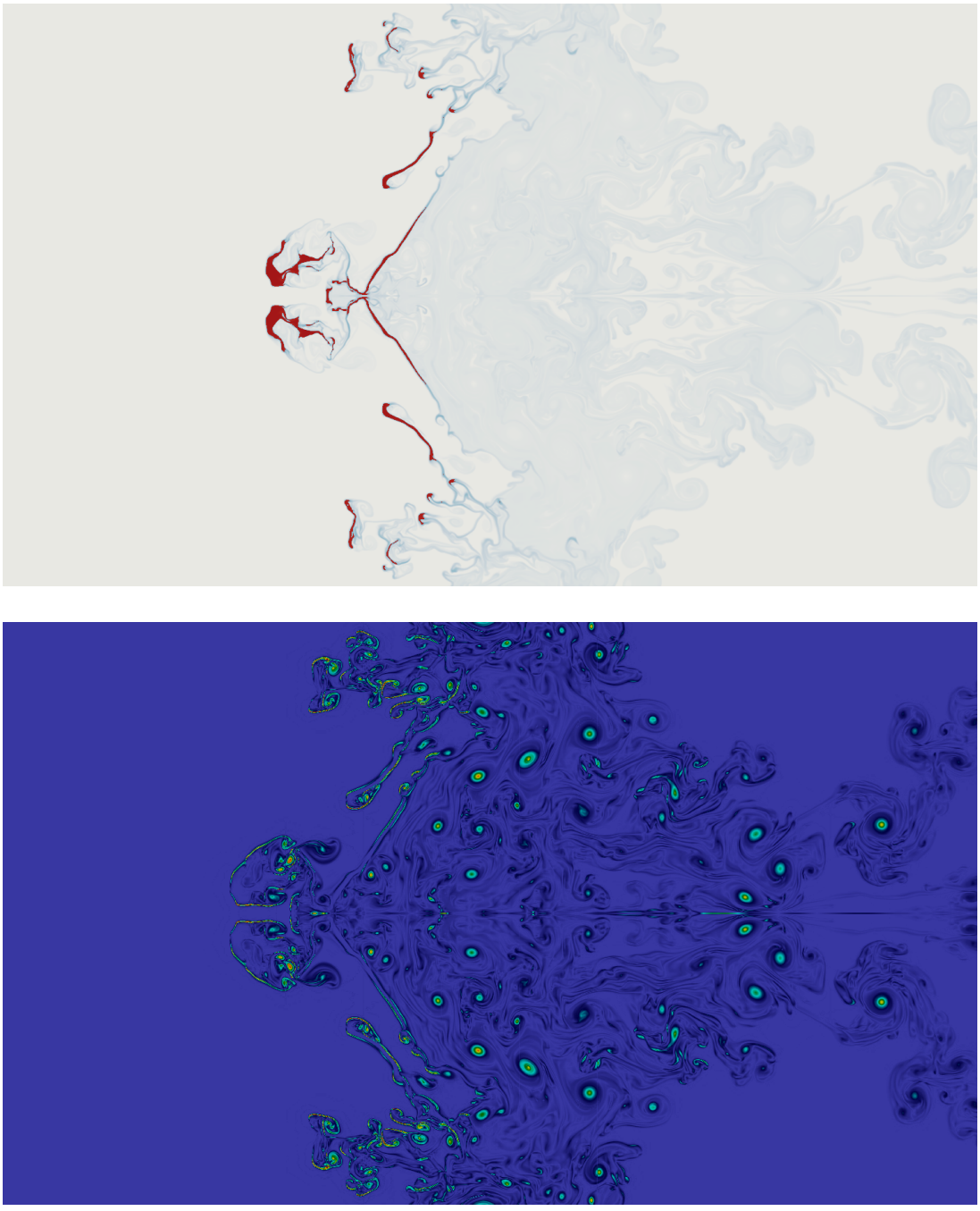

Figure 1.17: Vue agrandie de la simulation de l'atomisation d'une colonne d'eau par un écoulement à grande vitesse provoqué par une onde de choc avec un nombre de Mach de $1,3$ dans de l'air à condition atmosphérique, choc se propageant de la gauche vers la droite. Les résultats sont présentés au temps $2\ 200\mu s$. Dans l'image supérieure, l'eau est représentée en rouge en utilisant un seuil avec $\alpha \geqslant 0,1$ et le brouillard de gouttelettes d'eau micrométrique est représenté en bleu en utilisant la fonction $\alpha^{\frac{1}{3}}$. Dans l'image inférieure, le champ de vorticité est présenté.

1.5.2 3D: l'atomisation d'une goutte d'eau

Dans le cadre de cette thèse, des simulations 3D sont réalisées pour présenter les capacités du modèle et de la méthode numérique qui ont été construits. Deux rapides études sur le temp de calcul et les problèmes d'alignement avec le maillage sont réalisées. Elles ne sont pas developpées dans ce résumé mais il est démontré que l'utilisation d'une méthode AMR rend difficile l'estimation du temps de calcul total d'une simulation. Cependant, l'alignement avec le maillage diminue grandement lors de l'augmentation du nombre maximum de niveau de raffinement. De plus, est souligné le principal avantage de l'utilisation d'une méthode AMR : réduire significativement le nombre maximum de cellules au cours d'une simulation. Ce nombre s'élève à 14 682 190 pour la simulation effectuée, contre 2 560 000 000 dans le cas d'une simulation équivalente utilisant une méthode non-AMR, soit seulement $0,57\%$.

Un exemple de résultat est donc présenté dans la figure 1.18 avec une vue du contour de la goutte au temps 1 000μs. $\alpha = 0,001$ est utilisé pour les contours afin de représenter tous les filaments et toutes les gouttelettes potentielles.

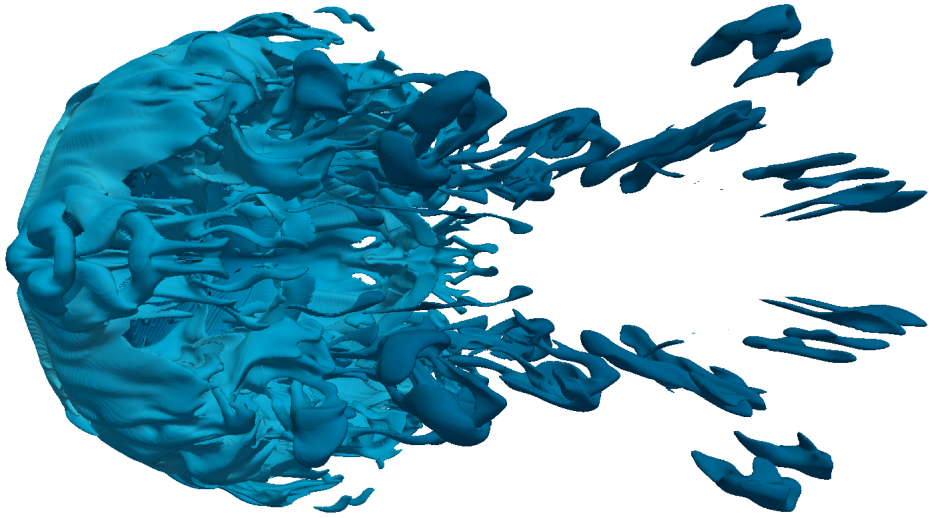

Figure 1.18: Vue du contour des gouttelettes pour l'atomisation 3D. Le résultat est présenté en utilisant $\alpha = 0,001$ pour les contours et au temps 1 000μs.

Chapitre 2

Un modèle et une méthode numérique pour les écoulements compressibles avec effets capillaires

A model and numerical method for compressible flows with capillary effects

This chapter almost corresponds to the Schmidmayer et al. [82] publication.

2.1 Introduction

The breakup of liquid droplets induced by high speed flows has a wide range of engineering and scientific applications and has given rise to a large number of publications. In some cases, this phenomenon causes damages as for example when droplets are impacting aircrafts in supersonic flight causing erosion of its surface (Engel [17], Joseph et al. [42], Igra and Takayama [37, 38]). Studying of droplets behavior in a high speed flow may also be encountered when security issues are considered as, for example, for shock wave attenuation (Chauvin et al. [9, 10]). Other applications can be found in explosive science or in combustion systems where a liquid jet is atomized (Welch and Boyle [96], Meng and Colonius [59], Devassy et al. [15]). Detailed reviews on droplet breakup can be found in Pilch and Erdman [71], Wierzba and Takayama [97], Hsiang and Faeth [34].

Concerning numerical simulations, the breakup study is usually focused on the first stages of droplet deformation when Richtmyer-Meshkov and/or Rayleigh-Taylor instabilities appear (Yang et al. [99], Quirk and Karni [74], Layes and Le Metayer [51], Meng and Colonius [59]), but not on the further stages when capillary and/or viscous effects become significant.

In the last decades, several theoretical studies have been performed to treat capillary effects in multiphase flows. The seminal work of Brackbill et al. [8] succeeded in transforming a surface force into a volume force, quite easy to treat as a source term in a multiphase flow model. The surface tension volume force is expressed thanks to a color function $\tilde{c}(\mathbf{x})$. This approach has been used in Chen and Doolen [12], Sussman et al. [87], Gueyffier et al. [25], Osher and Fedkiw [62, 63], Tryggvason et al. [94], Périgaud and Saurel [66], Le Martelot et al. [52] where capillary effects are added into the momentum and the energy equations.

The aim of this work is to develop a mathematical model for fluid flows with capillary effects that is hyperbolic, verifies conservation principles and entropy inequality together

with a suitable numerical method capable to treat the effect of the flow on the droplet from the short time scale when the shock wave interacts with the droplet to the long time scale when capillary effects become significant. We focus in this study on multiphase compressible fluid flows only. Viscous and heat conduction are not taken into account and will be a part of future works. Some ideas on the treatment of heat conduction in multiphase compressible flows can already be found in [68].

Section 2 presents the Brackbill et al. [8] method to treat the surface tension and a review of existing models with a conservative form of the capillary terms. In Section 3, the new model with capillary effects is presented. The model is in agreement with the conservation principles and with the second law of thermodynamics. It is shown that the model is weakly hyperbolic. It has two sound characteristics associated with the classical compression waves and two new sound characteristics associated with the capillary effects. However, for multiple contact characteristics one eigenvector is always missing. Section 4 is devoted to the building of a numerical method able to solve capillary terms in a conservative manner. The method is based on split models that are separately hyperbolic or weakly hyperbolic. These submodels are solved thanks to adequate numerical schemes. Section 5 presents the validation of the method on 2D test cases. It shows that the model and the numerical method are able to treat accurately both capillary effects and shock wave propagation. Quantitative comparisons are done with other methods based on source terms integration to show the importance of the conservative formulation. To illustrate the capabilities of the model, the aerodynamic breakup of a water column induced by a shock wave is numerically solved and is compared with experiments. In Appendix B, the model derivation is given.

2.2 Compressible two-phase capillary flows: state of the art

2.2.1 Surface tension force and color function

The main difficulty in modeling the capillary effects is about considering a surface force in numerical models that solve volume average quantities. The seminal work of Brackbill et al. [8], called CSF (Continuum Surface Force) method, succeeded to do it by using a color function, $\tilde{c}(\mathbf{x})$. Thanks to this function, the surface tension volume force is then expressed:

$$\mathbf{F}_v(\mathbf{x}) = \sigma\kappa(\mathbf{x})\frac{\boldsymbol{\nabla}\tilde{c}(\mathbf{x})}{[\tilde{c}]},$$

where σ is the surface tension coefficient and $\kappa(\mathbf{x})$ the local curvature of the interface defined by:

$$\kappa(\mathbf{x}) = -\boldsymbol{\nabla}\cdot\mathbf{n}(\mathbf{x}),$$

where $\mathbf{n}(\mathbf{x})$ is the normal vector to the interface between the both phases:

$$\mathbf{n}(\mathbf{x}) = \frac{\boldsymbol{\nabla}\tilde{c}(\mathbf{x})}{\|\boldsymbol{\nabla}\tilde{c}(\mathbf{x})\|}.$$

The color function $\tilde{c}(\mathbf{x})$ allows locations of the different fluids and the interface. $\tilde{c}(\mathbf{x})$ is defined as:

$$\tilde{c}(\mathbf{x}) = \begin{cases} c_1 & \text{in fluid 1,} \\ c_2 & \text{in fluid 2,} \\ c_1 \leqslant \tilde{c}(\mathbf{x}) \leqslant c_2 & \text{in the transition region.} \end{cases} \tag{2.1}$$

In the transition region $\tilde{c}(\mathbf{x})$ is given by interpolation, meaning that the interface has a non zero thickness. $[\tilde{c}] = c_2 - c_1$ is the jump of the color function.

It is assumed that the color function obeys a transport equation [8]:

$$\frac{\partial \tilde{c}(\mathbf{x})}{\partial t} + \mathbf{u}_I \cdot \boldsymbol{\nabla} \tilde{c}(\mathbf{x}) = 0,$$

where $\mathbf{u}_I$ is the interface velocity.

Numerical results using this force can be found in [12, 52, 62, 63, 87, 94]. In these references, the surface tension force is treated as source terms in the momentum and the energy equations. Nevertheless, this treatment of capillary effects violates conservation principles.

2.2.2 Review of existing compressible models with capillary effects

Two family of methods are available to treat interface problems.

- The first family of methods considers interfaces as sharp. Sharp interfaces can be obtained using interface-tracking methods, where usually a level set function tracks the interface (Osher and Sethian [64]). However, such formulations often involve slight modifications of the governing equations. For example a pressure evolution equation can replace the energy equation around interfaces (Karni [44, 45]). In the Ghost Fluid Method (Fedkiw et al. [21]) and its simplified version (Koren et al. [48]), thermodynamically similar variables are added across interfaces to complete stencils. These methods do not generate spurious oscillations at interfaces, however, they are basically not conservative (Liu et al. [54]). Even if progress has been recently done concerning this aspect (Hu et al. [35], Luo et al. [55], Han et al. [29], Schranner et al. [83]), that makes them less desirable for problems where shock waves are involved.

- The second family of methods is described below and is called diffuse interface methods. In this class of methods, interfaces are not explicitly tracked but allowed to diffuse numerically (Abgrall and Karni [2], Saurel and Abgrall [76]). These methods are particularly interesting because they are able to deal with dynamic appearance and disappearance of interfaces. Moreover, this is also the only class of models where the thermodynamics of mixture cells is well defined, thanks to a specific equation of state for each phase (liquid or gas).

The study of capillary effects within the framework of the diffuse interface methods is based on the generalization of the Allaire et al. [4] model. This model originally does not include capillary effects. The second law of thermodynamics is verified only if the

condition of thermal equilibrium $T = T_k$, with $k = \{1, 2\}$, is retained. Périgaud and Saurel [66] extended this model by including the capillary effects. As a result, the surface tension volume force appears as a flux term in the momentum equation as well as the work of this force $\mathbf{F}_v(\mathbf{x}) \cdot \mathbf{u}$ in the total energy equation. In this reference, as Gueyffier et al. [25] did within the incompressible flows framework, a conservative formulation was obtained:

$$\begin{cases} \frac{\partial \alpha_1}{\partial t} + \mathbf{u} \cdot \boldsymbol{\nabla} \alpha_1 & = 0, \\ \frac{\partial \alpha_k \rho_k}{\partial t} + \boldsymbol{\nabla} \cdot (\alpha_k \rho_k \mathbf{u}) & = 0, \\ \frac{\partial \rho \mathbf{u}}{\partial t} + \boldsymbol{\nabla} \cdot \left(\rho \mathbf{u} \otimes \mathbf{u} + P \overline{\overline{I}} - \sigma \left(\|\boldsymbol{\nabla} \alpha_1\| \overline{\overline{I}} - \frac{\boldsymbol{\nabla} \alpha_1 \otimes \boldsymbol{\nabla} \alpha_1}{\|\boldsymbol{\nabla} \alpha_1\|} \right) \right) & = 0, \\ \frac{\partial \rho E + \varepsilon_\sigma}{\partial t} + \boldsymbol{\nabla} \cdot \left(\mathbf{u} (\rho E + \varepsilon_\sigma + P) - \sigma \left(\|\boldsymbol{\nabla} \alpha_1\| \overline{\overline{I}} - \frac{\boldsymbol{\nabla} \alpha_1 \otimes \boldsymbol{\nabla} \alpha_1}{\|\boldsymbol{\nabla} \alpha_1\|} \right) \cdot \mathbf{u} \right) & = 0, \end{cases}$$

where α_k and ρ_k are the volume fraction and the density of phase k. ρ, $\mathbf{u}$, P, $E = e + \frac{1}{2}\|\mathbf{u}\|^2$ and e are respectively the mixture variables for density, velocity, pressure, total energy and internal energy. The specific mixture internal energy is defined as $e = \sum_k Y_k e_k(\rho_k, P)$ and each fluid is governed by its own equation of state (EOS) $e_k = e_k(\rho_k, P)$. Introducing the capillary effects in fluxes (conservative formulation) leads to a new term in the mixture total energy equation, $\varepsilon_\sigma = \sigma \|\boldsymbol{\nabla} \alpha_1\|$ which is defined as a capillary potential energy. Note that α_1 obeys a transport equation and plays the role of the color function (2.1) because $\mathbf{u}_I = \mathbf{u}$ when the velocity equilibrium is considered. In [66], the authors used a pressure equilibrium closure, allowing the resolution of interface problems dedicated to high speed flows. Nevertheless, this closure does not allow to respect the second law of thermodynamics for the mixture.

Le Martelot et al. [52] corrected this drawback by including the capillary effects in a velocity, pressure and temperature equilibrium system of equations by considering the mass fraction as the color function: the second law of thermodynamics is then respected. However, the characteristic velocities were estimated under assumption that the local curvature is fixed. Even if such an approach is physically reasonable, it does not allow us to rigorously estimate the propagation speeds. Also, the thermal equilibrium closure is reasonable for the description of the boiling phenomenon, but it is too drastic for droplet breakup study under high speed flows.

It becomes then obvious that the introduction of a new model having clearly defined sound speeds with the capillary effects in conservative form that can still be compatible with the mixture entropy increase without the temperature equilibrium assumption is necessary.

2.3 Mechanical equilibrium model with capillary effects

2.3.1 The model

The new model we propose is reminiscent that of the Kapila et al. model [43]. This last model has been shown to be suitable to treat interface problems between compressible fluids. Multiple extensions of this model have been developped to solve several concrete problems dealing with phase transition (Massoni et al. [56], Saurel et al. [79]), cavitation

(Petitpas et al. [69]), detonation in high energetic materials (Petitpas et al. [70]), solid-fluid interaction and compaction of granular media (Favrie and Gavrilyuk [19, 18]) and low Mach number flows (Murrone and Guillard [60]). It considers compressible two-phase flows in mechanical equilibrium (pressure and velocity equilibrium). In this model, the volume fraction obeys the following equation coming from the pressure equilibrium condition:

$$\frac{\partial \alpha_1}{\partial t} + \mathbf{u} \cdot \boldsymbol{\nabla} \alpha_1 = K \boldsymbol{\nabla} \cdot \mathbf{u}, \tag{2.2}$$

where the term $K\boldsymbol{\nabla}\cdot\mathbf{u}$ accounts for the differences in the acoustic behaviour of both phases. K is given by:

$$K = \frac{\rho_2 a_2^2 - \rho_1 a_1^2}{\frac{\rho_2 a_2^2}{\alpha_2} + \frac{\rho_1 a_1^2}{\alpha_1}},$$

a_k being the speed of sound of phase k.

The capillary effects are then added in conservative form. Because the color function is a purely geometric variable, a supplementary equation for the color function is added. It will be shown in the following that the introduction of this supplementary equation is an important ingredient to perform the hyperbolicity study. Two methodologies are available to obtain the new model. The first is to add the surface tension force of Brackbill et al. and his work to the Kapila et al. model, then to modify them in a conservative form (this calculation is presented in Appendix A). The second methodology is to give oneself an energy, that obviously takes into account the capillary energy, and to apply the Hamilton principle for the model derivation (this calculation is presented in Appendix B). The model is thus as follows:

$$\begin{cases} \frac{\partial \alpha_1}{\partial t} + \mathbf{u} \cdot \boldsymbol{\nabla} \alpha_1 - K \boldsymbol{\nabla} \cdot \mathbf{u} & = 0, \\ \frac{\partial \alpha_k \rho_k}{\partial t} + \boldsymbol{\nabla} \cdot (\alpha_k \rho_k \mathbf{u}) & = 0, \\ \frac{\partial \rho \mathbf{u}}{\partial t} + \boldsymbol{\nabla} \cdot \left(\rho \mathbf{u} \otimes \mathbf{u} + P \overline{\overline{I}} + \overline{\overline{\Omega}} \right) & = 0, \\ \frac{\partial \rho E + \varepsilon_\sigma}{\partial t} + \boldsymbol{\nabla} \cdot \left((\rho E + \varepsilon_\sigma + P) \mathbf{u} + \overline{\overline{\Omega}} \cdot \mathbf{u} \right) & = 0, \\ \frac{\partial c}{\partial t} + \mathbf{u} \cdot \boldsymbol{\nabla} c & = 0, \end{cases} \tag{2.3}$$

with $\overline{\overline{\Omega}}$ being the capillary tensor given by:

$$\overline{\overline{\Omega}} = -\sigma \left(\|\boldsymbol{\nabla} c\| \overline{\overline{I}} - \frac{\boldsymbol{\nabla} c \otimes \boldsymbol{\nabla} c}{\|\boldsymbol{\nabla} c\|} \right). \tag{2.4}$$

The capillary energy is equal to $\varepsilon_\sigma = \sigma \|\boldsymbol{\nabla} c\|$ and the color function is normalized by its jump: $c = \tilde{c}/[\tilde{c}]$.

The surface tension terms do not affect the pressure and the entropy equations. The pressure equation evolution then reads:

$$\frac{dP}{dt} + \rho a^2 \boldsymbol{\nabla} \cdot (\mathbf{u}) = 0.$$

where a is the Wood mixture speed of sound [98]:

$$a^2 = \left(\rho \sum_k \frac{\alpha_k}{\rho_k a_k^2} \right)^{-1}. \tag{2.5}$$

As in Kapila et al. [43], the entropy equations remain unchanged in continuous motion:

$$\frac{ds_k}{dt} = 0,$$

with the material derivative operator $d(\cdot)/dt = \partial(\cdot)/\partial t + \mathbf{u} \cdot \boldsymbol{\nabla}(\cdot)$. The mixture entropy equation is obviously assured:

$$\frac{ds}{dt} = \sum_k \frac{dY_k s_k}{dt} = 0.$$

2.3.2 Hyperbolicity

In this section, the study of the hyperbolicity of system (2.3) is done. Thanks to the rotational invariance of the equations, the study can be reduced to the study of only 1D equation.

2.3.2.1 Primitive form

The model needs to be transformed into a vector form:

$$\frac{\partial \mathbf{W}}{\partial t} + \overline{\overline{A}}\,(\mathbf{W})\,\frac{\partial \mathbf{W}}{\partial x} = 0. \tag{2.6}$$

The color function is first rewritten by taking its gradient to obtain a conservative equation for $\mathbf{w} = \boldsymbol{\nabla} c$:

$$\frac{\partial \mathbf{w}}{\partial t} + \boldsymbol{\nabla}\,(\mathbf{u} \cdot \mathbf{w}) = 0.$$

Or, in an equivalent form:

$$\frac{\partial \mathbf{w}}{\partial t} + \left(\frac{\partial \mathbf{w}}{\partial \mathbf{x}}\right)^T \cdot \mathbf{u} + \left(\frac{\partial \mathbf{u}}{\partial \mathbf{x}}\right)^T \cdot \mathbf{w} = 0. \tag{2.7}$$

Since $\mathbf{w}$ is a gradient, we have:

$$\operatorname{curl}(\mathbf{w}) = \mathbf{0}, \tag{2.8}$$

i.e.,

$$\left(\frac{\partial \mathbf{w}}{\partial \mathbf{x}}\right)^T = \left(\frac{\partial \mathbf{w}}{\partial \mathbf{x}}\right).$$

Thus, equation (2.7) with the constraint (2.8) becomes:

$$\frac{\partial \mathbf{w}}{\partial t} + \left(\frac{\partial \mathbf{w}}{\partial \mathbf{x}}\right) \cdot \mathbf{u} + \left(\frac{\partial \mathbf{u}}{\partial \mathbf{x}}\right)^T \cdot \mathbf{w} = \mathbf{0}. \tag{2.9}$$

Constraint (2.8) also appears in solid mechanics where the formulation of the extended system under a "curl" constraint is important in the hyperbolicity study (see Ndanou

et al. [61]). Equation (2.9) may be developed in three dimensions, where we denote $\mathbf{u} = (u, v, w)^T$, $\mathbf{w} = (w_1, w_2, w_3)^T$ and $\mathbf{x} = (x, y, z)^T$:

$$\left\{\begin{array}{ll} \frac{\partial w_1}{\partial t} + \frac{\partial w_1}{\partial x}u + \frac{\partial w_1}{\partial y}v + \frac{\partial w_1}{\partial z}w + \frac{\partial u}{\partial x}w_1 + \frac{\partial v}{\partial x}w_2 + \frac{\partial w}{\partial x}w_3 & = 0, \\ \frac{\partial w_2}{\partial t} + \frac{\partial w_2}{\partial x}u + \frac{\partial w_2}{\partial y}v + \frac{\partial w_2}{\partial z}w + \frac{\partial u}{\partial y}w_1 + \frac{\partial v}{\partial y}w_2 + \frac{\partial w}{\partial y}w_3 & = 0, \\ \frac{\partial w_3}{\partial t} + \frac{\partial w_3}{\partial x}u + \frac{\partial w_3}{\partial y}v + \frac{\partial w_3}{\partial z}w + \frac{\partial u}{\partial z}w_1 + \frac{\partial v}{\partial z}w_2 + \frac{\partial w}{\partial z}w_3 & = 0. \end{array}\right. \tag{2.10}$$

In the case where all the variables depend only on (t, x), (2.10) reduces to:

$$\left\{\begin{array}{ll} \frac{\partial w_1}{\partial t} + \frac{\partial w_1}{\partial x}u + \frac{\partial u}{\partial x}w_1 + \frac{\partial v}{\partial x}w_2 + \frac{\partial w}{\partial x}w_3 & = 0, \\ \frac{\partial w_2}{\partial t} + \frac{\partial w_2}{\partial x}u & = 0, \\ \frac{\partial w_3}{\partial t} + \frac{\partial w_3}{\partial x}u & = 0. \end{array}\right.$$

The vector $\mathbf{w}$ is introduced to rewrite components for the capillary tensor $\overline{\overline{\Omega}}$ (2.4) in the x-direction:

$$\Omega_{11} = \sigma\left(\frac{-w_2^2 - w_3^2}{\sqrt{w_1^2 + w_2^2 + w_3^2}}\right),$$

$$\Omega_{12} = \sigma\left(\frac{w_1 w_2}{\sqrt{w_1^2 + w_2^2 + w_3^2}}\right),$$

$$\Omega_{13} = \sigma\left(\frac{w_1 w_3}{\sqrt{w_1^2 + w_2^2 + w_3^2}}\right).$$

Finally, the system rewritten in vector form reads for two phases:

$$\left\{\begin{array}{ll} \frac{\partial \alpha_1}{\partial t} + u\frac{\partial \alpha_1}{\partial x} - K\frac{\partial u}{\partial x} & = 0, \\ \frac{\partial u}{\partial t} + u\frac{\partial u}{\partial x} + \frac{1}{\rho}\left(\frac{\partial P}{\partial x} + \frac{\partial \Omega_{11}}{\partial w_1}\frac{\partial w_1}{\partial x} + \frac{\partial \Omega_{11}}{\partial w_2}\frac{\partial w_2}{\partial x} + \frac{\partial \Omega_{11}}{\partial w_3}\frac{\partial w_3}{\partial x}\right) & = 0, \\ \frac{\partial v}{\partial t} + u\frac{\partial v}{\partial x} + \frac{1}{\rho}\left(\frac{\partial \Omega_{12}}{\partial w_1}\frac{\partial w_1}{\partial x} + \frac{\partial \Omega_{12}}{\partial w_2}\frac{\partial w_2}{\partial x} + \frac{\partial \Omega_{12}}{\partial w_3}\frac{\partial w_3}{\partial x}\right) & = 0, \\ \frac{\partial w}{\partial t} + u\frac{\partial w}{\partial x} + \frac{1}{\rho}\left(\frac{\partial \Omega_{13}}{\partial w_1}\frac{\partial w_1}{\partial x} + \frac{\partial \Omega_{13}}{\partial w_2}\frac{\partial w_2}{\partial x} + \frac{\partial \Omega_{13}}{\partial w_3}\frac{\partial w_3}{\partial x}\right) & = 0, \\ \frac{\partial P}{\partial t} + u\frac{\partial P}{\partial x} + \rho a^2\frac{\partial u}{\partial x} & = 0, \\ \frac{\partial w_1}{\partial t} + u\frac{\partial w_1}{\partial x} + w_1\frac{\partial u}{\partial x} + w_2\frac{\partial v}{\partial x} + w_3\frac{\partial w}{\partial x} & = 0, \\ \frac{\partial w_2}{\partial t} + u\frac{\partial w_2}{\partial x} & = 0, \\ \frac{\partial w_3}{\partial t} + u\frac{\partial w_3}{\partial x} & = 0, \\ \frac{\partial s_1}{\partial t} + u\frac{\partial s_1}{\partial x} & = 0, \\ \frac{\partial s_2}{\partial t} + u\frac{\partial s_2}{\partial x} & = 0, \\ \frac{\partial Y_1}{\partial t} + u\frac{\partial Y_1}{\partial x} & = 0, \\ \frac{\partial c}{\partial t} + u\frac{\partial c}{\partial x} & = 0. \end{array}\right.$$

2.3.2.2 Eigenvalues

The vector $\mathbf{W}$ and the matrix $\overline{\overline{A}}$ in (2.6) are then defined by:

$$\mathbf{W} = [\alpha_1, u, v, w, P, w_1, w_2, w_3, s_1, s_2, Y_1, c]^T,$$

$$\overline{\overline{A}}(\mathbf{W}) = \begin{bmatrix} u & -K & 0 & 0 & 0 & 0 & 0 & 0 & 0 & 0 & 0 & 0 \\ 0 & u & 0 & 0 & \frac{1}{\rho} & \frac{1}{\rho}\frac{\partial \Omega_{11}}{\partial w_1} & \frac{1}{\rho}\frac{\partial \Omega_{11}}{\partial w_2} & \frac{1}{\rho}\frac{\partial \Omega_{11}}{\partial w_3} & 0 & 0 & 0 & 0 \\ 0 & 0 & u & 0 & 0 & \frac{1}{\rho}\frac{\partial \Omega_{12}}{\partial w_1} & \frac{1}{\rho}\frac{\partial \Omega_{12}}{\partial w_2} & \frac{1}{\rho}\frac{\partial \Omega_{12}}{\partial w_3} & 0 & 0 & 0 & 0 \\ 0 & 0 & 0 & u & 0 & \frac{1}{\rho}\frac{\partial \Omega_{13}}{\partial w_1} & \frac{1}{\rho}\frac{\partial \Omega_{13}}{\partial w_2} & \frac{1}{\rho}\frac{\partial \Omega_{13}}{\partial w_3} & 0 & 0 & 0 & 0 \\ 0 & \rho a^2 & 0 & 0 & u & 0 & 0 & 0 & 0 & 0 & 0 & 0 \\ 0 & w_1 & w_2 & w_3 & 0 & u & 0 & 0 & 0 & 0 & 0 & 0 \\ 0 & 0 & 0 & 0 & 0 & 0 & u & 0 & 0 & 0 & 0 & 0 \\ 0 & 0 & 0 & 0 & 0 & 0 & 0 & u & 0 & 0 & 0 & 0 \\ 0 & 0 & 0 & 0 & 0 & 0 & 0 & 0 & u & 0 & 0 & 0 \\ 0 & 0 & 0 & 0 & 0 & 0 & 0 & 0 & 0 & u & 0 & 0 \\ 0 & 0 & 0 & 0 & 0 & 0 & 0 & 0 & 0 & 0 & u & 0 \\ 0 & 0 & 0 & 0 & 0 & 0 & 0 & 0 & 0 & 0 & 0 & u \end{bmatrix}$$

The determinant of matrix $\overline{\overline{A}}$ can be calculated:

$$\det\left(\overline{\overline{A}}(\mathbf{W}) - \lambda\overline{\overline{I}}\right) = (u-\lambda)^8\left[(u-\lambda)^4 + L(u-\lambda)^2 + M\right],$$

where:

$$L = -a^2 - \frac{1}{\rho}\left(w_1\frac{\partial \Omega_{11}}{\partial w_1} + w_2\frac{\partial \Omega_{12}}{\partial w_1} + w_3\frac{\partial \Omega_{13}}{\partial w_1}\right),$$

$$M = \frac{a^2}{\rho}\left(w_2\frac{\partial \Omega_{12}}{\partial w_1} + w_3\frac{\partial \Omega_{13}}{\partial w_1}\right).$$

8 real eigenvalues are straightforward found:

$$\lambda_{1,2,3,4,5,6,7,8} = u.$$

The 4 other eigenvalues are the roots of the quadratic equation:

$$X^2 + LX + M = 0, \tag{2.11}$$

with $X = (u-\lambda)^2$. If the discriminant Δ is positive, the roots of equation (2.11) are real and complex numbers otherwise. Defining the components of the normal vector $n_k = w_k/\|\mathbf{w}\|$, after some calculations the discriminant is:

$$\Delta = \left(a^2 + \frac{\sigma\|\mathbf{w}\|}{\rho}\left(n_2^2 + n_3^2\right)\right)^2 - 4a^2\frac{\sigma\|\mathbf{w}\|}{\rho}\left(n_2^2 + n_3^2\right)^2.$$

But:

$$\left(n_2^2 + n_3^2\right) \leqslant 1.$$

Hence:

$$\Delta \geqslant \left(a^2 + \frac{\sigma\|\mathbf{w}\|}{\rho}\left(n_2^2 + n_3^2\right)\right)^2 - 4a^2\frac{\sigma\|\mathbf{w}\|}{\rho}\left(n_2^2 + n_3^2\right)$$

$$= \left(a^2 - \frac{\sigma\|\mathbf{w}\|}{\rho}\left(n_2^2 + n_3^2\right)\right)^2 \geqslant 0.$$

The roots of the quadratic equation (2.11) are then all real. Thus, the corresponding eigenvalues of model (2.3) are real, explicit and given by:

$$\lambda_{9,10} = u \pm a_s, \tag{2.12}$$

$$\lambda_{11,12} = u \pm a_c, \tag{2.13}$$

where:

$$a_s^2 = \frac{a^2 + b + \sqrt{\left(a^2+b\right)^2 - 4a^2 b\left(n_2^2 + n_3^2\right)}}{2},$$

$$a_c^2 = \frac{a^2 + b - \sqrt{\left(a^2+b\right)^2 - 4a^2 b\left(n_2^2 + n_3^2\right)}}{2},$$

a is the Wood mixture speed of sound previously defined (2.5) and:

$$b = \frac{\sigma\|\mathbf{w}\|}{\rho}\left(n_2^2 + n_3^2\right).$$

Finally, there are 8 multiple eigenvalues $\lambda = u$ and 4 eigenvalues corresponding to sound waves (2.12) and capillary waves (2.13) (see Figure 2.1).

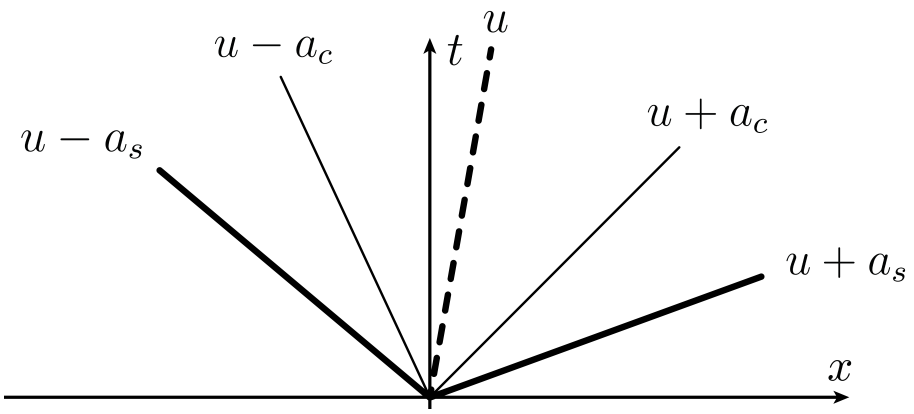

Figure 2.1: Model (2.3) admits two types of acoustic waves.

The system is hyperbolic if the multiple eigenvalues $\lambda = u$ have exactly 8 linearly independent eigenvectors. One can prove that it is not the case, one eigenvector is missing (see Appendix C), so the system is only weakly hyperbolic. The whole system of the eigenvectors will not be given because this equilibrium system will not be numerically solved in this form (see Section 2.4 for discussion of the numerical method).

2.4 Numerical resolution of model (2.3)

2.4.1 Basic ideas

The numerical resolution of model (2.3) represents a challenge regarding the two following points:

- The first difficulty is due to the $K\boldsymbol{\nabla}\cdot\mathbf{u}$ term in the volume fraction evolution equation. This is the precious ingredient leading to the respect of the mixture entropy equation when a pressure equilibrium assumption is retained. Nevertheless, the presence of this non-conservative term considerably complicates the numerical method which crucially depends on the choice of appropriate Rankine-Hugoniot relations (see [23] and [80] for details). This is a reason why a non-equilibrium pressure model is preferred with a pressure relaxation term instead of the non-conservative term $K\boldsymbol{\nabla}\cdot\mathbf{u}$ in the volume fraction equation. This model is presented below.

- The second difficulty is in the simultaneous treatment of 5 waves which are present in the model. This difficulty is circumvented by the use of split models that are proven to be hyperbolic and weakly hyperbolic respectively.

2.4.1.1 Pressure relaxation model with capillary effects

Because the non-conservative volume fraction equation presents a major problem regarding numerical resolution, the following weakly hyperbolic non-equilibrium pressure model is proposed:

$$\left\{\begin{array}{ll}
\frac{\partial\alpha_1}{\partial t}+\mathbf{u}\cdot\nabla\alpha_1 & =\mu\left(P_1-P_2\right),\\
\frac{\partial\alpha_1\rho_1}{\partial t}+\boldsymbol{\nabla}\cdot\left(\alpha_1\rho_1\mathbf{u}\right) & =0,\\
\frac{\partial\alpha_2\rho_2}{\partial t}+\boldsymbol{\nabla}\cdot\left(\alpha_2\rho_2\mathbf{u}\right) & =0,\\
\frac{\partial\rho\mathbf{u}}{\partial t}+\boldsymbol{\nabla}\cdot\left(\rho\mathbf{u}\otimes\mathbf{u}+P\overline{\overline{I}}+\overline{\overline{\Omega}}\right) & =\mathbf{0},\\
\frac{\partial\alpha_1\rho_1e_1}{\partial t}+\boldsymbol{\nabla}\cdot\left(\alpha_1\rho_1e_1\mathbf{u}\right)+\alpha_1P_1\boldsymbol{\nabla}\cdot\mathbf{u} & =-\mu P_I\left(P_1-P_2\right),\\
\frac{\partial\alpha_2\rho_2e_2}{\partial t}+\boldsymbol{\nabla}\cdot\left(\alpha_2\rho_2e_2\mathbf{u}\right)+\alpha_2P_2\boldsymbol{\nabla}\cdot\mathbf{u} & =\mu P_I\left(P_1-P_2\right),\\
\frac{\partial c}{\partial t}+\mathbf{u}\cdot\boldsymbol{\nabla}c & =0,
\end{array}\right. \tag{2.14}$$

where μ is the pressure relaxation coefficient, $P_I=\frac{Z_2P_1+Z_1P_2}{Z_1+Z_2}$ (see [77] for details) and $Z_k=\rho_ka_k$ is the acoustic impedance of the phase k. The mixture pressure is given by:

$$P=\alpha_1P_1+\alpha_2P_2.$$

Due to the condition $P_1\neq P_2$ in this model, the total energy equation of the mixture is replaced by the internal energy equation for each phase. Nevertheless, the mixture total energy equation of the system can be written in usual form:

$$\frac{\partial\rho E+\varepsilon_\sigma}{\partial t}+\boldsymbol{\nabla}\cdot\left(\left(\rho E+\varepsilon_\sigma+P\right)\mathbf{u}+\overline{\overline{\Omega}}\cdot\mathbf{u}\right)=0. \tag{2.15}$$

The equation (2.15) is redundant when both phasic internal energy equations are solved, but it will appear to be an important ingredient for numerical method to ensure the energy conservation and to preserve a correct treatment of shock waves.

Following Section 2.3.2, one can prove that model (2.14) is also weakly hyperbolic.

One can note that the surface tension effects are missing in the phasic energy equations since it is only a mixture characteristic.

The entropy equations for system (2.14) can also be written:

$$\alpha_1\rho_1 T_1 \frac{ds_1}{dt} = \mu(P_1 - P_2)^2 \frac{Z_1}{Z_1 + Z_2},$$

$$\alpha_2\rho_2 T_2 \frac{ds_2}{dt} = \mu(P_1 - P_2)^2 \frac{Z_2}{Z_1 + Z_2},$$

that insures the mixture entropy ($s = Y_1 s_1 + Y_2 s_2$) increases.

Model (2.3) can be recovered as the asymptotic limit of Model (2.14) when the pressure of each phase tends to be equal. A special splitting procedure will be done for the numerical resolution of model (2.14).

2.4.1.2 Splitting procedure

Model (2.14) without the relaxation terms is split in two submodels. The first submodel does not take into account the surface tension terms. The hyperbolicity is then easily verified. The second submodel contains the only capillary terms and is proven weakly hyperbolic. Such an approach was first proposed in Favrie et al. [20] where the splitting procedure was used to separate the treatment of longitudinal and shear waves in hyperelasticity. The submodels are presented below only in the x-direction.

Hyperbolic submodel 1

The first submodel is similar to that presented in [80] with additional decoupled equations for the gradient of the color function:

$$\begin{cases} \dfrac{\partial \alpha_1}{\partial t} + u\dfrac{\partial \alpha_1}{\partial x} & = 0, \\ \dfrac{\partial \alpha_1\rho_1}{\partial t} + \dfrac{\partial \alpha_1\rho_1 u}{\partial x} & = 0, \\ \dfrac{\partial \alpha_2\rho_2}{\partial t} + \dfrac{\partial \alpha_2\rho_2 u}{\partial x} & = 0, \\ \dfrac{\partial \rho u}{\partial t} + \dfrac{\partial \rho u^2 + \alpha_1 P_1 + \alpha_2 P_2}{\partial x} & = 0, \\ \dfrac{\partial \rho v}{\partial t} + \dfrac{\partial \rho u v}{\partial x} & = 0, \\ \dfrac{\partial \rho w}{\partial t} + \dfrac{\partial \rho u w}{\partial x} & = 0, \\ \dfrac{\partial \alpha_1\rho_1 e_1}{\partial t} + \dfrac{\partial \alpha_1\rho_1 e_1 u}{\partial x} + \alpha_1 P_1 \dfrac{\partial u}{\partial x} & = 0, \\ \dfrac{\partial \alpha_2\rho_2 e_2}{\partial t} + \dfrac{\partial \alpha_2\rho_2 e_2 u}{\partial x} + \alpha_2 P_2 \dfrac{\partial u}{\partial x} & = 0, \\ \dfrac{\partial w_1}{\partial t} + \dfrac{\partial w_1 u}{\partial x} & = 0, \\ \dfrac{\partial w_2}{\partial t} + u\dfrac{\partial w_2}{\partial x} & = 0, \\ \dfrac{\partial w_3}{\partial t} + u\dfrac{\partial w_3}{\partial x} & = 0. \end{cases} \tag{2.16}$$

This system describes only the transport and the compression waves. The equation for w_1 is taken in conservative form to let the possibility to consider weak solutions. The other terms in this equation will be treated in the second submodel.

Model (2.16) may be rewritten in a vector form (2.6) with:

$$\mathbf{W} = [\alpha_1, s_1, s_2, u, v, w, P_1, P_2, w_1, w_2, w_3]^T$$

$$\overline{\overline{A}}(\mathbf{W}) = \begin{bmatrix} u & 0 & 0 & 0 & 0 & 0 & 0 & 0 & 0 & 0 & 0 \\ 0 & u & 0 & 0 & 0 & 0 & 0 & 0 & 0 & 0 & 0 \\ 0 & 0 & u & 0 & 0 & 0 & 0 & 0 & 0 & 0 & 0 \\ \frac{P_1-P_2}{\rho} & 0 & 0 & u & 0 & 0 & \frac{\alpha_1}{\rho} & \frac{\alpha_2}{\rho} & 0 & 0 & 0 \\ 0 & 0 & 0 & 0 & u & 0 & 0 & 0 & 0 & 0 & 0 \\ 0 & 0 & 0 & 0 & 0 & u & 0 & 0 & 0 & 0 & 0 \\ 0 & 0 & 0 & \rho_1 a_1^2 & 0 & 0 & u & 0 & 0 & 0 & 0 \\ 0 & 0 & 0 & \rho_2 a_2^2 & 0 & 0 & 0 & u & 0 & 0 & 0 \\ 0 & 0 & 0 & w_1 & 0 & 0 & 0 & 0 & u & 0 & 0 \\ 0 & 0 & 0 & 0 & 0 & 0 & 0 & 0 & 0 & u & 0 \\ 0 & 0 & 0 & 0 & 0 & 0 & 0 & 0 & 0 & 0 & u \end{bmatrix}$$

The eigenvalues of the system are:

$$\lambda_{1,2,3,4,5,6,7,8,9} = u,$$

$$\lambda_{10} = u - a_f,$$

$$\lambda_{11} = u + a_f,$$

where a_f is the frozen mixture sound speed:

$$a_f^2 = Y_1 a_1^2 + Y_2 a_2^2.$$

The hyperbolicity of this first submodel is proven in [80].

Weakly hyperbolic submodel 2

The second submodel is:

$$\begin{cases} \frac{\partial \alpha_1}{\partial t} & = 0, \\ \frac{\partial \alpha_1 \rho_1}{\partial t} & = 0, \\ \frac{\partial \alpha_2 \rho_2}{\partial t} & = 0, \\ \frac{\partial \rho u}{\partial t} + \left(\frac{\partial \Omega_{11}}{\partial w_1}\frac{\partial w_1}{\partial x} + \frac{\partial \Omega_{11}}{\partial w_2}\frac{\partial w_2}{\partial x} + \frac{\partial \Omega_{11}}{\partial w_3}\frac{\partial w_3}{\partial x} \right) & = 0, \\ \frac{\partial \rho v}{\partial t} + \left(\frac{\partial \Omega_{12}}{\partial w_1}\frac{\partial w_1}{\partial x} + \frac{\partial \Omega_{12}}{\partial w_2}\frac{\partial w_2}{\partial x} + \frac{\partial \Omega_{12}}{\partial w_3}\frac{\partial w_3}{\partial x} \right) & = 0, \\ \frac{\partial \rho w}{\partial t} + \left(\frac{\partial \Omega_{13}}{\partial w_1}\frac{\partial w_1}{\partial x} + \frac{\partial \Omega_{13}}{\partial w_2}\frac{\partial w_2}{\partial x} + \frac{\partial \Omega_{13}}{\partial w_3}\frac{\partial w_3}{\partial x} \right) & = 0, \\ \frac{\partial \alpha_1 \rho_1 e_1}{\partial t} & = 0, \\ \frac{\partial \alpha_2 \rho_2 e_2}{\partial t} & = 0, \\ \frac{\partial w_1}{\partial t} + w_2 \frac{\partial v}{\partial x} + w_3 \frac{\partial w}{\partial x} & = 0, \\ \frac{\partial w_2}{\partial t} & = 0, \\ \frac{\partial w_3}{\partial t} & = 0. \end{cases} \tag{2.17}$$

This second system describes the capillary effects. Also, the non-conservative product in the equation for w_1 is well defined because w_2 and w_3 are continuous through the shock.

Model (2.17) may be rewritten in a vector form (2.6) with:

$$\mathbf{W} = [\alpha_1, s_1, s_2, u, v, w, P_1, P_2, w_1, w_2, w_3]^T$$

$$\overline{\overline{A}}(\mathbf{W}) = \begin{bmatrix} 0 & 0 & 0 & 0 & 0 & 0 & 0 & 0 & 0 & 0 & 0 \\ 0 & 0 & 0 & 0 & 0 & 0 & 0 & 0 & 0 & 0 & 0 \\ 0 & 0 & 0 & 0 & 0 & 0 & 0 & 0 & 0 & 0 & 0 \\ 0 & 0 & 0 & 0 & 0 & 0 & 0 & 0 & \frac{1}{\rho}\frac{\partial \Omega_{11}}{\partial w_1} & \frac{1}{\rho}\frac{\partial \Omega_{11}}{\partial w_2} & \frac{1}{\rho}\frac{\partial \Omega_{11}}{\partial w_3} \\ 0 & 0 & 0 & 0 & 0 & 0 & 0 & 0 & \frac{1}{\rho}\frac{\partial \Omega_{12}}{\partial w_1} & \frac{1}{\rho}\frac{\partial \Omega_{12}}{\partial w_2} & \frac{1}{\rho}\frac{\partial \Omega_{12}}{\partial w_3} \\ 0 & 0 & 0 & 0 & 0 & 0 & 0 & 0 & \frac{1}{\rho}\frac{\partial \Omega_{13}}{\partial w_1} & \frac{1}{\rho}\frac{\partial \Omega_{13}}{\partial w_2} & \frac{1}{\rho}\frac{\partial \Omega_{13}}{\partial w_3} \\ 0 & 0 & 0 & 0 & 0 & 0 & 0 & 0 & 0 & 0 & 0 \\ 0 & 0 & 0 & 0 & 0 & 0 & 0 & 0 & 0 & 0 & 0 \\ 0 & 0 & 0 & 0 & w_2 & w_3 & 0 & 0 & 0 & 0 & 0 \\ 0 & 0 & 0 & 0 & 0 & 0 & 0 & 0 & 0 & 0 & 0 \\ 0 & 0 & 0 & 0 & 0 & 0 & 0 & 0 & 0 & 0 & 0 \end{bmatrix}$$

The eigenvalues of the system are:

$$\lambda_{1,2,3,4,5,6,7,8,9} = 0,$$

$$\lambda_{10} = -\left(n_2^2 + n_3^2\right)\sqrt{\frac{\sigma\|\mathbf{w}\|}{\rho}},$$

$$\lambda_{11} = \left(n_2^2 + n_3^2\right)\sqrt{\frac{\sigma\|\mathbf{w}\|}{\rho}}.$$

The eigenvalues of the system are all real but, as in the case of model (2.3), there are not as much linearly independent eigenvectors as eigenvalues: one eigenvector is always missing. So, the second submodel is weakly hyperbolic.

2.4.2 Numerical Method

Finally, the numerical method is presented as a 3-step method. Each step is successively performed in order to circumvent specific numerical problems:

- First, the hyperbolic non-equilibrium pressure model (2.16) is solved using a Godunov-type method.
- Second, model (2.17) is solved. A specific attention is paid to the choice for the flux terms in order to ensure the momentum and energy conservation.
- Third, a relaxation procedure leads to the pressure equilibrium.

The chain of these three steps is equivalent to solve model (2.3). Each step of the method is presented in details hereafter.

The full system of equations is first rewritten in the following vector form:

$$\frac{\partial \mathbf{U}}{\partial t} + \frac{\partial \left(\mathbf{F}_h^x\left(\mathbf{U}\right) + \mathbf{F}_c^x\left(\mathbf{U}\right)\right)}{\partial x} + \frac{\partial \left(\mathbf{F}_h^y\left(\mathbf{U}\right) + \mathbf{F}_c^y\left(\mathbf{U}\right)\right)}{\partial y}$$

$$+ \frac{\partial \left(\mathbf{F}_h^z\left(\mathbf{U}\right) + \mathbf{F}_c^z\left(\mathbf{U}\right)\right)}{\partial z} + \mathbf{H}_{nc}\boldsymbol{\nabla}\cdot\mathbf{u} = \mathbf{H}_{relax}.$$

The vector $\mathbf{U}$ contains the unknown quantities defined in the system:

$$\mathbf{U} = \left[\alpha_1, \alpha_1\rho_1, \alpha_2\rho_2, \rho u, \rho v, \rho w, \alpha_1\rho_1 e_1, \alpha_2\rho_2 e_2, c, \rho E + \varepsilon_\sigma\right]^T$$

The vectors $\mathbf{F}_h^\beta\left(\mathbf{U}\right)$, $\mathbf{F}_c^\beta\left(\mathbf{U}\right)$, $\mathbf{H}_{nc}$ and $\mathbf{H}_{relax}$, with $\beta = \{x, y, z\}$, contain respectively the hydrodynamic fluxes, the capillary fluxes, the non-conservative terms and the relaxation terms:

$$\mathbf{F}_h^x\left(\mathbf{U}\right) = \begin{bmatrix} \alpha_1 u \\ \alpha_1\rho_1 u \\ \alpha_2\rho_2 u \\ \rho u^2 + P \\ \rho uv \\ \rho uw \\ \alpha_1\rho_1 e_1 u \\ \alpha_2\rho_2 e_2 u \\ cu \\ \left(\rho E + P\right) u \end{bmatrix} \quad \mathbf{F}_h^y\left(\mathbf{U}\right) = \begin{bmatrix} \alpha_1 v \\ \alpha_1\rho_1 v \\ \alpha_2\rho_2 v \\ \rho uv \\ \rho v^2 + P \\ \rho vw \\ \alpha_1\rho_1 e_1 v \\ \alpha_2\rho_2 e_2 v \\ cv \\ \left(\rho E + P\right) v \end{bmatrix} \quad \mathbf{F}_h^z\left(\mathbf{U}\right) = \begin{bmatrix} \alpha_1 w \\ \alpha_1\rho_1 w \\ \alpha_2\rho_2 w \\ \rho uw \\ \rho vw \\ \rho w^2 + P \\ \alpha_1\rho_1 e_1 w \\ \alpha_2\rho_2 e_2 w \\ cw \\ \left(\rho E + P\right) w \end{bmatrix}$$

$$\mathbf{F}_c^x\left(\mathbf{U}\right) = \begin{bmatrix} 0 \\ 0 \\ 0 \\ \Omega_{11} \\ \Omega_{12} \\ \Omega_{13} \\ 0 \\ 0 \\ 0 \\ \varepsilon_\sigma u + \Omega_{11} u + \Omega_{12} v + \Omega_{13} w \end{bmatrix} \quad \mathbf{F}_c^y\left(\mathbf{U}\right) = \begin{bmatrix} 0 \\ 0 \\ 0 \\ \Omega_{21} \\ \Omega_{22} \\ \Omega_{23} \\ 0 \\ 0 \\ 0 \\ \varepsilon_\sigma u + \Omega_{21} u + \Omega_{22} v + \Omega_{23} w \end{bmatrix}$$

$$\mathbf{F}_c^z(\mathbf{U}) = \begin{bmatrix} 0 \\ 0 \\ 0 \\ \Omega_{31} \\ \Omega_{32} \\ \Omega_{33} \\ 0 \\ 0 \\ 0 \\ \varepsilon_\sigma u + \Omega_{31} u + \Omega_{32} v + \Omega_{33} w \end{bmatrix}$$

$$\mathbf{H}_{nc} = \begin{bmatrix} -\alpha_1 \\ 0 \\ 0 \\ 0 \\ 0 \\ \alpha_1 P_1 \\ \alpha_2 P_2 \\ -c \\ 0 \end{bmatrix} \qquad \mathbf{H}_{relax} = \begin{bmatrix} \mu(P_1 - P_2) \\ 0 \\ 0 \\ 0 \\ 0 \\ 0 \\ -\mu P_I(P_1 - P_2) \\ \mu P_I(P_1 - P_2) \\ 0 \\ 0 \end{bmatrix}$$

It is important to note that the additional equation for the mixture total energy has been added to the system for numerical solution purposes. This equation is obviously in agreement with the complete system (2.14) and will be necessary to correct the energy conservation equation during the final relaxation step.

The unknown vector $\mathbf{U}^{n+1}$ is obtained from the initial condition $\mathbf{U}^n$ by application of the three successive operators according to the sequence:

$$\mathbf{U}^{n+1} = L_{relax} L_{cap} L_{hyper}(\mathbf{U}^n).$$

Each step of the numerical method corresponds to the application of one of the three operators detailed below in a cartesian 2D framework.

2.4.2.1 Hyperbolic operator

The application of the first operator L_{hyper} corresponds to the resolution of the hyperbolic submodel (2.16) using a Godunov-type method [24] extended to an high-order scheme with a MUSCL-Hancock procedure. The solution for this step is given for the cell (i, j) by:

$$\mathbf{U}_{i,j}^{hyper} = \mathbf{U}_{i,j}^n - \mathbf{G}\Delta t,$$

$$\mathbf{G} = \left\{ \begin{array}{l} \frac{1}{\Delta x}\left(\mathbf{F}^{*}_{h;i+\frac{1}{2},j}\left(\mathbf{U}^{n+\frac{1}{2}}_{i,j,R},\mathbf{U}^{n+\frac{1}{2}}_{i+1,j,L}\right)-\mathbf{F}^{*}_{h;i-\frac{1}{2},j}\left(\mathbf{U}^{n+\frac{1}{2}}_{i-1,j,R},\mathbf{U}^{n+\frac{1}{2}}_{i,j,L}\right)\right) \\ +\frac{1}{\Delta y}\left(\mathbf{F}^{*}_{h;i,j+\frac{1}{2}}\left(\mathbf{U}^{n+\frac{1}{2}}_{i,j,T},\mathbf{U}^{n+\frac{1}{2}}_{i,j+1,B}\right)-\mathbf{F}^{*}_{h;i,j-\frac{1}{2}}\left(\mathbf{U}^{n+\frac{1}{2}}_{i,j-1,T},\mathbf{U}^{n+\frac{1}{2}}_{i,j,B}\right)\right) \\ +\frac{\mathbf{H}^{n}_{nc;i,j}}{\Delta x}\left(u^{*}_{i+\frac{1}{2},j}\left(\mathbf{U}^{n+\frac{1}{2}}_{i,j,R},\mathbf{U}^{n+\frac{1}{2}}_{i+1,j,L}\right)-u^{*}_{i-\frac{1}{2},j}\left(\mathbf{U}^{n+\frac{1}{2}}_{i-1,j,R},\mathbf{U}^{n+\frac{1}{2}}_{i,j,L}\right)\right) \\ +\frac{\mathbf{H}^{n}_{nc;i,j}}{\Delta y}\left(v^{*}_{i,j+\frac{1}{2}}\left(\mathbf{U}^{n+\frac{1}{2}}_{i,j,T},\mathbf{U}^{n+\frac{1}{2}}_{i,j+1,B}\right)-v^{*}_{i,j-\frac{1}{2}}\left(\mathbf{U}^{n+\frac{1}{2}}_{i,j-1,T},\mathbf{U}^{n+\frac{1}{2}}_{i,j,B}\right)\right) \end{array} \right\}.$$

The superscript * represents the solution of the Riemann problem on the corresponding cell boundary using the extrapolated values to the cell boundary $\mathbf{U}^{n+\frac{1}{2}}$ in the case of high order method (the subscripts R, L, T, B represent respectively the right, left, top and bottom neighbouring cells). These fluxes can be computed by any Riemann solver. Here a Harten-Lax-van Leer Contact (HLLC) approximate Riemann solver is used. Details of this method can be found in Saurel et al. [80]. Since the time marching scheme is explicit, the time step obeys a classical Courant-Friedrichs-Lewy (CFL) criterion.

2.4.2.2 Capillary operator

The second operator L_{cap} introduces capillary terms and corresponds to the resolution of submodel (2.17):

$$\mathbf{U}^{cap} = L_{cap}\left(\mathbf{U}^{hyper}\right).$$

Application of the operator L_{cap} to vector $\mathbf{U}^{hyper}$ is done in the finite volume framework using a first order scheme:

$$\mathbf{U}^{cap}_{i,j} = \mathbf{U}^{hyper}_{i,j} - \Delta t \left\{ \begin{array}{l} \frac{1}{\Delta x}\left(\mathbf{F}^{x}_{c;i+\frac{1}{2},j}\left(\mathbf{U}^{hyper}_{i+\frac{1}{2},j}\right)-\mathbf{F}^{x}_{c;i-\frac{1}{2},j}\left(\mathbf{U}^{hyper}_{i-\frac{1}{2},j}\right)\right) \\ +\frac{1}{\Delta y}\left(\mathbf{F}^{y}_{c;i,j+\frac{1}{2}}\left(\mathbf{U}^{hyper}_{i,j+\frac{1}{2}}\right)-\mathbf{F}^{y}_{c;i,j-\frac{1}{2}}\left(\mathbf{U}^{hyper}_{i,j-\frac{1}{2}}\right)\right) \end{array} \right\}.$$

The only equations affected by the capillary effects are the momentum and the total energy equations. These equations are developed in two dimensions:

$$(\rho u)^{cap}_{i,j} = (\rho u)^{hyper}_{i,j} - \sigma\Delta t \left\{ \begin{array}{c} -\frac{\|\mathbf{w}\|^{hyper}_{i+\frac{1}{2},j}-\|\mathbf{w}\|^{hyper}_{i-\frac{1}{2},j}}{\Delta x}+\frac{\left(\frac{w_1^2}{\|\mathbf{w}\|}\right)^{hyper}_{i+\frac{1}{2},j}-\left(\frac{w_1^2}{\|\mathbf{w}\|}\right)^{hyper}_{i-\frac{1}{2},j}}{\Delta x} \\ +\frac{\left(\frac{w_1 w_2}{\|\mathbf{w}\|}\right)^{hyper}_{i,j+\frac{1}{2}}-\left(\frac{w_1 w_2}{\|\mathbf{w}\|}\right)^{hyper}_{i,j-\frac{1}{2}}}{\Delta y} \end{array} \right\},$$

$$(\rho v)^{cap}_{i,j} = (\rho v)^{hyper}_{i,j} - \sigma\Delta t \left\{ \begin{array}{c} -\frac{\|\mathbf{w}\|^{hyper}_{i,j+\frac{1}{2}}-\|\mathbf{w}\|^{hyper}_{i,j-\frac{1}{2}}}{\Delta y}+\frac{\left(\frac{w_1 w_2}{\|\mathbf{w}\|}\right)^{hyper}_{i+\frac{1}{2},j}-\left(\frac{w_1 w_2}{\|\mathbf{w}\|}\right)^{hyper}_{i-\frac{1}{2},j}}{\Delta x} \\ +\frac{\left(\frac{w_2^2}{\|\mathbf{w}\|}\right)^{hyper}_{i,j+\frac{1}{2}}-\left(\frac{w_2^2}{\|\mathbf{w}\|}\right)^{hyper}_{i,j-\frac{1}{2}}}{\Delta y} \end{array} \right\},$$

$$(\rho E+\varepsilon_\sigma)^{cap}_{i,j} = (\rho E+\varepsilon_\sigma)^{hyper}_{i,j}$$
$$-\sigma\Delta t \left\{ \begin{array}{c} \frac{\left(\frac{w_1^2 u}{\|\mathbf{w}\|}\right)^{hyper}_{i+\frac{1}{2},j}-\left(\frac{w_1^2 u}{\|\mathbf{w}\|}\right)^{hyper}_{i-\frac{1}{2},j}}{\Delta x}+\frac{\left(\frac{w_1 w_2 v}{\|\mathbf{w}\|}\right)^{hyper}_{i+\frac{1}{2},j}-\left(\frac{w_1 w_2 v}{\|\mathbf{w}\|}\right)^{hyper}_{i-\frac{1}{2},j}}{\Delta x} \\ +\frac{\left(\frac{w_1 w_2 u}{\|\mathbf{w}\|}\right)^{hyper}_{i,j+\frac{1}{2}}-\left(\frac{w_1 w_2 u}{\|\mathbf{w}\|}\right)^{hyper}_{i,j-\frac{1}{2}}}{\Delta y}+\frac{\left(\frac{w_2^2 v}{\|\mathbf{w}\|}\right)^{hyper}_{i,j+\frac{1}{2}}-\left(\frac{w_2^2 v}{\|\mathbf{w}\|}\right)^{hyper}_{i,j-\frac{1}{2}}}{\Delta y} \end{array} \right\}.$$

The different capillary terms at the cell boundary are obtained by the means of an arithmetic average of quantities of neighbouring cells. The vector $\mathbf{w}$ requires derivatives of the color function which are computed by using second-order finite difference approximations.

2.4.2.3 Pressure relaxation operator

To go through the operators chain, the solution at time $n+1$ is obtained by a pressure relaxation algorithm and corrects the components of $\mathbf{U}^{cap}$:

$$\mathbf{U}^{n+1} = L_{relax}\left(\mathbf{U}^{cap}\right).$$

The details about the pressure relaxation algorithm as well as the correction procedure used to guarantee total energy conservation can be found in Saurel et al. [80].

2.5 Numerical results and validations

In this section, 2D test cases are proposed to prove that the model and the numerical method are able to treat accurately both capillary effects and shock wave propagation.

In each presented cases, the equation of state (EOS) for the air obeys to the ideal gas law:

$$P_{air} = \left(\gamma_{air} - 1\right)\rho_{air} e_{air},$$

with $\gamma_{air} = 1.4$.

The liquid obeys the stiffened gas EOS:

$$P_{liquid} = \left(\gamma_{liquid} - 1\right)\rho_{liquid} e_{liquid} - \gamma_{liquid} P_{\infty,liquid},$$

where the stiffened gas EOS parameters are :

- $\gamma_{liquid} = 2.1$ and $P_{\infty,liquid} = 1.10^6 Pa$ for the capillary verification test cases of Section 2.5.1 and 2.5.2.
- $\gamma_{liquid} = 4.4$ and $P_{\infty,liquid} = 6.10^8 Pa$ for water in the compressible validation test case of Section 2.5.3.

2.5.1 Static capillary effects validation

2D tests are proposed to study the ability of the method to treat accurately capillary effects. The proposed method described in the present paper is compared with previous existing methods that use source terms integration. A particular attention is paid to the convergence, the numerical reliability, the conservative property, the accuracy with respect to the Laplace pressure law and the dynamics of capillary flows. It is shown that the present method is able to simulate capillary effects in presence of pressure waves. In the following, "conservative method" will always mean the numerical method of Section 2.4 to distinguish it from the source terms integration method that do not conserve neither the momentum nor the energy.

The first test cases are static tests and they consist in finding the equilibrium state of a cylindrical column of liquid (2D liquid droplet) placed in air. The initial density in air is equal to 1 $kg.m^{-3}$ and $1,000$ $kg.m^{-3}$ in the liquid. The radius of the liquid column R is set to $0.15m$ and the surface tension coefficient is equal to $800N.m^{-1}$. These unrealistic values are chosen to magnify the model properties. The pressure is initially uniform in the whole domain ($75cm$ x $75cm$) and is set to 1 bar (the initial conditions are presented in Figure 2.2).

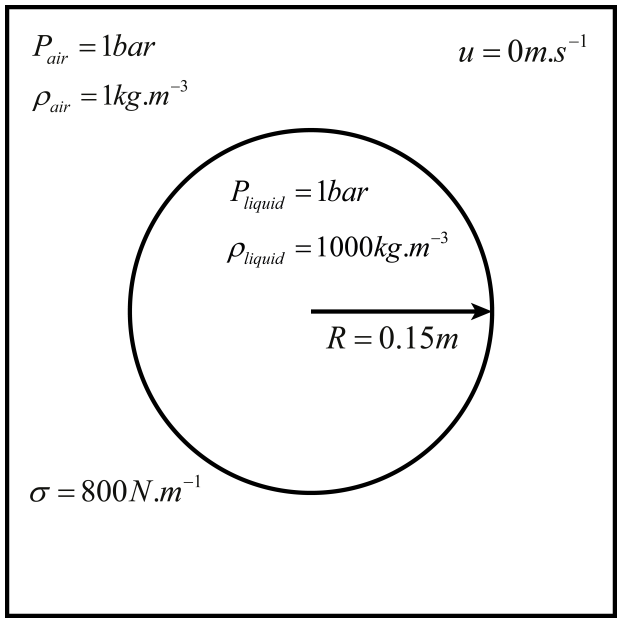

Figure 2.2: Sketch of the initial conditions for the simulations of a cylindrical liquid column (2D liquid droplet) placed in air.

2.5.1.1 Accuracy regarding Laplace law and mesh convergence

The following test cases treating mesh convergence and accuracy regarding the Laplace law are performed using outgoing pressure wave boundary conditions. It consists in imposing the Neumann boundary conditions for the pressure and imposing in-outgoing conditions expressed in terms of the Riemann invariants.

Because of the capillary effects, the pressure of the liquid column converges to satisfy the Laplace law. The expression of the theoretical pressure jump of Laplace in 2 dimensions is:

$$[P] = \frac{\sigma}{R},$$

where $[P]$ expresses the pressure jump between inside and outside the droplet, here $P_{liquid} - P_{air}$.

The pressure convergence is analyzed using the relative residual:

$$\epsilon = Max\left(\frac{|P^n_{i,j} - P^{n-1}_{i,j}|}{P^n_{i,j}}\right).$$

The convergence is considered to be reached when the criterion $\epsilon \leqslant 1.10^{-4}$ is verified. An example of evolution of this relative residual with a mesh of 120x120 cells is presented in Figure 2.3 for both conservative method and source terms integration method. It is clear that the pressure convergence is obtained faster using the conservative method than using the source terms integration one.

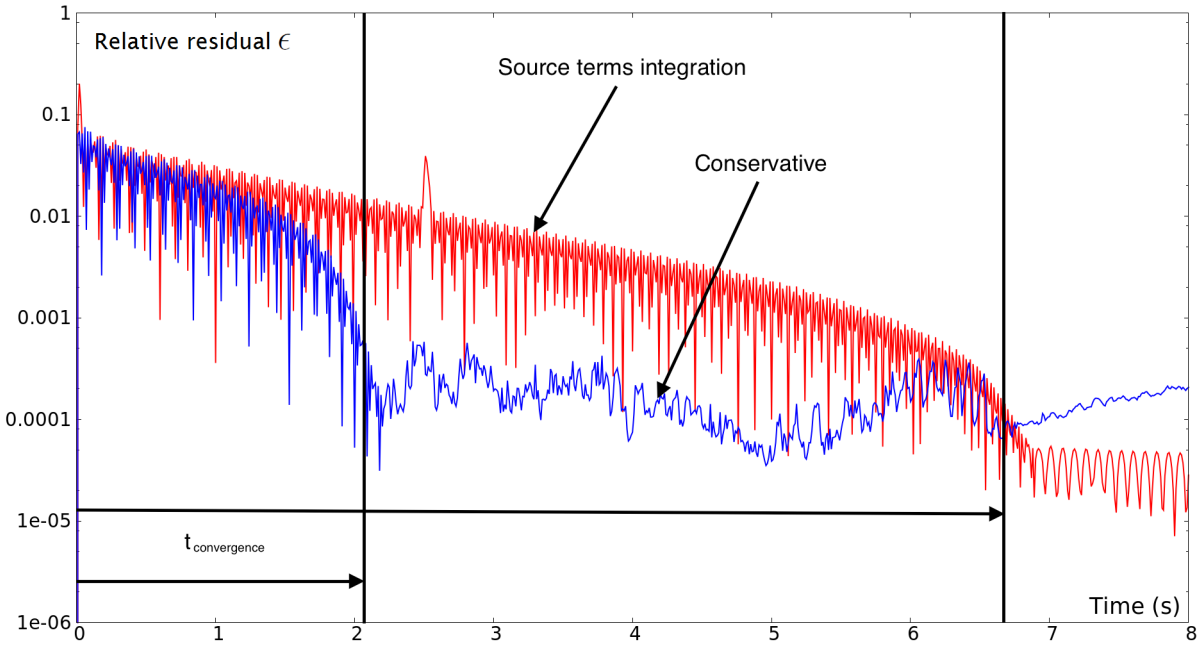

Figure 2.3: Relative residual ϵ function of the physical time for the 2D liquid column test case with a mesh of 120x120 cells. Source terms integration (red) and conservative (blue) methods. Convergence is reached after 2 seconds with the conservative method compared to more than 6 seconds with the source terms integration method.

The pressure profiles through the liquid column is presented in Figure 2.4 for the mesh with 120x120 computational cells. Pressure profiles are presented for both methods after the pressure convergence time mentioned previously. The new conservative method has a better accuracy than the source terms integration one.

The mesh convergence study is performed on 4 different meshes containing 60x60 up to 120x120 computational cells. For each chosen mesh, the relative residual ϵ is used to match pressure convergence. Then the relative pressure error ξ is computed by:

$$\xi = \frac{|[P_{num}] - [P_{th}]|}{[P_{th}]},$$

where $[P_{num}]$ is the pressure jump between the averaged pressure inside the column ($P_{num} = \sum \alpha_{liquid} P_{liquid} / \sum \alpha_{liquid}$ when $\alpha_{liquid} \geqslant 0.99$) and the pressure of the air P_{air}. The theoretical pressure jump $[P_{th}]$ is calculated using the following relation:

$$[P_{th}] = \sigma \sqrt{\frac{\pi}{S}},$$

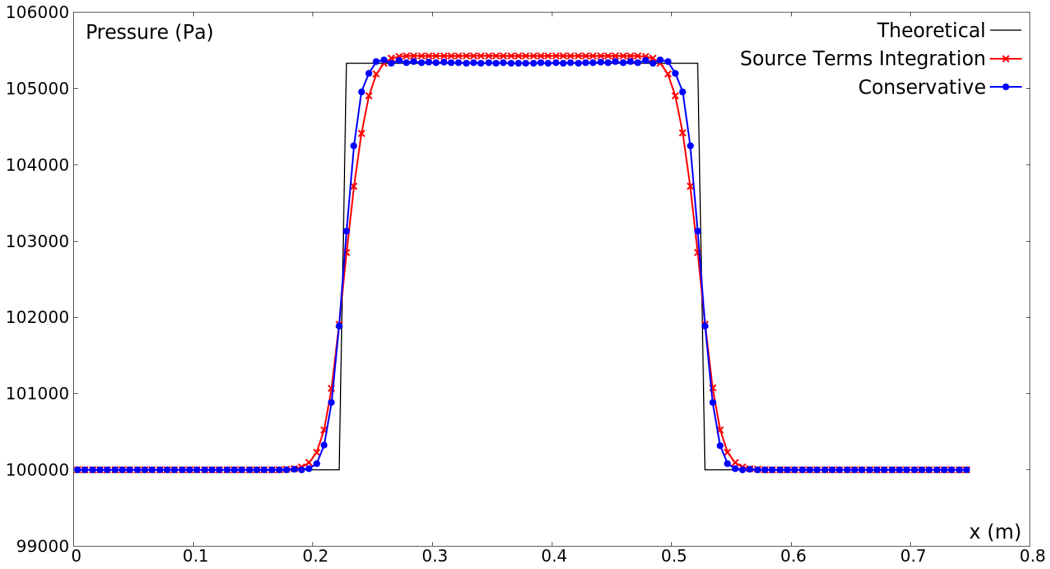

Figure 2.4: Pressure jump in a centered section of a steady 2D liquid column in air. $\sigma = 800N.m^{-1}$, $R = 0.1496m$ and so $[P] = 5,347Pa$. Theoretical (black line) and converged simulations results with source terms integration (red crosses) and conservative (blue dots) methods are shown at times $6.68s$ and $2.07s$, respectively.

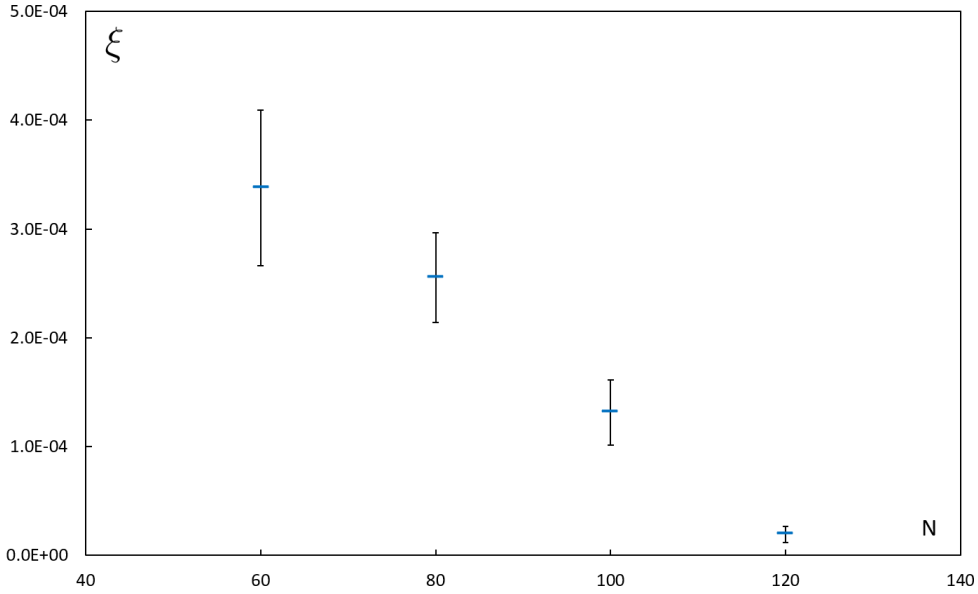

Figure 2.5: Relative pressure error ξ averaged in time when the convergence is reached versus the number of cells in one direction N for the 2D liquid column test case. Grid convergence toward the theoretical pressure jump of Laplace is shown for the conservative method proposed in the paper. The error bars show the domain of variation of ξ over time after the convergence criteria is reached, associated to each mesh. The interval of variation always decreases with the cells refinement.

where S represents the 2D volume of the droplet. It is determined doing the sum of the volume fraction of liquid over the whole domain multiplied by the cell volume: $S = \sum \alpha_{liquid} S_{cell}$. The relative pressure error ξ is averaged in time and plotted versus grid resolution in Figure 2.5 for the conservative method proposed in the paper. Grid convergence is validated and the variation of ξ over time, when convergence is reached, decreases with the cells refinement.

2.5.1.2 Reliability

Regarding the reliability of the method, contours of the liquid column are presented in Figure 2.6. Wall boundary conditions are used in this example on a mesh containing 120x120 cells. The left hand side of the figure shows the initial contour together with the mesh. Effect of the mesh on the initial circle is noticeable. The two other pictures show contour positions immediately after the convergence is reached, corresponding to a physical time of about $3.68s$ for the source term integration method and $2.32s$ for the conservative method. In this test case, if the source term integration method is used, one can observe a slight move of the gravity center of the column before a converged solution is reached. In fact the gravity center starts to move at a physical time about $2.57s$. At the converged time ($3.68s$), the position of the gravity center is still incorrect (picture in the middle of Figure 2.6). This drift may be considered as a visible result of the non-conservation of the momentum. This is crippling, for example, when studying interaction between a droplet and a shock wave (see the last subsection): the droplet must be at rest before the interaction with the shock wave. With the conservative method of the present paper, it becomes possible to consider the treatment of this kind of problem.

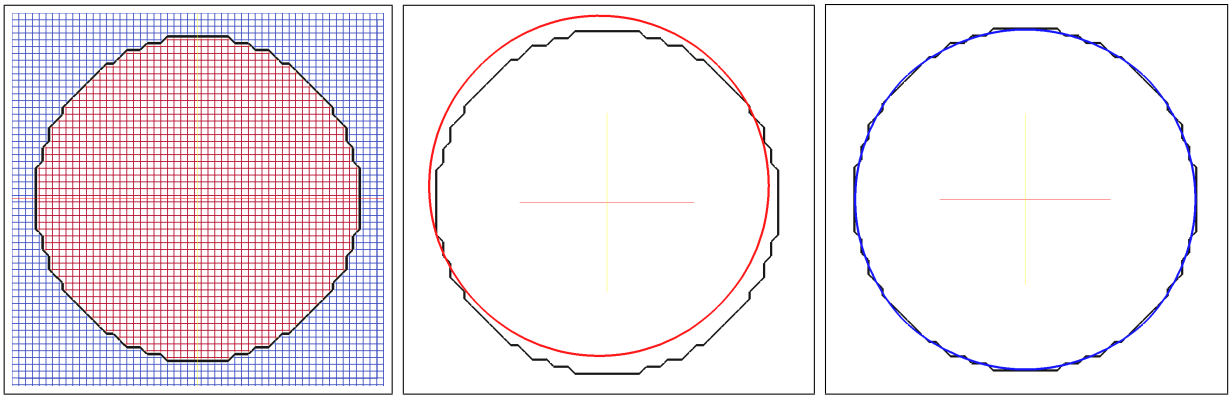

Figure 2.6: Magnified view of column contours through color function ($c = 0.5$). Initial contour (black contour) together with cartesian mesh is on the left hand side; Contours after convergence is reached: source terms integration method is in the middle (red contour) and conservative method is on the right hand side (blue contour) for physical times about $3.68s$ and $2.32s$, respectively. With source terms integration method, the position of the column as already changed when convergence is reached.

Nevertheless, the gravity center starts to move after a long time in the two methods. In this example, with the conservative method, it is about $4.52s$ so well after the convergence

is reached ($2.32s$). But these displacements cannot be compared with the drift observed for the source terms integration method. In other words, one can consider that the new method maintains the position of the gravity center at the converged solution. For longer time, with the accumulation of rounding errors, some spurious motions can be seen as traces of numerical instabilities. They do not have the same origin as the drift observed with the source terms integration method as soon as the calculation begins.

2.5.1.3 Energy conservation

The conservative property of the new model is verified by plotting the evolution of the relative error for the total mixture energy over the whole domain for the liquid column using wall boundary conditions with a mesh containing 120x120 cells (Figure 2.7). The energy is obviously conserved with the conservative method but not with the source terms integration one. Moreover, for the source terms integration method, the error does not saturate and then still increases when the convergence is reached. It is also noticeable that the difference in energies appears even initially and comes from the capillary energy ε_σ which does not appear in the source term form expression of the total mixture energy equation. Note that its value is here: $\varepsilon_\sigma = 2.10^7 J.m^{-3}$.

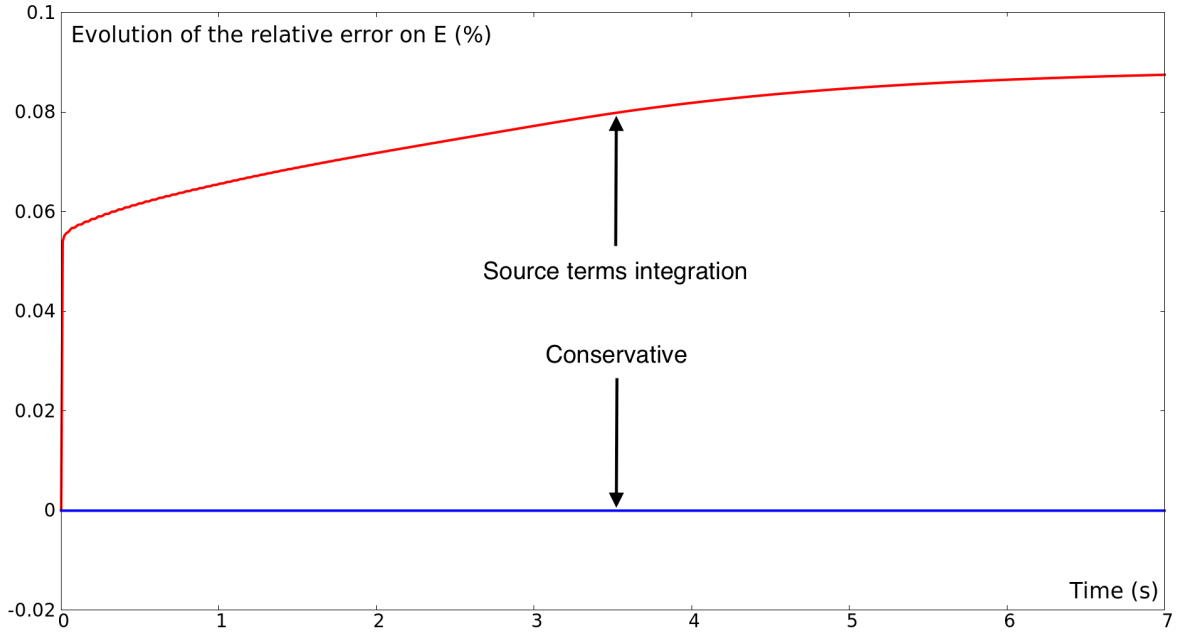

Figure 2.7: Evolution of the relative error for the total mixture energy over the whole domain for the liquid column with wall boundary conditions. Expression for the evolution of the relative error is: $100\left(E\left(t\right)-E\left(t_0\right)\right)/E\left(t_0\right)$. Source terms integration (red) and conservative (blue) methods.

2.5.2 Dynamic capillary effects validation

The next two test cases for the dynamic verification of surface tension are slightly different from the previous ones.

2.5.2.1 Recovering a circle shape

In this test case we are looking for the shape recovering and the volume evolution of an initially square liquid column, with $L_{square} = 0.2m$, placed in an atmospheric air with the same pressure P_{air}. Because of the capillary terms the solution should evolve to a circle shape of the liquid interface and the pressure should verify the Laplace jump: $P_{final} = P_{air} + \sigma/R$. The successive dynamic stages leading to the converged circle shape are presented in Figure 2.8.

Moreover, the mass conservation implies a variation of the liquid column volume. This variation is following an isentropic transformation leading to the final volume:

$$V_{final} = V_{initial} \left(\frac{P_{initial} + P_\infty}{P_{final} + P_\infty} \right)^{\frac{1}{\gamma}}.$$

In the simulation, the volume of the liquid column is measured by the sum of the volume fraction of water for each cell on the whole domain, multiplied by the cell volume. Initially the area of the square column is $V_{initial} = 0.04m^2$ and it converges to the theoretical value of $V_{final} = 0.039878m^2$ with a precision equal to 0.011% at time $t = 3s$ with a mesh made of 200x200 cells. In Figure 2.9, the relative variation of the liquid 2D volume $\left((V - V_{final})/V_{final}\right)$ is plotted versus time for 3 different meshes. Grid convergence toward the theoretical value is observed.

2.5.2.2 Uniform velocity flow

In this section, we focus on the ability of the method to maintain a cylindrical column with a correct pressure jump in a uniform velocity flow. A sketch of the initial condition is presented in Figure 2.10. It consists in a liquid column with an initial radius of $R = 0.15m$ moving in a uniform velocity field ($u = 50m.s^{-1}$). At the initialization, the liquid column is in equilibrium with the ambient air. Simulations are performed on 4 different meshes containing 180x60 up to 360x120 computational cells for a physical domain of $2.25m$ x $0.75m$.

In Figure 2.11, the relative pressure error ξ defined previously is averaged in time and plotted versus grid resolution. Mesh convergence is observed and results show that the Laplace pressure jump is well verified.

During the simulations, the position of the liquid column is in perfect agreement with the theoretical one (Figure 2.12). It is then important to note that surface tension effects have influence only on the shape of the column, since initially there is a grid impact (see Figure 2.6 for an example), but not on the position. This validates the method for this simple advection test case.

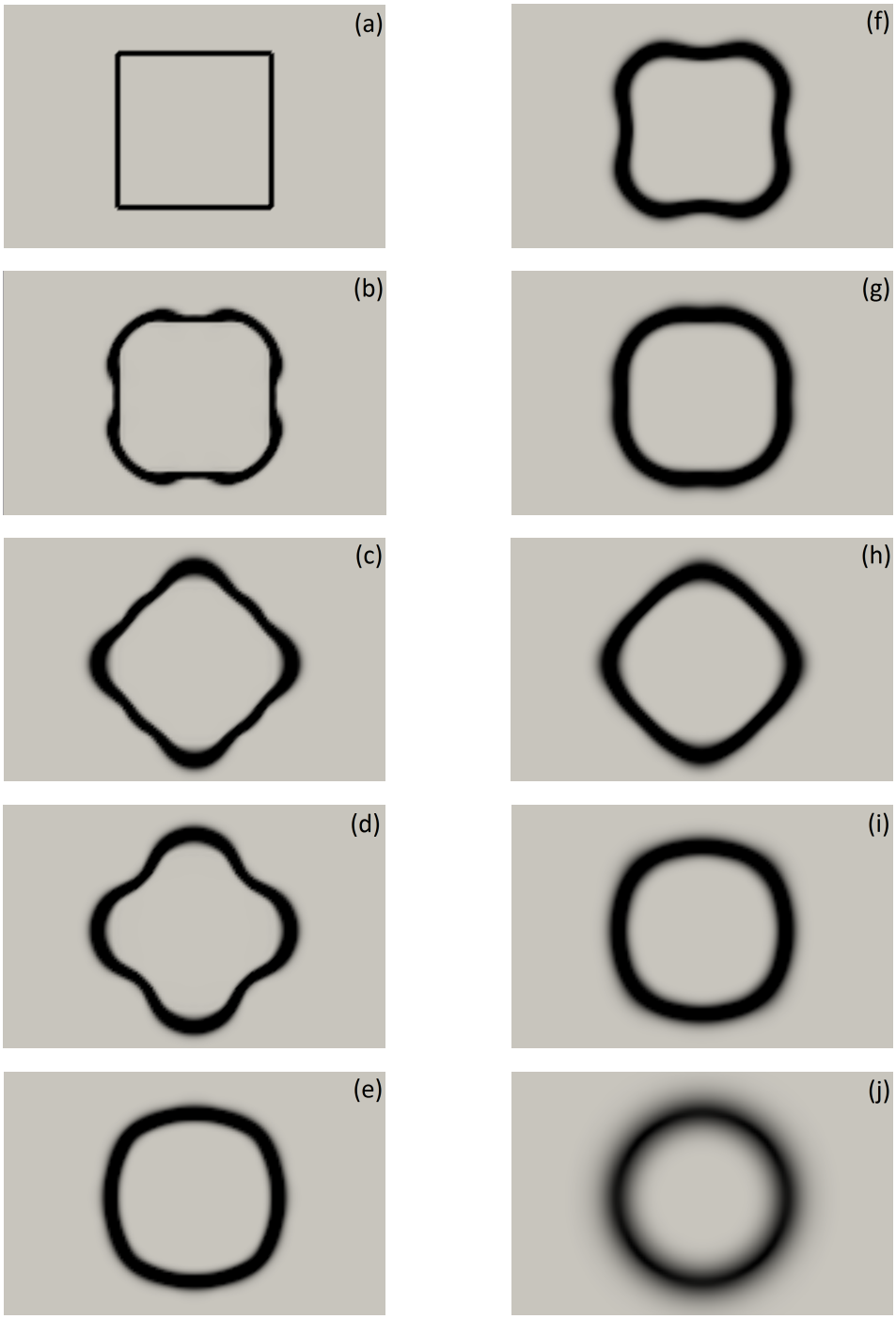

Figure 2.8: Magnified schlieren images of the mixture density of the 2D liquid column under a square shape in an air environment converging to a circle shape. Initially $\sigma = 800N.m^{-1}$ and $L_{square} = 0.2m$. Simulation at different times with a mesh of 150x150 cells: (a) initialization, (b) 5ms, (c) 15ms, (d) 20ms, (e) 30ms, (f) 35ms, (g) 45ms, (h) 50ms, (i) 105ms and (j) 3,000ms.

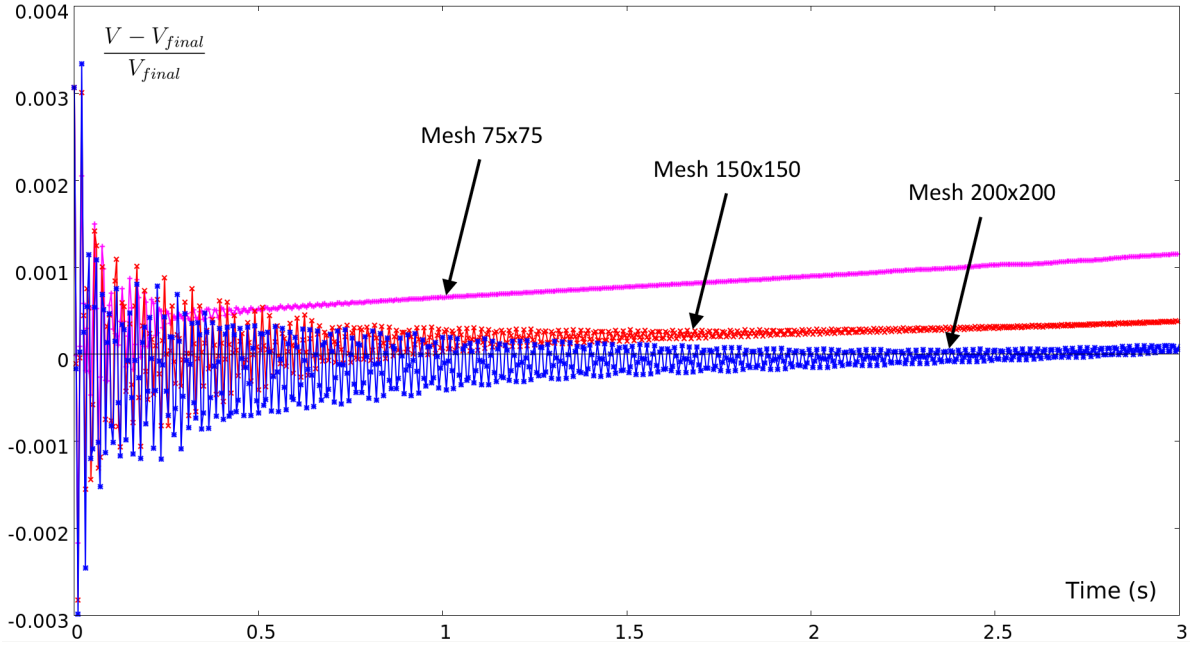

Figure 2.9: Evolution of the relative variation of the 2D volume of the liquid column $((V - V_{final})/V_{final})$ for 3 different meshes. The final isentropic 2D volume ($S = 0.039878m^2$) is numerically recovered with an error of 0.011% for the mesh with 200x200 cells.

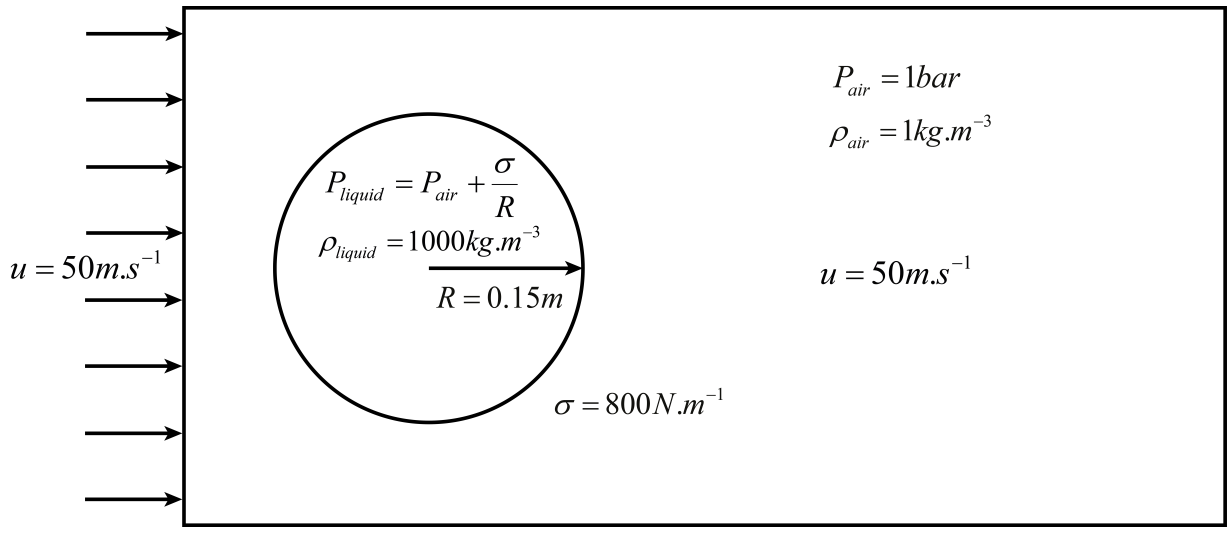

Figure 2.10: Sketch of the initial conditions for the simulation of a cylindrical liquid column (2D liquid droplet) in air, coupled with advection of the whole domain.

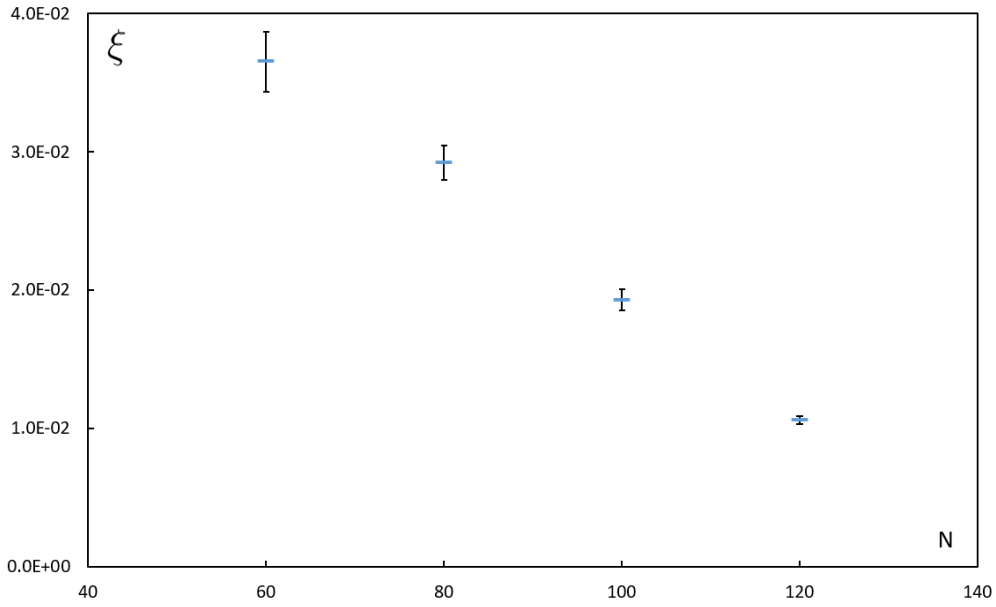

Figure 2.11: Relative pressure error ξ averaged in time versus the number of cells in the y-direction N_y for the 2D liquid column test case with surface tension and advection of the whole domain. The error bars show the domain of variation of ξ over time. Mesh convergence is observed. The results show that the Laplace pressure jump is well verified using the new method.

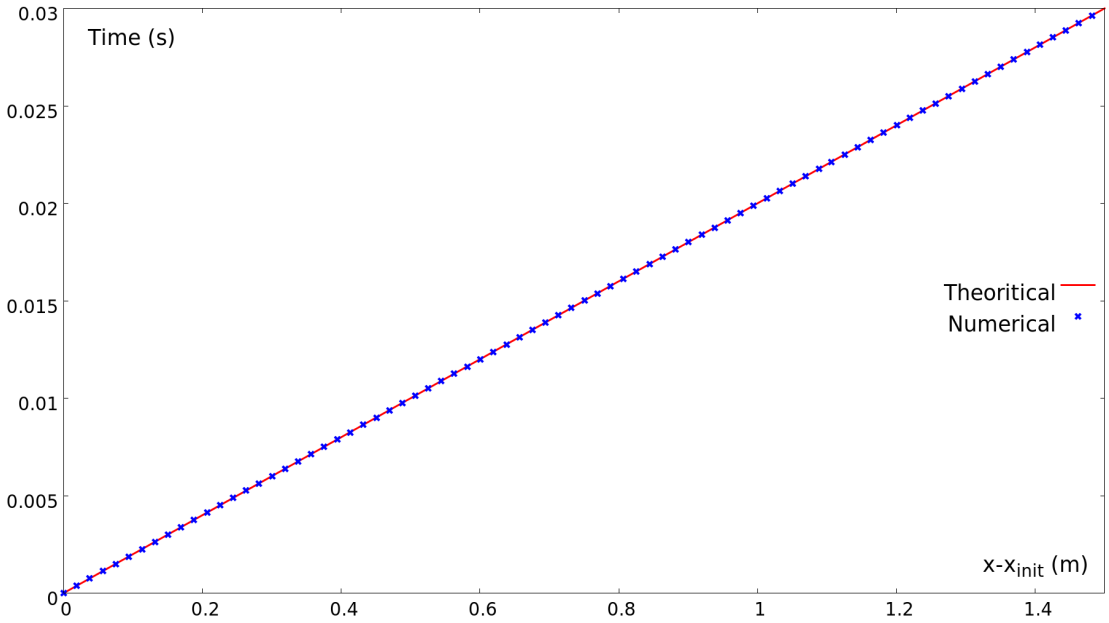

Figure 2.12: Evolution of the position of the liquid column along the x axis minus its initial position for the 2D liquid column test case with surface tension and advection of the whole domain. Numerical results using the new method are in perfect agreements with the theoretical one.

2.5.3 Shock wave interaction with a water column

We focus here on the early stages of droplet breakup in the high speed flow behind a shock wave.

The numerical simulations are performed in two dimensions to simulate the interaction of an air flow and a water column. Comparisons with Igra and Takayma experiments [38, 39] are carried out.

A cylindrical water column with initial diameter of $D = 6.4mm$ is exposed to a shock wave at Mach number 1.3 in atmospheric air (see Figure 2.13 for initialization sketch). The initial densities are $\rho_{air} = 1.2kgm^{-3}$ and $\rho_{water} = 1,000kg.m^{-3}$. The corresponding initial Weber number ($We = \rho_{air}u^2D/\sigma$) in these conditions is 3,690. 2D computations are performed on a cartesian mesh containing 3,200x1,200 cells representing a physical domain of 220mm x 82.5mm. Shocked air is entering at the left. Outgoing pressure wave boundary condition is used at the right and the Newmann boundary conditions is used at the top and the bottom.

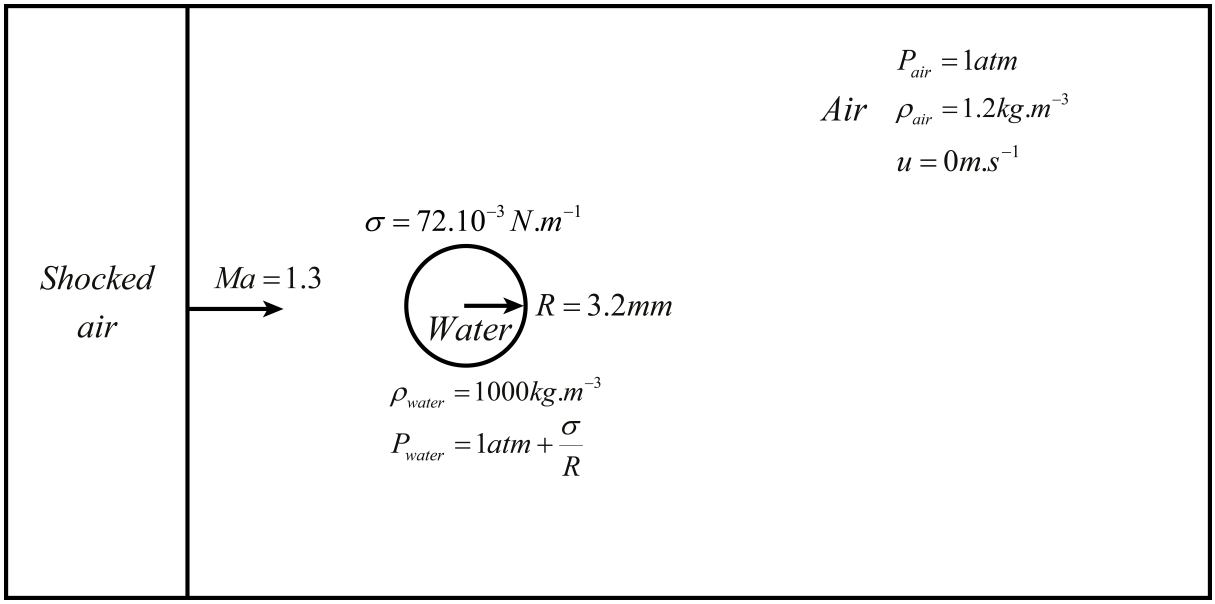

Figure 2.13: Sketch of the initialization for interaction of a shock wave with a water column.

The results are presented at three different stages. Each stage is representative of a typical physical effect:

- The first stage is presented in Figure 2.14 where the flow dynamics is governed by the wave pattern. This is a totally compressible stage corresponding to the shock-column interaction for a large Weber number. Comparisons with experiments are presented in Figure 2.15.

- After the shock wave propagation, the column shape is changing due to inertial effects. Liquid-gas interface is stretched and the first liquid filaments are appearing. The interface location is compared with experiments in Figure 2.16.

- At the third stage, the breakup begins because of high inertia of the water column. This effect has already been observed in bubble breakup (Yang et al. [99], Quirk and Karni [74], Layes and Le Metayer [51]). The Weber number is lower (due to diameter change and also because the velocity gap is reducing) and the capillary effects tend to tear the filaments out the main column (last pictures of Figure 2.17).

In Figure 2.18, results obtained for a flow without capillary effects (left picture) and a flow with capillary effects (right picture) are compared at time $t = 1.2ms$. One can see that the capillary effects begin to have influence on the flow topology, particularly on the filaments shape where the surface tension effects tend to break the filaments to form little droplets.

2.6 Summary

A new multiphase model treating interface problems and capillary effects has been derived. Hyperbolicity study has been completely done and a splitting numerical method that guarantees conservation of the mass, the momemtum and the energy has been built. Comparison with "source terms integration method" and with experiments have shown the advantages of the new model and numerical method. The simulation of an aerodynamic breakup of a water column induced by a shock wave showed that the method is able to treat accurately both pressure waves interaction and capillary effects in the same formulation.

In the goal to simulate the atomization of an isolated droplet by a high speed flow, e.i., obtain little droplets, some work has to be done to perform it in computationally reasonnable time. For that an adaptive mesh refinement (AMR) method is undertaken and presented in the following chapter.

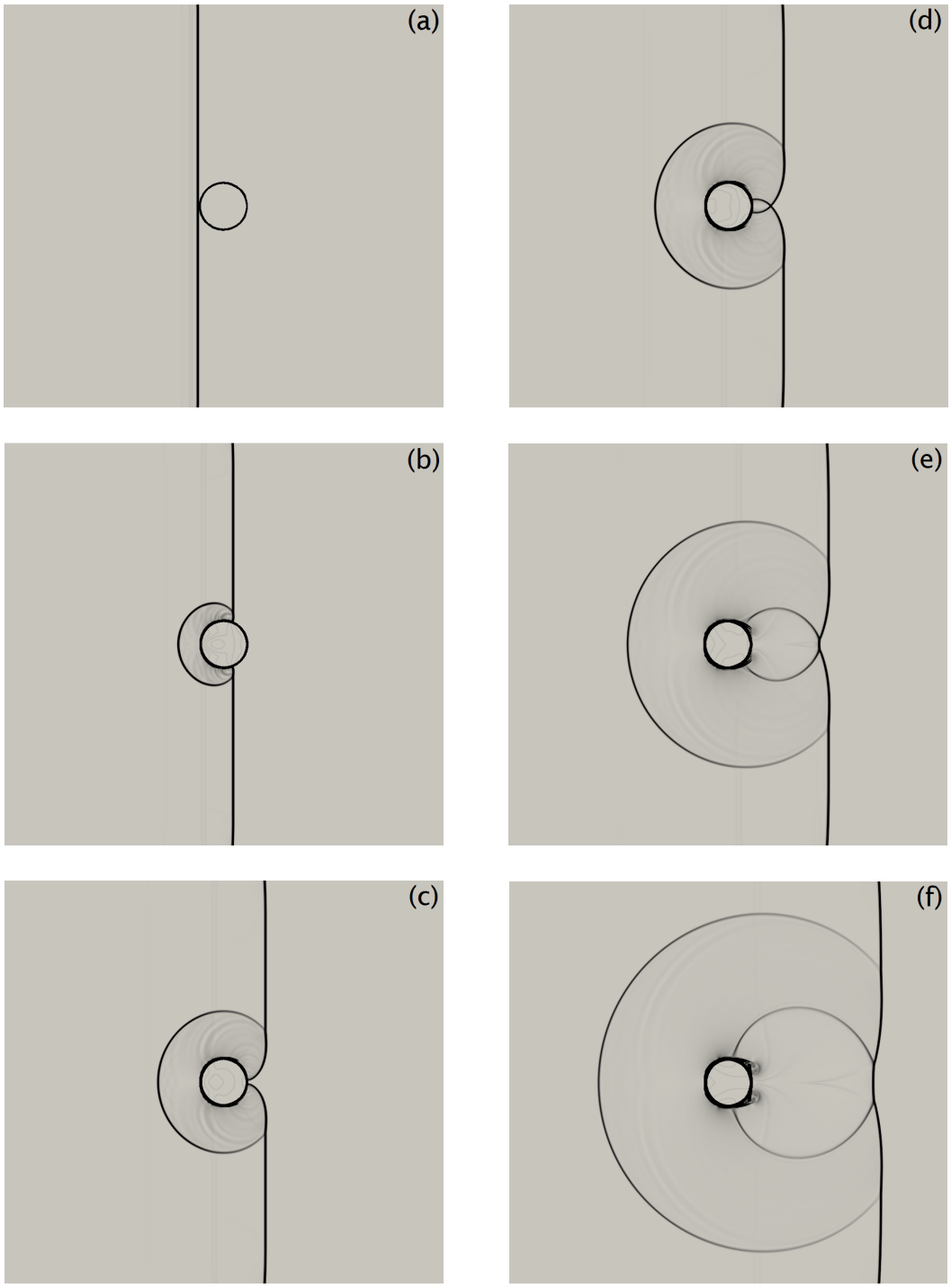

Figure 2.14: Magnified view of the early stages of the aerodynamic breakup of the water column in the high-speed airstream behind the shock wave of Mach number 1.3 in atmospheric air propagating from the left to the right. 2D simulation with a mesh of 3,200x1,200 cells and schlieren images of the mixture density are given at the following times: (a) $0\mu s$, (b) $10\mu s$, (c) $20\mu s$, (d) $24\mu s$, (e) $37\mu s$ and (f) $55\mu s$.

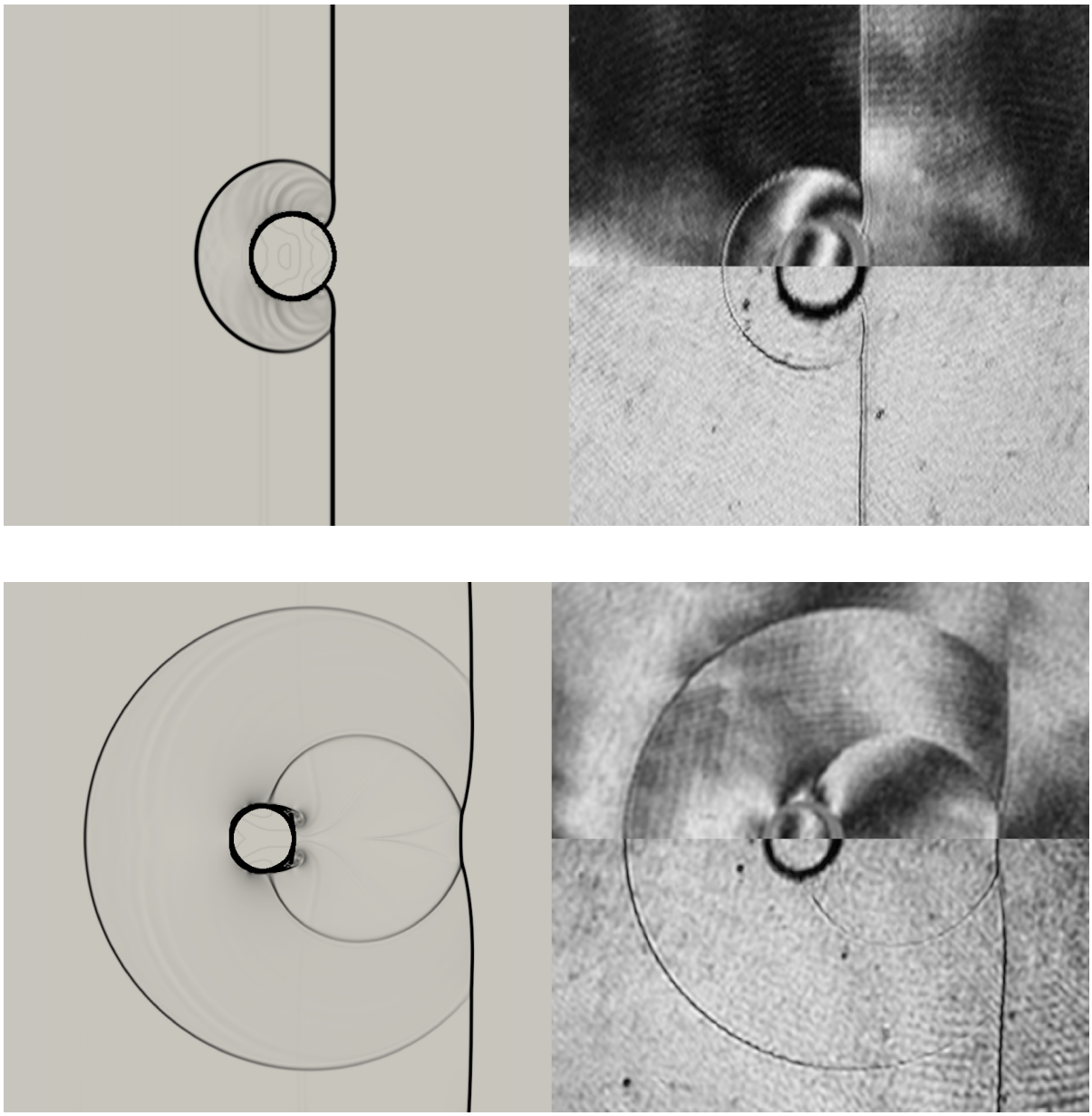

Figure 2.15: Magnified view of the early stages of the aerodynamic breakup of the water column in the high-speed airstream behind the shock wave of Mach number 1.3 in atmospheric air propagating from the left to the right. 2D simulation on the left with a mesh of 3,200x1,200 cells and a schlieren image of the mixture density. Experiment on the right from Igra and Takayama [39] with an interferogram on the upper half and an unreconstructed hologram on the lower half. Results are shown at times $15\mu s$ (top) and $55\mu s$ (bottom).

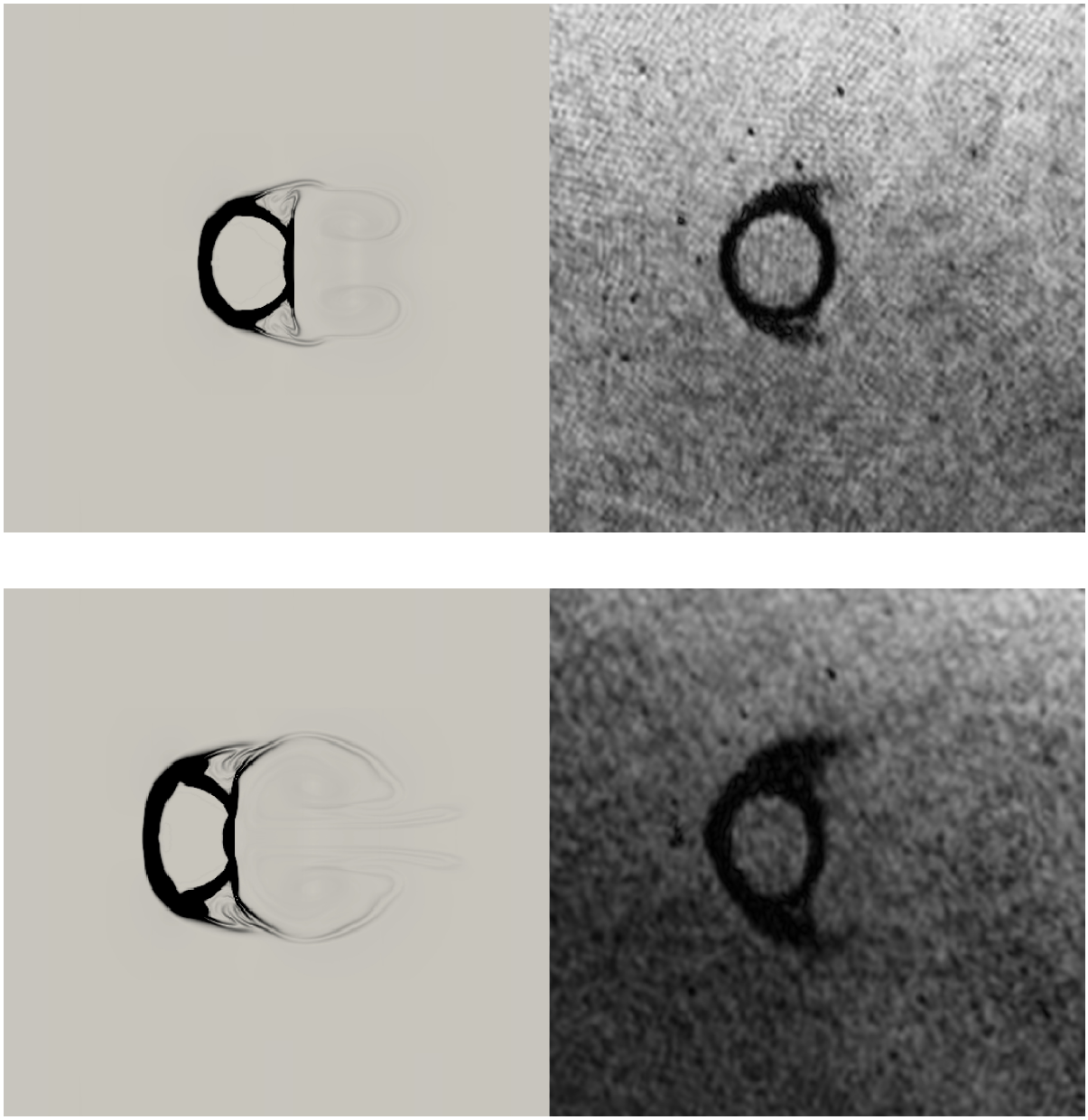

Figure 2.16: Magnified view of the aerodynamic breakup of the water column in the high-speed airstream behind the shock wave of Mach number 1.3 in atmospheric air propagating from the left to the right. 2D simulation on the left with a mesh of 3,200x1,200 cells and a schlieren image of the mixture density. Experiment on the right from Igra and Takayama [39]. Results are shown at times $200\mu s$ (top) and $300\mu s$ (bottom).

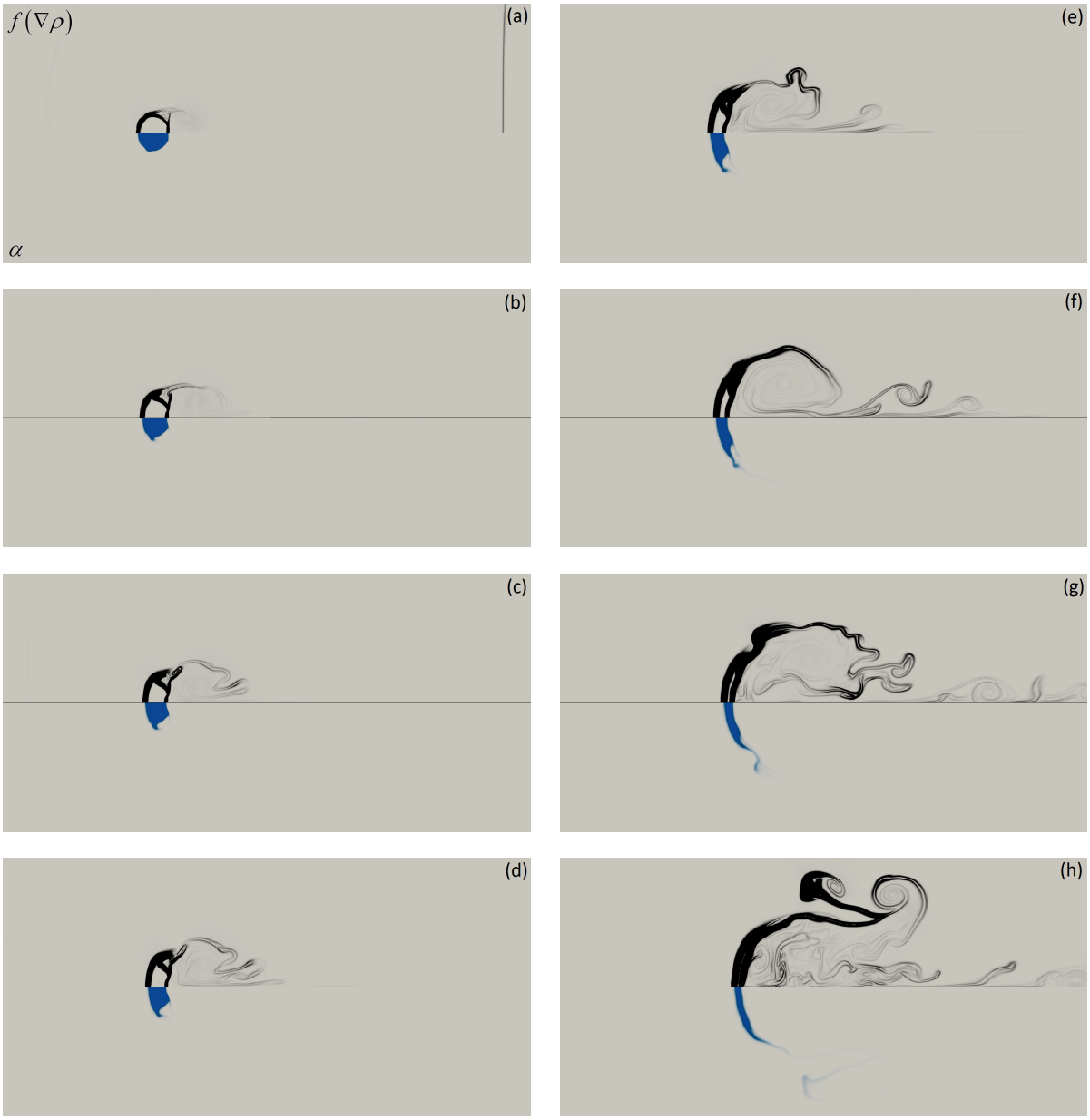

Figure 2.17: Magnified view of the aerodynamic breakup of the water column in the high-speed airstream behind the shock wave of Mach number 1.3 in atmospheric air propagating from the left to the right. 2D simulation with a mesh of 3,200x1,200 cells and schlieren images of the mixture density (upper half) coupling with volume fraction of water visualization (lower half, in white the air and in blue the water) are given at the following times: (a) $160\mu s$, (b) $320\mu s$, (c) $420\mu s$, (d) $500\mu s$, (e) $660\mu s$, (f) $820\mu s$, (g) $1,000\mu s$ and (h) $1,200\mu s$.

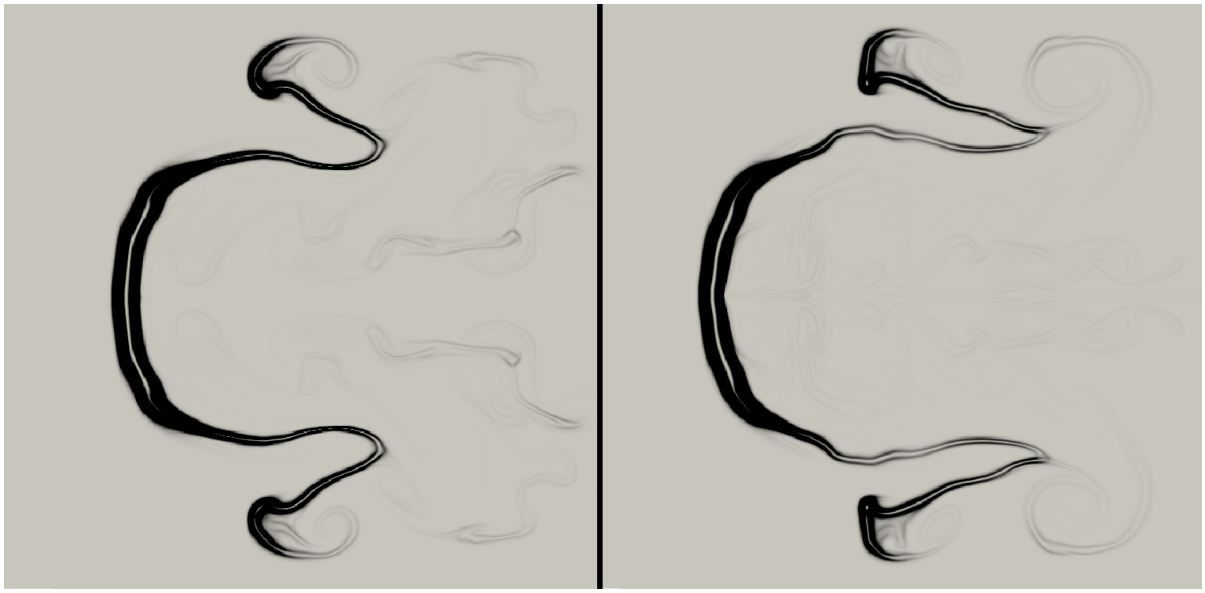

Figure 2.18: Magnified view of the aerodynamic breakup of the water column in the high-speed airstream behind the shock wave of Mach number 1.3 in atmospheric air propagating from the left to the right. 2D simulations respectively without (left) and with (right) capillary effects taken into account, with a mesh of 3,200x1,200 cells and a schlieren image of the mixture density. Results are shown at time $1.2ms$.

Chapitre 3

Un algorithme simplifié de raffinement adaptatif de maillage basée sur des arbres de cellules et de bords pour les écoulements compressibles multiphasiques

Simplified Adaptive Mesh Refinement algorithm based on dual cell-boundary trees for multiphase compressible flows

This chapter almost corresponds to the Schmidmayer et al. [81] publication.

3.1 Introduction

In computational fluids dynamics, the accuracy of results is conditioned by the refinement level of the computational grid. Nevertheless, the finer is the grid, the more expensive is the computational cost regarding CPU time as well as memory. For the computations of steady flows, the use of unstructured grid and mesh refinement technics at well-defined locations can lead to very accurate results (see for example simulations around hydrofoils [33]). For the computations of strongly unsteady flows with shock waves or traveling interfaces, achievement of accurate results is conditioned by the use of a very small cell size. Thus, a large amount of computational time is wasted to compute solutions in cells where almost nothing occurs (example in Figure 3.1).

When dealing with multiphase flows, especially in the framework of diffuse interface methods [78], the previous remark is amplified by the complexity of the model:

- an important number of evolution equations may be solved (Hank et al. [30], Petitpas et al. [70]),
- iterative solvers for relaxation procedure may also be required (Saurel et al. [80], Han et al. [27]),
- expensive Riemann solvers are sometimes needed to account for real material effects (Le Métayer et al. [53]).

On the strength of these observations, the use of Adaptive Mesh Refinement (AMR) technics represents an interesting option to reduce the CPU time cost when dealing with complex multiphase compressible flows. This is the aim of this study.

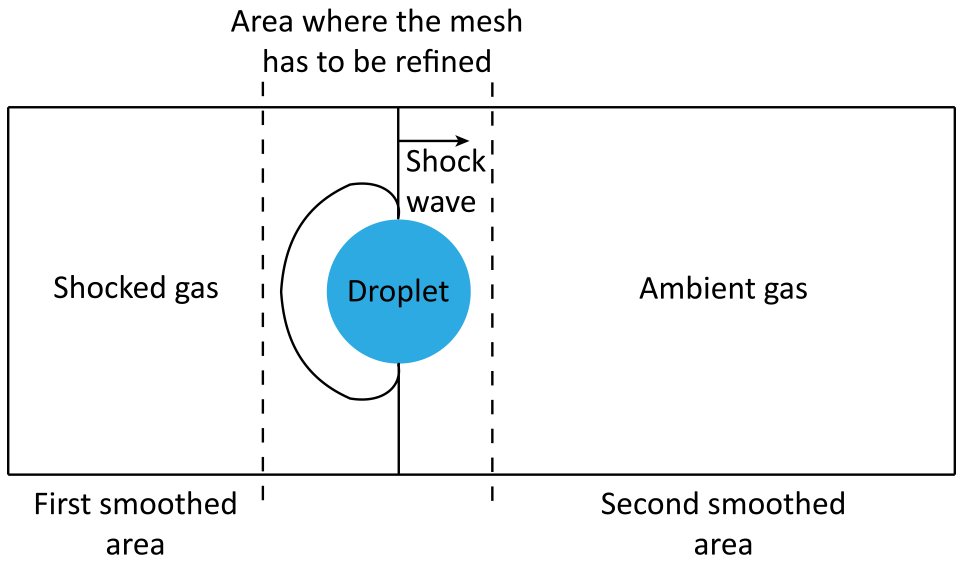

Figure 3.1: Sketch of a choc-droplet interaction where two parts are distinguished: one where the mesh has to be refined and one where it does not.

When AMR is embedded in a computational fluid dynamics code, the computational grid is dynamically adapted in order to be refined where it is necessary and to maintain a coarse grid elsewhere. These AMR methods are suitable and already massively used for many applications:

- magnetohydrodynamics (Anderson et al. [5], Dumbser et al. [16]),
- uncompressible multiphase flows as for the droplet motions in a microchannel and the atomization of liquid impinging jets (Chen and Yang [13], Popinet and Rickard [72]),
- compressible flows in porous media as for the leakage of gas from a liquefied petroleum gas storage cavern (Pau et al.[65]).

The analysis of literature shows that there are mainly two existing approaches in the context of finite volume scheme:

- The first one is an approach where cells are organized in Cartesian grids (Berger and Oliger [7], Berger and Colella [6]). The entire computational domain is represented by a coarse base grid and when more resolution is required, finer and nested grids are laid over coarser grids. This defines a grid hierarchy from the coarsest to the most refined grid that may be organized as a "grid tree". The grid generation or destruction occurs when the local relative error between calculations done on the current grid and a finer or a coarser grid, respectively, passes a given criterion. The main advantage of this approach is that the flow solver is independent of the grid, thus the same flow solver can be applied whatever the grid considered. That also means that any single-grid fluid flow solver can be used without important modifications for AMR.

The drawbacks is due to the rigid structure of the grid. It induces that the simulation of complex flows requires the covering with an important number of grids and several grids of the same level of refinement may then overlap. A duplication of cells is inherit from this overlapping and also a substantial number of new computational cells can be wasted in smooth flow regions. Besides, the periodic rebuilding of the entire grid hierarchy is required when the flow evolves with time.

- In the second approach, the refinement occurs on an individual cell and this directly defines a tree of cells (cells tree method) (Young et al. [100]). Each cell can be refined or unrefined independently of others. Moreover, the mesh refinement occurs locally where it is necessary, then at every level of the tree, the mesh may have a non-uniform shape. The main advantage of the cells tree approach is the flexibility in refinement and unrefinement. This flexibility is paid by the fact that standard grid-based solvers cannot be used directly on a tree. Fluxes calculation and time stepping strategy on a tree is different from that on a grid, that means that the flow solver is slightly dependent on the level computed. In addition, an access to neighboring cells is more difficult in a tree than in an array and scanning the tree to access the nearest neighbors is a difficult procedure to vectorize and parallelize. Moreover, the memory cost oscillates between an additional or a lesser cost than the first approach because there are fewer cells to be stored but a tree generates an additional cost to be maintained.

  In Khokhlov [46], the use of a different structure of data allowed to circumvent these two last problems. The structure of Khokhlov involves a fully threaded tree where cells have not only knowledge of their child cells but also of their parent cells and neighboring cells. This thread provides an efficient parallel access to information on a tree. Khokhlov also improves the memory cost for maintaining the tree by regrouping cells in a so-called "oct" structure. Besides, the refinement criterion is based on physical variations between neighboring cells. This dynamical refinement is generally ensured by tracking discontinuities (as shock waves or contact discontinuities). The refinement evolves with the flow features which makes it more suitable for resolution of highly dynamical flows.

In this work, we retain the second approach for its ability to easily adapt the mesh for unsteady flows. Thus, a modified version of Khokhlov's method is presented. It is important to mention that the original method was developed in the late nineties and the goal was to compute single phase compressible flows using AMR method with the best performance concerning the efficiency and the memory. Even if the development of an efficient algorithm is still a key problem nowadays, the constraints on memory are not as crucial as they were. Today's problems are linked to multiphysics complex flows (including several phases, solids, phase transition, chemical reactions, viscosity, capillarity, etc.) that are well described by complex mathematical models for which the computational cost represents the limitation, much more than memory. That is why two specificities of Khokhlov method have to be pointed out:

- The first one is that, the fully threaded tree involves a lot a operations to find

the neighboring cells. This becomes a critical point when the algorithm is used to solve complex model coupled with high-order method where the procedure to find the neighbors occurs many times (flux calculations at each step of the high-order method, gradient calculations for numerical purpose or physical description, etc.).

- The second one is that if the AMR method is implemented in a code where the mesh can be either Cartesian or not, finding the neighbors could involve many complex operations.

The new method we propose has two advantages: the general AMR algorithm is first simple and also cell neighboring searching is improved. The key point is the role plays by cells boundaries (geometrical contour): obviously for the flux calculations and also because these boundaries naturally define neighbors between two cells. This new method extends Khovhlov approach on two points: the cell tree structure is slightly modified and a second tree is used to store some cell boundaries information. Addition of this second tree boundaries structure presents the advantages to reduce the number of operations during the time step integration and to simplify the algorithm. The drawback is to reasonably increase the memory involved. Reasonably because the number of additional information stored for each cell boundary is relatively small in comparison to what is needed in a cell.

The chapter is then organized as follows: First, the extended AMR data structure is described. Second, the general AMR algorithm in the context of finite volume scheme (coupled with Riemann solvers for fluxes calculations) is presented. The time-stepping strategy, the advancing and the mesh refinement procedures are detailed. Third, the extension of the AMR method to the multiphase flow model of Schmidmayer et al. [82] is presented. Its application on different tests - transport, shock tube, capillary flow in 1D, 2D and 3D - is performed with quantitative comparisons regarding exact solutions or non-AMR method results in order to analyze the benefit of this new method. Shock-droplet interaction tests are given is the following chapter 4.

3.2 Description of AMR data structure

Let us first recall the data structure of AMR method based on cells trees. A computational cell is represented by a node at a given level in a tree. Each node of a tree is linked thanks to edges to:

- A parent node representing a computational cell at lower level. The root of a tree is a particular node with no parent.

- A given number of child nodes representing computational cells at higher level. The number of child nodes depends on the geometry and the dimension of the problem. A leaf of a tree is a particular node with no child and the calculation of physical quantities (not linked to AMR) only occur on a node that is a leaf.

Each cell in AMR method may be split in a given number of child cells. An example of possible splitting in 1D/2D/3D Cartesian grid is shown on the right part of Figure 3.2 and an example of a tree representing data for a 1D AMR method is shown in on its left part.

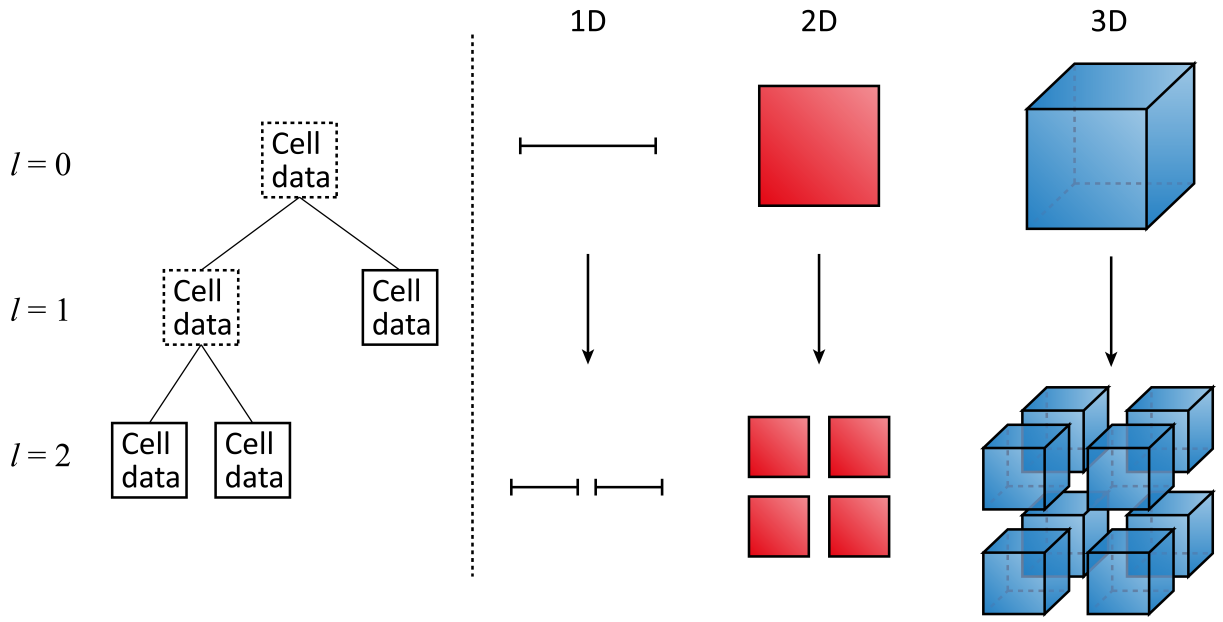

Figure 3.2: Figure split in two parts. On the left, an example of a tree representing the data structure for a 1D AMR method. "l" accounts for the level in the tree. On the right, possible cell splitting. A 1D, 2D and 3D cell will give birth in a Cartesian grid to 2, 4 and 8 child cells, respectively.

3.2.1 Recall of Khokhlov method [46]: FTT

The tree structure is the most obvious structure to define and optimize the cells data storage in an AMR method. Its flexibility allows refinement and unrefinement *via* destruction and reconstruction of chosen nodes in the tree. The cornerstone of such method resides in the chosen way to browse cells in the tree that can be a complex and expensive operation depending on the links between cells. In its simplest version, a node can only be accessed from browsing the tree from its root. One can easily understand that the simple operation that consists in locating neighbors of a given cell (for example to calculate inter-cell fluxes) rapidly becomes a source of computational waste. An alternative solution is the use of a so called Fully Threaded Tree (FTT) where each nodes has the knowledge of its parent node, child nodes and neighbors nodes. This improvement renders easy the browsing of the tree in every direction (from parent to child, child to parent and even between neighbors). This ability to browse the tree in all directions has nevertheless the drawback to increase considerably the amount of memory (by addition of multiple pointers acting as threads). It also renders maintenance operations on the tree more complicated when refinement and unrefinement occur.

Khokhlov proposes to group cells into octs in order to limit extra storage due to links between nodes and to limit maintenance operations costs. Each oct contains 8 organized cells (in 3D), a pointer to its parent cell at lower level and 6 pointers to parents cells of neighboring octs. Each cell contains physical flow variables and a pointer to a child oct at higher level. Most of the pointers, as well as the geometrical properties (level, position,

size, etc.), are thus grouped to be stored into octs rather than in cells. Consequently, the memory costs is significantly reduced (especially in 3D) in comparison to a FTT simple version without oct structure.

The memory cost saving is undeniable when dealing with Euler equations, it is more disputable when dealing with complex models traducing multiphysics problems. In such applications of AMR, the ratio between physical flow variables and geometrical/AMR variables increases drastically. Khokhlov explains that the cost of his oct-FTT AMR version is 2 words of memory per cell instead of 17 words/cell for a non oct version of FTT. These additional memory costs have to be compared with physical flow variables that are necessary to store (5 words/cell for Euler equations but 6N words/cell for a general N-phase flow without extra physics).

In addition to the ratio of memory cost saving that decreases when the model, and then the physic, becomes complicated, another drawback of oct-trees is that the computational time associated with computing cell pointers from oct pointers and oct pointers from cell pointers, or in other words extra time needed to look for neighbors cells, is estimated to about 20% when computing single phase flow with a first order scheme. Here again, when complex models coupled with high-order numerical solvers are of interest (involves neighborhood seeking for each flux calculation of the high order scheme, for each gradient calculation, etc.), this extra computational time involved by the structure may be no longer negligible.

3.2.2 Basic idea of the new AMR data structure: The extra cells boundaries trees

An efficient way to avoid increasing CPU time and difficulty in searching neighbors in parallel computations is to take benefit of information related to cells boundaries. In the finite volume framework, a cell boundary may be defined as a geometrical contour between two computational cells that is the seat of fluxes calculations. A boundary may be defined as an object that stores two pointers, one for a "left" cell and another one for a "right" cell. Availability of such objects prevents from neighbors seeking when solving inter-cell fluxes in a computational CFD code. In a more general context of unstructured grids, it also prevents from using a connectivity table. It implies that finite volume algorithms using such data structure can be easily used whatever the grid structure is.

In addition to cells trees, we thus propose to define boundaries trees. In these boundaries trees, cells boundaries are represented by nodes that are linked to other boundary nodes by edges. The duality of cells tree and boundaries trees represents a complex data structure that greatly simplifies the algorithm and reduces computational costs. Up to this remark, the new data structure is composed of:

- cells that are organized in tree structures (oct tree or not). They may also be linked to boundaries.
- boundaries that are also organized in trees structures. They can also be grouped in quad tree to mimic Khokhlov's oct cell trees structures (a boundary will be split in up to 4 child boundaries in 3D).

Boundaries trees in the AMR method implies additional memory costs. Nevertheless, with this new data structure, calculations at boundaries (fluxes, gradients, etc.) are naturally accessed without seeking for neighbors. This important point renders the method easily extensible to unstructured meshes. Moreover, the oct structure used in Khokhlov's work can be kept to regroup information regarding geometrical properties in the Cartesian framework.

3.2.3 Detailed description of trees

For convenience in presentation, data structure is presented for non-oct trees. The alert reader will easily extend the method to oct-trees if needed.

The main tree of the method is quite similar to those of a FTT classical method. The computational cells constitute the nodes of the cells tree. In particular they contain the physical flow properties (depending on the flow model under interest) as well as geometrical data. These cells nodes also includes additional data specific to the AMR method:

* an integer for its level (0 for the root, > 0 otherwise),
* a pointer for each of its child cells nodes (up to 8 in Cartesian 3D),
* an additional pointer for each of its boundary (up to 6 in Cartesian 3D),
* a pointer for root of each new internal boundary tree (up to 12 in Cartesian 3D). The particular case of the internal boundaries is presented in the following.

Compared to a classical FTT method, the novelty resides in the pointers to boundaries that represent an additive memory cost of maximum 11 pointers/cell in 3D (12 new pointers for internal boundaries, 1 less because pointer to parent cell is no longer needed in the method). Up to this point, a given cell can be either split or not (if its pointers to child cells nodes are null).

The second novel data structure is represented by new boundaries trees. A cell boundary is a new object that includes two cell pointers (one for the left cell and one for the right cell). The interest of the presence of such objects in a finite volume method resides in a better access to fluxes calculation between two computational cells. In the present AMR method, cells boundaries constitute nodes of new boundaries trees. These boundaries nodes then includes additional data specific to the AMR method:

* an integer for its level,
* a pointer to each of its child boundaries nodes (up to 4 in 3D).

This new data structure possesses some particular specificity. Indeed, let us consider the example of a 2D Cartesian cell represented in Figure 3.3. This cell is surrounded by 4 boundaries (blue edges). Refinement of this cell will give birth to 4 new computational cells and 12 new boundaries. Among these 12 boundaries, 8 of them are originated from parent cell's boundaries splitting (dashed red edges) and appear naturally as children of parent boundaries. Also, 4 new boundaries appear inside the parent cell as the result of

cell's splitting and are considered as root of new boundaries trees (dashed point green edges). Consequently, splitting of a given cell will act on boundaries trees in two ways:

- It will increase the depth of already existing trees. "External" boundaries of the parent cell, that were leaves before splitting, will become parent of new boundaries (up to 4 in 3D), the last ones are thus leaves.
- In the same time, it will also generate new "internal" boundaries that are roots (and leaves) of new boundaries trees.

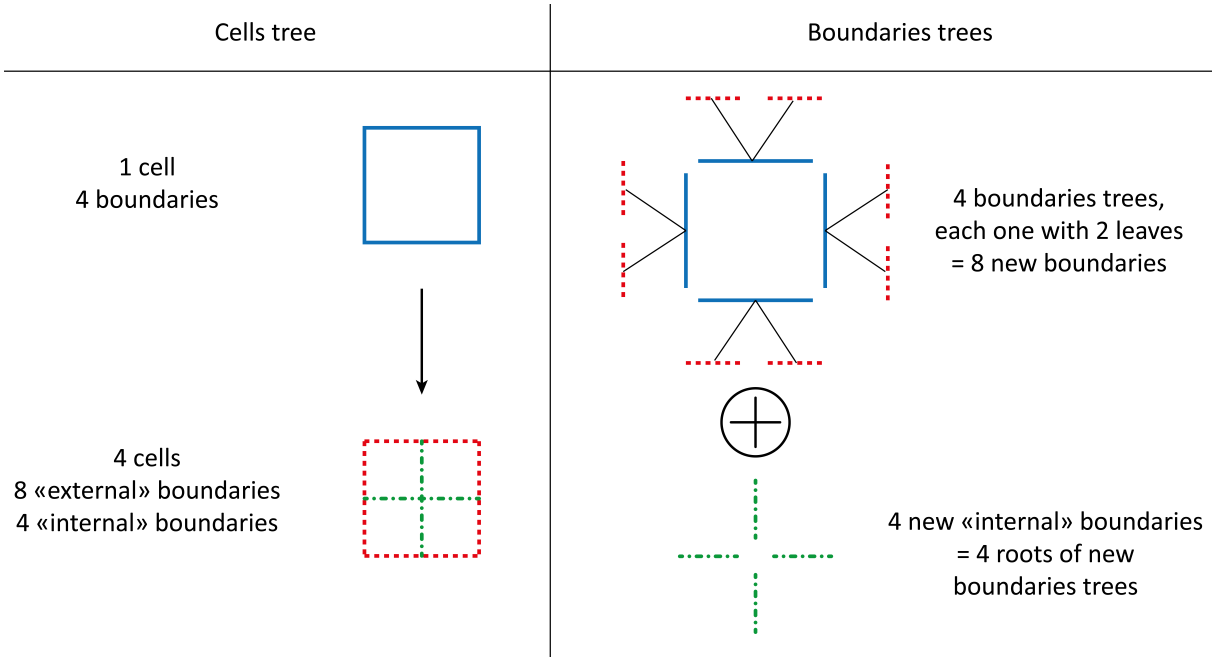

Figure 3.3: 2D example of cells tree and boundaries trees duality.

A 2D example of the links between cells and boundaries trees is illustrated in Figure 3.4. In this example, 3 levels are present. The figure is decomposed in three parts:

- The top part shows 2 successive refinements occurring from a given level-0 cell. The following cells and boundaries trees correspond to this particular splitting.
- The middle part shows the corresponding cells tree represented by square nodes and composed with 4 level-1 cells and 4 level-2 cells.
- The bottom part shows the corresponding boundaries trees represented by circles nodes. 4 level-0 boundaries trees, 12 level-1 boundaries (including 4 new level-1 boundaries trees) and 12 level-2 boundaries (including 4 new level-2 boundaries trees) are generated.

The adopted numeration is 'XYZ' with X being C (for cell) or B (for boundary), Y corresponds to level number (here from 0 to 2) and Z is the letter corresponding to the entity (A

to N in the present case). Pointers between cells in cell tree are shown with black lines as well as pointers between boundaries in boundaries trees. In order to facilitate comprehension, the pointers between cells and boundaries are non exhaustively presented but only some typical examples:

- In yellow lines, cell C0A will point to the 4 boundaries B0A, B0B, B0C and B0D of level 0. Such pointers are present for each cell and are needed for gradient calculations.
- In dashed dotted green lines, are represented pointers from a boundary of level 1 (B1N) to two level-1 cells (C1C and C1D).
- In dotted blue lines, an example of a boundary (B2J) linked to two cells from different levels (C1C and C2D).
- The last example in dashed red lines shows a boundary (B1A) linked to a level-1 cell (C1A) and another cell neighbor (level-0) of cell C0A or one of her child (level-1 cell) not shown in the figure.

This last 3 kind of links are used for fluxes calculation (only if the boundary is a leaf).

	Data type	Classical FTT AMR	New AMR
Words number / Cell data	Cell level	1	1
	Refinement indicator	1	1
	Pointer to parent cell	1	-
	Pointers to child cells	8	8
	Pointers to neighboring cells	6	-
	Pointers to cell boundaries	-	6
	Pointers to internal cell boundaries	-	12
Words number / Cell boundary (x3)	Boundary level	-	1
	Pointers to children boundaries	-	4
	Total number of words / cell	17	43

Table 3.1: Memory costs comparison between classical AMR FTT method and new AMR method using boundaries trees. For a given 3D hexahedron cell, the new method requires 11 additional words. Noticing that a boundary is common to 2 neighboring cells, a cell requires approximately 3 boundaries (instead of 6), each of them requiring 7 words. The global over-cost of the new method is thus 32 words/cell.

One can note that the number of boundaries may be important. Nevertheless, the boundaries trees reasonably increase the memory involved since they only need a few additional pointers for each boundary. Comparison with a classical FTT structure of the required memory is presented in Table 3.1. The table shows the detailed number of words for each cell and each boundary. The total number of words reported to a cell is also given. For a given 3D hexahedron cell, the new method requires 11 additional words. Noticing that a boundary is common to 2 neighboring cells, a cell requires approximately 3 boundaries (instead of 6), each of them requiring 7 words. The global over-cost of the new

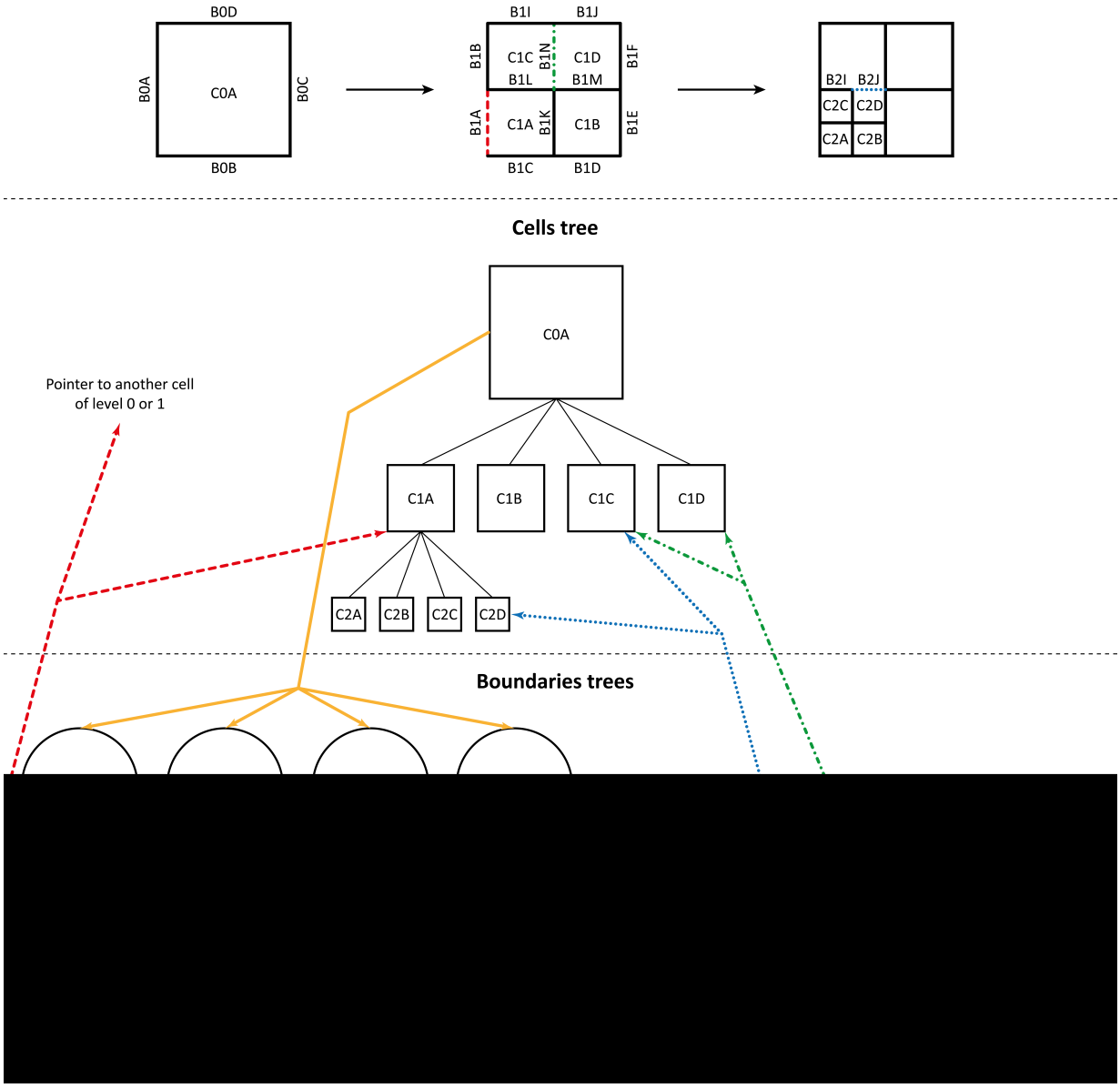

Figure 3.4: 2D example of links between cells and boundaries trees. Here, some details are given for a cell and its 2 levels of refinement. The top represents the cells appearing from the two successive refinement form a level-0 parent cell. The middle and bottom sketches are representing the cell tree and boundaries trees, respectively. Connections between both cells and boundaries trees are presented in some typical situations.

method is thus 32 words/cell. This has to be compared to the memory cost for storage of geometrical and physical variables that may represent the larger part of memory costs in a multiphase and multiphysic computation.

Saving may be done regarding memory costs by using Khokhlov-like oct tree method for particular Cartesian grids. Indeed, it is possible to group cells in oct ([46]) as well as boundaries, where grouping is also possible: "external" boundaries are grouped in quad

and "internal" boundaries are grouped in dodeca. This improvement in term of memory cost is possible but complicates the AMR algorithm. We present in Table 3.2 these possible savings in memory costs and the global over-cost of the new method is thus reduced to 3.75 words/cell.

	Data type	Khokhlov AMR	New AMR
Words number / Cell data	Cell level	1/8	1/8
	Refinement indicator	1	1
	Pointer to parent cell	1/8	-
	Pointers to child oct	1	1
	Pointers to neighboring octs	6/8	-
	Pointers to oct's quad boundaries	-	6/8
	Pointers to oct's internal dodeca boundaries	-	1/8
Words number / Cell boundary (x3)	Boundary level	-	1/4
	Pointers to children boundaries	-	1
	Total number of words / cell	3	6.75

Table 3.2: Possible savings using oct tree for cells and quad/dodeca trees for boundaries.

However, as mentioned in 3.2.1, these AMR structure memory savings are balanced by the memory needed for physical quantities as well as extra quantities stored for computational conveniences. For these reasons we decide to highlight algorithm simplicity and computational efficiency and thus not retain the oct tree structure.

3.3 General AMR algorithm

3.3.1 Finite volume scheme for conservation laws

We consider a system of conservation laws under the following form:

$$\frac{\partial \mathbf{U}}{\partial t} + \boldsymbol{\nabla} \cdot \overline{\overline{F}}\left(\mathbf{U}\right) = \mathbf{S} \tag{3.1}$$

with $\mathbf{U}$ the conservative variable vector, $\overline{\overline{F}}$ the fluxes tensor and $\mathbf{S}$ the source terms vector. Integration of system 3.1 on a computational cell of volume V_i delimited by surfaces A of normal unit vector $\mathbf{n}$ (a two-dimensional example is presented in Figure 3.5) reads:

$$\frac{\partial}{\partial t}\int_{V_i} \mathbf{U} \mathrm{d}V + \int_A \overline{\overline{F}}\left(\mathbf{U}\right) \cdot \mathbf{n} \mathrm{d}A = \int_{V_i} \mathbf{S} \mathrm{d}V, \tag{3.2}$$

The first and last terms of Eq. (3.2) are interpreted as the time-rate of change of the conservative variable and source terms vectors volume average:

$$\frac{\partial}{\partial t}\int_{V_i} \mathbf{U} \mathrm{d}V = V_i \frac{\partial \overline{\mathbf{U}}}{\partial t},$$

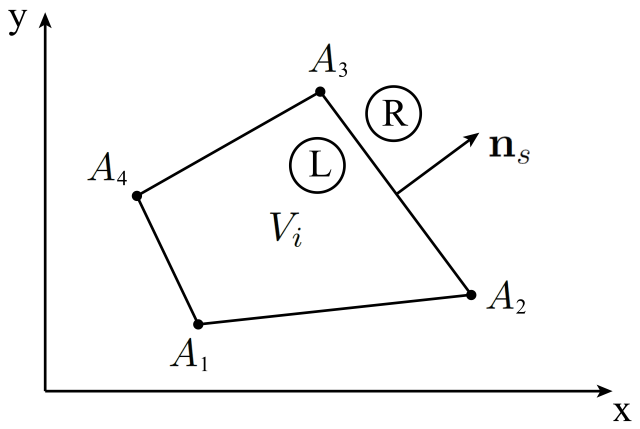

Figure 3.5: Scheme example for a 2D computational cell

$$\int_{V_i} \mathbf{S} \mathrm{d}V = V_i \overline{\mathbf{S}}.$$

As boundary A of V_i is the union of N straight segments $[A_s, A_{s+1}]$, where $A_{N+1} = A_1$ and the normal unit vector is expressed by $\mathbf{n}_s$, the second term of (3.2) becomes:

$$\int_A \overline{\overline{F}} \cdot \mathbf{n} \mathrm{d}A = \sum_{s=1}^{N} \int_{A_s}^{A_{s+1}} \overline{\overline{F}} \cdot \mathbf{n}_s \mathrm{d}A,$$

Assuming that the fluxes are constant along each segment, it becomes:

$$\int_A \overline{\overline{F}} \cdot \mathbf{n} \mathrm{d}A = \sum_{s=1}^{N} L_s \overline{\overline{F}}_s \cdot \mathbf{n}_s,$$

where L_s is the length of segment $[A_s, A_{s+1}]$ (a surface in 3D).

After time integration, the evolution of the conservative part of system (3.2) is given for cell i by the scheme:

$$\mathbf{U}_i^{n+1} = \mathbf{U}_i^n - \frac{\Delta t}{V_i} \sum_{s=1}^{N} L_s \overline{\overline{F}}_s^{\star} \cdot \mathbf{n}_s + \Delta t \mathbf{S}_i, \tag{3.3}$$

where $\overline{\overline{F}}_s^{\star}$ represents the fluxes tensor solution of the Riemann problem between left (L) and right (R) states separated by the segment $[A_s, A_{s+1}]$ with respect to normal $\mathbf{n}_s$.

3.3.2 Time-stepping strategy

The efficiency of an AMR method necessitates the implementation of a specific time-stepping strategy. Following the works of Khokhlov [46], this time-stepping strategy is based on two key points:

- Cells at different levels evolve with different time-steps according to their level of refinement. In order to maintain the global time-step coherence for unsteady simulations, if cells of level l evolve at a given time-step, cells of level $l+1$ will then evolve 2 times with a time-step 2 times smaller. It results in CPU time saving.
- This time-stepping strategy permits interleaving between time integration and tree refinement. It results in memory save as it limit excessive buffer layer of refinement ahead of a discontinuity [46].

The global time-step is determined using the minimum tree level where there are leaf cells (l_{min}) and the CFL condition:

$$\Delta t = \Delta t\left(l_{min}\right) = cfl \frac{L}{2^{l_{min}} \max\left(\left|\left(\mathrm{u}+\mathrm{a}\right)_{\mathrm{s}}^{*}\right|\right)}$$

where $cfl < 1$ is a constant, L is the characteristic length of the coarser cells (at level $l = 0$) and the maximum speed is determined going through each leaf cell boundary where u is the fluid velocity in the corresponding face direction and a is the sound waves speed. Time-steps at various levels are:

$$\Delta t\left(l\right) = 2^{l_{min}-l} \Delta t.$$

The general integration procedure occurs at the different levels of the tree as an interleaving of advances and refinements. It is expressed as a recursive procedure $I(l_{min})$ with:

$$\begin{array}{lcll} I\left(l_{min}\right) & = & A\left(l_{min}\right) I\left(l_{min}+1\right) R\left(l_{min}\right) & \\ I\left(l\right) & = & A\left(l\right) I\left(l+1\right) A\left(l\right) I\left(l+1\right) R\left(l\right), & \text{for} \quad l \neq l_{min}, l_{max} \\ I\left(l_{max}\right) & = & A\left(l_{max}\right) A\left(l_{max}\right) R\left(l_{max}\right) & \end{array} \tag{3.4}$$

where $A(l)$ represent the advancement procedure of level l described in Section 3.3.3 and $R(l)$ is the refinement/unrefinement procedure of level l detailed in Section 3.3.4. All procedures in (3.4) are performed from right to left, *i.e.*, $R\left(l\right)$ first, and $A\left(l\right)$ last. An example of the sequence generated by (3.4) could be, for $l_{min} = 0$ and $l_{max} = 2$:

$$[R\left(0\right) \quad [R\left(1\right) \quad [R\left(2\right) A\left(2\right) A\left(2\right)] \quad A\left(1\right) \quad [R\left(2\right) A\left(2\right) A\left(2\right)] \quad A\left(1\right)] \quad A\left(0\right)].$$

One can note that the generality of the new method in the present finite volume framework simplifies the recursive integration procedure in comparaison to [46] where directional time-step splitting is computed. Indeed, the procedure of the lower level l_{min} is simplified, *i.e.*, only one advancing procedure is undertaken, and each advancing procedure is identical (only the referred level changes). The last one has to be compared with [46] where two advancing procedures have to be undertaken, one for the sequence of XYZ one-dimensional sweeps and one for its reversed.

Because of the recursive evolution algorithm, trees browsing will be traduce by an important amount of test to detect cells and boundaries levels. A possibility to avoid going through all the trees and then accelerate the procedures is to add lists for cells and boundaries and for each level of the simulation. Then loops on cells or boundaries become straightforward and constantly efficient.

3.3.3 Advancing procedure

The advancing procedure A is called at each time-step ($\Delta t\,(l)$) to advance the solution at the time $t + \Delta t\,(l)$ using the numerical scheme (3.3). This advancement procedure is decomposed in 3 steps:

- The first step is solving the hyperbolic part of System 3.3. A loop is first performed on leaves boundaries of level l where fluxes are estimated (using Riemann solvers) and stack in a buffer flux variable (initially set to 0) in each of "left" (L subscript) and "right" (R subscript) neighboring cells. This fluxes buffer is denoted by $\widetilde{\mathbf{F}}$. It is important to notice that possible contribution to these buffers comes from higher boundaries level (during preceding advancement procedures at higher levels).
  At the end of this boundary loop, buffers for cells of level l are complete. Indeed whatever the neighbors level are, fluxes have been stacked either in these advancement procedure or in those of higher levels. Then, conservative variable for leaves cells of level l should be evolved and corresponding buffers fluxes reset to 0 for next time step.

- The second step consists in upgrading leaves cells of level l using source terms integration.

- The third step is an averaging procedure consisting in updating split cells of level l. This step is useful for the correct computation of the refinement procedure (presented in details in Section 3.3.4).

The $A\,(l)$ procedure is described in a form of the following pseudocode:

1. — Hyperbolic resolution —

   for (leaf boundaries s of level l) {
   Compute the hyperbolic fluxes tensor $\overline{\overline{F}}^{\star}_{s} = \overline{\overline{F}}^{\star}_{s}\,(\mathbf{U}^n_L, \mathbf{U}^n_R)$;
   $\widetilde{\mathbf{F}}_L = \widetilde{\mathbf{F}}_L - l_{diff,L} L_s \overline{\overline{F}}^{\star}_{s} \cdot \mathbf{n}_s$;
   $\widetilde{\mathbf{F}}_R = \widetilde{\mathbf{F}}_R + l_{diff,R} L_s \overline{\overline{F}}^{\star}_{s} \cdot \mathbf{n}_s$;
   }
   for (leaf cells i of level l) {
   $\mathbf{U}^1_i = \mathbf{U}^n_i + \frac{\Delta t}{V_i} \widetilde{\mathbf{F}}_i$;
   $\widetilde{\mathbf{F}}_i = \mathbf{0}$;
   }

2. — Source terms resolution —

   for (leaf cells i of level l) {
   $\mathbf{U}^{n+1}_i = \mathbf{U}^1_i + \Delta t \mathbf{S}_i\,(\mathbf{U}^1_i)$;
   }

3. — Averaging of the children for the parent cells —

for (parent cells i of level l) {
  for (child cells j of parent cell i) {
    $\widetilde{\mathbf{F}}_i = \widetilde{\mathbf{F}}_i + \mathbf{U}_j^{n+1}$;
  }
  $\mathbf{U}_i^{n+1} = \widetilde{\mathbf{F}}_i /$ Number of child cells;
  $\widetilde{\mathbf{F}}_i = \mathbf{0}$;
}

The l_{diff} factor appearing in fluxes buffer stacking takes into account potential level differences between "left" and "right" cells on the considered boundary. It would take the value $l_{diff} = 1$ if the two neighboring cells have the same level or if the flux is applied to the cell with the higher level, and the value $l_{diff} = 0.5$ if the flux is applied to the cell with the lower level. In the example of cells C2D and C1B in Figure 3.4, the one with the higher level (C2D) will have 2 time-step integrations while the one with the lower level (C1B) will have just 1. In that case, for the fluxes calculation between these two cells, $l_{diff,L} = 1$ for cell C2D and $l_{diff,L} = 0.5$ for cell C1B. In that way, it makes a time average flux in the cell with the lower level.

Extension of this advancement procedure will be done in Section 3.4.2 for non conservative system of multiphase flows.

3.3.4 Mesh refinement procedure

If the data structure and integration algorithm represents key points to ensure AMR simulations efficiency, the ability to refine or unrefine at required locations is an other key point obviously linked to the quality of numerical results. This is also the most problem-dependent part and the choice for the refinement criteria is undeniably the most difficult point for the user of an AMR method. This point will be discussed in the results part. The cells refinement is always linked to a refinement indicator $0 \leqslant \xi \leqslant 1$ which is computed and stored for every computational cell. This indicator will be used to detect which are the cells that needs to be refined or unrefined:

- If a leaf cell has $\xi \geqslant \xi_{split}$, it indicates that the corresponding cell must be refined.
- If a split cell has $\xi < \xi_{join}$, the corresponding cell can be unrefined.

where ξ_{split} and ξ_{join} are two predefined constant parameters controlling the cell refinement dynamics forward and backward a discontinuity. We also impose an extra condition to control refinement: two neighboring cells cannot possess more than one level difference.

3.3.4.1 ξ indicator setup

The approach we use to calculate the refinement ξ indicator is based on locations of significant gradients (Coirier [14], Aftosmis et al. [3], Melton et al. [57]) and it acts in two steps:

- For each computational cell, ξ is calculated by:

$$\begin{aligned} \xi &= 1 \quad \text{if}: \quad \frac{|(\mathrm{X})_{\mathrm{Nb(i,j)}} - (\mathrm{X})_{\mathrm{i}}|}{\min\left((\mathrm{X})_{\mathrm{Nb(i,j)}}, (\mathrm{X})_{\mathrm{i}}\right)} > \epsilon, \\ \xi &= 0 \quad \textit{otherwise} \end{aligned} \tag{3.5}$$

  where X can be pertinent physical variable (for example p, $\|\mathbf{u}\|$, ρ, α). $Nb(i,j)$ represents neighboring cells (j accounts for a corresponding neighbor of cell i). The choice of the variable will discriminate shocks, contact discontinuities, interfaces or any kind of gradients. ϵ is a constant parameter that controls the limit in term of stiffness of the detected gradients. Attention should be paid with velocity to avoid division by zero. A combination of several gradients may also been used to improve detection.

- The second step consists in smoothing the refinement indicator. This operation is very important for several reasons. First it prevents cells from being falsely refined (mesh trashing). Secondly, smoothing will allow cells forward a discontinuity to be refined before the discontinuity arrival and by this way prevent oscillations as well as a loss of precision. To perform smoothing, we consider the ξ indicator obeys to a diffusion equation:

$$\frac{\delta \xi}{\delta \tilde{t}} = K \nabla^2 \xi, \tag{3.6}$$

  where $\tilde{t}$ is a fictive diffusion time only used to advance the solution for the diffusion of ξ into the domain. So, this diffusion has no link or impact on the treated physical characteristic. $K = 2^{-2l} L^2$ is a constant diffusion coefficient. This equation is solved with an explicit time advancement where the time step is chosen to preserve the diffusion stability ($dt = CFL_{diff} K/2$, where CFL_{diff} corresponds to the CFL condition pf the diffusion equation). Note that when this equation is solved, the number of fictive time iterations indirectly gives the number of cells where the indicator will be diffused. Typically, 3 or 4 time iterations are enough.

The splitting and joining criteria (explained previously) are then used to determine if the cell has to be refine or unrefine. The refinement around the contact discontinuity is presented in Figure 3.6 as a typical example.

3.3.4.2 Refinement and unrefinement of cells and boundaries

Due to the dual data structure, refinement (unrefinement) acts in two steps: first the refinement (unrefinement) of the cells and second of the boundaries.

Once the ξ indicator of every cell of the current level l is smoothed, the refinement of a cell occurs if $\xi \geqslant \xi_{split}$ and then the two steps are:

- First, the cell refinement. It does not involve special difficulties as it follows the scheme of Figure 3.2. A refined cell will give birth to up to 8 child cells (in Cartesian 3D) of level $l+1$ and each child will be built with the same physical characteristics than its parent cell.

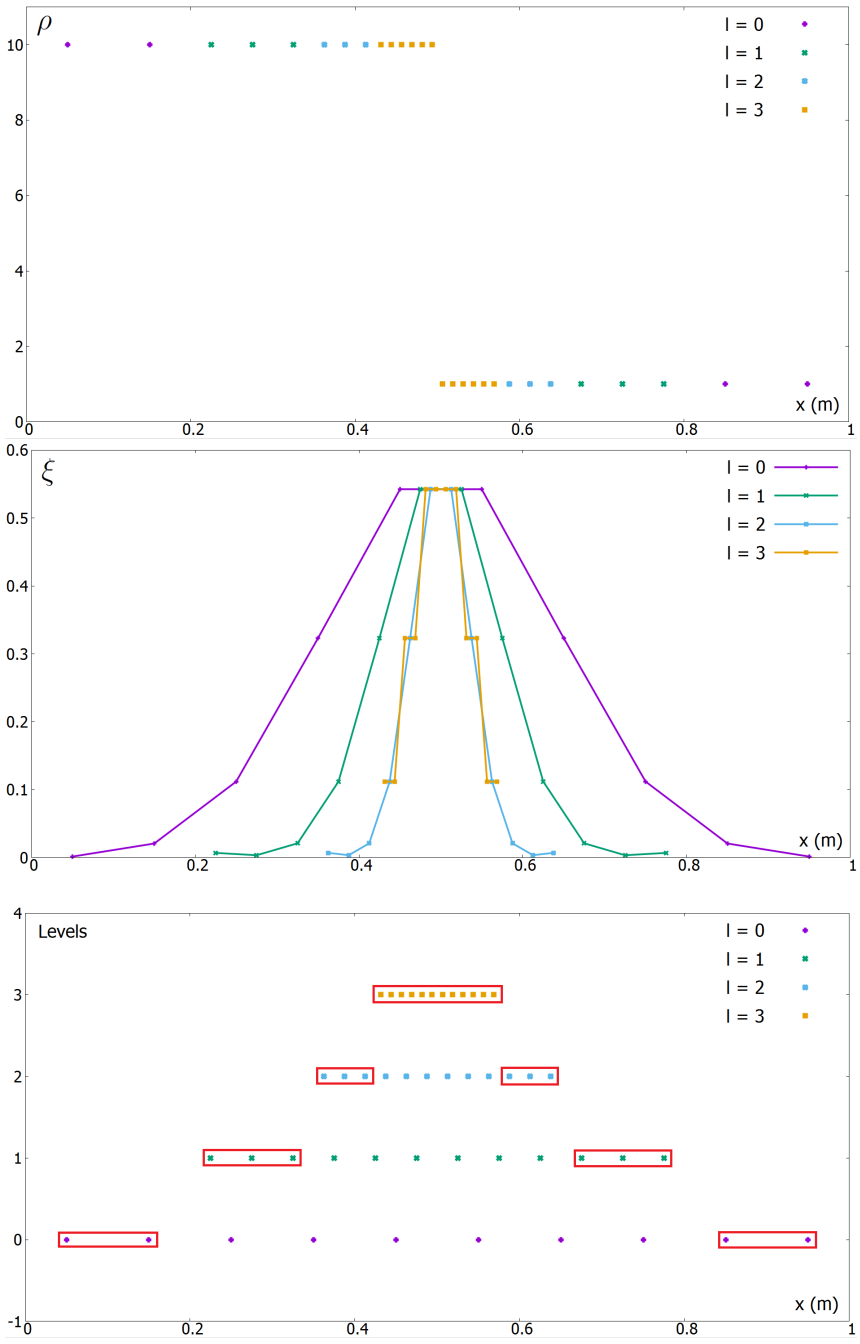

Figure 3.6: Result of the successive mesh refinement procedures around a density discontinuity. The top plot shows the density discontinuity, the center plot shows the values of the indicator for each level and the bottom plot shows the cells levels distribution (the red surrounded leaf cells are the cells where the integration occurs).

- Second, the boundaries refinement. It is also performed in two steps for each splitting cell. The first one is the creation of the internal child boundaries of level $l+1$ that belong to the parent cell and then creates new boundaries trees (up to 12 in Cartesian 3D). In the second step, the creation of the external child boundaries of level $l+1$ for each of the boundaries of the parent cell (level l) is executed only if it was not already done by the corresponding neighboring cell. The child boundaries belong to their parent boundary (see Figure 3.3).

For the unrefinement, it occurs if $\xi < \xi_{join}$ and then the corresponding two steps are:

- First, the cell unrefinement. The physical characteristics of the child cells are conservatively averaged to overwrite the ones of the parent cell (see point 3 of Section 3.3.3). Then, child cells are removed.

- Second, the boundaries unrefinement. Again it is performed in two steps for each joining cell. The first one is the removal of the internal child boundaries that belong to the parent cell. In the second step, the removal of the external child boundaries is done only if the corresponding neighboring cell is not split.

All the pointers are obviously redirected to the corresponding cell or boundary if necessary.

3.3.4.3 Mesh refinement procedure pseudocode

The $R(l)$ refinement procedure is thus described as the following pseudocode:

1. — ξ setup —

   for (cells i of level l) {
   $\xi = 0$;
   if (one of the gradient criteria is respected) { $\xi = 1$; }
   }

2. — Smoothing of ξ —

   for (x diffusion iterations) {
   for (cells i of level l) {
   Compute the diffusion equation for ξ (Eq. (3.6));
   }
   }

3. — Refinement —

   if ($l < l_{max}$) {
   for (non-split cells i of level l) {
   if ($\xi \geqslant \xi_{split}$ & level of each neighboring cells $> l-1$) { Cell i is refined; }
   }
   }

4. — Unrefinement —

if ($l < l_{max}$) {
  for (split cells i of level l) {
    if ($\xi < \xi_{join}$ & level of each neighboring cells $\leqslant l+1$ & children cells non-split) {
      Cell i is unrefined with children averaging (see point 3 of Section 3.3.3) to overwrite the values of cell i;
    }
  }
}

3.4 Extension to multiphase flow model of Chapter 2

The AMR method presented in this paper is devoted to applications to multiphase compressible flows and particularly to diffuse interface models. The model retained is the one presented in the previous chapter 2 and in Schmidmayer et al. [82] for capillary flows. However, the presented AMR method can be easily adapted to treat extra physics as for example phase transition (Massoni et al. [56], Saurel et al. [79], cavitation (Petitpas et al. [69]), detonation in high energetic materials (Petitpas et al. [70]), solid-fluid interaction and compaction of granular media (Favrie and Gavrilyuk [19, 18]) and low Mach number flows (Murrone and Guillard [60]).

We recall here a brief overview of the basic numerical scheme in the context of non AMR methods.

3.4.1 Numerical Method without AMR

The numerical method is presented as a 3-step method. Each step is successively performed in order to circumvent specific numerical problems:

- First, the hyperbolic non-equilibrium pressure model (2.16) is solved using a Godunov-type method [82].
- Second, model (2.17) is solved. A specific attention is paid to the choice for the flux terms in order to ensure the momentum and energy conservation.
- Third, a relaxation procedure leads to the pressure equilibrium.

The unknown vector $\mathbf{U}^{n+1}$ is obtained from the initial condition $\mathbf{U}^n$ by application of the three successive operators according to the sequence:

$$\mathbf{U}^{n+1} = L_{relax} L_{cap} L_{hyper} \left(\mathbf{U}^n\right),$$

where the vector $\mathbf{U}$ contains the unknown quantities defined in the system:

$$\mathbf{U} = \left[\alpha_1, \alpha_1\rho_1, \alpha_2\rho_2, \rho u, \rho v, \rho w, \alpha_1\rho_1 e_1, \alpha_2\rho_2 e_2, c, \rho E + \varepsilon_\sigma\right]^T$$

Each step of the numerical method is fully detailed in Chapter 2 and in Schmidmayer et al. [82]. It is important to note that, for the different capillary terms, the vector $\mathbf{w}$ is computed *via* derivatives of the color function which are computed by using second-order finite difference approximations. Plus, to go through the operators chain, the solution at time $n+1$ is obtained by a pressure relaxation algorithm and corrects the components of $\mathbf{U}^{cap}$:

$$\mathbf{U}^{n+1} = L_{relax}\left(\mathbf{U}^{cap}\right).$$

The details about the pressure relaxation algorithm as well as the correction procedure used to guarantee total energy conservation can be found in Saurel *et al.* [80].

3.4.2 Extension of the AMR algorithm for multiphase flow

The extension of the AMR algorithm to treat multiphase flow model (2.14) implies several modification to the method:

1. Model (2.14) is non-conservative. It is thus necessary to take into account for non conservative terms in the advancement procedure,

2. The global time-step of integration is slightly modified to add a cell gradient procedure G that computes the color function gradients required in the capillary effects formulation. It is done before going to the higher tree level and integration procedure now reads:

$$\begin{array}{lcll} I\left(l_{min}\right) & = & A\left(l_{min}\right) I\left(l_{min}+1\right) G\left(l_{min}\right) R\left(l_{min}\right), & \\ I\left(l\right) & = & A\left(l\right) I\left(l+1\right) A\left(l\right) I\left(l+1\right) G\left(l\right) R\left(l\right), & for \quad l \neq l_{min}, l_{max}, \\ I\left(l_{max}\right) & = & A\left(l_{max}\right) A\left(l_{max}\right) R\left(l_{max}\right) & \end{array} \tag{3.7}$$

   The same precedent example thus implies now a a sequence generated by (3.7) for $l_{min} = 0$ and $l_{max} = 2$ gives:

$$\left[R\left(0\right) G\left(0\right) \quad \left[R\left(1\right) G\left(1\right) \quad \left[R\left(2\right) A\left(2\right) A\left(2\right)\right]\right.\right.$$

$$\left.\left.A\left(1\right) \quad \left[R\left(2\right) A\left(2\right) A\left(2\right)\right] \quad A\left(1\right)\right] \quad A\left(0\right)\right].$$

3. Model (2.14) also contains relaxation terms that implies modification in the algorithm.

In the following part, the modification of advancing procedure as well as the cell gradient and relaxation procedures specific to multiphase capillary flows are detailed.

3.4.2.1 Cell gradient procedure

The cell gradient procedure G is the procedure to compute the different cell gradients which could be needed to treat a specific physic, here the capillary effects. Indeed, when the computation of the capillary effects is done, the fluxes calculation on a boundary uses the color function cell gradient of each neighboring cell of this boundary. And to avoid the

cell gradient calculation multiple times for each cell, it is computed in a loop going through each cell, and not when the calculation of the fluxes are involved. Thus, in the case where one of the two neighboring cell of a boundary has a smaller level than this boundary, the cell gradient in this cell has to be computed before doing the fluxes calculation. But, in the recursive integration procedure (Equation (3.7)), if the cell gradient procedure $G(l_{min})$ is not done before going to the integration procedure of the higher level $I(l+1)$, the needed cell gradient for the fluxes calculation of the advancing procedure of this higher level $A(l+1)$ would not have been computed. It thus explains why this procedure is necessary. So, the procedure is done at the level l before going to the recursive integration procedure $I(l+1)$ and it follows the pseudocode:

if $(l < l_{max})$ {
  for (leaf cells i of level l) {
    Compute the color function gradients $\mathbf{G}_i(\mathbf{U}_i^n)$;
  }
}

One should note that using cell gradients involves a particularity when coupling with AMR method. Indeed, the cell gradients calculation is always done at a particular time in a given cell and thus it does not take into account that neighboring cells with other levels could be at other times due to the recursive integration procedure. Nevertheless, this particularity should not be problematic because it happens in zones where the gradients are small. An example could be the computation of a droplet: the color function gradients in cells are significant at the interface position and when the refinement criteria are well chosen, the zones at and around the interface are fully refined and then this particularity does not appear.

3.4.2.2 Advancing procedure

For the resolution of model (2.14), the advancing procedure have to take into account three additional points: one is related to the additional physics (here the capillary effects), another for the relaxation step and a last one for non conservative terms. Source terms are absent in the model, thus the corresponding point is avoided. If there were some, they would have been added in the following pseudocode between the point 2 and 3, and under the same formulation than in the pseudocode of Section 3.3.3. Consequently, the pseudocode of the $A(l)$ procedure is:

1. — Hyperbolic resolution —

   for (leaf boundaries s of level l) {
     Compute the hyperbolic fluxes tensor $\overline{\overline{F}}_s^\star = \overline{\overline{F}}_s^\star(\mathbf{U}_L^n, \mathbf{U}_R^n)$ and its corresponding contact discontinuity velocity $\mathbf{u}_s^\star$;
     $\widetilde{\mathbf{F}}_L = \widetilde{\mathbf{F}}_L - l_{diff,L} L_s \left(\overline{\overline{F}}_s^\star + \mathbf{H}_{nc,s}(\mathbf{U}_L^n)\, \mathbf{u}_s^\star \right) \cdot \mathbf{n}_s$;
     $\widetilde{\mathbf{F}}_R = \widetilde{\mathbf{F}}_R + l_{diff,R} L_s \left(\overline{\overline{F}}_s^\star + \mathbf{H}_{nc,s}(\mathbf{U}_R^n)\, \mathbf{u}_s^\star \right) \cdot \mathbf{n}_s$;

}
for (leaf cells i of level l) {
$\mathbf{U}_i^1 = \mathbf{U}_i^n + \frac{\Delta t}{V_i}\widetilde{\mathbf{F}}_i$;
$\widetilde{\mathbf{F}}_i = \mathbf{0}$;
}

2. — Capillary effects resolution —

for (leaf cells i of level l) {
Compute the color function gradients $\mathbf{G}_i = \mathbf{G}_i\left(\mathbf{U}_i^1\right)$;
}
for (leaf boundaries s of level l) {
Compute the capillary fluxes tensor $\overline{\overline{F}}_s^{cap}\left(\mathbf{U}_L^1, \mathbf{U}_R^1, \mathbf{G}_L, \mathbf{G}_R\right)$;
$\widetilde{\mathbf{F}}_L = \widetilde{\mathbf{F}}_L - l_{diff,L} L_s \overline{\overline{F}}_s^{cap} \cdot \mathbf{n}_s$;
$\widetilde{\mathbf{F}}_R = \widetilde{\mathbf{F}}_R + l_{diff,R} L_s \overline{\overline{F}}_s^{cap} \cdot \mathbf{n}_s$;
}
for (leaf cells i of level l) {
$\mathbf{U}_i^2 = \mathbf{U}_i^1 + \frac{\Delta t}{V_i}\widetilde{\mathbf{F}}_i$;
$\widetilde{\mathbf{F}}_i = \mathbf{0}$;
}

3. — Relaxations resolution —

for (leaf cells i of level l) {
Compute the relaxation procedure to obtain $\mathbf{U}_i^{n+1}$ from $\mathbf{U}_i^2$;
}

4. — Averaging of the children for the parent cells —

for (parent cells i of level l) {
for (child cells j of parent cell i) {
$\widetilde{\mathbf{F}}_i = \widetilde{\mathbf{F}}_i + \mathbf{U}_j^{n+1}$;
}
$\widetilde{\mathbf{F}}_i = \widetilde{\mathbf{F}}_i /$ Number of child cells;
Compute the relaxations procedure to obtain $\mathbf{U}_i^{n+1}$ from $\widetilde{\mathbf{F}}_i$;
$\widetilde{\mathbf{F}}_i = \mathbf{0}$;
}

where the hyperbolic fluxes tensor $\overline{\overline{F}}^{\star} = \left(\mathbf{F}_x^{\star}, \mathbf{F}_y^{\star}, \mathbf{F}_z^{\star}\right)$, the non-conservative vector $\mathbf{H}_{nc}$ and the capillary fluxes tensor $\overline{\overline{F}}^{cap} = \left(\mathbf{F}_x^{cap}, \mathbf{F}_y^{cap}, \mathbf{F}_z^{cap}\right)$ are given in a Cartesian expression by:

$$\mathbf{F}_x^\star(\mathbf{U}) = \begin{bmatrix} \alpha_1 u \\ \alpha_1\rho_1 u \\ \alpha_2\rho_2 u \\ \rho u^2 + P \\ \rho uv \\ \rho uw \\ \alpha_1\rho_1 e_1 u \\ \alpha_2\rho_2 e_2 u \\ cu \\ (\rho E + P)\, u \end{bmatrix} \quad \mathbf{F}_y^\star(\mathbf{U}) = \begin{bmatrix} \alpha_1 v \\ \alpha_1\rho_1 v \\ \alpha_2\rho_2 v \\ \rho uv \\ \rho v^2 + P \\ \rho vw \\ \alpha_1\rho_1 e_1 v \\ \alpha_2\rho_2 e_2 v \\ cv \\ (\rho E + P)\, v \end{bmatrix} \quad \mathbf{F}_z^\star(\mathbf{U}) = \begin{bmatrix} \alpha_1 w \\ \alpha_1\rho_1 w \\ \alpha_2\rho_2 w \\ \rho uw \\ \rho vw \\ \rho w^2 + P \\ \alpha_1\rho_1 e_1 w \\ \alpha_2\rho_2 e_2 w \\ cw \\ (\rho E + P)\, w \end{bmatrix}$$

$$\mathbf{F}_x^{cap}(\mathbf{U}) = \begin{bmatrix} 0 \\ 0 \\ 0 \\ \Omega_{11} \\ \Omega_{12} \\ \Omega_{13} \\ 0 \\ 0 \\ 0 \\ \varepsilon_\sigma u + \Omega_{11} u + \Omega_{12} v + \Omega_{13} w \end{bmatrix} \quad \mathbf{F}_y^{cap}(\mathbf{U}) = \begin{bmatrix} 0 \\ 0 \\ 0 \\ \Omega_{21} \\ \Omega_{22} \\ \Omega_{23} \\ 0 \\ 0 \\ 0 \\ \varepsilon_\sigma u + \Omega_{21} u + \Omega_{22} v + \Omega_{23} w \end{bmatrix}$$

$$\mathbf{F}_z^{cap}(\mathbf{U}) = \begin{bmatrix} 0 \\ 0 \\ 0 \\ \Omega_{31} \\ \Omega_{32} \\ \Omega_{33} \\ 0 \\ 0 \\ 0 \\ \varepsilon_\sigma u + \Omega_{31} u + \Omega_{32} v + \Omega_{33} w \end{bmatrix}$$

$$\mathbf{H}_{nc} = \begin{bmatrix} -\alpha_1 \\ 0 \\ 0 \\ 0 \\ 0 \\ 0 \\ \alpha_1 P_1 \\ \alpha_2 P_2 \\ -c \\ 0 \end{bmatrix}$$

3.4.2.3 Relaxation procedure

The relaxation procedure is required two times in the multiphase AMR algorithm, *i.e.*, at the end of each time step (reference to the relaxations resolution in point 3 of the advancing procedure Section 3.4.2.2) and in the unrefinement procedure (see next paragraph). This relaxation procedure is fully detailed in [80] and its aim is to take into account the mechanical equilibrium *via* pressure relaxation and its respective impact on the volume fraction and density of each phase. If pressure relaxation is activated, the mechanical equilibrium model 2.3 is solved using the pressure desequilibrium model (2.14).

When cells are joined (during a refinement) an operation of averaging has to be performed before removing children cells (see point 4 of Section 3.3.4.3). When dealing with a multiphase model as model 2.14, a supplementary relaxation procedure has to be also added. The point 4 of Section 3.3.4.3 is then replaced by the pseudocode:

```
if (l < l_max) {
  for (split cells i of level l) {
      if (ξ < ξ_join & level of each neighboring cells ⩽ l + 1 & children cells non-split) {
        Cell i is unrefined with children averaging and relaxations procedure to
        overwrite the values of cell i;
      }
  }
}
```

3.5 Numerical results

The ability of the new AMR method to solve different multiphase flow applications is proven in 1D, 2D and 3D configrations. Comparisons with theoretical results and non-AMR method are also shown. The results are obtained thanks to an high-order scheme with a MUSCL-Hancock procedure and using the Harten-Lax-van Leer Contact (HLLC) approximate Riemann solver.

In each presented cases, the equation of state (EOS) for the air obeys to the ideal gas law:

$$P_{air} = (\gamma_{air} - 1)\,\rho_{air} e_{air},$$

with $\gamma_{air} = 1.4$.

The water obeys the stiffened gas EOS:

$$P_{water} = (\gamma_{water} - 1)\,\rho_{water} e_{water} - \gamma_{water} P_{\infty,water},$$

where the stiffened gas EOS parameters are $\gamma_{water} = 4.4$ and $P_{\infty,water} = 6.10^8 Pa$.

3.5.1 1D transport test

The goal of the first test is to show the influence of the different criteria of refinement in comparison to a fully refined non-AMR mesh on a 1D transport test case. To avoid any potential complex interaction with a multiphase model, this first test is done for only one phase and then the Euler model is computed. Note that for comparison equivalence, the size of the cells for the non-AMR mesh and for the cells at the highest level (l_{max}) using the AMR method are identical.

Thus, a simple transport of a different density along the axis is done. The fluid is air with a density discontinuity of $\rho_{discontinuity} = 10 kg.m^{-3}$ in a density environment of $\rho_{environment} = 1 kg.m^{-3}$. The velocity of the whole domain is set to $u = 50 m.s^{-1}$, the pressure is uniform and the Neumann boundary condition is used. At the initialization the center of the density discontinuity is set at the coordinate $0.3m$ and has a length of $0.2m$. The simulation time is $t = 8ms$. Only the density is shown since all the other variables remain uniform.

Concerning the AMR method, 4 refinement levels ($l_{max} = 4$) are involved which means that there are 5 levels in total with the initial one. The mesh is initialized with $N = 10$ cells and then the corresponding number of cells with a the full refinement is $N \text{x} 2^{l_{max}} = 160$. The choice of the refinement criteria is one of the most difficult part in an AMR method and it is completely case-dependent. However, the gradient refinement criterion in this first test is obvious and is based on density variation, thus the rest of the different criteria (ϵ, ξ_{split} and ξ_{join}) are tested to observe their impact on the results. The information concerning the AMR data is given in Table 3.3 for 4 different test cases.

Test case	Initial number of cells	l_{max}	Equivalent mesh	ϵ	ξ_{split}	ξ_{join}	Max number of cells involved
AMR 1	10	4	160	0.1	0.5	0.5	50
AMR 2	10	4	160	0.1	0.5	0.1	61
AMR 3	10	4	160	0.1	0.1	0.1	73
AMR 4	10	4	160	1	0.1	0.1	56

Table 3.3: AMR data for the 1D transport test case using the Euler model.

Figure 3.7 shows the results comparison with the different criteria of Table 3.3. The initialization using AMR method is shown in blue and it is identical for each test as the

different criteria only has an influence during the evolution of the discontinuity transport. The non-AMR result is also shown in red but it is partially hidden by the AMR result of the third test (in purple) because this third AMR test gives as good result as the non-AMR one.

On the top image of Figure 3.7, results using three combinations of ξ_{split} and ξ_{join} are compared:

- First, one can observe the difference concerning the shape of the results for the test AMR 1 (yellow), where the previously cited criteria are taken equal to $\xi_{split} = \xi_{join} = 0.5$, and AMR 2 (black), where they have different values $\xi_{split} = 0.5$ and $\xi_{join} = 0.1$. The result with a lower ξ_{join} is closer to the non-AMR one at the head of this heaviside function but at the rear, the results are similar between the two AMR tests and they have a lower density than the non-AMR result. In the two cases the matching with the non-AMR result is better at the head of the discontinuity. One can conclude that the refinement and unrefinement process gives better results in the upwind direction and that having the same value of the criteria yield to better results concerning the symmetrical aspect. In the following tests, to avoid a maximum this non-symmetrical aspect the values of those two criteria are always taken equal. One can also note that the maximum number of cells involved is higher in the second test case than in the first one (see Table 3.3) because the joining criteria is smaller in the second test and then the joining occurs less often.

- Second, in the case where the two criteria are taken with a lower value ($\xi_{split} = \xi_{join} = 0.1$), the result (AMR 3 test case in purple) is in better agreement with the one of the non-AMR method, not only at the head of the discontinuity but also at the rear. In fact, the values of these criteria indirectly give the number of refined cells around a detected discontinuity (detected through the gradient criterion limited value ϵ). More the values of ξ_{split} and ξ_{join} are small, more the number of refined cells around the discontinuity is important. Note that the number of fictive time iteration for the diffusion equation (3.6) of ξ also indirectly control the number of refined cells around the discontinuity. 4 iterations are involved in the presented tests.

The results on the bottom image of Figure 3.7 shows the importance of the gradient criterion limited value ϵ with the comparison between tests AMR 3 (purple) and 4 (green) where $\epsilon = 0.1$ and $\epsilon = 1$, respectively. Lower is the value of the criterion, closer to the non-AMR method is the result. However, as shown in Table 3.3 with the maximum number of cells involved, it is important to notice that this value has to be well chosen, not only to be close to the equivalent solution, but also not to be a value where all the mesh is refined, or in that case the AMR principal advantage is lost. Furthermore, this criterion compares the normalized variation of the chosen physical variable, here density, with the value of ϵ (Equation (3.5)). And because it is normalized with the minimum density of the cell where the calculation is done or of its neighboring cells, plus because the absolute numerical diffusion is the same on the two sides of the discontinuity, the normalized variation is higher on the side of the smaller density and then this side is more refined. Thus, the head of the heaviside discontinuity moves in a refined mesh containing

more cells at the highest level than in its rear and it explains the non-symmetrical aspect that is clearly observable for high values of ϵ.

The variation of the initial number of cells and number of levels for a constant equivalent non-AMR mesh is not shown here because it yields to close results, even if the total number of cells involved are different. Then, having the lower initial number of cells with the higher number of refinement levels seems the best option since the results are similar but the computational time should be lower. "Should be" because of the balance between the computational time lost in the recursive integration and refinement procedures with a high number of levels and the gain between the computation of two different initial meshes. Moreover, using high order methods reduce the number of cells involved in the calculation due to the stiffer discontinuities. This last point partially counterbalances the additional computational time involved by these high order methods.

In the following, the impact of the criteria is no more shown but it is important to keep in mind that the choice of those ones is crucial to obtain as good results as expected and to not involved to much cells in the computation. Thus, a set of chosen criteria that is one good balanced possible solution between computational time involved and quality of the results is proposed for each test.

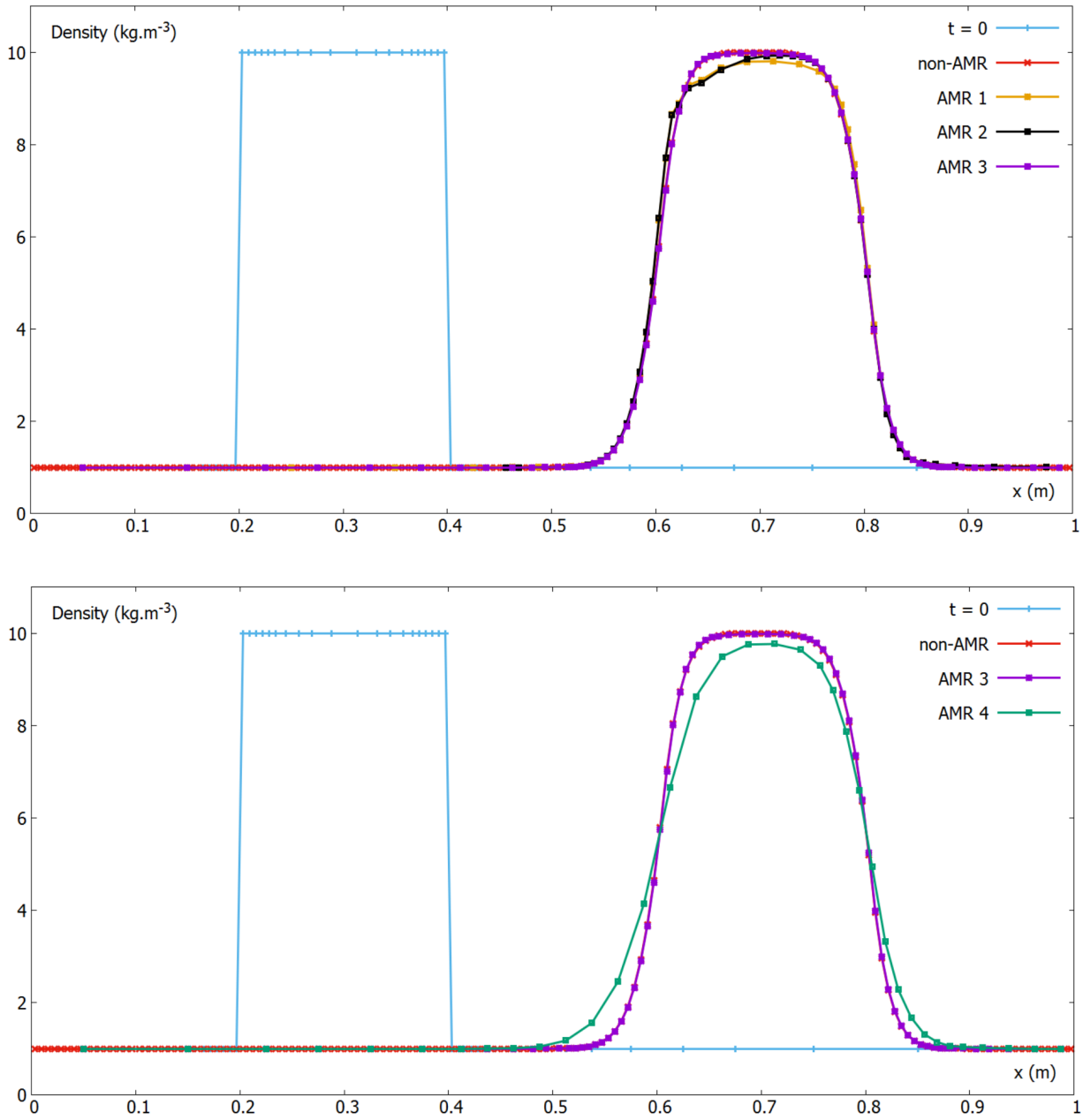

Figure 3.7: Density ρ along the x-direction for the 1D transport test case using the Euler model. Initialization setup (blue) is shown using the AMR method and results are given for different tests: non-AMR (red) and four AMR (yellow, black, purple and green) with different AMR criteria.

3.5.2 Liquid/gas shock tube

The shock tube test for multiphase flow is the flow creates by the initial contact of a high and a low pressurization chamber. The high pressure chamber is filled with water at the pressure $P = 1.10^9 Pa$ and with a density of $\rho = 1,000 kg.m^{-3}$. In the low pressure chamber, there is air with a pressure of $P = 1.10^5 Pa$ and a density of $\rho = 50 kg.m^{-3}$. In both chambers the fluid velocity is $u = 0 m.s^{-1}$. The length of the tube is $1m$ and the initial discontinuity is located at $0.7m$ with high pressure chamber on the left and low pressure one on the right. The simulation time is $t_{final} = 241 \mu s$.

As previously explained, there is no predefined obvious refinement criteria to use, it is case-dependent. Specially, which thermodynamic variables variations to look at to compute the gradient refinement criterion. In the shock tube test, because of the physics involved, the mixture density and mixture pressure variations are chosen. The other information concerning the AMR data is given in Table 3.4 where the equivalent mesh indicates the number of cells of a fully refined mesh and thus indicates the number of cells of the non-AMR method it is compared with.

Initial number of cells	l_{max}	Equivalent mesh	ϵ	ξ_{split}	ξ_{join}	Max number of cells involved
10	8	2,560	0.1	0.1	0.1	210

Table 3.4: AMR data for the 1D shock tube test case.

Figure 3.9 shows the exact solution (black line) and the simulation solutions for the non-AMR mesh (top image, red line) and for the AMR mesh (bottom image, blue crosses and line). A shock is propagated from the left to the right, following by the contact discontinuity and the expansion waves are propagated in the opposite direction. In that case, the non-AMR mesh has $2,560$ cells while the AMR mesh starts with 10 cells and has $l_{max} = 8$. The maximum number of cells involved using the AMR method is indicated in Table 3.4 and it is of 210 cells which is significantly different from the non-AMR number of cells. This high number of points for the non-AMR method explains why its result is only shown with a line while for the AMR method, each point corresponds to each cell where calculations occur.

Globally the simulation results between the two methods are very close but there are still few things to notice:

- First, with the AMR method, the shock wave and the contact discontinuity are always as well reproduced as the non-AMR one. In fact, the gradient criteria are easily respected at these locations and then the mesh is fully refined.

- Second, concerning the expansion waves. Even if the result is still satisfactory, one can observe that the number of cells at the head of the expansion waves (left part of the expansion waves in the images) decreases. This point is clearly observable in Figure 3.8 where the levels of refinement distribution is shown, in purple is the initial distribution and in blue is the distribution for the end of the simulation corresponding to the results shown in Figure 3.9. Initially, the mesh is only fully refined around the

discontinuity (located at $0.7m$) and at the end of the simulation, the mesh is fully refined around the shock, the contact discontinuity and the tail of the expansion waves (right part of the expansion waves in the images). In fact, due to the smooth variation of the thermodynamics variables, it is difficult to find a good criterion to refined the expansion waves without refining most of the domain. Here is only fully refined the tail of the expansion waves because of the normalized variations which is sufficient at this location but not for the rest of the expansion waves.

A supplementary table (Table 3.5) is presented to point out the ability of the AMR method to bring a real gain in comparison to the non-AMR method concerning the computational time (a CPU time ratio of 26 is reached) and the memory involved, even in 1D simulation. Note that the recorded memory involved is only the highest memory used during the simulation for the AMR method, this one evolves during the simulation in function of the mesh distribution.

			Based on AMR	
Mesh	Computational time	Memory (highest involved for AMR)	Computational time factor	Memory factor
non-AMR	26s	6.0Mo	26.0	2.61
AMR	1s	2.3Mo	1	1

Table 3.5: Performances for the different tests for the 1D shock tube test case.

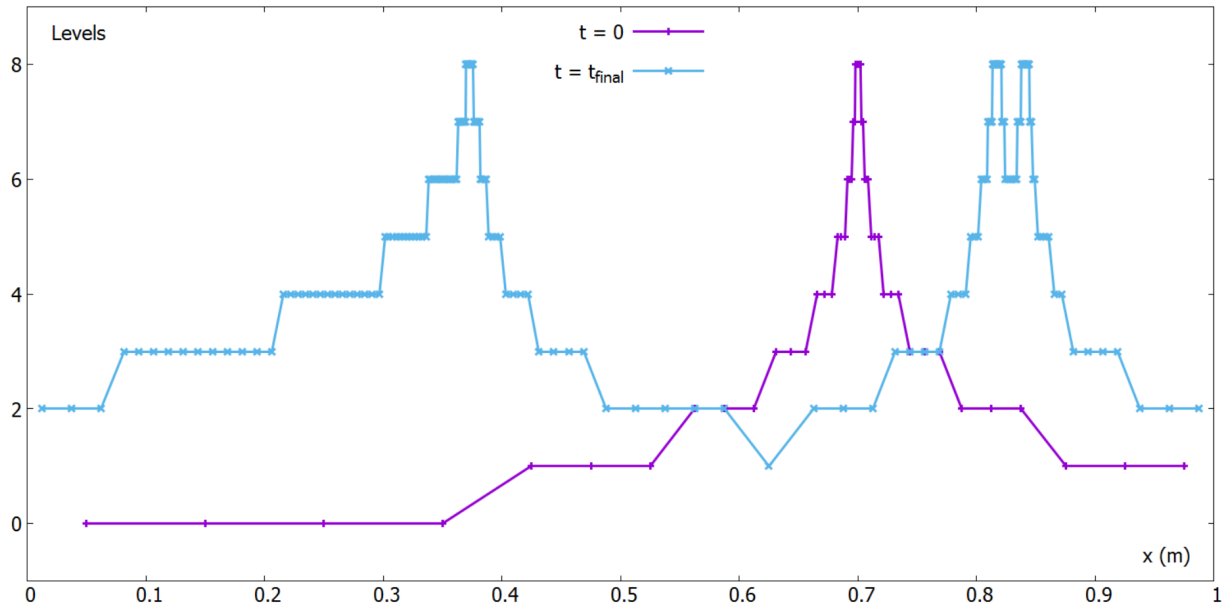

Figure 3.8: Levels of refinement distribution along the x-direction for the 1D shock tube test case using the AMR method. Initialization (purple crosses) and final result (blue diagonal crosses) are shown. Each cross correspond to a cell where the physical calculations occur.

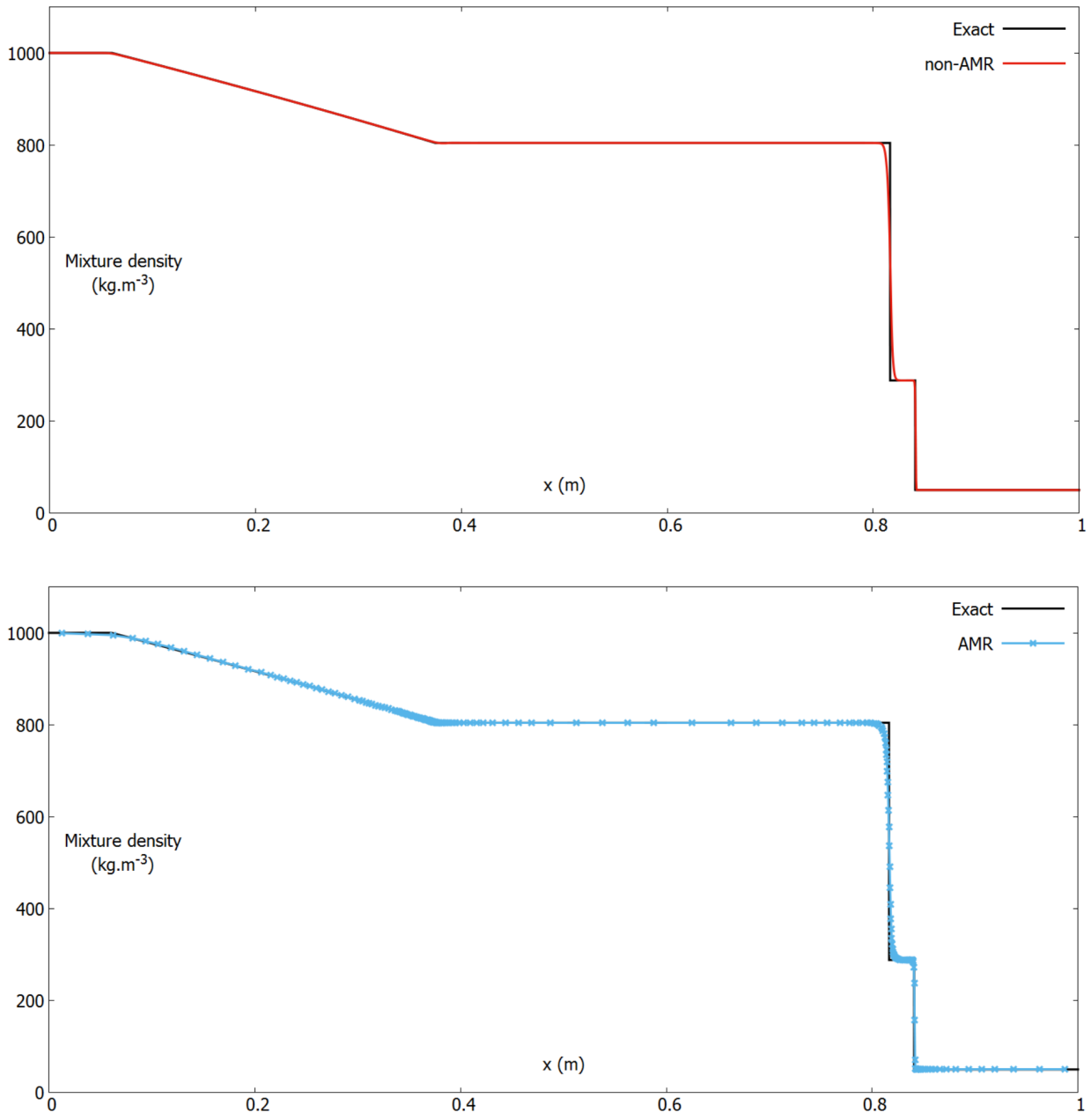

Figure 3.9: Density ρ along the x-direction for the 1D shock tube test case. Exact solution (black line) is shown and results are given for different tests: non-AMR (top image, red line) and AMR (bottom image, blue crosses and line).

3.5.3 2D transport test

A 2D transport test is done here by solving the advection problem of a square of water ($\rho_{water} = 1,000 kg.m^{-3}$) in air ($\rho_{air} = 1 kg.m^{-3}$). The dimension of the domain is $1m$ x $1m$ and at the initialization the center of the square of water is set at the coordinates $0.3m$ on x and y, and its side length is $0.2m$. The velocity of the whole domain is set to $u = 50m.s^{-1}$ in the x-direction and $v = 50m.s^{-1}$ in the y-direction, the pressure P is uniform and the Neumann boundary condition is used at each boundary. The simulation time is $t = 8ms$. The left image in Figure 3.10 shows the initial state with the AMR mesh (in blue the water and white the air).

Concerning the AMR data, the gradient refinement criterion ϵ can be based on two variables variations: the mixture density and the volume fraction. But, only one is useful since they have a similar shape, then arbitrarily the volume fraction is chosen. The initial mesh is of $N^2 = 10$x10 cells and the maximum number of refinement level is $l_{max} = 4$, then the equivalent fully refined mesh for this test case is of $\left(N^{l_{max}}\right)^2 = 25,600$ cells. l_{max} is not taken as high as in the 1D case ($l_{max} = 8$) due to the induced computational time, specially for the comparison with the non-AMR method (it would have been $6,553,600$ cells). As previously said, the values of the different criteria are case-dependent and due to the 2D accentuate diffusion, the criteria are chosen lower than the ones of the 1D tests, *i.e.*, $\epsilon = 0.08$, $\xi_{split} = 0.05$ and $\xi_{join} = 0.05$. All the information for the AMR data are summarize in Table 3.6.

Initial number of cells	l_{max}	Equivalent mesh	ϵ	ξ_{split}	ξ_{join}	Max number of cells involved
10x10	4	25,600	0.08	0.05	0.05	3,040

Table 3.6: AMR data for the 2D transport test case.

On the right of Figure 3.10 is shown the 2D result of the simulation with the AMR mesh. One can observe that the square of water is well transported: the centre of gravity is at the correct position and the shape is well preserved. Figure 3.11 shows the mixture density ρ along the diagonal direction ($x = y$) for the initialization state (purple crosses) using the AMR method and for the simulation results using the non-AMR method (red diagonal crosses) and the AMR one (blue stars). It then shows that the AMR method gives almost identical results than the non-AMR one for the 2D transport test case. Note that only the mixture density is shown since all the other variables remain uniform and because the volume fraction has a similar shape than the mixture density.

Even if the number of levels are lower that in the 1D shock tube test case, the performances concerning the computational time and the memory involved are always good for the AMR method in comparison to the non-AMR one (Figure 3.7). A gain of almost 14 times is obtain for the computational time, which is a bit lower than the previous test case, but the memory factor is higher and it is about 5. The conclusion is that, even if the presented AMR method is not optimized concerning the memory involved, a good factor compared to non-AMR method is obtained. Moreover, if the number of refinement levels is increased, the computational time and the memory involved drastically increase for the

non-AMR method while it is not the case for the AMR one. Indeed, the ratio of computational cells between the AMR and non-AMR methods decreases. Specially adding the fact that the interface is sharper than in the presented case and then a smaller domain of cells at the highest level is computed. In conclusion, even higher performances are expected for the AMR method.

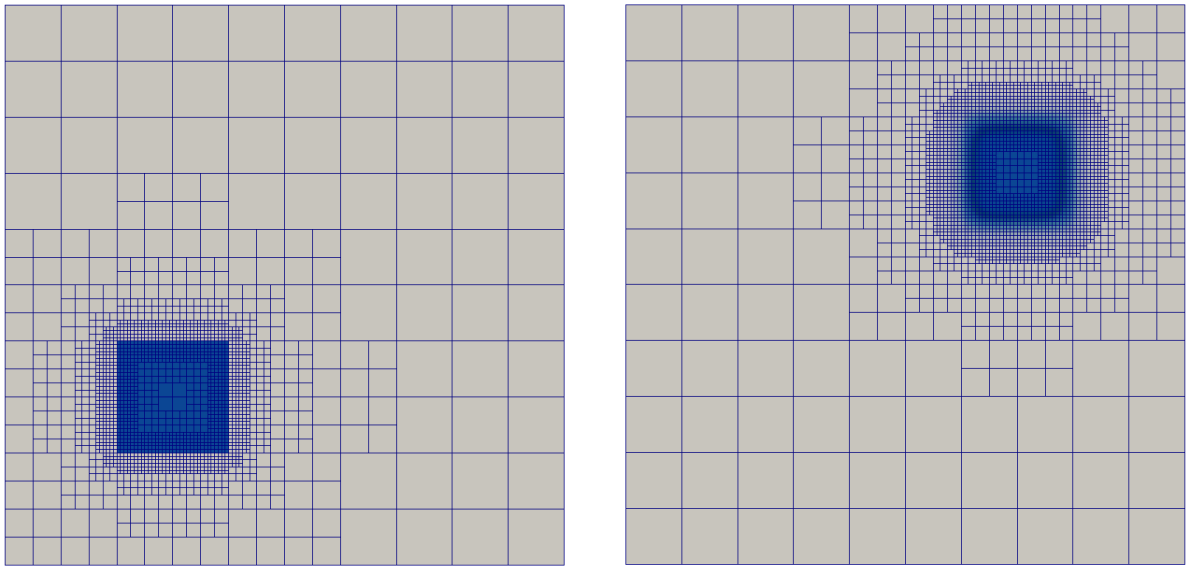

Figure 3.10: Volume fraction of water α_{water} for the 2D transport test case. In blue the water and white the air. On the left, initialization state, and on the right, the correctly transported result.

			Based on AMR	
Mesh	Computational time	Memory (highest involved for AMR)	Computational time factor	Memory factor
non-AMR (160x160 cells)	36m 49s	57.3Mo	13.636	5.209
AMR	2m 42s	11.0Mo	1	1

Table 3.7: Performances for the different meshes for the 2D transport test case.

3.5.4 3D capillary effects test: Laplace jump

In the following 3D simulation test, a droplet of water is placed in an air environment. When the droplet is at the steady state, the Laplace pressure jump must be recovered thanks to the capillary effects. The expression of the theoretical pressure jump for a sphere is:

$$[P] = \frac{2\sigma}{R},$$

where $[P]$ expresses the pressure jump between inside the droplet and the air, here $P_{water} - P_{air}$.

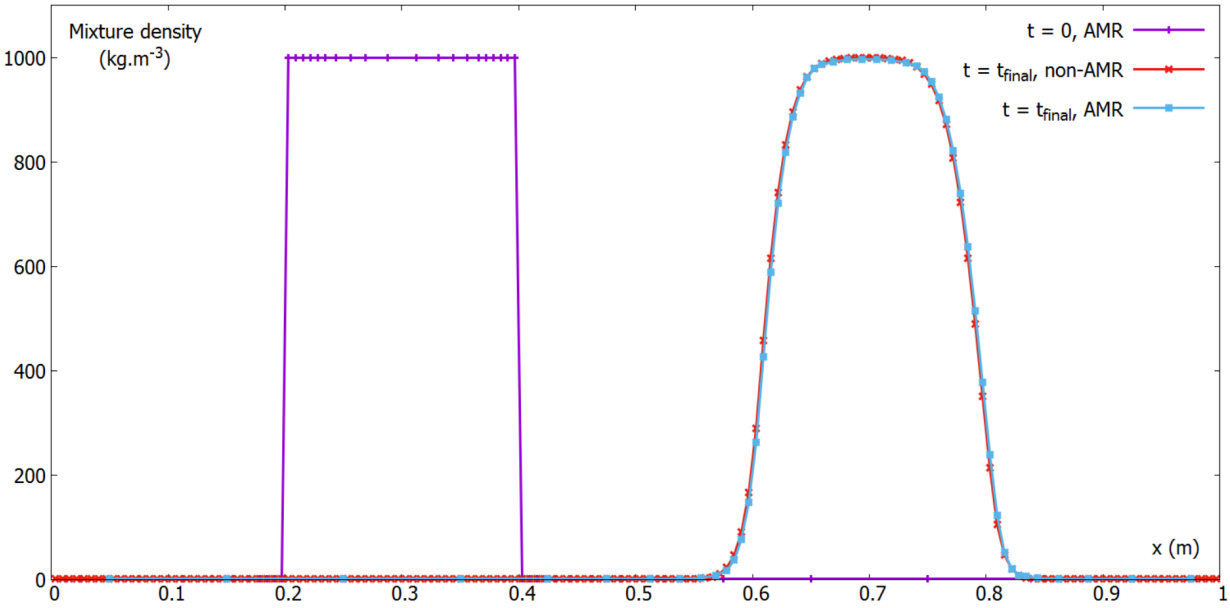

Figure 3.11: Mixture density ρ along the diagonal direction ($x = y$) for the 2D transport test case. Initialization (purple crosses) and simulation results for the thin mesh (red diagonal crosses) and the AMR mesh (blue stars) are shown.

For the simulation, initially the droplet of water is on a 3D domain filled with air. To accentuate the impact of the surface tension force, the stiffened gas EOS for the water with parameters $\gamma_{water} = 2.1$ and $P_{\infty,water} = 1.10^6 Pa$ is used, the size of the droplet is emphasized (radius of $0.15m$) as the surface tension coefficient $\sigma = 800N.m^{-1}$. At the initialization the pressure is the same in each fluid and is equal to $P = 1.10^5 Pa$, the velocity is null ($\mathbf{u} = \mathbf{0}m.s^{-1}$), the densities are $\rho_{air} = 1kg.m^{-3}$ in the air and $\rho_{water} = 1,000kg.m^{-3}$ in the water, and the outgoing pressure waves boundary condition is used. The volume of the whole domain is $0.75m$ x $0.75m$ x $0.75m$ and at the initialization the droplet is set at the center (see Figure 3.12). The simulation time to obtain a converged result is $t = 0.59s$.

The information concerning the AMR data is given in Table 3.8. To correctly treat the capillary effects, only the thickness and the curvature of the interface are important. Thus, the gradient refinement criterion is only based on volume fraction variation. Moremover, as explained for the previous test case, the diffusion is accentuated when dealing with higher dimensions and it directly impact the smoothing of the ξ variable. Thus, the ξ criteria are taking lower than the 2D case, *i.e.*, $\xi_{split} = 0.02$ and $\xi_{join} = 0.02$.

For this test, only the AMR method was computed due to the too long computation of a non-AMR method in 3D. As shown in Table 3.8, the number of cells that involves a non-AMR calculation is of $4,096,000$ cells while the AMR one only involves a maximum of $267,224$ cells, and this last one already took more than 16 days (on one CPU: Intel® Xeon® CPU E7-4850 v2). Moreover, even if it is not shown here, waves induced by the computation of the capillary effects are coming from the interface locations at the beginning of the simulation. Those ones slowly decrease and disappear while reaching the steady state. In the case of the AMR method, the waves are smooth in- and out-side the droplet

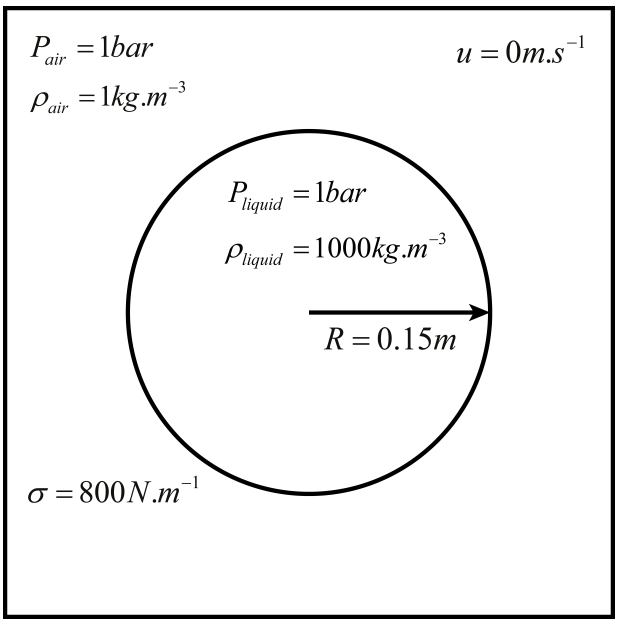

Figure 3.12: 2D sketch of the initial conditions for the 3D simulation of a liquid droplet placed in air.

because of the coarser mesh and thus less oscillations occur than with the fully non-AMR mesh. It results that the AMR method accelerate the convergence of the simulation to a steady state in comparison to non-AMR method.

Initial number of cells	l_{max}	Equivalent mesh	ϵ	ξ_{split}	ξ_{join}	Max number of cells involved	Computational time
20x20x20	3	4,096,000	0.1	0.02	0.02	267,224	16d 21h 53m

Table 3.8: AMR data for the 3D capillary effects test case.

The theoretical pressure jump of Laplace for this test case is $[P] = 10720Pa$ and it is well recovered in the 3D simulation when using the AMR method as shown in Figures 3.13 and 3.14.

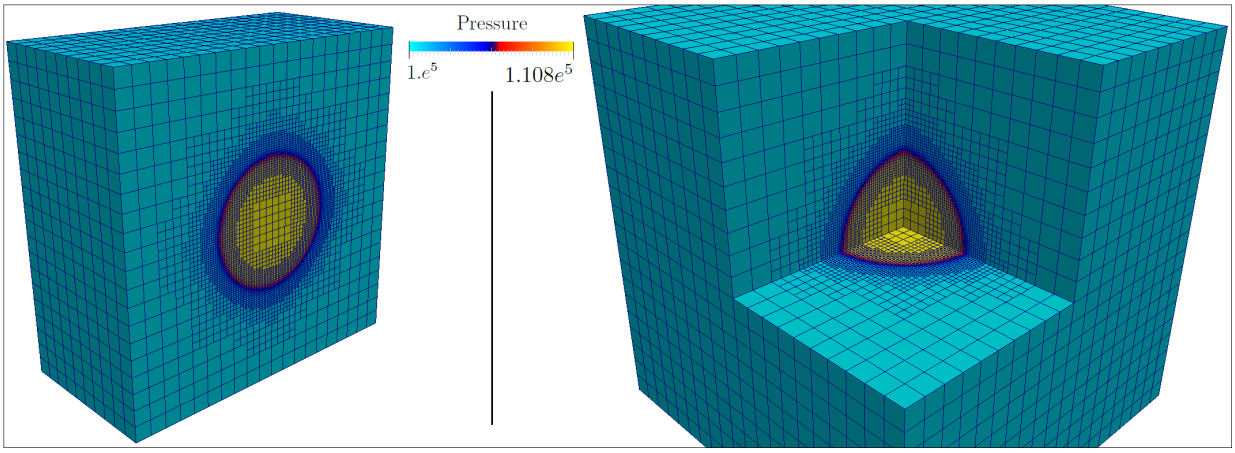

Figure 3.13: Two different cut views of the the 3D capillary effects test case. Pressure P is shown for the converged state.

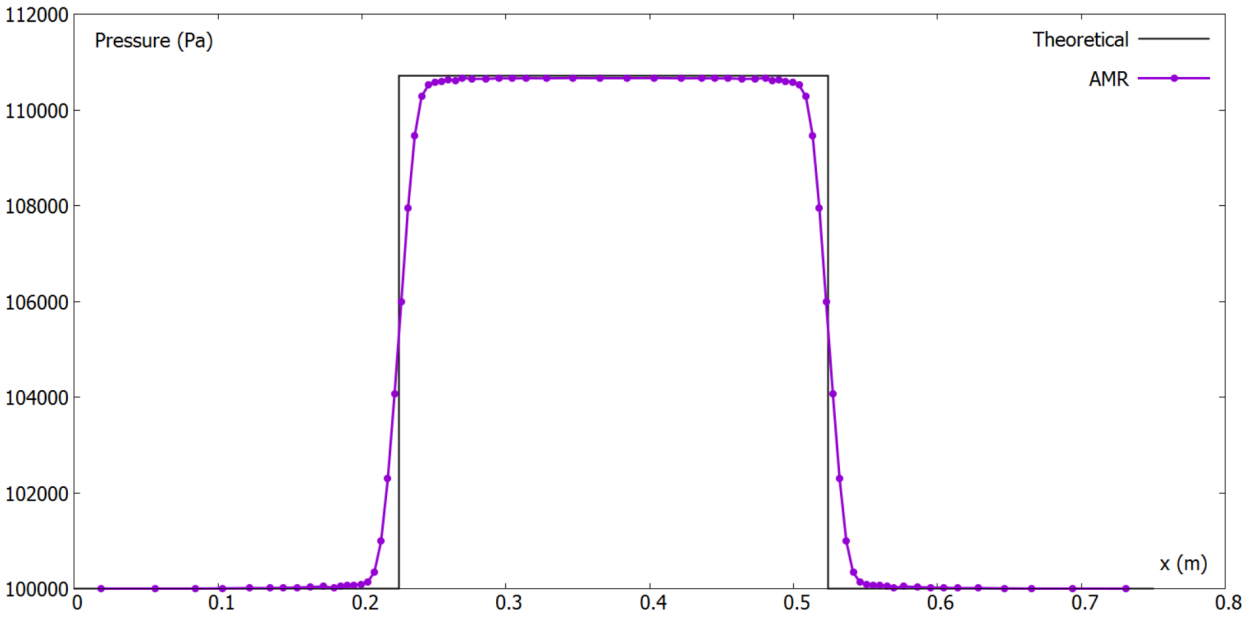

Figure 3.14: Pressure P at the converged state for the 3D capillary effects test case. Theoretical (black line) and simulation results (purple points) are shown. The converged time is $t = 0.59s$.

3.6 Summary

A new adaptive mesh refinement (AMR) method using cells boundaries trees has been presented with an extension for multiphase flows. The addition of this second tree boundaries structure presents the advantages to reduce the number of operations during the time step integration (cell neighboring searching is improved) and to simplify the general algorithm in comparison to a fully threaded tree method. The drawback is that the memory involved is not optimized. It is reasonably increased since the number of additional information stored for each cell boundary is relatively small in comparison to what is needed in a cell for the AMR structure as well as for the physical quantities.

The application of the new AMR method on different tests - transport, shock tube and capillary flow in 1D, 2D and 3D - was performed with quantitative comparisons regarding exact solutions or non-AMR method results in order to analyze the benefit of this new method. Computational time efficiency and reasonably memory cost have been shown.

A complete study on shock-droplet interaction using the presented model and methods, with the goal to obtain droplets of reduced sizes on longer simulation time, is then the purpose of the following chapter.

Chapitre 4

L'atomisation d'une goutte isolée dans un écoulement à grande vitesse

Atomization of an isolated droplet by a high speed flow

4.1 Introduction

Only at the beginning of the century, direct numerical simulation (DNS) has emerged as a valuable tool capable of studying aerobreakup. Unfortunately, due to the high computational costs of fully three-dimensional simulations, aerodynamic numerical studies were often performed in two dimensions (Chen [11], Igra and Takayama [36, 38, 39]) or with the axi-symmetry approximations (Aalburg et al. [1], Han and Tryggvason [28], Wadhwa et al. [95]). In addition, fluid density ratios are often assumed to be small, or fluids are considered incompressible (Aalburg et al. [1], Han and Tryggvason [28], Jalaal and Mehravaran [41], Quan and Schmidt [73]). Subsequently, the studies were focused on the early instants of aerobreakup with low density ratio, when the Richtmyer-Meshkov and/or Rayleigh-Taylor instabilities appeared (Yang et al. [99], Quirk and Karni [74], Layes and Le Metayer [51]. It is only recently that an in-depth study was carried out by Meng and Colonius [59, 58] for fluids with a high density ratio and for two-dimensional and three-dimensional direct numerical simulations. They have thus begun to fill a gap in the phenomenological description and the identification of the processes involved during the first moments of the breakup. However, a dimensional analysis was presented in the introduction of the present thesis (Chapter 1) on the Weber (We = inertial forces/capillary forces) and the Reynolds (Re = inertial forces/viscous forces) numbers. It is stated that for water droplet atomization in an air environment, Weber and Reynolds numbers decrease along the breakup. This behavior is mainly due to the characteristic length of the different parts of the broken droplet and due to the velocity of the airstream at the vicinity of these different parts. Those numbers tend to $We \approx 1$ and $Re \approx 10$ for the smallest droplets but neither capillary nor viscous effects have been taken into account in the work of Meng and Colonius. This point constitutes a first barrier to the study of longer times, where these effects become significant and the formation of new droplets appears. Because viscous effects seems to have less influence than the surface tension ones, viscosity has been neglected in the present work and the impact of taking capillary effects into account over long periods of time will be presented in this chapter. A second barrier intervenes and always corresponds to the computational cost to obtain a sufficient spatial resolution in order to observe finely the physics taking place on these long times. These costs are too high if the use of an appropriate numerical method is not undertaken.

Thus, the goal that was fixed for this thesis was to find a good model and a good numerical method to treat the droplet atomization as far as possible in time. A study on the physical mechanisms of the complete atomization is now done and presented for few test cases. The following is then organized in different parts where first is presented the impact of the slope limiter to stiff the interface when coupling with surface tension. Second, the two-dimensional results on a water column are presented for different refinement criteria. The symmetry condition and the capillary effects influence on the simulations is shown. A comparison with experimental results and a complete analysis of the flow structure is also given. Third, the three-dimensional results are shown for the droplet atomization computation.

4.2 Slope limiters impact

When computing the atomization of an isolated droplet by a high speed flow with diffuse numerical method, one problem is that the diffusive aspect can be predominant and thus the reduced size droplets from the atomization could be difficult to capture. The two principal ways to reduce the impact of the numerical diffusion are:

- First, increase the mesh refinement. But another problem appears and is the induced computational time, even with an adaptive mesh refinement method. So, the mesh refinement with the AMR method has to be performed in a way to avoid too much computational time but to still refine the interface and capture the different physical processes. This point was discuss in the previous chapter.

- Second, use high order numerical method. But, for this one, the problem is the numerical stability when coupling with capillary effects. For stability purposes, in the previous test cases, the second order in space and time method named MUSCL-Hancock was used with the Minmod limiter. Choosing another slope limiter is an easy and efficient way to decrease the numerical diffusion, but as said before the stability would be put in default, even with a TVD limiter. One idea is to use a stiffer limiter but only on the interface variable α and c and to use the Minmod limiter for the others (ρ, $\mathbf{u}$ and P). In that way the interface is stiffened but the stability on the other variables is conserved. This point has to be proved and it is then the purpose of this section.

One can add that another way could be to use interface sharpening methods as the ones of Shyue and Xiao [85], Shyue [84] and Tiwari et al. [92]. Those methods add non-conservative terms in each equation of the system to sharp the interface and it could be a substantial point to limit the numerical diffusion. However, the issues are the non-conservative aspect, especially with long simulations as the atomization of a droplet, and also the non-physical dynamics that it brings in some situations. Then, such methods has to be deeper tested in the future.

To show the impact of a stiffer limiter on a capillary effects test case, the simulation of the circle shape recovering from an initial square one is done. It is initialized with a

square part of liquid ($\gamma_{liquid} = 2.1$ and $P_{\infty,liquid} = 1.10^6 Pa$) on a 2D domain filled with air ($\gamma_{air} = 1.4$). At the initialization the pressure is the same in all the fluids and is equal to $P = 1.10^5 Pa$, the velocity is null ($u = v = 0m.s^{-1}$), the densities are $\rho_{air} = 1kg.m^{-3}$ in the air and $\rho_{liquid} = 1,000kg.m^{-3}$ in the liquid, and the outgoing pressure waves boundary condition is used. The surface of the whole domain is $0.75m$ x $0.75m$ and at the initialization, the liquid square is set at the center of the domain and has a length of $0.2m$.

The information concerning the AMR data is given in Table 4.1. The gradient refinement criterion is based on volume fraction variation.

Initial number of cells	l_{max}	Equivalent mesh	ϵ	ξ_{split}	ξ_{join}
20x20	4	102,400	0.08	0.05	0.05

Table 4.1: AMR data for the 2D capillary effects test cases with the circle shape recovering.

As said before, the stiffer limiters are only applied on the interface variables, so on the volume fraction α and the color function c. Furthermore, it was observed that to improve the results and also for stability reason, the color function c has to be reinitialized at each time step using the volume fraction. Thus, one can ask in this context: why keep this color function instead of directly using the volume fraction? The response is that the color function is always kept and well separated from the volume fraction during each time step in order to preserve the hyperbolicity of the model. Indirectly, the interface, which is taking into account the pressure effects, is thus tracked to compute the capillary effects.

Four slope limiters, plus the Minmod one, have been tested and in all the tests the circle shape is recovered (see examples with the Minmod limiter in Figure 4.1 and with the Superbee limiter in Figure 4.2) as well as the Laplace pressure jump value (see Figures 4.3-4.4). Few oscillations, that are not avoidable with some of them (specially van Albada and Superbee) when using the capillary effects, are observable.

Those results show that the stiffening of the interface is working as expected. Indeed, the 2D column is much more diffuse at the converged state for example when using the Minmod limiter (image f of Figure 4.1) than when using the Superbee one (image f of Figure 4.2). It is even more observable with the 1D pressure profiles along the x-axis (Figures 4.3-4.4) where the number of cells in the interface for each limiter is:

- 22 cells for Minmod,
- 18 cells for van Leer,
- 20 cells for van Albada,
- 12 cells for MC (Monotonized Central),
- 7 cells for Superbee,

The Superbee limiter is clearly the stiffer but this last one has shown some stability issue with appearance of over and undershoots (Figure 4.4). Note that the van Albada limiter has also shown the same issue (Figure 4.3). Meng [58] evoked similar problem with another

capillary model which has similarities with the one presented in Chapter 2, and with a different but stiff high order numerical method (third-order WENO scheme). It is well known that a stiff limiter induces stability problem when applied on every variables, even for an Euler system of equations (Toro [93]). In the current case, the limiter is only applied on the interface variables but the capillary terms induced by this stiffening are directly impacted and then create strong discrepancies which cause this stability issue. Even when using very low CFL number, the stability stays an issue. Thus, the MC limiter is taken for the following due to its ability to stiff the interface and to be reliable with a reasonable CFL number (0.5 and 0.3 in 2D and in 3D, respectively).

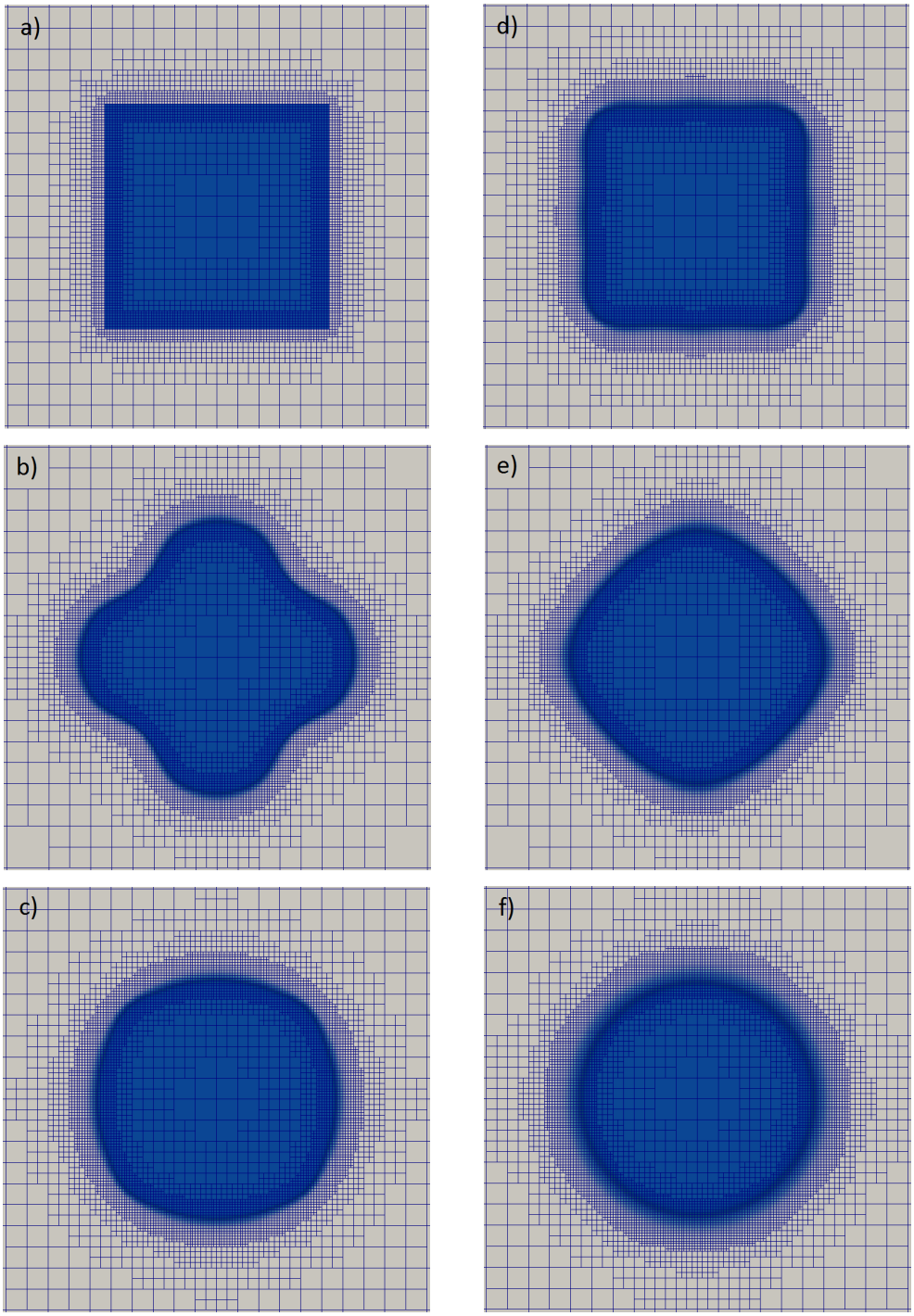

Figure 4.1: Volume fraction of liquid α_{liquid} at different times for the 2D capillary effects test case with the circle shape recovering. Results using the Minmod limiter and for times: a) initialization, b) $0.02s$, c) $0.03s$, d) $0.04s$, e) $0.05s$ and f) $1.1s$ (converged time).

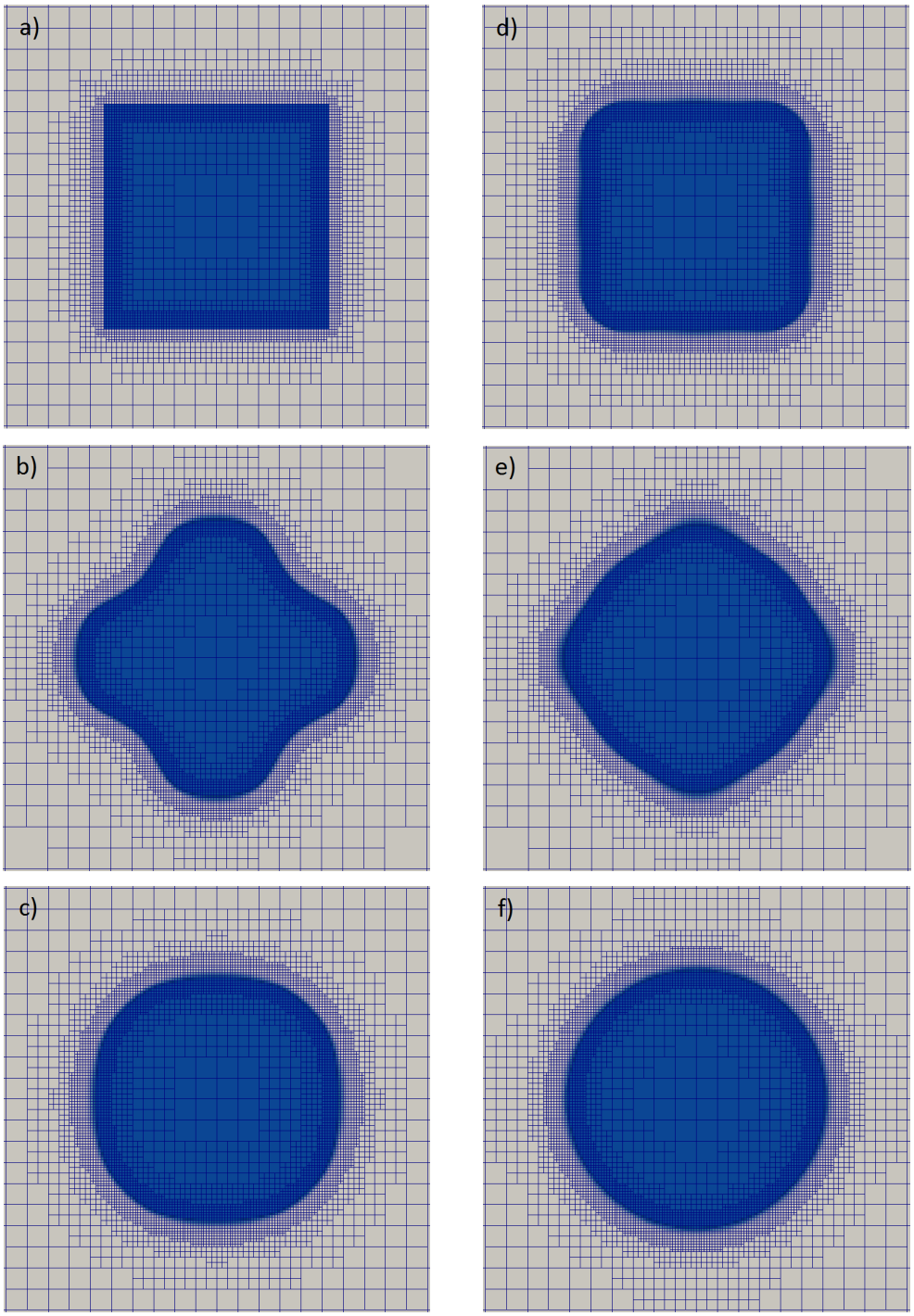

Figure 4.2: Volume fraction of liquid α_{liquid} at different times for the 2D capillary effects test case with the circle shape recovering. Results using the Superbee limiter and for times: a) initialization, b) $0.02s$, c) $0.03s$, d) $0.04s$, e) $0.05s$ and f) $1.1s$ (converged time).

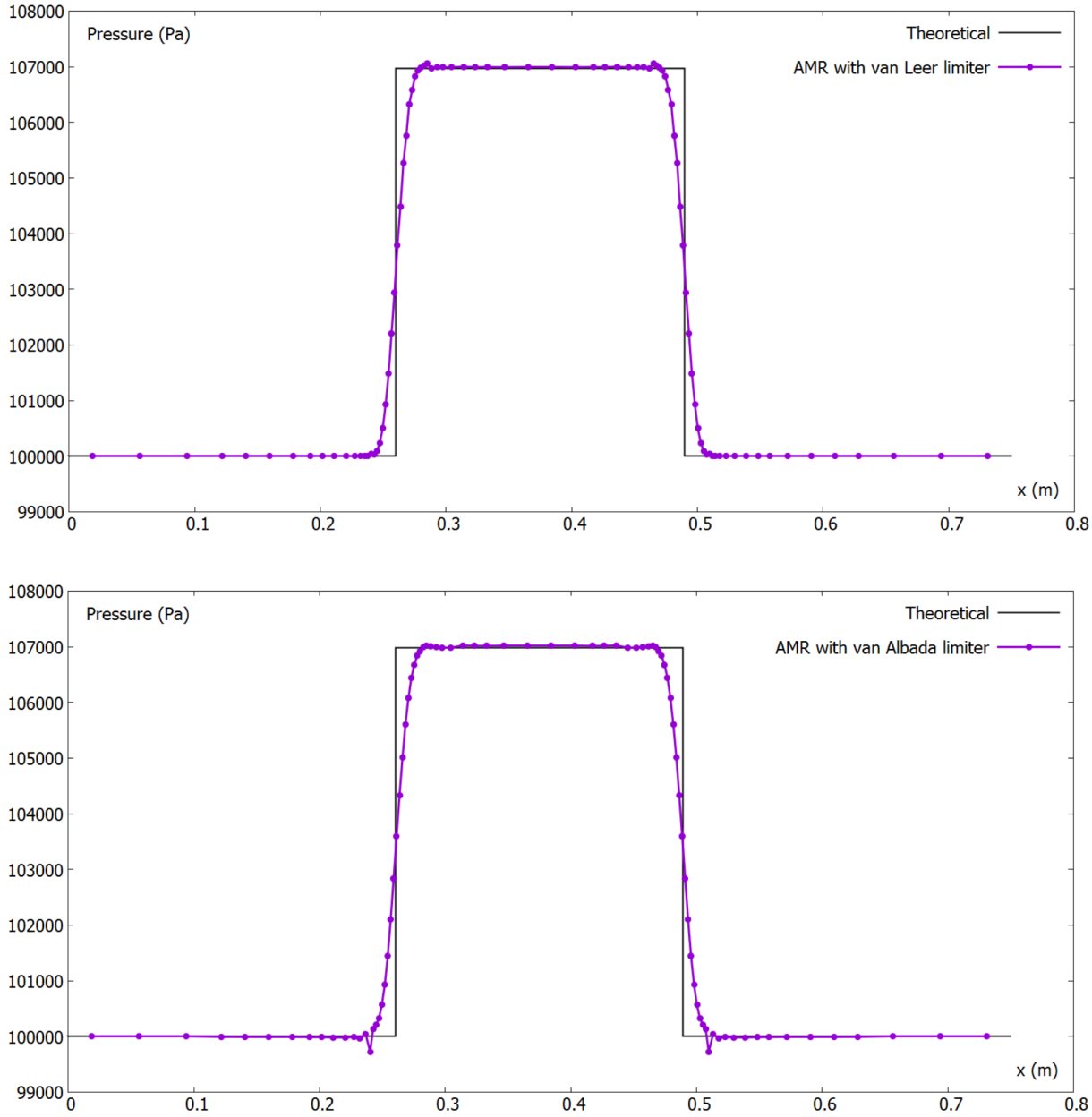

Figure 4.3: Pressure P at the converged state for the second 2D capillary effects test case with the circle shape recovering. Theoretical (black line) and simulations results at, respectively, $1.1s$ and $1.6s$ using the van Leer limiter (top) and the van Albada limiter (bottom).

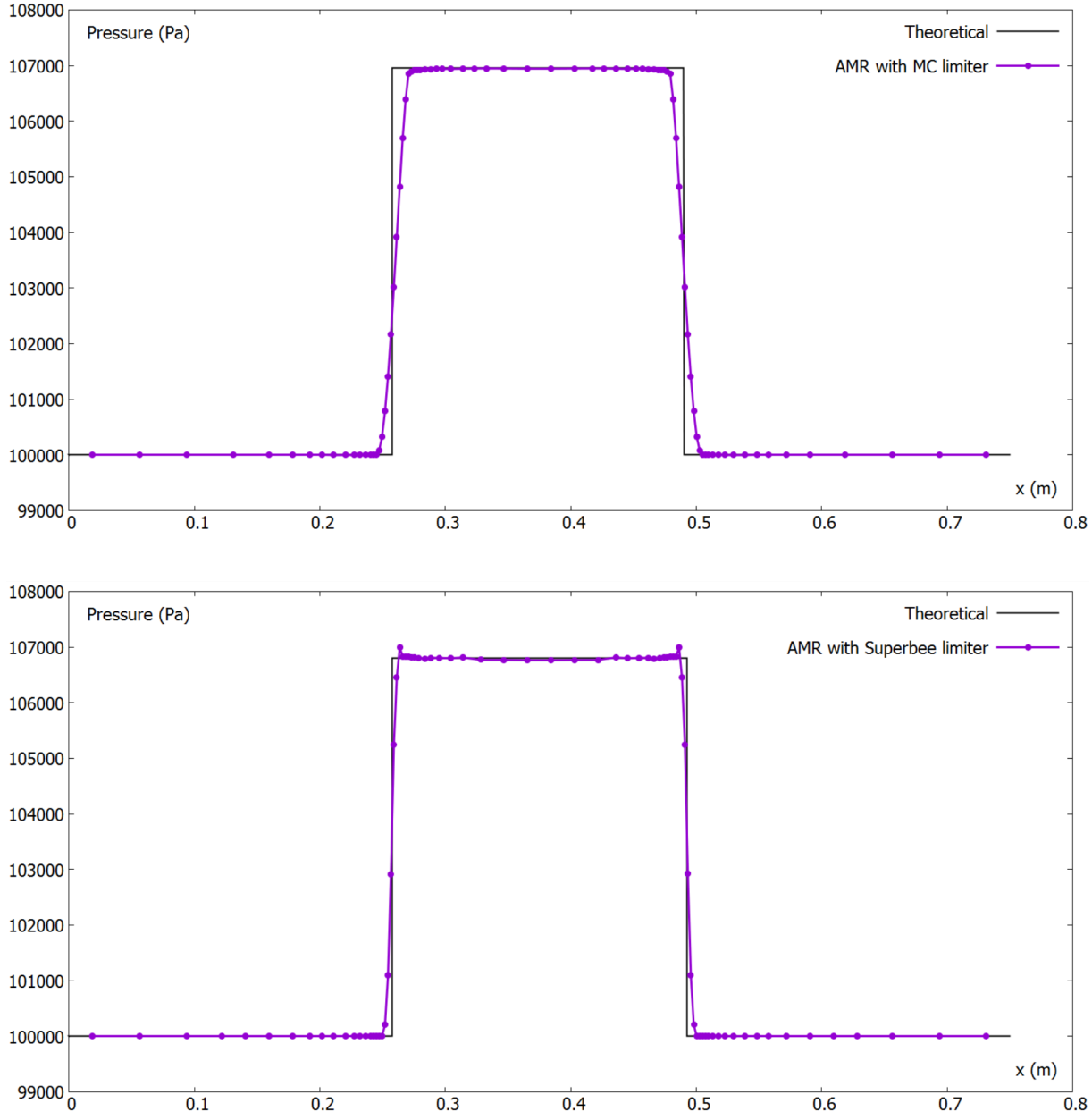

Figure 4.4: Pressure P at the converged state for the second 2D capillary effects test case with the circle shape recovering. Theoretical (black line) and simulations results at, respectively, $1.3s$ and $1.35s$ using the MC limiter (top) and the Superbee limiter (bottom).

4.3 2D: atomization of a cylindrical water column by a high speed flow

4.3.1 Problem presentation

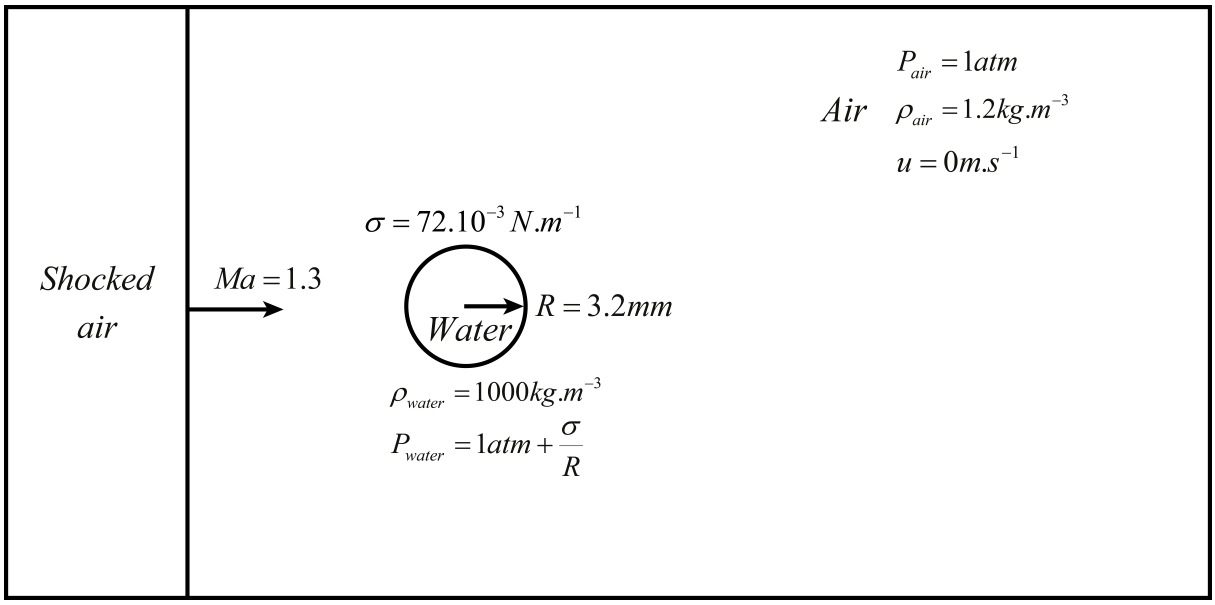

Figure 4.5: Sketch of the initialization for interaction of a shock wave with a water column.

The setup of the 2D simulation of the atomization of a cylindrical water column by a high speed flow is similar to the one that was presented in Chapter 2, the only differences concern the size of the domain and the mesh. The cylindrical water column is placed in an air environment, its initial diameter is $D = 6.4mm$ and it is exposed to a shock wave of Mach number 1.3 in atmospheric air (see Figure 4.5 for initialization sketch). The initial densities are $\rho_{air} = 1.2kg.m^{-3}$ and $\rho_{water} = 1,000kg.m^{-3}$. The corresponding initial Weber number ($We = \rho_{air}u^2D/\sigma$) in these conditions is 3,690. Shocked air is entering at the left and the Newmann boundary conditions is used elsewhere. The 2D computations are performed on an AMR mesh containing initially 1,000x400 cells representing a physical domain of 250mm x 100mm and the maximum number of levels is $l_{max} = 2$, corresponding to an equivalent non-AMR mesh of 4,000x1600 cells. The complete information concerning the AMR data is given in Table 4.2. The gradient refinement criterion is based on volume fraction and mixture pressure variations (mixture density variation shows no results difference when the volume fraction variation is activated).

Initial number of cells	l_{max}	Equivalent mesh	ϵ	ξ_{split}	ξ_{join}
1,000x400	2	6,400,000	0.02	0.05	0.05

Table 4.2: AMR data for the 2D atomization test case.

The goal in the following is to find the better possible parameters to compute the simulation of the atomization. To reach this goal, a few tests are done, in particular on the influence of the AMR parameters, on the symmetry approximation and on the impact of the capillary effects.

4.3.2 Refinement criterion using velocity gradient

The impact of most of the different refinement criteria was previously tested in Chapter 3, thus the optimal parameters seems to be the one listed in Table 4.2, *i.e.*, $\epsilon = 0.02$ for variations based on volume fraction and on mixture pressure, and $\xi_{split} = \xi_{join} = 0.05$.

To evaluate the reliability of the AMR simulations, it is stated as an hypothesis that the AMR simulations should yield to the same results as the non-AMR ones. But, when an AMR simulation with the previously cited parameters is computed and compared with the non-AMR results, a slight divergence of the results occurs. In Figures 4.6 and 4.7 are shown results for two relatively long times ($1,200\mu s$ and $1,400\mu s$) and for comparison between the AMR and the non-AMR methods. In the first approach, the results seem to correspond between the two methods and one might therefore think that they are satisfactory. However, when one observes more precisely, one discovers a slight discrepancy between the two methods. Indeed, the AMR method tends to slightly less stretch the column than the non-AMR method. The most visible effect here is thus the thickness of this column (around 15% difference), which is a center of interest. The problem is that this trend is only increasing for the longest time, which results in a clear divergence (Figure 4.8). Recalling that the aim of this study is to reach these long times in order to observe the formation of reduced size droplets, it is necessary to apply parameters related to the AMR which are the best choice, *i.e.*, parameters that do not alter the solution.

For this reason, the second step is to observe closely the evolution of the column aerobreakup in order to understand the mechanisms involved in the divergence of the results when using the AMR method in comparison to those of the non-AMR one. Figure 4.9 indicates that there are strong pressure variations around the column, particularly between the front of the drop (upstream side of the flow, left in the image) and the rear (downstream side of the flow, right on the image). However, when the variation in pressure is observed on one side separately from the other, this variation is relatively small, indicating that the pressure refinement criterion should be relatively low to refine in these regions where smooth variations appear. Obviously, it is not a good solution because it would involve too much refinement in several regions where highly resolution is not necessary.

Finally, if we observe the evolution of the velocity, always around the column (Figure 4.10), it clearly indicates the existence of strong variations in more localized regions than for the pressure. It is also evident that it is these gradients of velocity at the contours of the column that mainly participates in the stretching of the latter and thus in its aerobreakup (detailed in the section 4.3.6). As a result, it seems necessary to take into account an AMR criterion, not used up to now in the literature, that is related to the variation of velocity.

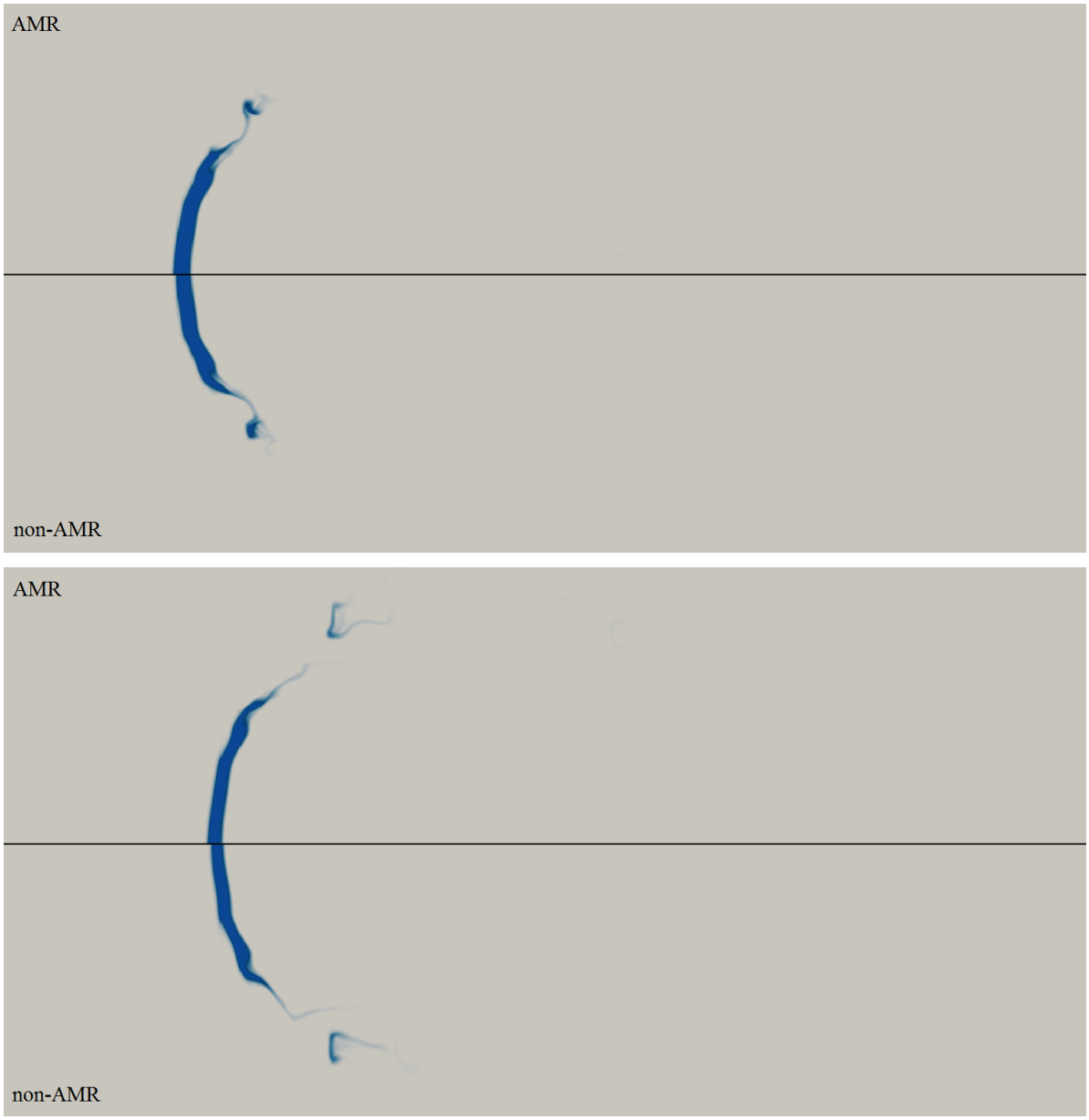

Figure 4.6: Magnified view of the simulation of the atomization of the cylindrical column by the high speed flow behind the shock wave of Mach number 1.3 in atmospheric air propagating from the left to the right. 2D simulations respectively with (upper half) and without (lower half) the AMR method (using the volume fraction and mixture pressure variations). Results are shown at times $1,200\mu s$ (top) and $1,400\mu s$ (bottom) with volume fraction visualization.

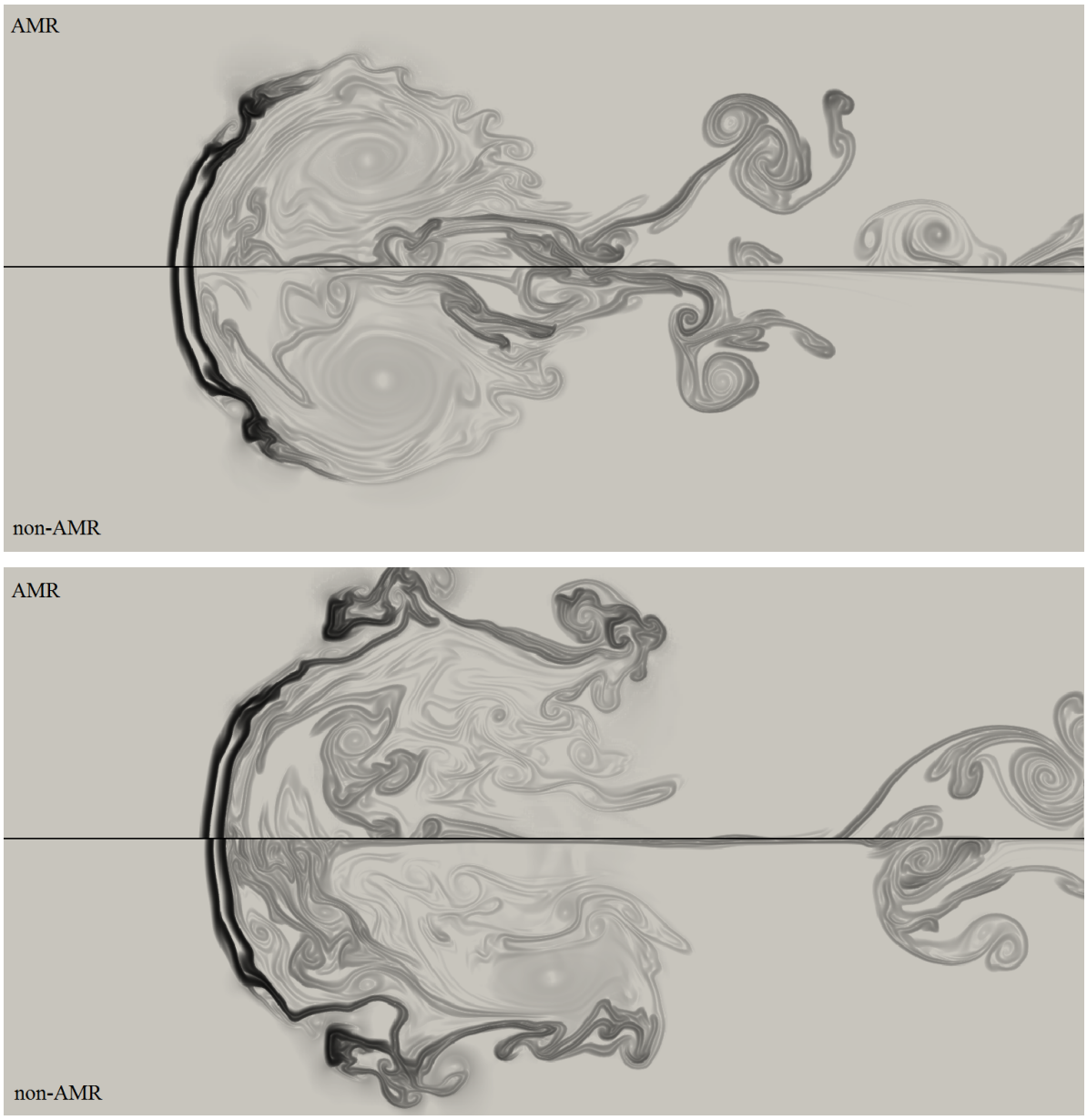

Figure 4.7: Magnified view of the simulation of the atomization of the cylindrical column by the high speed flow behind the shock wave of Mach number 1.3 in atmospheric air propagating from the left to the right. 2D simulations respectively with (upper half) and without (lower half) the AMR method (using the volume fraction and mixture pressure variations). Results are shown at times $1,200\mu s$ (top) and $1,400\mu s$ (bottom) with schlieren visualization of the mixture density.

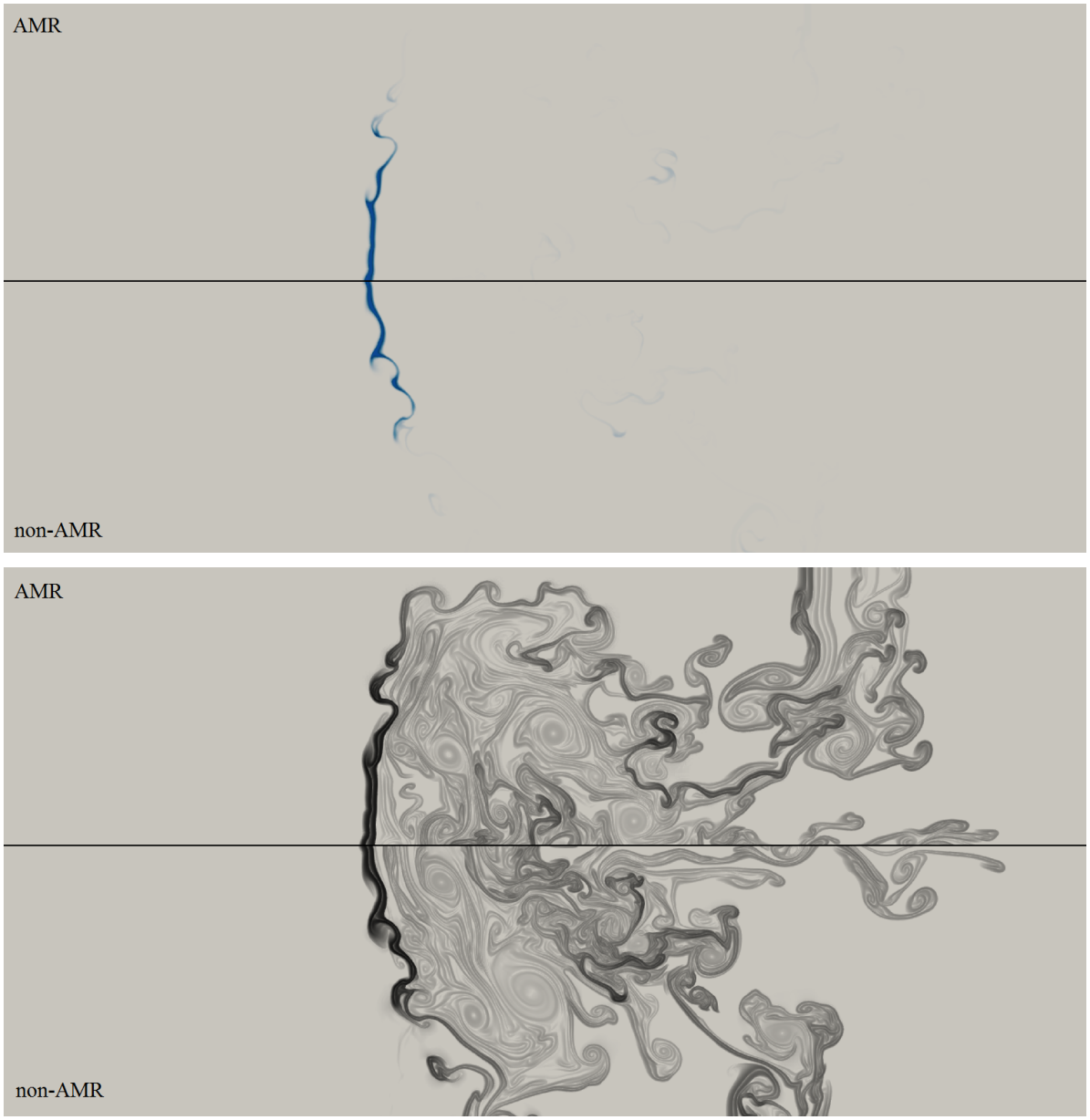

Figure 4.8: Magnified view of the simulation of the atomization of the cylindrical column by the high speed flow behind the shock wave of Mach number 1.3 in atmospheric air propagating from the left to the right. 2D simulations respectively with (upper half) and without (lower half) the AMR method (using the volume fraction and mixture pressure variations). Results are shown at time $2,000\mu s$ with volume fraction (top) and schlieren of the mixture density (bottom) visualizations.

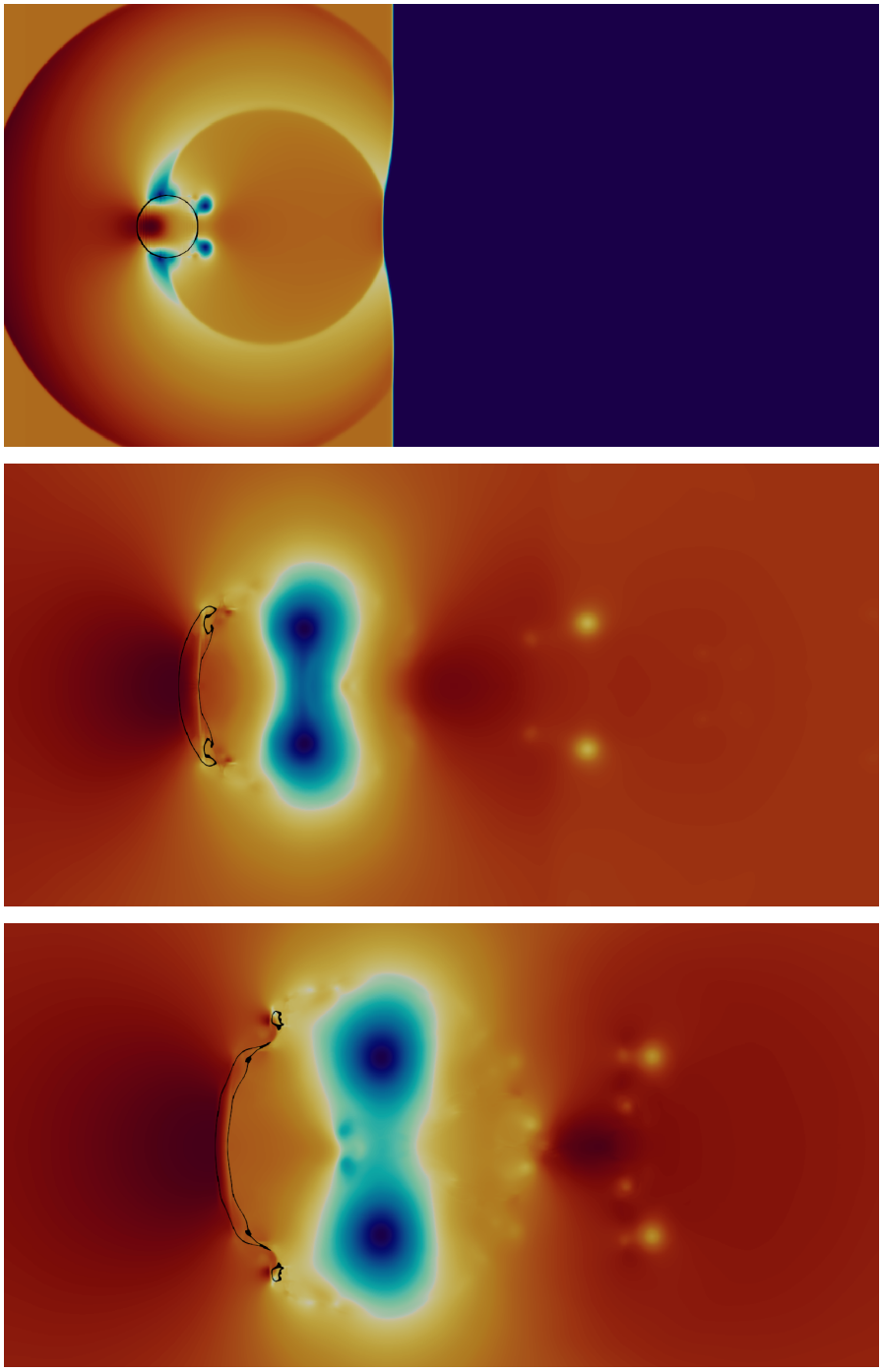

Figure 4.9: Magnified view of the simulation of the atomization of the cylindrical column by the high speed flow behind the shock wave of Mach number 1.3 in atmospheric air propagating from the left to the right. 2D simulations with the non-AMR mesh. Results are shown at times $60\mu s$ (top), $800\mu s$ (center) and $1,200\mu s$ (bottom) with mixture pressure visualization (dark red account for high pressures and dark blue for low ones).

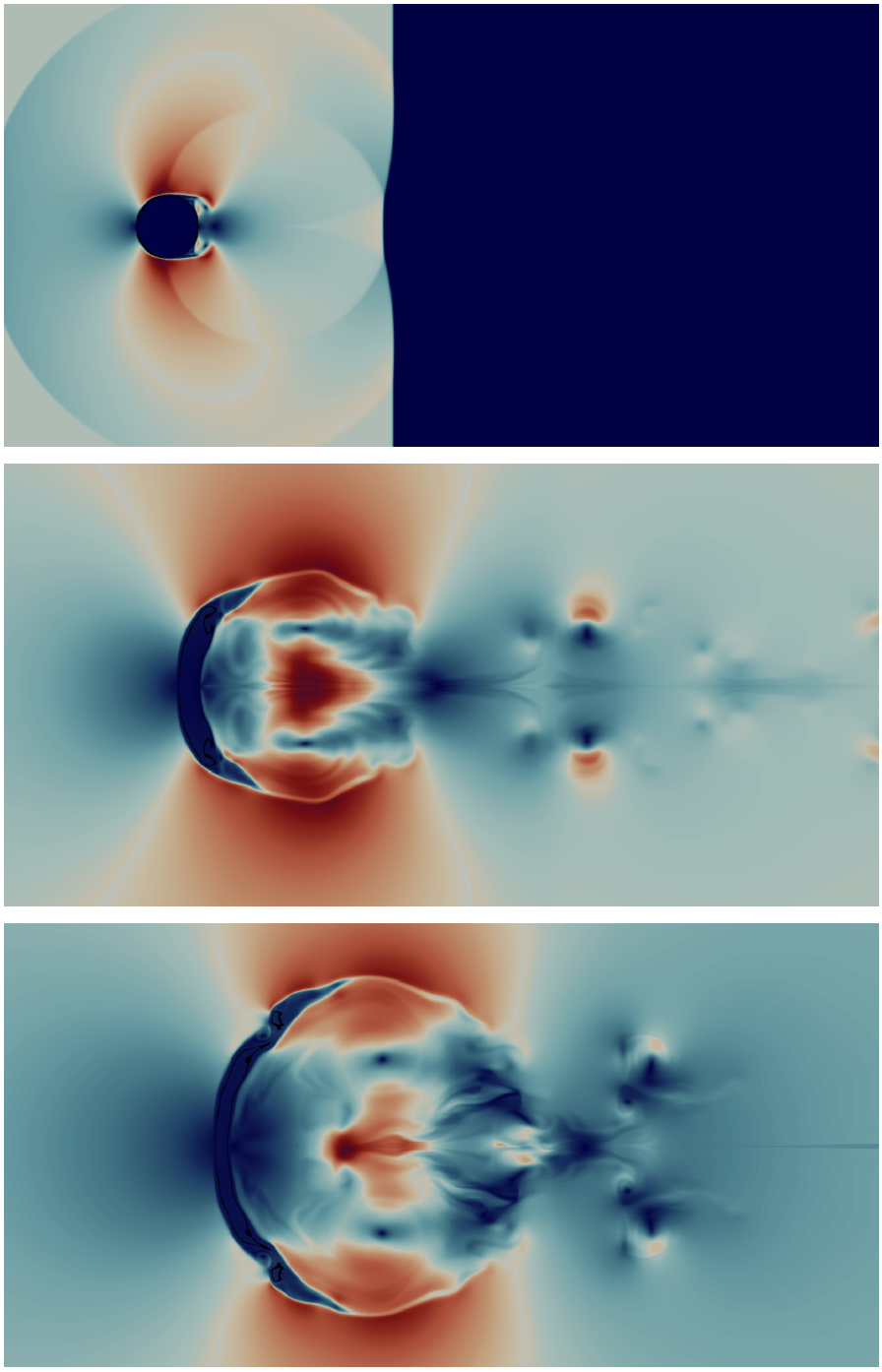

Figure 4.10: Magnified view of the simulation of the atomization of the cylindrical column by the high speed flow behind the shock wave of Mach number 1.3 in atmospheric air propagating from the left to the right. 2D simulations with the non-AMR mesh. Results are shown at times $60\mu s$ (top), $800\mu s$ (center) and $1,200\mu s$ (bottom) with mixture velocity magnitude visualization (dark red account for high velocities and dark blue for low ones).

Once this new criterion (gradient refinement criterion based on mixture velocity variation) is taken into account, it can be observed that there are differences in the refinement of the mesh between the two cases with and without this criterion (Figure 4.11). With the mixture velocity criterion, the mesh is refined all around the column with a higher thickness, particularly at the front and at the rear of the column. The additional refinement rate between the two complete simulations is estimated to be around 15%. This one allows to correctly evaluate the stretching of the column without involving too much additional cells computation in comparison to the previous simulation. Finally, the comparison between these results and those of the non-AMR method shows that the previously explained divergence disappears and the AMR results, at least up to $1,200\mu s$ after the first interaction between the shock and the column, are thus satisfactory (Figure 4.12).

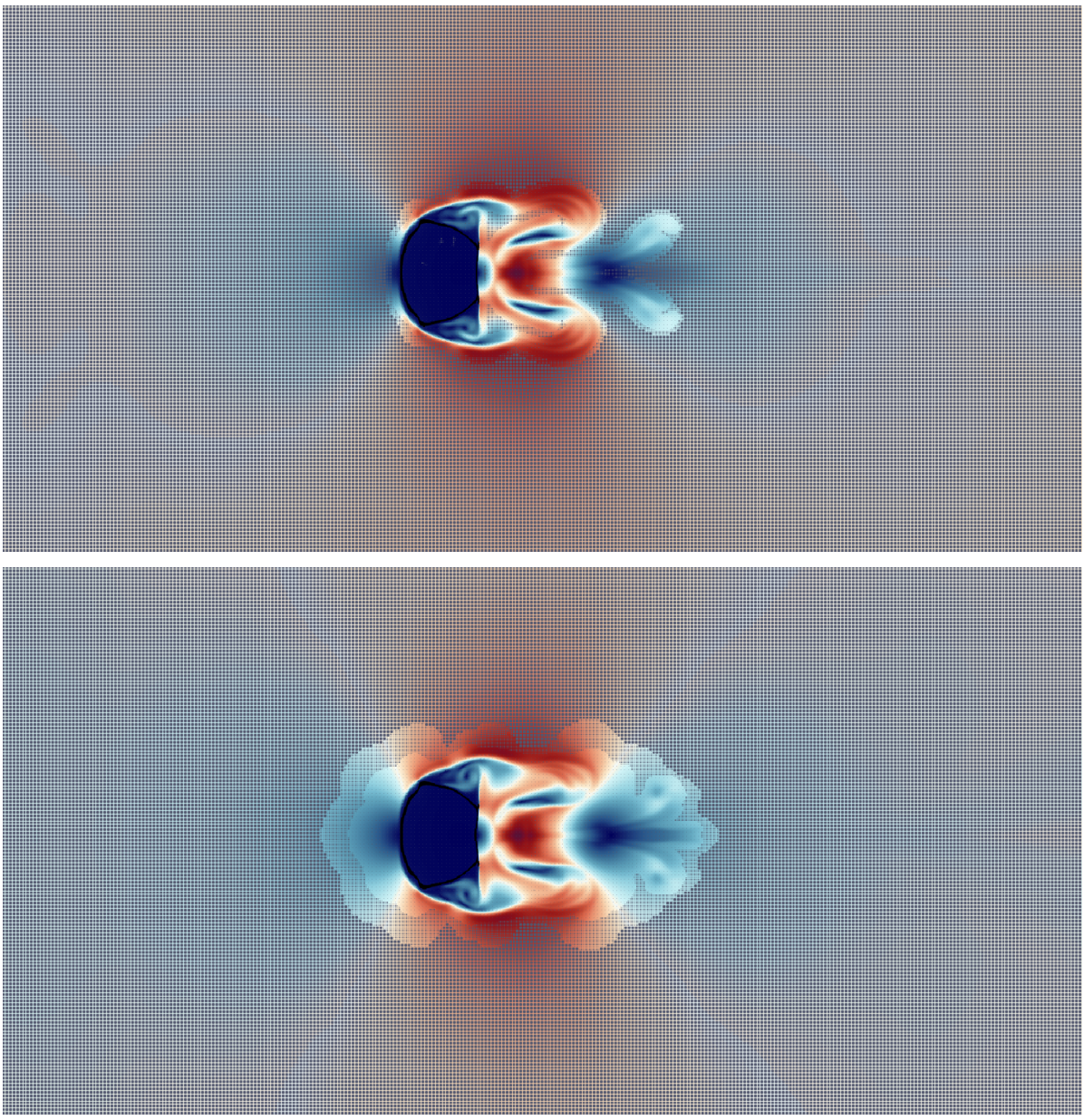

Figure 4.11: Magnified view of the simulation of the atomization of the cylindrical column by the high speed flow behind the shock wave of Mach number 1.3 in atmospheric air propagating from the left to the right. 2D simulations using the AMR method with the volume fraction and the mixture pressure variations, the mixture velocity variation is not used and is used in the simulation on the top and on the bottom, respectively. Results are shown at time $240\mu s$ with mixture velocity magnitude visualization (dark red account for high velocities and dark blue for low ones) and with apparent mesh.

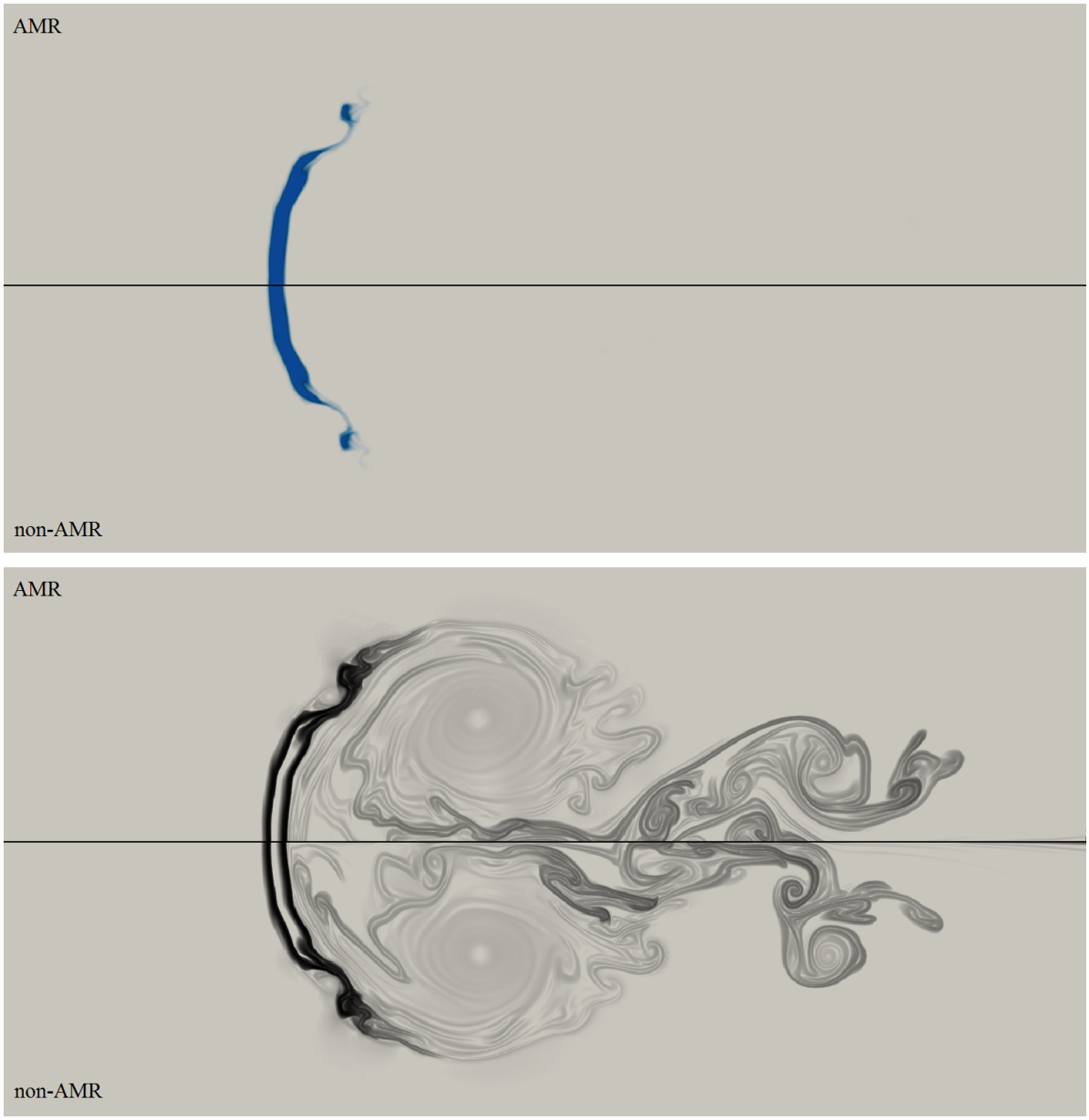

Figure 4.12: Magnified view of the simulation of the atomization of the cylindrical column by the high speed flow behind the shock wave of Mach number 1.3 in atmospheric air propagating from the left to the right. 2D simulations respectively with (upper half) and without (lower half) the AMR method (using the volume fraction, mixture pressure and mixture velocity variations). Results are shown at time $1,200\mu s$ with volume fraction (top) and schlieren of the mixture density (bottom) visualization.

4.3.3 Symmetry approximation

In the present case, vortices are observable at the rear of the column. Indeed, as shown in Figure 4.10, the flow is accelerated at the lateral edges of the column (top and bottom of the column in the images) and it is braked at the front of the column. These high velocities at the lateral edges coupled with a relatively low speed of the column displacement cause a depressurization at the rear of the column (see Figure 4.9). Then, the flow is driven to the rear of the column. Due to the reciprocity of this phenomenon from each lateral edge of the column, velocities with opposite directions and equal amplitudes are confronted at the rear of the column (between the upper half and the lower half in the images). Thus, at the locations aligned with the center of the column in the direction of the main flow, the flows from the upper and the lower half are respectively pushed back which then form the vortices.

These main vortices in the proximity of the column eject smaller vortices at a higher speed than the column displacement (Figure 4.13). In the case of the numerical simulation of the aerobreakup with a non-AMR mesh, one observes for the longer instants that these vortices generate Kelvin-Helmholtz instabilities. The Kelvin-Helmholtz instability is a wave motion in fluid dynamics that occurs when two thermally stable fluids are superimposed and move at different speeds at their contact surface. Indeed, the velocities with opposite directions and equal amplitudes undergo round-off numerical errors which do not allow to verify the perfect reciprocity and thus the Kelvin-Helmholtz instabilities appear.

An important point to observe is that these instabilities appear relatively late and far from the column. Even later, these instabilities disrupt the vortices in direct contact with the column but *a priori* without great influence (Figure 4.13). On the other hand, when using the AMR method, it can be observed that these instabilities appear sooner and with a larger amplitude (Figure 4.14). Indeed, the numerical scheme of the AMR method is different from the non-AMR one and when a first tiny instability appears, it is amplified since the refinement of the mesh will favor one side rather than the other and thus the conflict between refined and smoothed sides amplifies the speed of the instabilities evolution. The issue is that these amplified instabilities have a non-negligible impact on the aerobreakup. The amplification directly disturbs the flow in contact with the column and thus modifies in a non-symmetrical manner the stretching and hence the aerobreakup of the column. One can thus observed that for long time, the drift of the results between AMR and non-AMR methods does not stop to grow and in that sense, the non-symmetry of the aerobreakup, purely linked to the used method and despite the improvement of the results by adding the criterion on the mixture velocity variation, may be considered non-satisfactory (Figure 4.15).

To circumvent this issue and due to the weak influence that these instabilities should have on the aerobreakup process, a symmetry approximation is tested. It consists in dividing the domain in two and only conserving the upper-half. The symmetry condition is imposed on the new domain boundary corresponding to the cut (here along the x-axis).

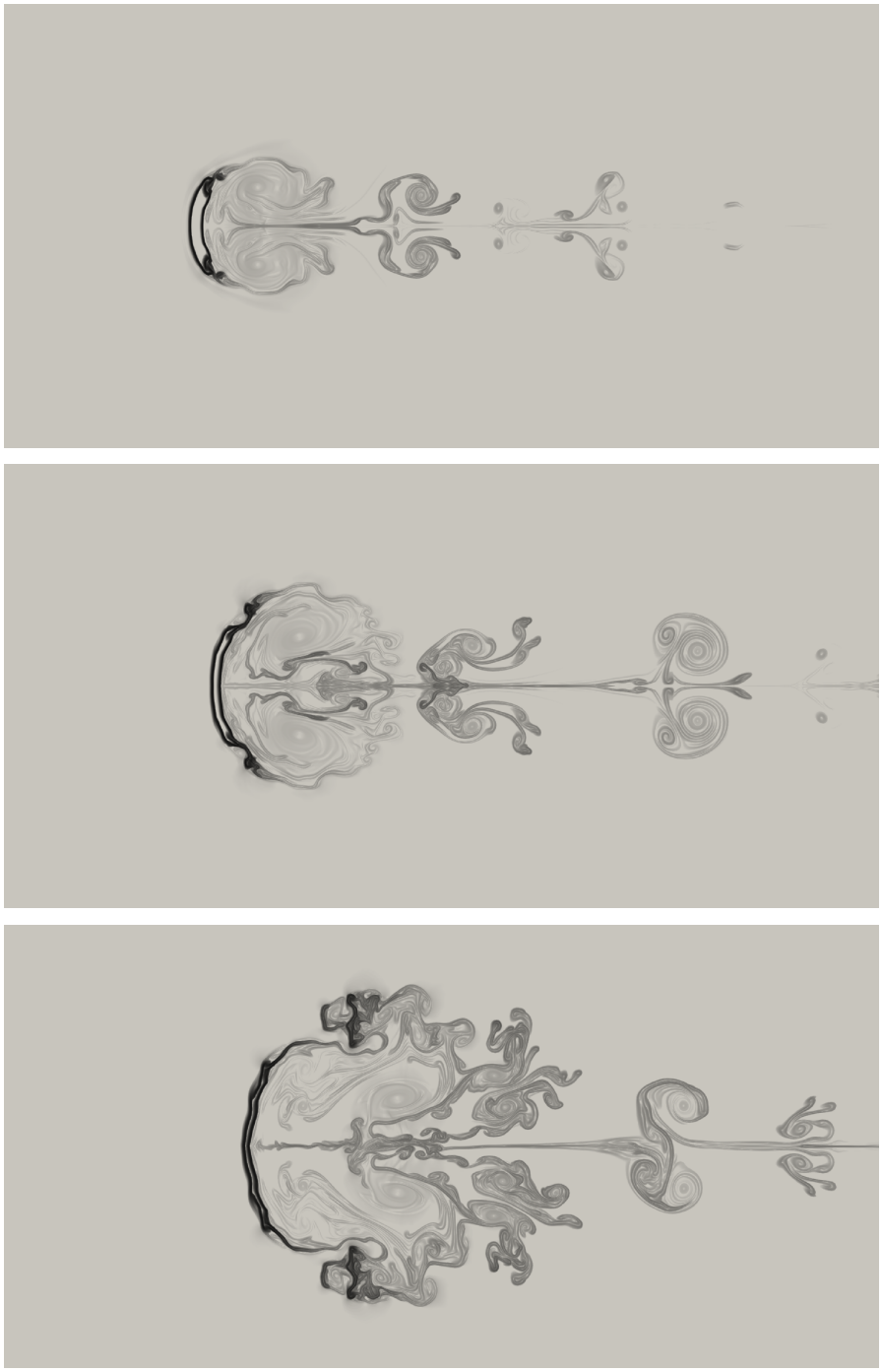

Figure 4.13: Magnified view of the simulation of the atomization of the cylindrical column by the high speed flow behind the shock wave of Mach number 1.3 in atmospheric air propagating from the left to the right. 2D simulations using the non-AMR method. Results are shown at times $800\mu s$ (top), $1,200\mu s$ (center) and $1,600\mu s$ (bottom) with schlieren visualization of the mixture density.

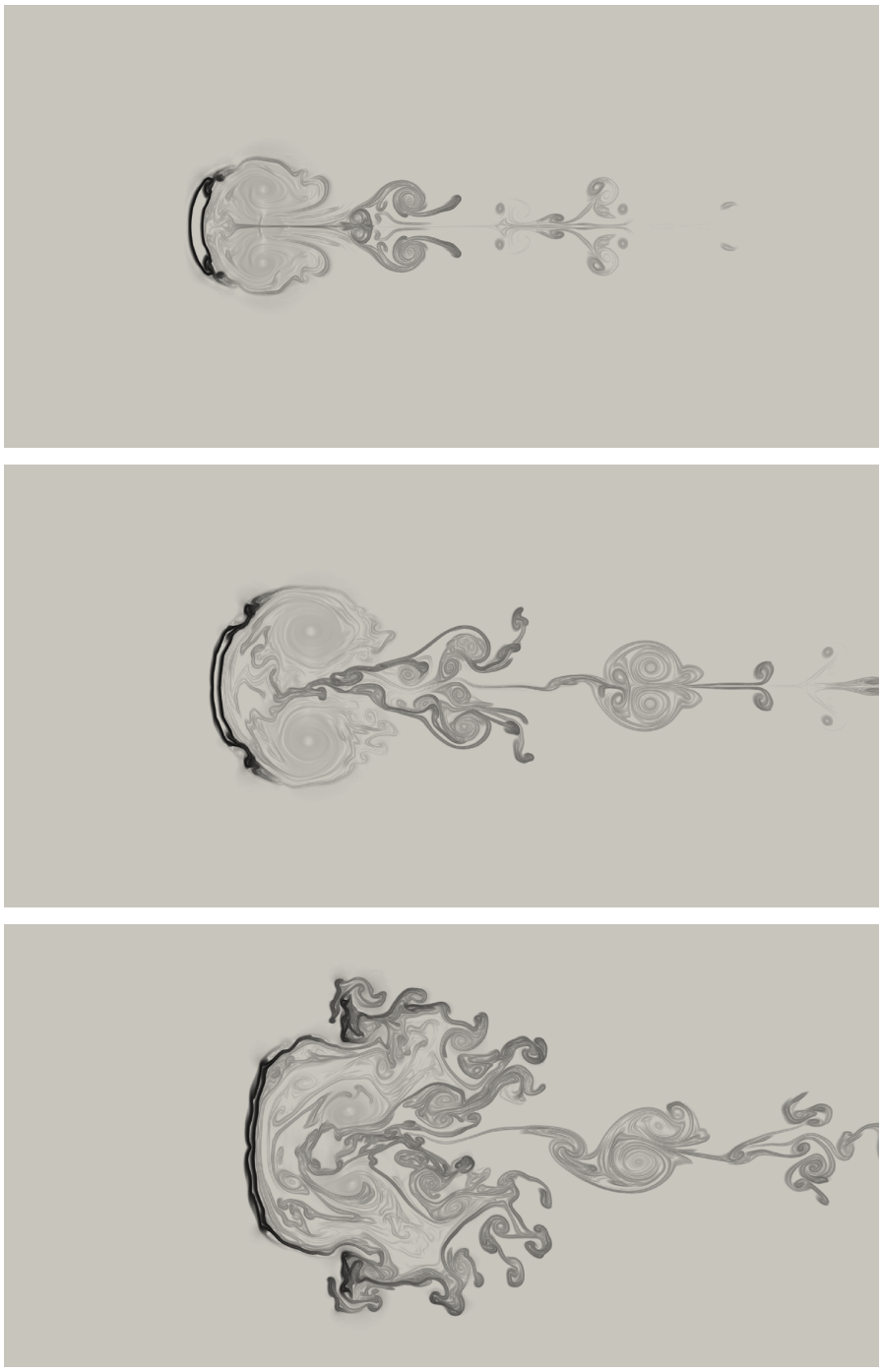

Figure 4.14: Magnified view of the simulation of the atomization of the cylindrical column by the high speed flow behind the shock wave of Mach number 1.3 in atmospheric air propagating from the left to the right. 2D simulations using the AMR method (using the volume fraction, mixture pressure and mixture velocity variations). Results are shown at times $800\mu s$ (top), $1,200\mu s$ (center) and $1,600\mu s$ (bottom) with schlieren visualization of the mixture density.

Figure 4.15: Two different magnified views of the simulation of the atomization of the cylindrical column by the high speed flow behind the shock wave of Mach number 1.3 in atmospheric air propagating from the left to the right. 2D simulations using the AMR (top) and non-AMR (bottom) methods (AMR using the volume fraction, mixture pressure and mixture velocity variations. Results are shown at time $2,000\mu s$ with volume fraction visualization. Drift of the AMR results is observable due to non-symmetrical amplification.

The results using the symmetry approximation with the AMR and the non-AMR methods are slightly different (Figure 4.16). But, these results are satisfactory because the breakup mechanisms occurring at the initial column level and at the reduced sizes columns levels, which are the center of interest, are similar. Note that the called reduced sizes columns here corresponds to the detached pieces of water from the initial column. They can be thus considered as 2D droplets in the simulation, while 3D droplets appears in the corresponding experiments. No drift of the solution is observed. Moreover, for numerical simulations over long times, the results between the two methods, even under the best possible conditions, cannot be perfectly similar due to the fact that the numerical scheme, then indirectly the numerical diffusion and the fluxes are not identical. Thus, the symmetry approximation results are considered as satisfactory and this methodology is performed for the continuation of the 2D test cases. Note that this symmetry approximation also obviously allows to accelerate the calculation by a factor of two.

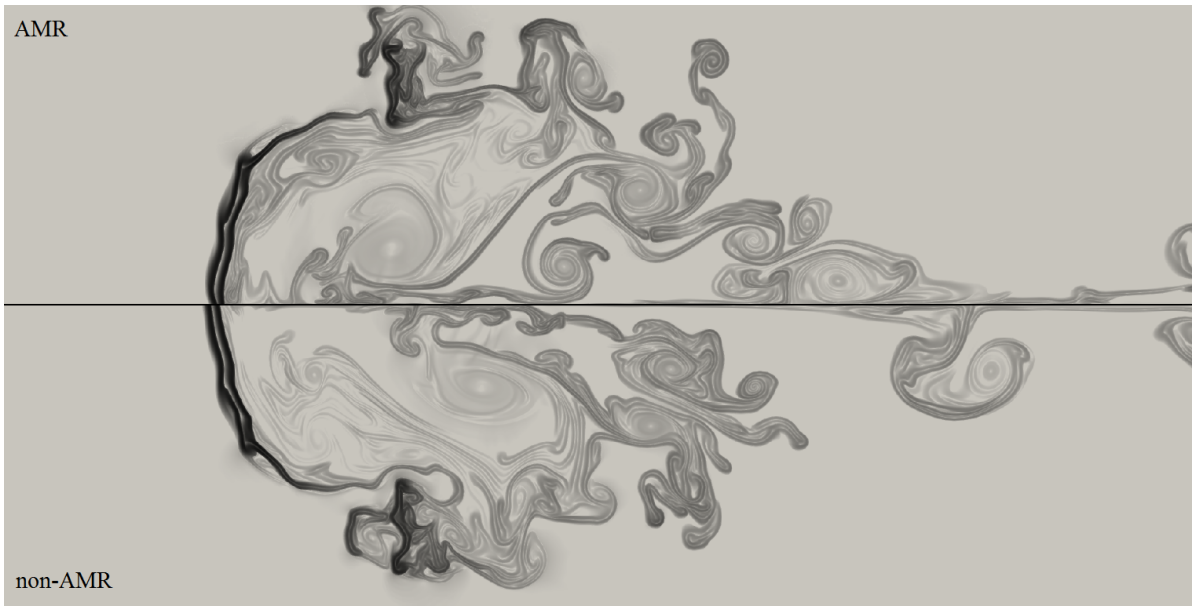

Figure 4.16: Magnified view of the simulation of the atomization of the cylindrical column by the high speed flow behind the shock wave of Mach number 1.3 in atmospheric air propagating from the left to the right. 2D simulations respectively with (upper half) and without (lower half) the AMR method (using the volume fraction, mixture pressure and mixture velocity variations) and with the axi-symmetry approximation. Results are shown at time $1,600\mu s$ with schlieren visualization of the mixture density.

4.3.4 Comparison between simulations with and without capillary effects

In this section is tested the influence of the capillary effects on the aerobreakup. The goal is to determine the time when the capillary effects become no more negligible, *i.e.*, having a role in the aerobreakup process. The dimensionless number of Weber:

$$We = \frac{\rho_{air} \|\mathbf{u}_{local}\|^2 L}{\sigma},$$

where ρ_{air} is the air density, $\|\mathbf{u}_{local}\|$ is the local relative velocity between the flow and the column, and L is the characteristic length which initially is the column diameter, is initially equal to $We = 3,690$. It thus shows that the inertial forces are much larger than the surface tension ones. On the other hand, the value of this dimensionless number is completely different for long times. The velocities at the edges of the initial column and of its detached parts (those separating from the initial column during the breakup) are changed and their characteristic lengths, equivalent to the thickness of the columns, decrease. Among these reduced sizes columns, the ones with the smallest diameter thus have the value of the Weber number tending to approximately 1.

The figures 4.17 and 4.18 show the evolution of the aerobreakup with and without taking into account the capillary effects. As expected, the influence of capillary effects is negligible for short times (before $1,200\mu s$). The estimated Weber number at $1,200\mu s$ is around $We \approx 300$ for the initial column ($\rho_{air} \approx 1.8kg.m^{-3}$, $\|\mathbf{u}_{local}\| \approx 100m.s^{-1}$ and $L \approx 1.2mm$) and around $We \approx 185$ for the reduced sizes columns ($\rho_{air} =\approx 1.7kg.m^{-3}$, $\|\mathbf{u}_{local}\| \approx 140m.s^{-1}$ and $L \approx 0.4mm$).

For longer times, the capillary effects have an impact on the dynamics of the smallest columns and also on the initial one. Indeed, when looking at Figure 4.18 at time $1,600\mu s$ (third line of images), we can see that the filaments are much more prone to break under under the effects of the surface tension, *i.e.*, with a greater curvature (see corresponding blue circles in each images), and in Figure 4.17 at time $2,000\mu s$ (bottom images), it can be clearly seen that the shape of the initial column is different, *i.e.*, the surface tension tends to break the column to form smaller columns, especially where the velocities are relatively small (in the center of the initial column, shown with a dark red oval). Then, the evaluation of the Weber number at $2,000\mu s$ on the initial column is $We \approx 65$ ($\rho_{air} \approx 1.9kg.m^{-3}$, $\|\mathbf{u}_{local}\| \approx 70m.s^{-1}$ and $L \approx 0.5mm$) and on the columns of reduced sizes (here those visible) it is $We \approx 10$ ($\rho_{air} \approx 1.65kg.m^{-3}$, $\|\mathbf{u}_{local}\| \approx 50m.s^{-1}$ and $L \approx 0.2mm$).

It is expected that the capillary effects have an even higher influence on the aerobreakup process when decreasing the characteristic length of the smaller cells, *i.e.*, decreasing the numerical diffusion, increasing the interface resolution and thus indirectly decreasing the visible characteristic length of the columns. The following simulations are thus only performed with capillary effects.

The same type of study should be done with the viscous effects, however it was shown in the introduction (Chapter 1) through a dimensional analysis that the viscous effects should have less influence than the surface tension ones. In the future, this point should be verified by adding the viscous effects in the model, for example by following the work of Thévand et al. [91].

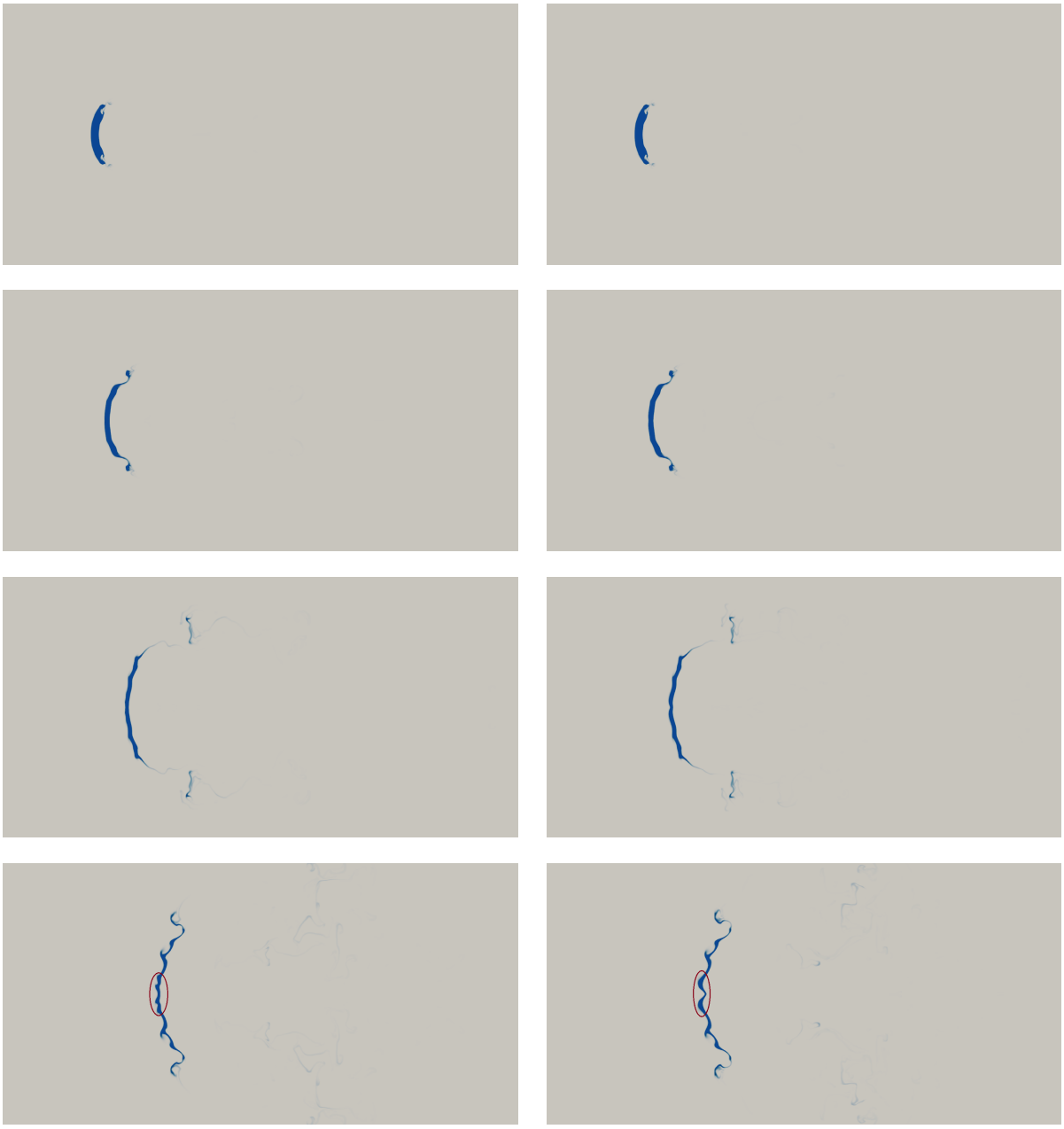

Figure 4.17: Magnified view of the simulation of the atomization of the cylindrical column by the high speed flow behind the shock wave of Mach number 1.3 in atmospheric air propagating from the left to the right. 2D simulations using the AMR method (using the volume fraction, mixture pressure and mixture velocity variations) and the axi-symmetry approximation. Results are shown from top to bottom at times $800\mu s$, $1,200\mu s$, $1,600\mu s$ and $2,000\mu s$, without (left column) and with (right column) capillary effects and with a volume fraction visualization (scale up to 0.5).

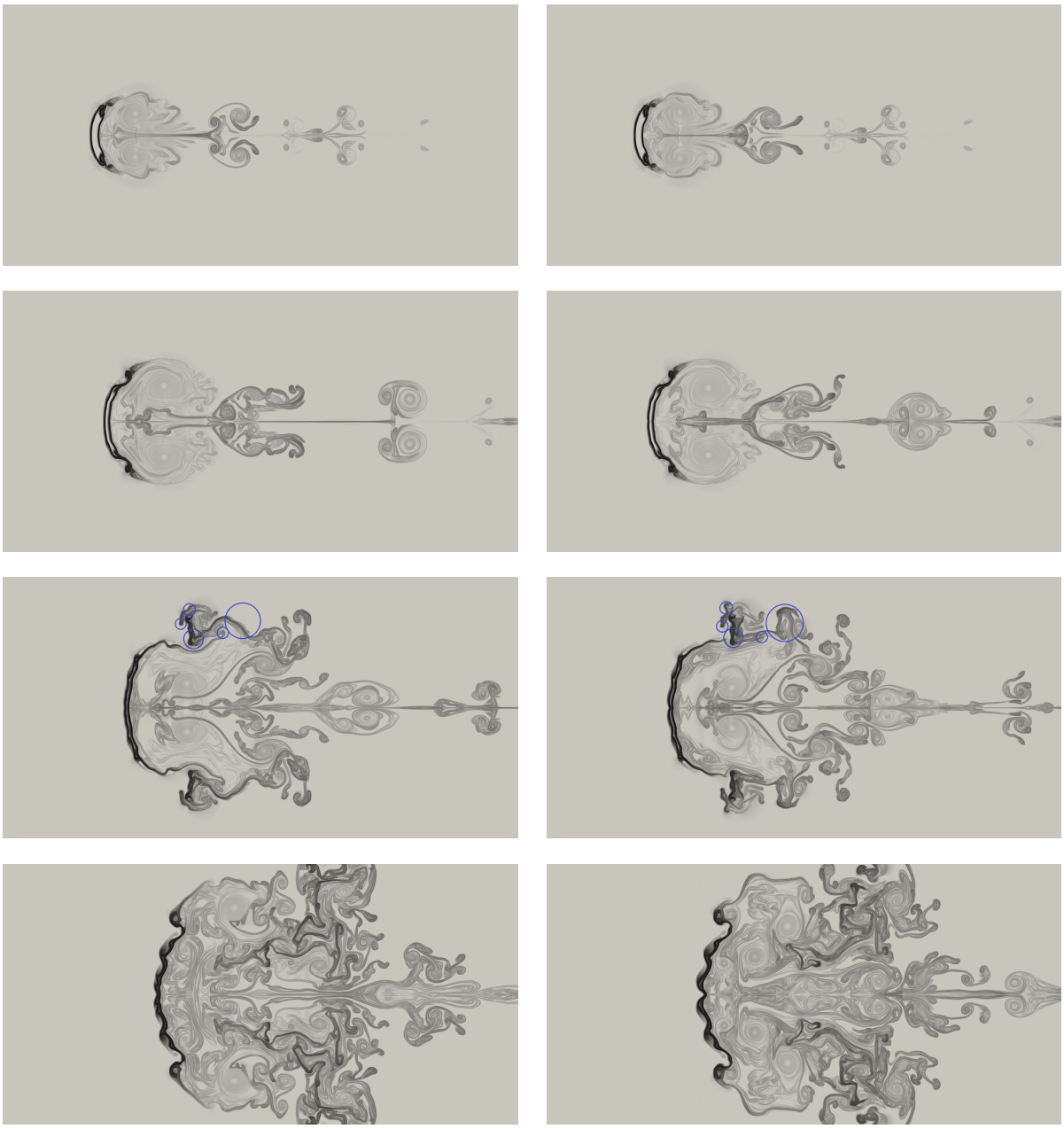

Figure 4.18: Magnified view of the simulation of the atomization of the cylindrical column by the high speed flow behind the shock wave of Mach number 1.3 in atmospheric air propagating from the left to the right. 2D simulations using the AMR method (using the volume fraction, mixture pressure and mixture velocity variations) and the axi-symmetry approximation. Results are shown from top to bottom at times $800\mu s$, $1,200\mu s$, $1,600\mu s$ and $2,000\mu s$, without (left column) and with (right column) capillary effects and with a schlieren visualization of the mixture density.

4.3.5 Experimental comparison

As the different simulation parameters have been previously studied, the experimental comparison with the work of Igra and Takayama [39] on the atomization of a water column in air environment is done considering:

- The MC limiter for the interface variables in the MUSCL-Hancock second order method (Minmod is used for the others).
- The volume fraction, mixture pressure and mixture velocity variations for the gradient refinement criterion ϵ.
- The symmetry approximation.
- The capillary effects.

Two simulations are performed:

- One, as previously done, with the maximum number of levels $l_{max} = 2$, corresponding to an equivalent non-AMR mesh of 4,000x800 $= 3,200,000$ cells.
- Another one using the advantage of the AMR method, *i.e.*, increasing the mesh size without totally compromising the computational time and post-processing, with $l_{max} = 3$, corresponding to an equivalent non-AMR mesh of 8,000x1$,600 = 12,800,000$ cells.

The complete information concerning the AMR data is given in Table 4.3.

Initial number of cells	l_{max}	Equivalent mesh	ϵ	ξ_{split}	ξ_{join}
1,000x200	2	3,200,000	0.02	0.05	0.05
1,000x200	3	12,800,000	0.02	0.05	0.05

Table 4.3: AMR data for the final 2D atomization tests.

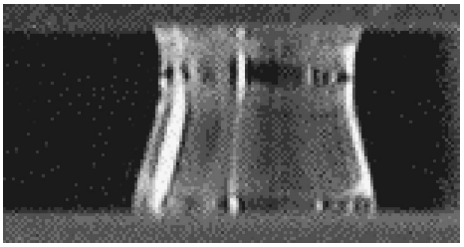

Figure 4.19: Reprinted from Igra and Takayama [40]. The shape of water column view from the side. © 2003, ASME.

In the experiment of Igra and Takayama, two transparent optical windows are placed in a shock tube. A separation of $4mm$ in height is present and the authors claim that

the shock wave propagating inside the $4mm$ high channel is only very slightly perturbed by the windows. The water column is initially produced and maintained between those two windows. The height of the water column is thus equal to the height of the channel. The windows are $150mm$ large to avoid any interaction of the water column with the side walls. The water column, whose diameter is of the same order as its height, is created inside the separation. A syringe is used to create the water column by slowly injecting water at the center of the test section. As soon as the hemispherical water droplet touches the windows, it becomes a cylindrical shape of $6.4mm$ diameter. An example of a water column is shown in Figure 4.19 with a side view photo. The shape of the water column is not exactly cylindrical due to the water surface tension.

The atomization visualization is done from above through the optical windows and then the column appears as a disk similar to the 2D simulations. Results on wave propagation and early instants of the aerobreakup were shown at the end of the chapter 2 (see Figures 2.15 and 2.16). A qualitative comparison between the experimental results and the simulations was carried out and the results were in perfect agreement.

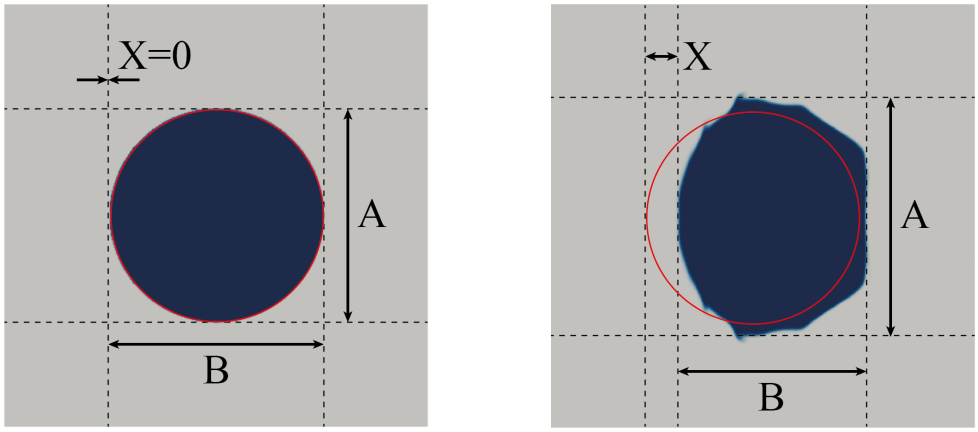

Figure 4.20: Schematic views of the parametric description of the water column with simulation at the initialization and time $t = 200\mu s$ for comparison against experiments of Igra and Takayama [39]. The flow is moving from the left to the right.

A quantitative comparison is now performed for longer times up to $1,200\mu s$ and it is necessary to define the parameters that are compared. These different parameters, as well as the time, are given under a dimensionless form:

- The column displacement $x^\star = X/D$, where X represents the distance between the position of the front of the column at the initialization and the position of this front at a given time after the first interaction between the shock and the column. D is the initial diameter of the water column, here $D = 6.4mm$.
- The lateral deformation of the column $\Delta y^\star = A/D$.
- The deformation of the column in the flow direction $\Delta x^\star = B/D$.
- The time $t^\star = tu_{shocked}/D$, where $u_{shocked}$ is the flow velocity behind the shock wave.

Figure 4.20 shows a schematic view of the parametric description of the water column. On the left image is the initialization and on the right image is the result of the aerobreakup at time $t = 200\mu s$. Determining the column displacement is straightforward at any time, but it is not so for the lateral and flow direction deformations at longer times. At $t = 200\mu s$ those last two parameters are simply obtained *via* a computing procedure. The problem appears when the filaments and/or reduced sizes columns are present, that is to say when the initial column starts to have a complex shape. Indeed, the calculations must only take into account the column deformations and a protocol for the calculation of A and B is thus needed. An example of how these parameters are calculated at a longer time of $800\mu s$ is shown in Figure 4.21. The lateral deformation is calculated without taking into account the filaments and the flow direction deformation is calculated with the thickness of the column. Note that the interface position is here considered using the volume fraction which takes into account the compressibility of each phase and thus the condition $\alpha = 0.5$ is used for the contour of the column.

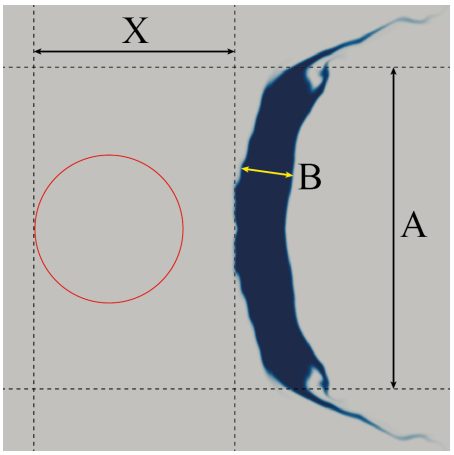

Figure 4.21: Schematic view of the parametric description of the water column with simulation at time $t = 800\mu s$ for comparison against experiments of Igra and Takayama [39]. The flow is moving from the left to the right.

Figures 4.22, 4.23 and 4.24 show the column displacement, the flow direction and lateral deformations, respectively. The results for the column displacement and for the flow direction deformation are plotted until $t^\star = 28.5$, which corresponds to a physical time of $1,200\mu s$. For the lateral deformation the results are plotted until $t^\star = 19$, equivalent to $t = 800\mu s$. Good agreements are obtained for the column displacement and for the flow direction deformation. Concerning the lateral deformation, it is more questionable. The simulations results expand more than the experiment ones while the time goes. Moreover, one can note that all the results of the simulation with two levels of refinement seem to match slightly better with the experiment than for the ones with three levels. But, the experiment and the simulations are not performed with the exact same configuration. The simulation forces the initial shocked flow at the entry and has the Newmann boundary conditions elsewhere. In the experiment, the boundaries are further and the reflected shock on the column thus slows down the incoming shocked flow for the whole experiment. In

the simulation, this last point is different because the reflected shock reaches the entry and then the incoming flow quickly tends to the forced initial shocked conditions. Plus, the column is sandwiched between the two windows in the experiment and this configuration, with the 3D curvatures of the cylindrical column and the wall presence, surely plays an important role in the breakup process and in the post-processing of the data. In conclusion, the better matching with the experiment for the simulation with two levels of refinement does not mean that there is no mesh convergence. Finally, the results are satisfactory in the two cases and to capture the reduced sizes columns at longer times, the simulation with the three levels of refinement is extended and shown in the next section.

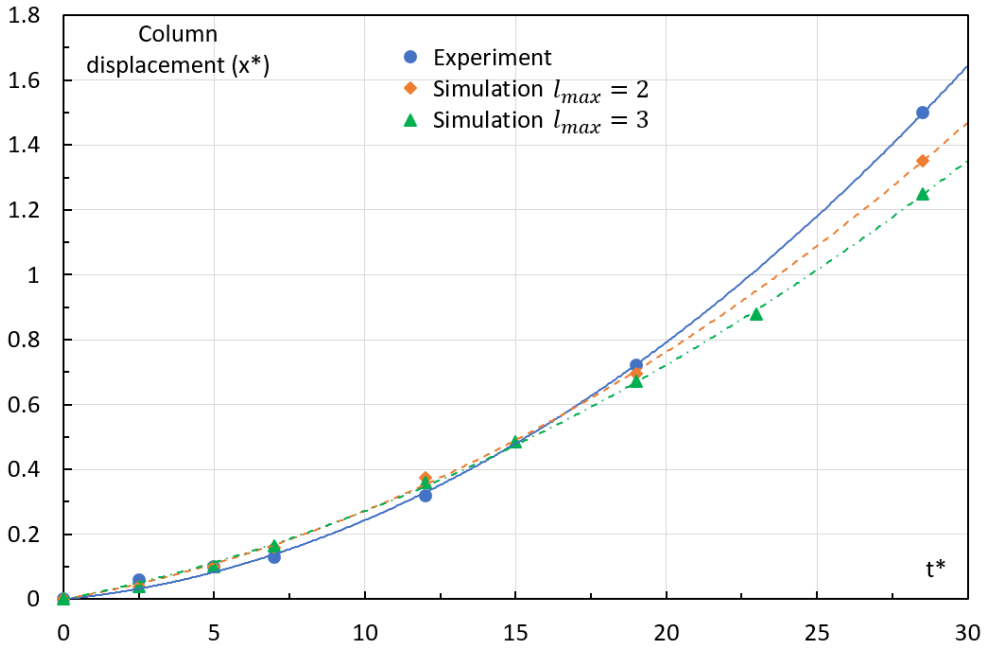

Figure 4.22: Dimensionless column displacement function of dimensionless time for the 2D atomization tests. Simulation results for $l_{max} = 2$ (orange squares) and $l_{max} = 3$ (green triangles) are shown with a comparison against the experiment of Igra and Takayama [39] (blue points).

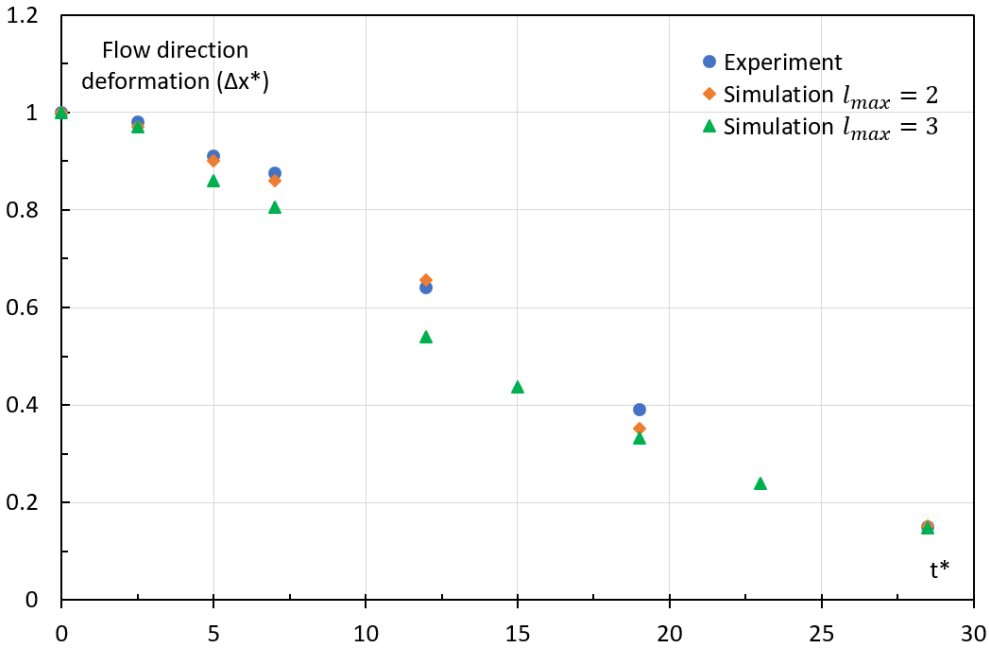

Figure 4.23: Dimensionless flow direction deformation function of dimensionless time for the 2D atomization tests. Simulation results for $l_{max} = 2$ (orange squares) and $l_{max} = 3$ (green triangles) are shown with a comparison against the experiment of Igra and Takayama [39] (blue points).

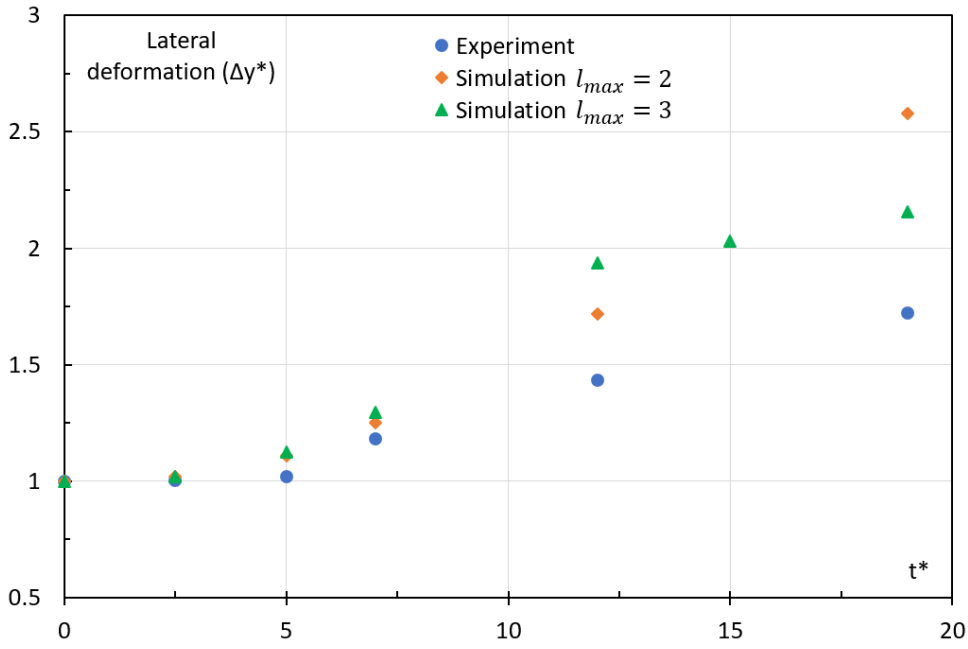

Figure 4.24: Dimensionless lateral deformation function of dimensionless time for the 2D atomization tests. Simulation results for $l_{max} = 2$ (orange squares) and $l_{max} = 3$ (green triangles) are shown with a comparison against the experiment of Igra and Takayama [39] (blue points).

4.3.6 Complete atomization

The previously presented simulation with three levels of refinement of the experimental comparison section is performed until $3,000\mu s$ after the first interaction between the shock and the water column. The goal is to observe the complete atomization of the isolated water column. Note that this physical time corresponds to a dimensionless time of $t^\star = 71.2$ which is around 2.5 times greater than what was presented for the experimental comparison.

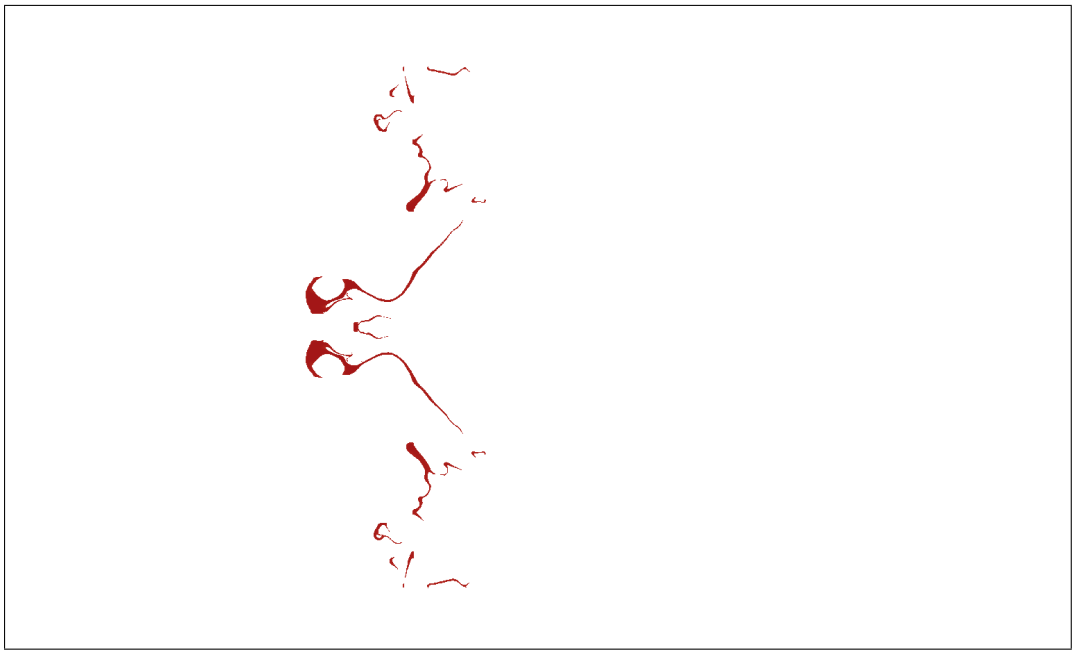

Figure 4.25: Magnified view of the simulation of the complete atomization of the water column by the high speed flow behind the shock wave of Mach number 1.3 in atmospheric air propagating from the left to the right. The water is shown in red using a threshold with $\alpha \geqslant 0.1$. Result is shown at time $2,000\mu s$.

Figure 4.25 presents in red a threshold on the volume fraction of water for values equal or superior to 0.1 ($\alpha \geqslant 0.1$) and for the atomization simulation at time $2,000\mu s$. Due to the high density variation between the water and the air, it is is assumed that this criterion allows to represent the water. At this time, the initial column is already broken in two pieces while at the same instant, for the simulation with two levels of refinement (last image of Figure 4.17 on the right column), the breakup of the column in two is not complete. Indeed, as previously stated in Section 4.3.4, increasing the refinement levels increases the impact of the capillary effects. The interface is treated with a greater resolution and thus indirectly the local curvature is more accurate. This can result in a higher surface tension, which is the current case. One can add that a called bag breakup occurs because the initial column is separated into two pieces by the following process: the front central portion of the column moves backwards at a speed greater than the one of its lateral parts. In addition, the filaments and the reduced sizes columns are more present with three levels of refinement.

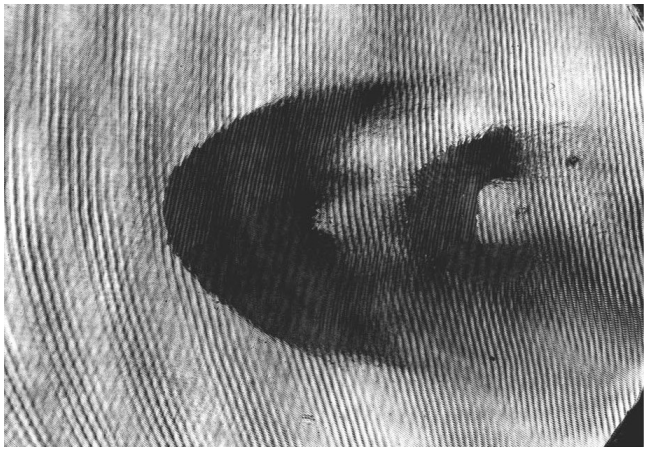

Figure 4.26: Reprinted from Igra and Takayama [40]. Two cylindrical water columns atomization at time $1,050\mu s$ *via* infinite fringe double exposure holographic interferogram visualization. © 2003, ASME.

When looking at the experiments, as the one of Igra and Takayama [40] in Figure 4.26, a mist of micrometer water droplets is observable. Those micrometer droplets are non-directly obtained in simulations because of the mesh resolution that should be performed, particularly with the effect of the numerical diffusion, and also here because of the 2D flow assumption. In the presented simulation, the volume fraction of water is diffused and follows the flow at the rear of the column as the mist would do. If a smaller water volume fraction value is thus taken to compute the threshold, here $\alpha \geqslant 0.001$, a mist of micrometer water columns (2D droplets) that has similarities with the experimental mist of micrometer water droplets is obtained (Figure 4.27). Nevertheless, decreasing the water volume fraction value is not a good option because the distinction between the initial column, its detached parts and the mist becomes difficult. One solution is to plot the function $\alpha^{\frac{1}{3}}$ that allows to observe more clearly the small values of the water volume fraction without amplify the large ones. Figure 4.28 shows the result of this function with a blue color.

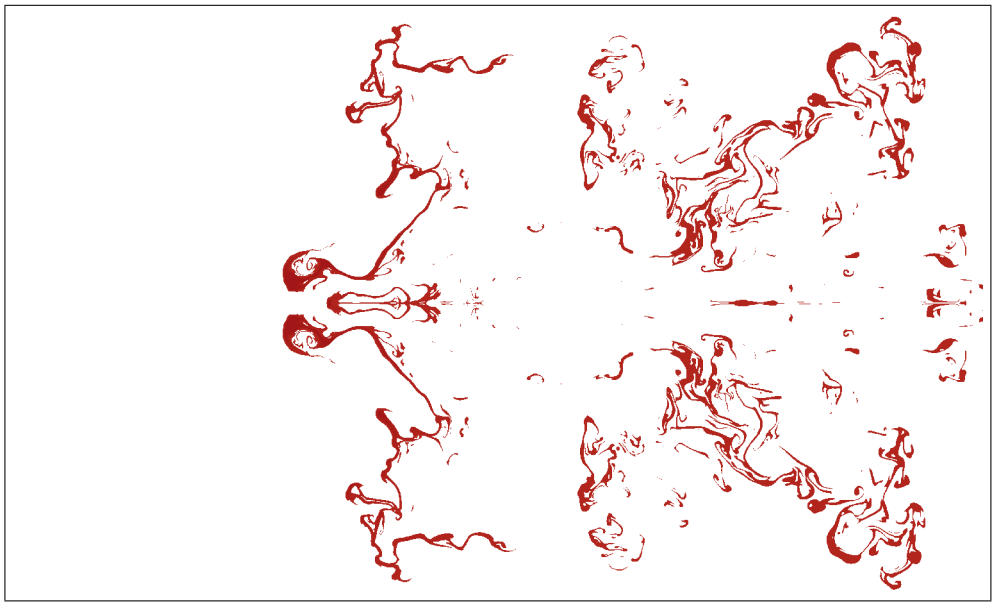

Figure 4.27: Magnified view of the simulation of the complete atomization of the water column by the high speed flow behind the shock wave of Mach number 1.3 in atmospheric air propagating from the left to the right. The water is shown in red using a threshold with $\alpha \geqslant 0.001$. Result is shown at time $2,000\mu s$.

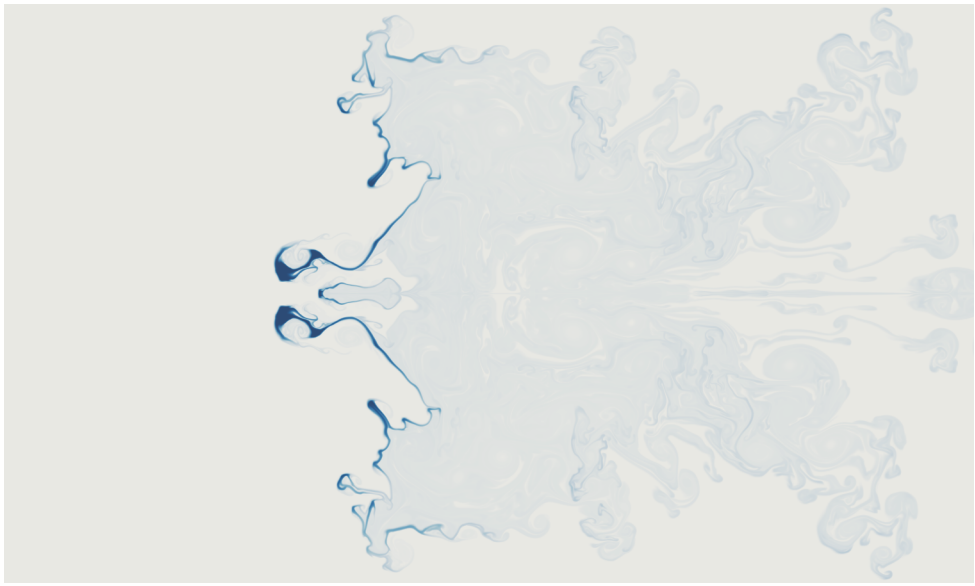

Figure 4.28: Magnified view of the simulation of the complete atomization of the water column by the high speed flow behind the shock wave of Mach number 1.3 in atmospheric air propagating from the left to the right. The initial column, its detached parts and the considered mist of micrometer water columns (2D droplets) are shown in blue using the function $\alpha^{\frac{1}{3}}$. Result is shown at time $2,000\mu s$.

But, to clearly distinguish the mist from the initial column and its detached parts, the red threshold is added using the previously considered limitation for the pieces of water, *i.e.*, using the criterion $\alpha \geqslant 0.1$. Figures 4.29 and 4.30 show the combination of the two for several times from the initial state until $3,000\mu s$. For a better understanding of the breakup process, the vorticity fields are also shown in Figures 4.31 and 4.32 for the corresponding times of the two previous figures. The color scale is given in the first image corresponding to the initialization (where vorticity is absent). Three main phases of the breakup are determined:

- The first phase concerns the compression and stretching of the initial isolated column until times around $800\mu s$. Filaments are also slowly appearing from the lateral parts of the column (Figure 4.29). Vortices are present at the rear of the column and at the rear of the filaments, particularly for the early instants of the breakup (Figure 4.31).

- Then for second phase, the compression and stretching continue until the vortices at the rear of the column, which pull the lateral parts far from the center, coupling with the capillary effects break the initial column in two pieces (around $1,500\mu s$). The bag breakup thus takes place. During this time, the filaments are created and thrown away from the column. Once detached, some of these filaments are turning into cylindrical columns (2D droplets). One can note that similar breakup phenomena, as the one on the initial column, are happening on the filaments and on the new formed columns. Small vortices at their rear are thus noticed.

- Finally, the third phase corresponds to the breakup of each small piece of water into even smaller ones, here until $3,000\mu s$ (Figure 4.30). One should note that, even if the smaller columns are disappearing due to the numerical diffusion and to the maximum mesh resolution, cylindrical-like shape columns are almost observable. This last point is synonym of low local Weber numbers (until values around $We \approx 2$). The characteristic diameters d of the observed reduced sizes columns with a cylindrical-like shape are around $0.2mm \leq d \leq 0.8mm$.

Atomization is thus achieved and the computation could be continued to process of the full atomization of all the pieces of water.

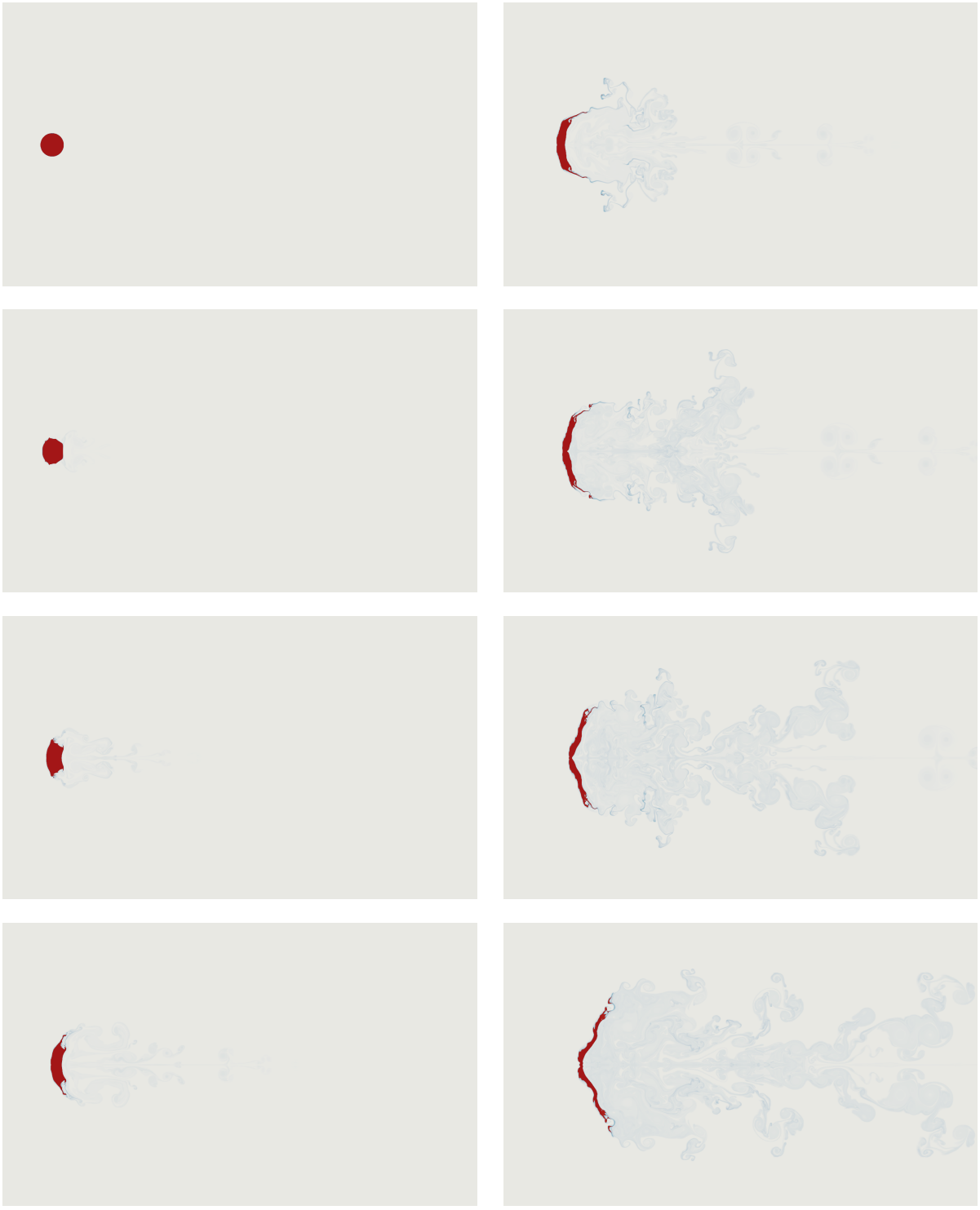

Figure 4.29: Magnified view of the simulation of the complete atomization of the water column by the high speed flow behind the shock wave of Mach number 1.3 in atmospheric air propagating from the left to the right. The water is shown in red using a threshold with $\alpha \geqslant 0.1$ and the considered mist of micrometer water columns (2D droplets) is shown in blue using the function $\alpha^{\frac{1}{3}}$. Results are shown at times $0\mu s$, $200\mu s$, $400\mu s$, $600\mu s$, $800\mu s$, $1,000\mu s$, $1,200\mu s$ and $1,400\mu s$ from the top to the bottom and from the left to the right.

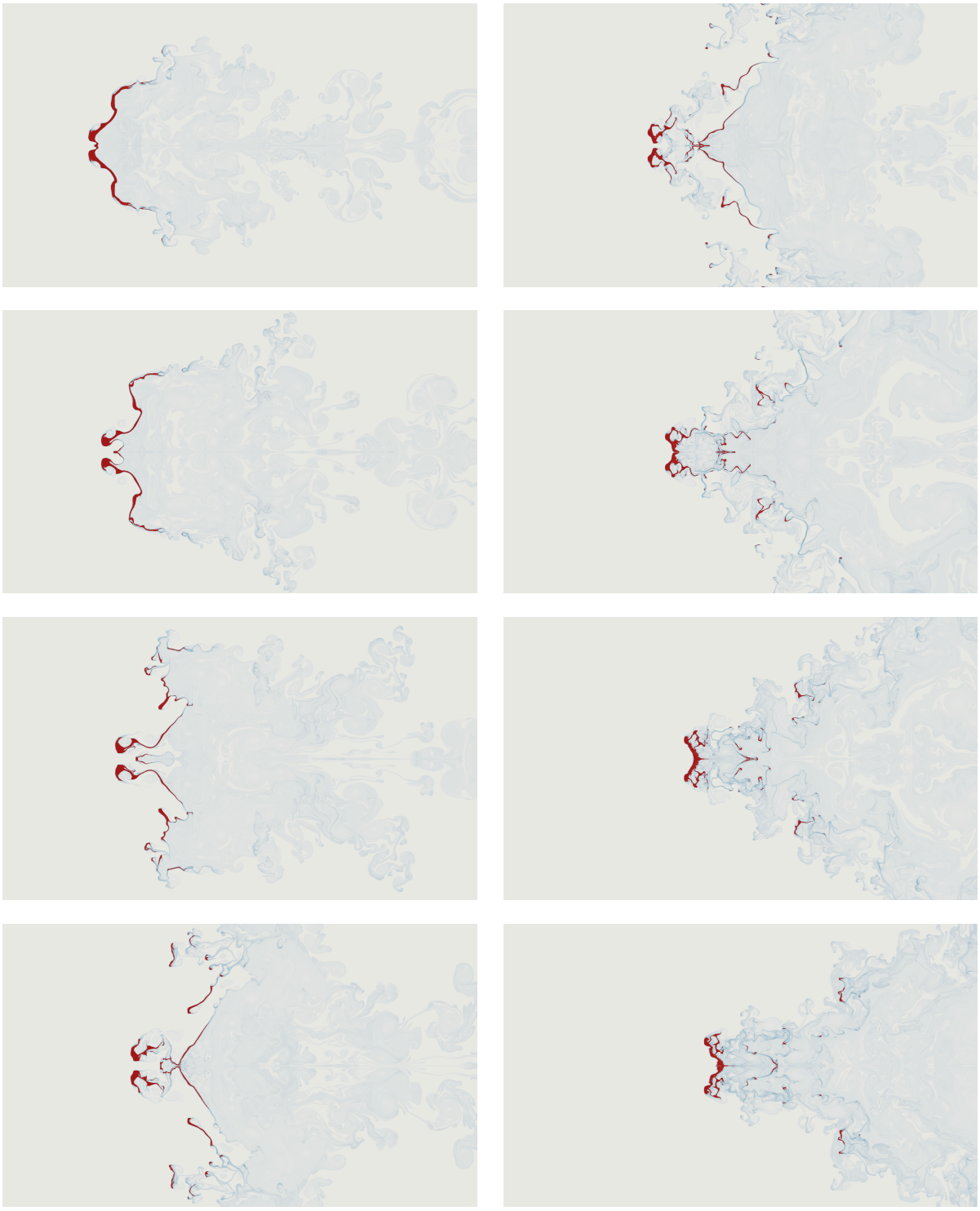

Figure 4.30: Magnified view of the simulation of the complete atomization of the water column by the high speed flow behind the shock wave of Mach number 1.3 in atmospheric air propagating from the left to the right. The water is shown in red using a threshold with $\alpha \geqslant 0.1$ and the considered mist of micrometer water columns (2D droplets) is shown in blue using the function $\alpha^{\frac{1}{3}}$. Results are shown at times $1,600\mu s$, $1,800\mu s$, $2,000\mu s$, $2,200\mu s$, $2,400\mu s$, $2,600\mu s$, $2,800\mu s$ and $3,000\mu s$ from the top to the bottom and from the left to the right.

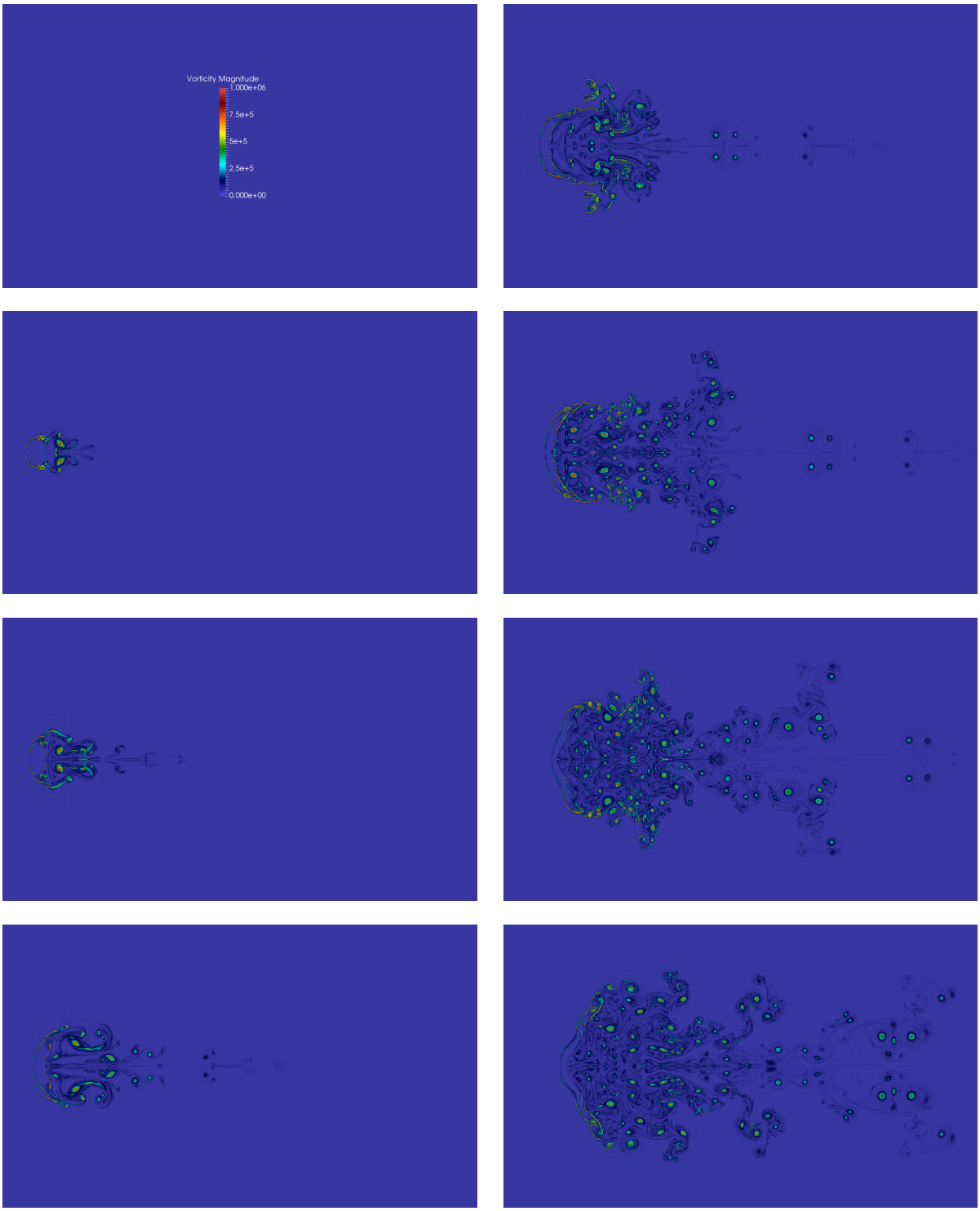

Figure 4.31: Magnified view of the simulation of the complete atomization of the water column by the high speed flow behind the shock wave of Mach number 1.3 in atmospheric air propagating from the left to the right. Vorticity results are shown at times $0\mu s$, $200\mu s$, $400\mu s$, $600\mu s$, $800\mu s$, $1,000\mu s$, $1,200\mu s$ and $1,400\mu s$ from the top to the bottom and from the left to the right. The vorticity scale is added for the initialization image (without vorticity).

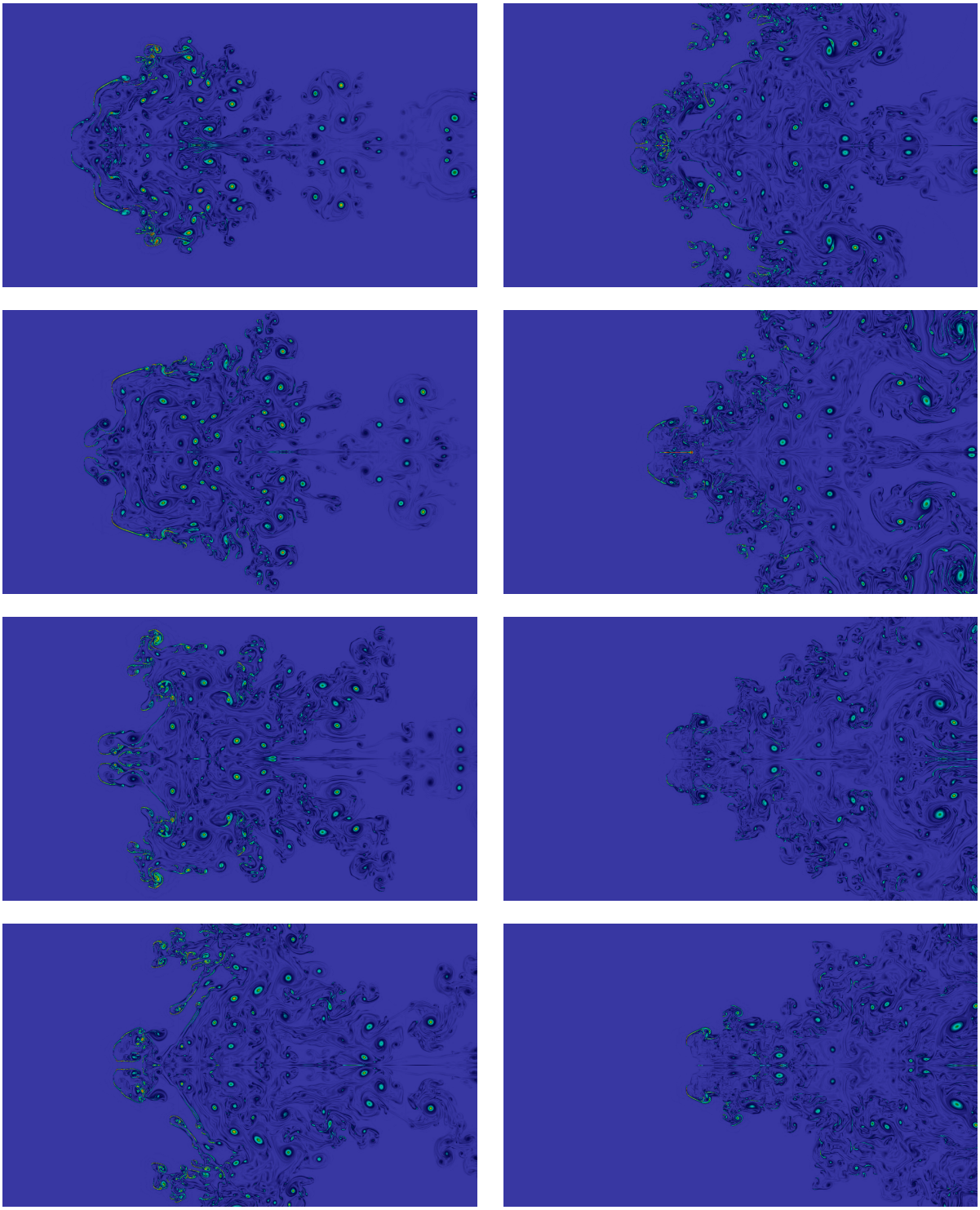

Figure 4.32: Magnified view of the simulation of the complete atomization of the water column by the high speed flow behind the shock wave of Mach number 1.3 in atmospheric air propagating from the left to the right. Vorticity results are shown at times $1,600\mu s$, $1,800\mu s$, $2,000\mu s$, $2,200\mu s$, $2,400\mu s$, $2,600\mu s$, $2,800\mu s$ and $3,000\mu s$ from the top to the bottom and from the left to the right.

4.4 3D: atomization of an isolated water droplet by a high speed flow

4.4.1 Problem presentation

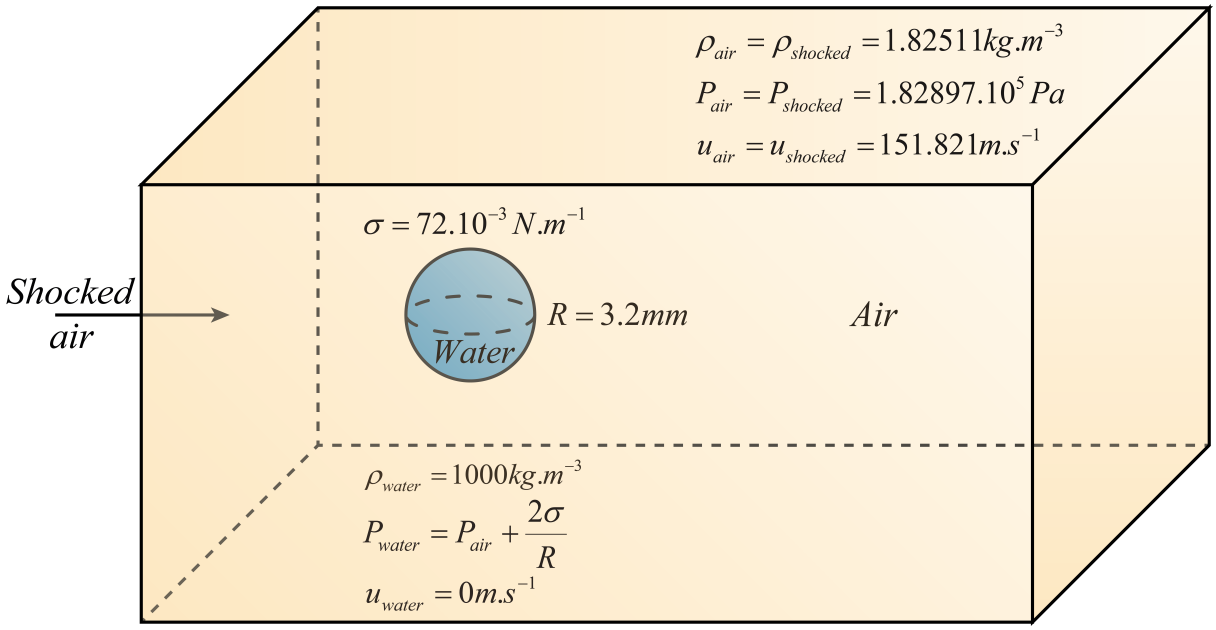

Figure 4.33: Sketch of the initialization for the 3D atomization test.

The setup of the 3D simulation of the atomization of an isolated water droplet by a high speed flow is not exactly an extension in the third coordinate of the 2D test that was presented in the previous section 4.3. The reason is due to the computational time. Indeed, the load balancing for AMR parallel simulations is not treated yet and the distribution of the CPU is done along the x-axis. Thus, when a shock is computed, it happens that the shock is fully treated on only one CPU, which deeply decreases the performances. To fix this problem, the initialization is not done with a shock moving across the domain but with the shocked state in the whole domain (except the droplet). The first instants are obviously not correct with respect to the shock-droplet interaction. Nevertheless, the aerobreakup dynamics are quickly similar as the shock is not directly breaking the droplet when moving across it, but the flow behind the shock (due to inertia of the droplet, contrary to bubble aerobreakup). One can add that a reflected shock appears at the droplet location but the performances are good because its curve allows to compute the shock on several CPU.

Then, the spherical water droplet is placed in an air environment already at a shocked state. The initial diameter of the droplet is $D = 6.4mm$ and the shocked state is the corresponding one behind a shock wave of Mach number 1.3 in atmospheric air (see Figure 4.33 for initialization sketch). The initial densities, pressures and velocities in the x-direction are:

- $\rho_{air} = \rho_{shocked} = 1.82511 kg.m^{-3}$, $P_{air} = P_{shocked} = 1.82897.10^5 Pa$ and $u_{air} = u_{shocked} = 151.821 m.s^{-1}$,
- $\rho_{water} = 1,000 kg.m^{-3}$, $P_{water} = P_{air} + 2\sigma/R$, and $u_{water} = 0 m.s^{-1}$.

The 3D computations are performed on a quarter of the whole domain with two symmetry boundary conditions. Shocked air is entering at the left boundary and the Newmann boundary conditions is used elsewhere. An AMR mesh containing initially 250x50x50 cells for a physical domain of 250mm x 50mm x 50mm is performed. Two tests are done where the maximum number of levels is $l_{max} = 3$ and 4, corresponding to an equivalent non-AMR mesh of $320,000,000$ and $2,560,000,000$ cells, respectively. The complete information concerning the AMR data is given in Table 4.4. The gradient refinement criterion is based on volume fraction, mixture pressure and mixture velocity variations.

Initial number of cells	l_{max}	Equivalent mesh	ϵ	ξ_{split}	ξ_{join}
250x50x50	3	320,000,000	0.02	0.02	0.02
250x50x50	4	2,560,000,000	0.02	0.02	0.02

Table 4.4: AMR data for the 3D atomization tests.

In the current case, two tests have been done, one with 3 levels of refinement and one with 4. An example of the mesh distribution is given in Figure 4.34 for the run with 4 levels of refinement and at time $t = 1,000 \mu s$. In the top image, the wireframe is represented for the performed domain with the mixture density gradients colors (dark red for strong gradients and dark blue for null ones). On the bottom image is shown three quarter of the complete domain with apparent surfaces. One of the two observable surfaces is shown with the mesh and the other without. The refinement at the highest level occurs around the droplet and at its rear due to the vortices that are involved.

4.4.2 Computational time analysis

One difficulty when computing simulations using AMR method is the estimation of the computational time it would involved, especially in the 3D case. Indeed, the mesh will refine where it matters, but when the physics that is happening is not known in detail, it is difficult to predict how long the runs could take.

Initially, the total numbers of cells for each test are similar (around 15% more for the test with 4 levels) and quickly the difference between the two tests greatly increases until a factor of almost 7 at $1,000 \mu s$ (Figure 4.35). This discrepancy should always increase and to predict the number of cells that is going to be involved is a difficult task. One can note that the maximum number of cells recorded for $l_{max} = 4$ is of $14,682,190$ which is only 0.57% of the cells that would have been involved with an equivalent non-AMR mesh ($2,560,000,000$ cells).

Concerning the computational time, a trend is observable between the two tests (Figure 4.36). Thus, it seems easier to predict the computational time for the run with the

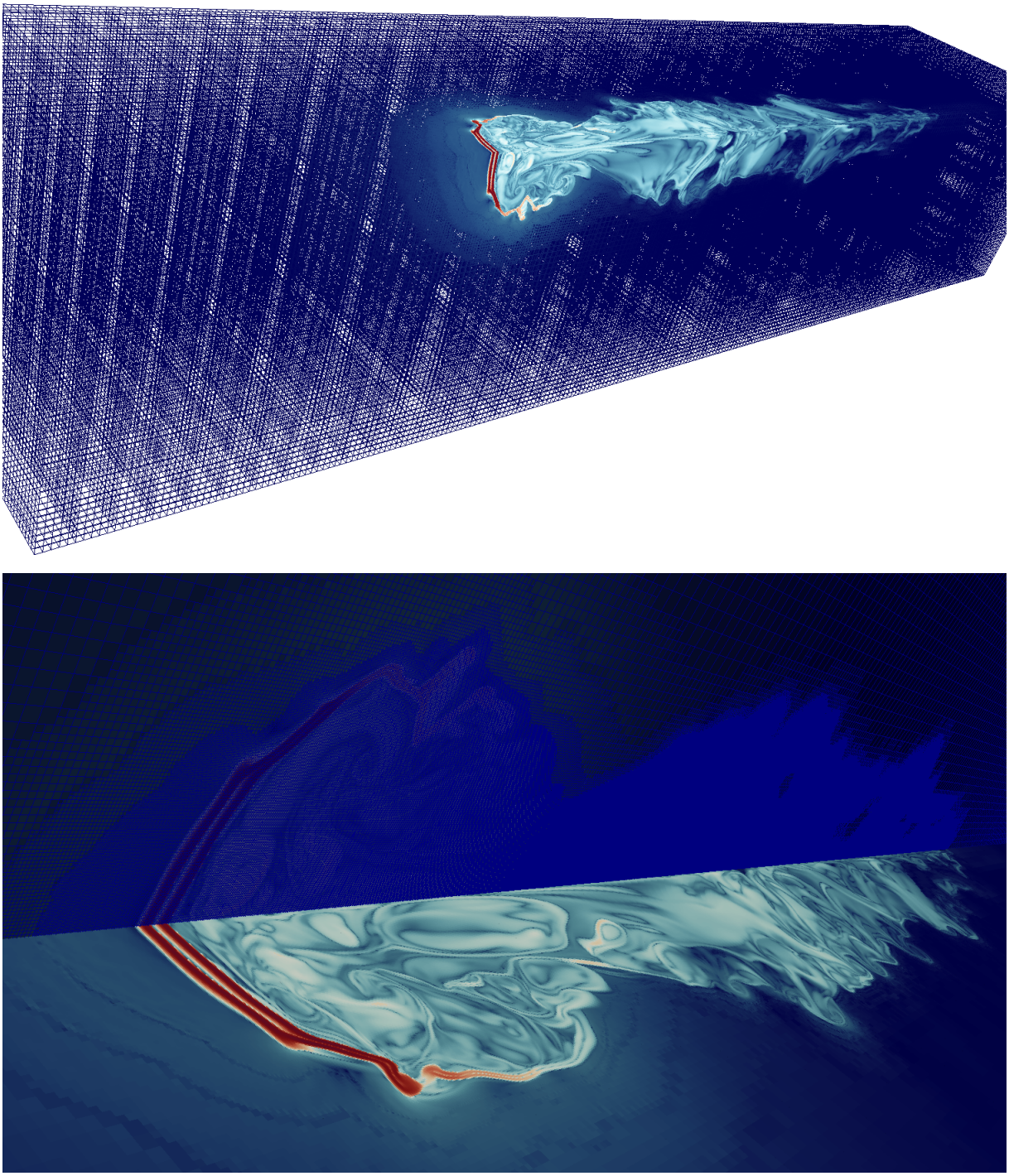

Figure 4.34: Two images with the mesh and the mixture density gradients apparent (strong gradients in dark red and nulls in dark blue) for the 3D atomization test with $l_{max} = 4$ at time $t = 1,000\mu s$. Refinement of the mesh is observable around the droplet and at its rear (vortices).

highest level of refinement when utilizing the one with one level less. In that case, the factor between the two is slightly lower than 10. Nevertheless, because the physics are described with less details and because the numerical diffusion has more impact, particularly for the long times, the run with only 3 levels of refinement will not capture all the physics, especially the reduced sizes droplets. Thus, it is still difficult to know if the run with the highest number of refinement level will or will not expand and then take more computational time than expected. This point is even more amplified in the case where the parallel load balancing is not undertaken. Note that the simulation with 4 refinement levels took about 43 days to reach $t = 1,000\mu s$ with 50 CPU.

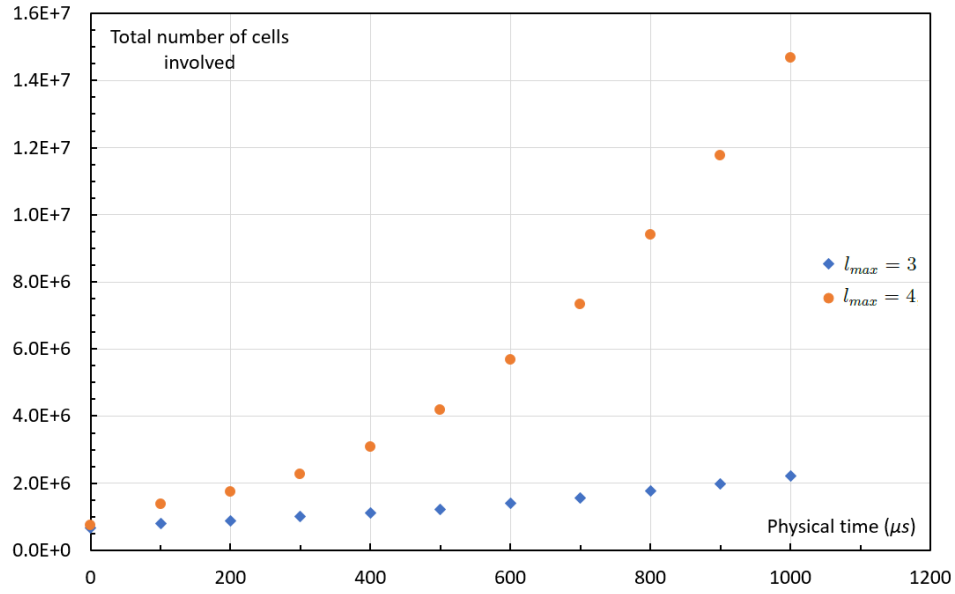

Figure 4.35: Total number of cells involved (also includes parent cells where few calculations are made) function of physical time for the 3D atomization tests.

4.4.3 Grid alignment issue

Apart from the long computational times, a problem arises and corresponds to the alignment of the solution with the grid. The Cartesian mesh combined with numerical methods privileges the directions aligned with the grid and the flow thus follows these guidelines. As a result, the physical solution is deteriorated and in the current case, the shape of the droplet tends to a square aligned or at 45° on the grid. An example of the contour of the droplet for the test with $l_{max} = 3$ is shown in Figure 4.37. This problem has already been raised by Meng [58] on a similar study for the atomization of an isolated droplet. Meng explains that this problem is permanent with numerical methods and is accentuated in 3D simulations. Highlights of these grid alignment phenomena in multiple works is shown, such as those of Khosla et al. [47] where the VOF method is used to investigate the aerobreakup of an ethanol drop in air, of Jalaal and Mehravaran [41] to study the initiation and growth of instabilities over droplets in a gas stream and in completely other contexts

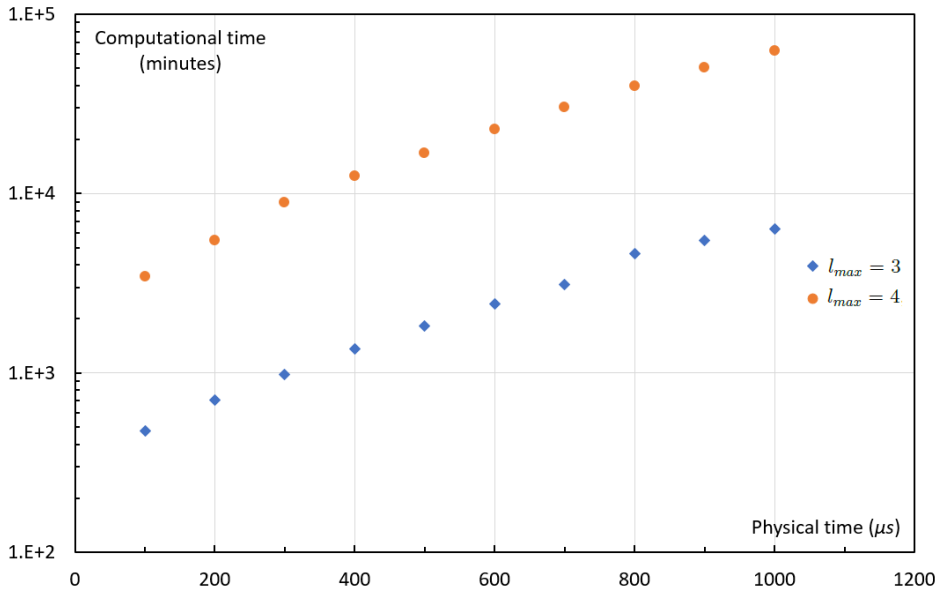

Figure 4.36: Computational time function of physical time for the 3D atomization tests.

such as astrophysics simulations [32]. A thorough study to remedy the problem was carried out with a large number of tests but without success. The solution opted by Meng was finally to use the cylindrical coordinates to match at best the directions of the flow with those of the grid. However, it is obvious that this solution is not satisfactory because it gives rise to other privileged directions which hinder the development of physics for long times when, in particular, reduced sizes droplets appear scattered in the field and are thus far from the center of the cylindrical mesh.

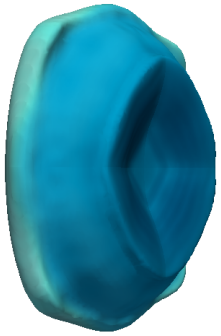

Figure 4.37: Side view of the droplet contour for the 3D atomization test with $l_{max} = 3$. Result is shown at time $600\mu s$ and using $\alpha = 0.5$ for the contour.

Figure 4.39 shows the observed differences between the droplet contours of the two runs for given times and with a front view. It is important to note that over time the square form becomes more critical when the refinement is not great enough. In our case,

the grid alignment tends to decrease with refinement and a mesh convergence can be assumed. This point bodes well for future work where deeper 3D study with comparison against experiments has to be performed. However, Figure 4.38 shows a visualization of the norm of the velocity on the contour of the droplet and then one can notice that the alignment is not completely canceled with grid refinement. It clearly appears according to the variables observed. One can thus conclude that to increase the resolution decreases the grid alignment but it should not be the only solution to undertake.

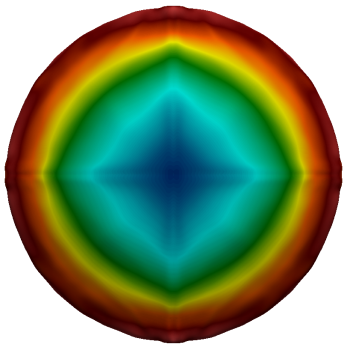

Figure 4.38: Front view of the contour of the droplet for the 3D atomization test with $l_{max} = 4$ and with visualization of the norm of the mixture velocity. Dark red shows strong mixture velocity norms and dark blue shows small ones. Result is shown at time $800\mu s$ and using $\alpha = 0.5$ for the contour.

4.4.4 Final results

In the context of this thesis, 3D simulations are performed to present the capacities of the model and numerical method that have been built. A comparison over time between the two runs with different maximum level of refinement is shown in Figure 4.40. The contour of the droplet is shown with visualization of the water density. The better accuracy of the results is well observable for the run with $l_{max} = 4$, particularly concerning the wave propagating on the sides of the droplet due to its compression and stretching. This wave is slowly making filaments all around the droplet and holes in these filaments are appearing at $1,000\mu s$, which later will produce the reduced sizes droplets. One can also note that the droplet for this last run with $l_{max} = 4$ is wider than the run with 3 levels, this point is explained by the numerical diffusion that has a weaker impact.

Figure 4.41 shows different views of the droplet contour for the test with $l_{max} = 4$ and at time $1,000\mu s$. $\alpha = 0.001$ is used for the contours to show all the filaments and potential reduced sizes droplets. Those last ones can also be interpreted as the mist of micrometer water droplets around and at the rear of the initial droplet. The mixture velocity norm is also shown on the right images to observe the speed of the smaller waves which occur on the surface of the droplet, and the velocity of the filaments and of the smaller droplets that are thrown away from the initial droplet (dark red shows strong mixture velocity norms and dark blue shows small ones).

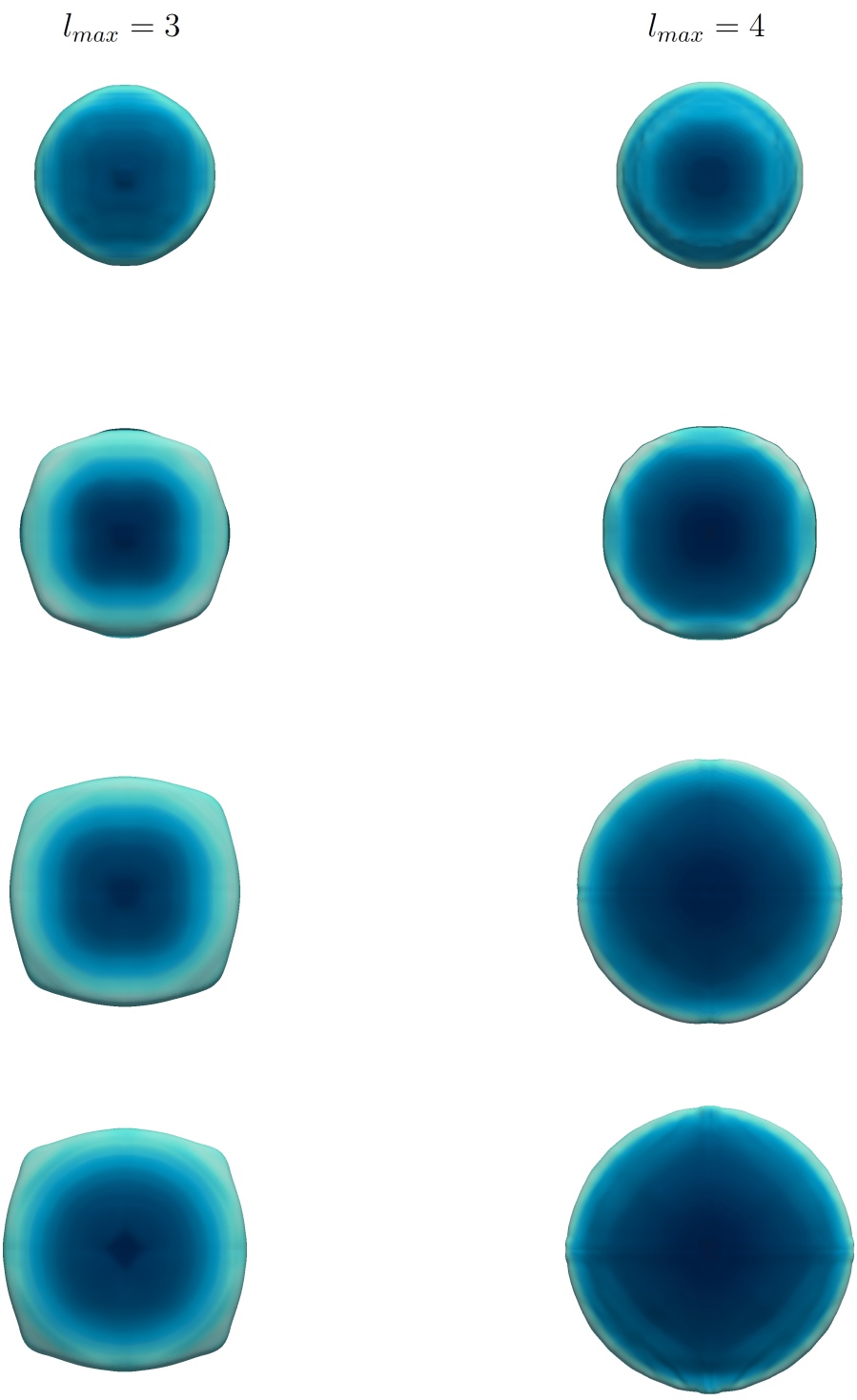

Figure 4.39: Front views of the droplet contour for the 3D atomization tests. $l_{max} = 3$ on the left column and $l_{max} = 4$ on the right one. Results are shown using $\alpha = 0.5$ for the contours and at times $300\mu s$, $500\mu s$, $700\mu s$ and $800\mu s$ from the top to the bottom.

$l_{max} = 3$

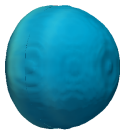

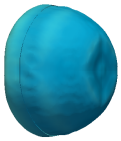

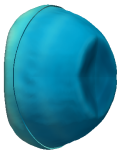

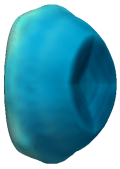

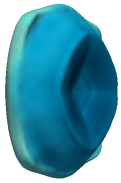

$l_{max} = 4$

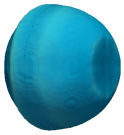

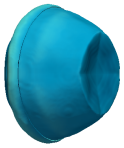

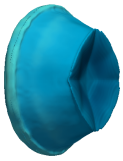

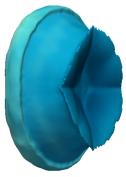

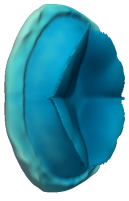

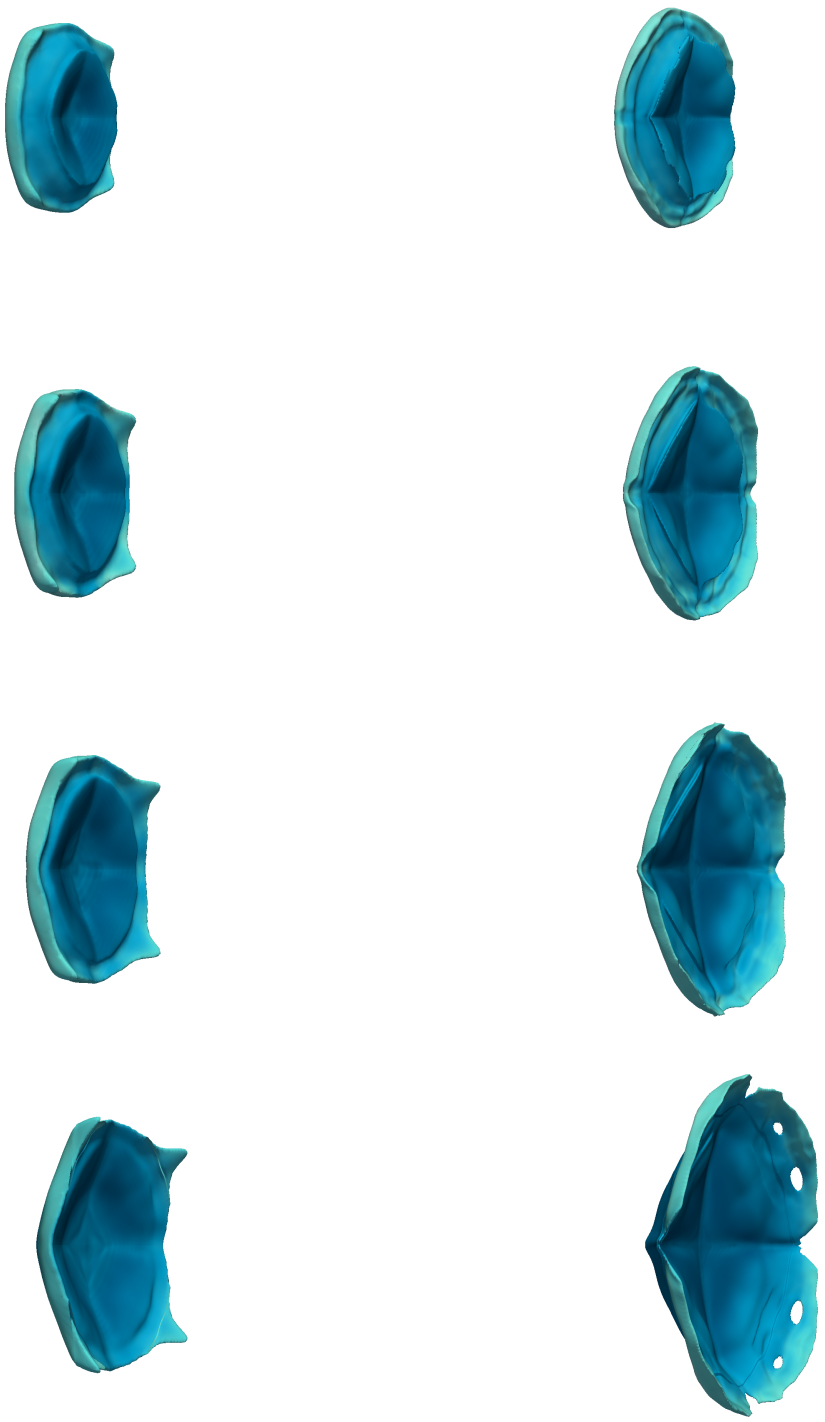

Figure 4.40: Side views of the droplet contour for the 3D atomization tests. $l_{max} = 3$ on the left column and $l_{max} = 4$ on the right one. Results are shown on two pages using $\alpha = 0.5$ for the contours and at times $200\mu s$, $300\mu s$, $400\mu s$, $500\mu s$, $600\mu s$, $700\mu s$, $800\mu s$, $900\mu s$ and $1,000\mu s$ from the top to the bottom.

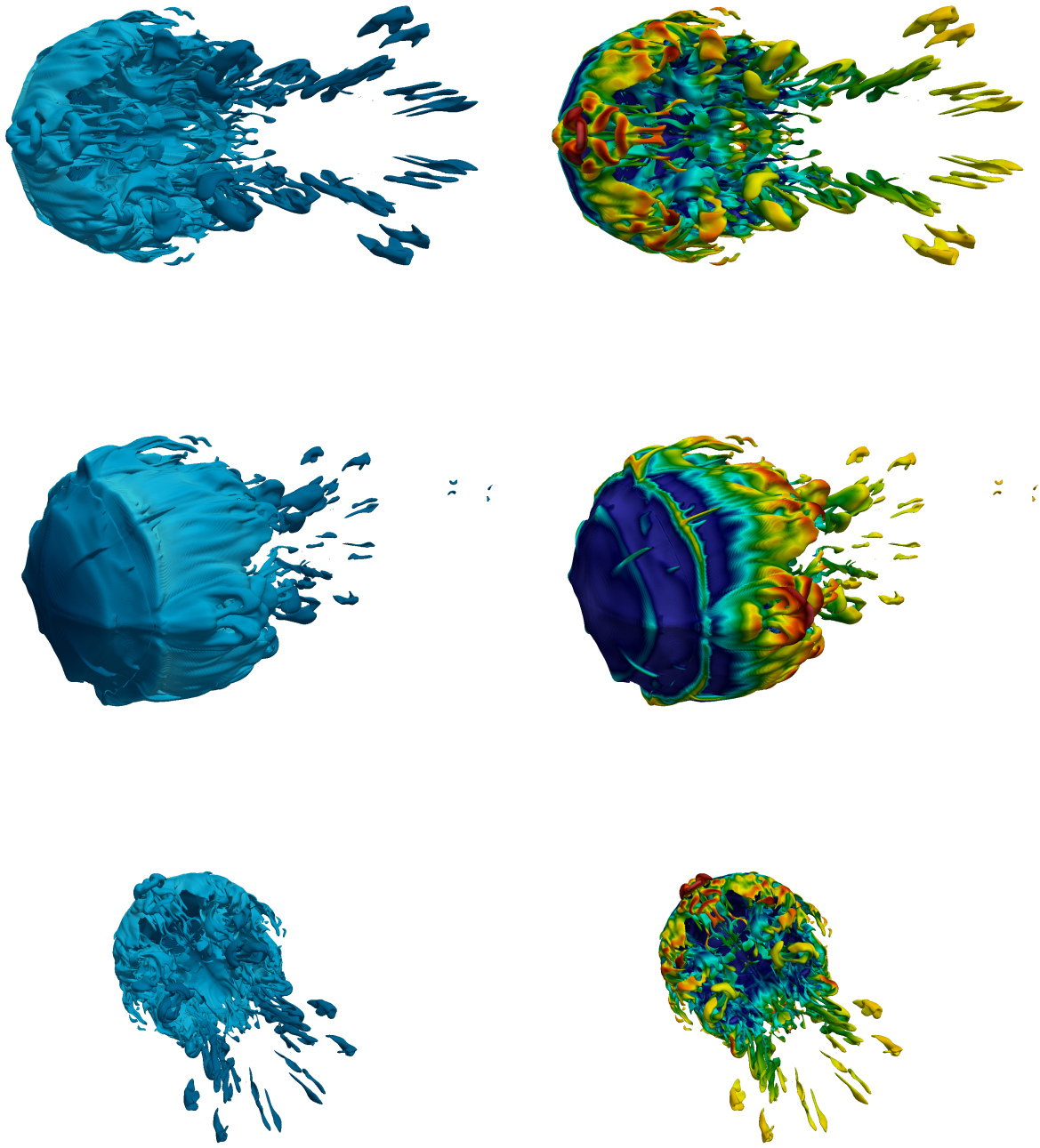

Figure 4.41: Different views of the droplet contour for the 3D atomization test with $l_{max} = 4$. Results are shown using $\alpha = 0.001$ for the contours and at time $1,000\mu s$. Blue contour visualization on the left column and mixture velocity norm visualization (dark red shows strong mixture velocity norms and dark blue shows small ones) on the right one.

Conclusion

In this manuscript was presented direct numerical simulations for studying the atomization of an isolated droplet by a high speed flow. The atomization can be divided into two distinct phases: the aerobreakup occurs first in the form of a flattening of the droplet (compression in the longitudinal flow direction and stretching in the transverse direction), also forming filaments, and then it ends by obtaining a multitude of reduced sizes droplets. The main objectives of this work were therefore to establish a model and a numerical method able to study these phenomena as accurately as possible.

Firstly, a new model is introduced that can handle multiphase compressible flows with capillary effects. Indeed, the compressible aspect for each of the fluids is an important element for the treatment of waves and fast dynamics during aerobreakup at high speed. Moreover, the Weber number tells us that the amplitude of the surface tension forces tends to the same order of magnitude as that of the inertial forces. The capillary effects therefore appear to have a significant impact on the behavior of the aerobreakup at long times and undoubtedly have an important impact on the formation of reduced sizes droplets. The model is in mechanical equilibrium, *i.e.*, with a mixture velocity and a mixture pressure. In addition, capillary effects are physically interpreted by a coupling between mechanics and geometry. Following the desire to distinguish these two phenomena, an additional equation is added to this model. It not only locates the interface but also allows to correctly carry out the study of hyperbolicity. A new numerical method of sub-models splitting that guarantees the conservation of mass, momentum and energy has also been built. Comparison with "source terms integration method" and with experiments have shown the advantages of the new model and numerical method. The simulation of an aerodynamic breakup of a water column induced by a shock wave showed that the method is able to treat accurately both pressure waves interaction and capillary effects in the same formulation.

Secondly, a new numerical method is required to obtain sufficient spatial resolution for reasonable computational costs. Thus, a new adaptive mesh refinement method, using not only a cells tree, but also cells boundaries trees, is proposed with an extension to multiphase flows. The addition of this second boundaries tree structure has the advantages of reducing the number of operations over a time step (cell neighboring searching is improved) and simplifying the general algorithm in comparison to a fully threaded tree method. The drawback is that the memory involved is not optimized. It is reasonably increased since the number of additional information stored for each cell boundary is relatively small in comparison to what is needed in a cell for the AMR structure as well as for the physical

quantities. The application of the new AMR method on different tests - transport, shock tube and capillary flows in 1D, 2D and 3D - was performed with quantitative comparisons regarding exact solutions or non-AMR method results in order to analyze the benefit of this new method. Computational time efficiency and reasonably memory cost have been shown.

Finally, the study on the atomization of an isolated droplet is presented. It involves an analysis on the different simulation parameters, as the slope limiters for the second order numerical method, the refinement criterion using velocity gradient, the symmetry approximation and the capillary effects. The comparison with the experiment of the atomization of a water column confirms the capacities of the model and method mentioned above to numerically simulate the different physical processes involved. In addition, essential information on atomization mechanisms, which cannot be exploited with experiments, are described and the objective of obtaining reduced sizes droplets is achieved.

Concerning the future works, some suggestions are proposed in order to keep on improving the simulation optimization and the knowledge about atomization of an isolated droplet:

- To optimize even more the choice of criteria for simulations. For example, the AMR numerical scheme includes a variation of the time step for each level and then it can generate stability issues when coupling with high order methods. If zero slope or Minmod slope limiter is considered for level transition zones, it would bring an additional stability that would allow the refinement at the maximum level on smaller areas.

- To extend the numerical method with interface sharpening methods. Note that it is important to pay attention to the conservation evolution when using these kinds of methods, especially for long simulation times.

- To perform load balancing for the parallel computation. The goal is to significantly reduce the computational time, especially in 3D simulations.

- To perform a study, as it was carried out for the capillary effects, on the influence of the viscous effects during the different processes of the atomization.

- To perform a more thorough experimental comparison on each of the available parameters and where the boundary conditions of the domain would be totally identical between the experiments and the simulations. The main advantage of the AMR method would be used, which is to compute simulations where large areas of the domain are not refined if the physics involved in these locations have smooth variations, *i.e.*, the computational time is optimized for a wide domain.

Appendices

Appendix A

Conservative form of the surface tension source terms of Brackbill et al. [8]

Consider the Kapila et al. [43] model with additional source terms that are the surface tension volume force of Brackbill et al. [8] and the work of this force, plus an additional equation for the color function:

$$\begin{cases} \frac{\partial \alpha_1}{\partial t} + \mathbf{u}\cdot\boldsymbol{\nabla}\alpha_1 - K\boldsymbol{\nabla}\cdot\mathbf{u} & = 0, \\ \frac{\partial \alpha_k\rho_k}{\partial t} + \boldsymbol{\nabla}\cdot(\alpha_k\rho_k\mathbf{u}) & = 0, \\ \frac{\partial \rho\mathbf{u}}{\partial t} + \boldsymbol{\nabla}\cdot\left(\rho\mathbf{u}\otimes\mathbf{u} + P\overline{\overline{I}}\right) & = -\sigma\boldsymbol{\nabla}\cdot\left(\frac{\boldsymbol{\nabla}c}{\|\boldsymbol{\nabla}c\|}\right)\boldsymbol{\nabla}c, \\ \frac{\partial \rho E}{\partial t} + \boldsymbol{\nabla}\cdot((\rho E + P)\,\mathbf{u}) & = -\sigma\boldsymbol{\nabla}\cdot\left(\frac{\boldsymbol{\nabla}c}{\|\boldsymbol{\nabla}c\|}\right)\boldsymbol{\nabla}c\cdot\mathbf{u}, \\ \frac{\partial c}{\partial t} + \mathbf{u}\cdot\boldsymbol{\nabla}c & = 0, \end{cases} \tag{A.1}$$

where the surface tension volume force is:

$$\mathbf{F}_v = -\sigma\boldsymbol{\nabla}\cdot\left(\frac{\boldsymbol{\nabla}c}{\|\boldsymbol{\nabla}c\|}\right)\boldsymbol{\nabla}c,$$

and its work is $\mathbf{F}_v\cdot\mathbf{u}$.

The goal is to express the surface tension source terms into a conservative form. First, the surface tension volume force can be rewritten under the following form:

$$\mathbf{F}_v = -\sigma\left(\boldsymbol{\nabla}\cdot\left(\frac{\boldsymbol{\nabla}c}{\|\boldsymbol{\nabla}c\|}\otimes\boldsymbol{\nabla}c\right) - \frac{\partial\boldsymbol{\nabla}c}{\partial\mathbf{x}}\frac{\boldsymbol{\nabla}c}{\|\boldsymbol{\nabla}c\|}\right).$$

But, the derivative of an absolute value is expressed:

$$\frac{\partial\|\boldsymbol{\nabla}c\|}{\partial\mathbf{x}} = \frac{\partial\boldsymbol{\nabla}c}{\partial\mathbf{x}}\mathrm{sign}\,(\boldsymbol{\nabla}c) = \frac{\partial\boldsymbol{\nabla}c}{\partial\mathbf{x}}\frac{\boldsymbol{\nabla}c}{\|\boldsymbol{\nabla}c\|},$$

thus:

$$\mathbf{F}_v = -\sigma\left(\boldsymbol{\nabla}\cdot\left(\frac{\boldsymbol{\nabla}c\otimes\boldsymbol{\nabla}c}{\|\boldsymbol{\nabla}c\|}\right) - \frac{\partial\|\boldsymbol{\nabla}c\|}{\partial\mathbf{x}}\right).$$

Second, one can note the following equality:

$$\boldsymbol{\nabla}\cdot\left(\|\boldsymbol{\nabla}c\|\overline{\overline{I}}\right)=\sum_{\alpha}\frac{\partial}{\partial x_{\alpha}}\mathbf{i}_{\alpha}\cdot\left(\|\boldsymbol{\nabla}c\|\sum_{\beta}\mathbf{i}_{\alpha}\mathbf{i}_{\alpha}\right)=\sum_{\alpha}\frac{\partial}{\partial x_{\alpha}}\|\boldsymbol{\nabla}c\|\mathbf{i}_{\alpha}=\frac{\partial\|\boldsymbol{\nabla}c\|}{\partial\mathbf{x}},$$

and finally for $\sigma=\text{cst}$, the surface tension volume force under a conservative form is:

$$\mathbf{F}_{v}=\boldsymbol{\nabla}\cdot\left(\sigma\left(\|\boldsymbol{\nabla}c\|\overline{\overline{I}}-\frac{\boldsymbol{\nabla}c\otimes\boldsymbol{\nabla}c}{\|\boldsymbol{\nabla}c\|}\right)\right),$$

$$\mathbf{F}_{v}=-\boldsymbol{\nabla}\cdot\overline{\overline{\Omega}},$$

with $\overline{\overline{\Omega}}$ being the capillary tensor given by:

$$\overline{\overline{\Omega}}=-\sigma\left(\|\boldsymbol{\nabla}c\|\overline{\overline{I}}-\frac{\boldsymbol{\nabla}c\otimes\boldsymbol{\nabla}c}{\|\boldsymbol{\nabla}c\|}\right).$$

One can note that the projector operator $\Pi=\overline{\overline{I}}-\mathbf{n}\otimes\mathbf{n}$, where $\mathbf{n}=\boldsymbol{\nabla}c/\|\boldsymbol{\nabla}c\|$, appears in this last expression.

The work of the surface tension volume force also has to be expressed under a conservative form:

$$\mathbf{F}_{v}\cdot\mathbf{u}=\boldsymbol{\nabla}\cdot\left(\sigma\left(\|\boldsymbol{\nabla}c\|\overline{\overline{I}}-\frac{\boldsymbol{\nabla}c\otimes\boldsymbol{\nabla}c}{\|\boldsymbol{\nabla}c\|}\right)\right)\cdot\mathbf{u}.$$

As the following formula is know:

$$\boldsymbol{\nabla}\cdot\left(\overline{\overline{A}}\cdot\mathbf{u}\right)=\boldsymbol{\nabla}\cdot\overline{\overline{A}}\cdot\mathbf{u}+\text{tr}\left(\overline{\overline{A}}\frac{\partial\mathbf{u}}{\partial\mathbf{x}}\right)=\boldsymbol{\nabla}\cdot\overline{\overline{A}}\cdot\mathbf{u}+\overline{\overline{A}}:\frac{\partial\mathbf{u}}{\partial\mathbf{x}},$$

the work can be expressed:

$$\mathbf{F}_{v}\cdot\mathbf{u}=\sigma\left(-\left(\|\boldsymbol{\nabla}c\|\overline{\overline{I}}-\frac{\boldsymbol{\nabla}c\otimes\boldsymbol{\nabla}c}{\|\boldsymbol{\nabla}c\|}\right):\frac{\partial\mathbf{u}}{\partial\mathbf{x}}+\boldsymbol{\nabla}\cdot\left(\left(\|\boldsymbol{\nabla}c\|\overline{\overline{I}}-\frac{\boldsymbol{\nabla}c\otimes\boldsymbol{\nabla}c}{\|\boldsymbol{\nabla}c\|}\right)\cdot\mathbf{u}\right)\right).$$

In this last expression, the right term is under a conservative form but the left term not yet. This left term can be rewrite:

$$\left(\|\boldsymbol{\nabla}c\|\overline{\overline{I}}-\frac{\boldsymbol{\nabla}c\otimes\boldsymbol{\nabla}c}{\|\boldsymbol{\nabla}c\|}\right):\frac{\partial\mathbf{u}}{\partial\mathbf{x}}=\|\boldsymbol{\nabla}c\|\boldsymbol{\nabla}\cdot\mathbf{u}-\frac{1}{\|\boldsymbol{\nabla}c\|}\left(\boldsymbol{\nabla}c\cdot\frac{\partial\mathbf{u}}{\partial\mathbf{x}}\right)\cdot\boldsymbol{\nabla}c. \tag{A.2}$$

Plus, the particle derivative of $\|\boldsymbol{\nabla}c\|$ is calculate:

$$\frac{d\|\boldsymbol{\nabla}c\|}{dt}=\frac{d\boldsymbol{\nabla}c}{dt}\cdot\text{sign}\left(\boldsymbol{\nabla}c\right)=\frac{d\boldsymbol{\nabla}c}{dt}\cdot\frac{\boldsymbol{\nabla}c}{\|\boldsymbol{\nabla}c\|},$$

where:

$$\frac{d\boldsymbol{\nabla}c}{dt}=\frac{\partial\boldsymbol{\nabla}c}{\partial t}+\mathbf{u}\cdot\frac{\partial\boldsymbol{\nabla}c}{\partial\mathbf{x}}.$$

Assuming that the Schwarz theorem can be applied here:

$$\frac{d\boldsymbol{\nabla} c}{dt} = \boldsymbol{\nabla}\left(\frac{\partial c}{\partial t}\right) + \mathbf{u}\cdot\boldsymbol{\nabla}\left(\frac{\partial c}{\partial \mathbf{x}}\right) = \boldsymbol{\nabla}\left(\frac{\partial c}{\partial t}\right) + \mathbf{u}\cdot\boldsymbol{\nabla}\left(\boldsymbol{\nabla} c\right),$$

and using the following:

$$\boldsymbol{\nabla}\left(\mathbf{u}\cdot\boldsymbol{\nabla} c\right) = \mathbf{u}\cdot\boldsymbol{\nabla}\left(\boldsymbol{\nabla} c\right) + \boldsymbol{\nabla} c\cdot\frac{\partial \mathbf{u}}{\partial \mathbf{x}},$$

the particle derivative of $\boldsymbol{\nabla} c$ is:

$$\frac{d\boldsymbol{\nabla} c}{dt} = \boldsymbol{\nabla}\left(\frac{\partial c}{\partial t}\right) + \boldsymbol{\nabla}\left(\mathbf{u}\cdot\boldsymbol{\nabla} c\right) - \boldsymbol{\nabla} c\cdot\frac{\partial \mathbf{u}}{\partial \mathbf{x}}.$$

$$\frac{d\boldsymbol{\nabla} c}{dt} = \boldsymbol{\nabla}\left(\frac{dc}{dt}\right) - \boldsymbol{\nabla} c\cdot\frac{\partial \mathbf{u}}{\partial \mathbf{x}}.$$

But, the particle derivative of the color function is zero, so the preceding equation reduces to the following expression:

$$\frac{d\boldsymbol{\nabla} c}{dt} = -\boldsymbol{\nabla} c\cdot\frac{\partial \mathbf{u}}{\partial \mathbf{x}}.$$

And then, the particle derivative of $\|\boldsymbol{\nabla} c\|$ is obtain:

$$\frac{d\|\boldsymbol{\nabla} c\|}{dt} = -\left(\boldsymbol{\nabla} c\cdot\frac{\partial \mathbf{u}}{\partial \mathbf{x}}\right)\cdot\frac{\boldsymbol{\nabla} c}{\|\boldsymbol{\nabla} c\|}.$$

Thus, the left term (A.2) becomes:

$$\left(\|\boldsymbol{\nabla} c\|\overline{\overline{I}} - \frac{\boldsymbol{\nabla} c\otimes\boldsymbol{\nabla} c}{\|\boldsymbol{\nabla} c\|}\right) : \frac{\partial \mathbf{u}}{\partial \mathbf{x}} = \|\boldsymbol{\nabla} c\|\boldsymbol{\nabla}\cdot\mathbf{u} + \frac{d\|\boldsymbol{\nabla} c\|}{dt} = \|\boldsymbol{\nabla} c\|\boldsymbol{\nabla}\cdot\mathbf{u} + \frac{\partial\|\boldsymbol{\nabla} c\|}{\partial t} + \mathbf{u}\cdot\boldsymbol{\nabla}\left(\|\boldsymbol{\nabla} c\|\right),$$

$$\left(\|\boldsymbol{\nabla} c\|\overline{\overline{I}} - \frac{\boldsymbol{\nabla} c\otimes\boldsymbol{\nabla} c}{\|\boldsymbol{\nabla} c\|}\right) : \frac{\partial \mathbf{u}}{\partial \mathbf{x}} = \frac{\partial\|\boldsymbol{\nabla} c\|}{\partial t} + \boldsymbol{\nabla}\cdot\left(\|\boldsymbol{\nabla} c\|\mathbf{u}\right),$$

and the surface tension work is:

$$\mathbf{F}_v\cdot\mathbf{u} = \sigma\left(-\frac{\partial\|\boldsymbol{\nabla} c\|}{\partial t} - \boldsymbol{\nabla}\cdot\left(\|\boldsymbol{\nabla} c\|\mathbf{u}\right) + \boldsymbol{\nabla}\cdot\left(\left(\|\boldsymbol{\nabla} c\|\overline{\overline{I}} - \frac{\boldsymbol{\nabla} c\otimes\boldsymbol{\nabla} c}{\|\boldsymbol{\nabla} c\|}\right)\cdot\mathbf{u}\right)\right).$$

$$\mathbf{F}_v\cdot\mathbf{u} = -\left(\frac{\partial\varepsilon_\sigma}{\partial t} + \boldsymbol{\nabla}\cdot\left(\varepsilon_\sigma\mathbf{u} + \overline{\overline{\Omega}}\cdot\mathbf{u}\right)\right).$$

where the capillary energy $\varepsilon_\sigma = \sigma\|\boldsymbol{\nabla} c\|$ appears.

Finally, system (A.1) becomes:

$$\begin{cases} \frac{\partial\alpha_1}{\partial t} + \mathbf{u}\cdot\boldsymbol{\nabla}\alpha_1 - K\boldsymbol{\nabla}\cdot\mathbf{u} & = 0, \\ \frac{\partial\alpha_k\rho_k}{\partial t} + \boldsymbol{\nabla}\cdot\left(\alpha_k\rho_k\mathbf{u}\right) & = 0, \\ \frac{\partial\rho\mathbf{u}}{\partial t} + \boldsymbol{\nabla}\cdot\left(\rho\mathbf{u}\otimes\mathbf{u} + P\overline{\overline{I}} + \overline{\overline{\Omega}}\right) & = 0, \\ \frac{\partial\rho E+\varepsilon_\sigma}{\partial t} + \boldsymbol{\nabla}\cdot\left(\left(\rho E + \varepsilon_\sigma + P\right)\mathbf{u} + \overline{\overline{\Omega}}\cdot\mathbf{u}\right) & = 0, \\ \frac{\partial c}{\partial t} + \mathbf{u}\cdot\boldsymbol{\nabla} c & = 0. \end{cases}$$

Appendix B

Variational principle for compressible mixtures with capillary effects

Consider a continuum characterized by the Lagrangian:

$$L = \rho\left(\frac{\|\mathbf{u}\|^2}{2} - e\right) - \sigma\|\boldsymbol{\nabla} c\|.$$

Here $\rho = \alpha_1\rho_1 + \alpha_2\rho_2$ is the mixture density, $e = Y_1 e_1 + Y_2 e_2$ is the mixture specific energy, $Y_i = \alpha_i\rho_i/\rho$ are the mass fractions, σ is the surface tension coefficient, c is the color function.

Consider the Hamilton action:

$$a = \int_{t_1}^{t_2}\int_D L dt dD, \tag{B.1}$$

where t_1 and t_2 are fixed time instants, and D is a material fluid volume.

The governing equations are extremal curves of the Hamilton action under the following constraints:

$$\begin{aligned}
&\frac{\partial\rho}{\partial t} + \boldsymbol{\nabla}\cdot(\rho\mathbf{u}) = 0,\\
&\frac{\partial Y_1}{\partial t} + \mathbf{u}\cdot\boldsymbol{\nabla}(Y_1) = 0,\\
&\frac{\partial s_1}{\partial t} + \mathbf{u}\cdot\boldsymbol{\nabla}(s_1) = 0,\\
&\frac{\partial s_2}{\partial t} + \mathbf{u}\cdot\boldsymbol{\nabla}(s_2) = 0,\\
&\frac{\partial c}{\partial t} + \mathbf{u}\cdot\boldsymbol{\nabla}(c) = 0.
\end{aligned} \tag{B.2}$$

The Eulerian variations of the unknown variables in terms of virtual displacement $\delta\mathbf{x}$ are given by (see Gavrilyuk [22] for details):

$$\delta\rho = -\boldsymbol{\nabla}\cdot(\rho\delta\mathbf{x}),$$

$$\delta Y_1 = -\boldsymbol{\nabla} Y_1 \cdot \delta\mathbf{x},$$
$$\delta s_1 = -\boldsymbol{\nabla} s_1 \cdot \delta\mathbf{x},$$
$$\delta s_2 = -\boldsymbol{\nabla} s_2 \cdot \delta\mathbf{x},$$
$$\delta c = -\boldsymbol{\nabla} c \cdot \delta\mathbf{x},$$
$$\delta\mathbf{u} = \frac{\partial \delta\mathbf{x}}{\partial t} + \frac{\partial \delta\mathbf{x}}{\partial \mathbf{x}} \cdot \mathbf{u} - \frac{\partial \mathbf{u}}{\partial \mathbf{x}} \cdot \delta\mathbf{x}.$$

Taking the variation of the Hamilton action (B.1) under the boundary conditions:

$$\delta\mathbf{x}|_{\partial D} = 0,$$
$$\delta\mathbf{x}|_{t=t_1} = 0,$$
$$\delta\mathbf{x}|_{t=t_2} = 0,$$

one can obtain the momentum equation:

$$\rho\left(\frac{\partial \mathbf{u}}{\partial t} + \frac{\partial \mathbf{u}}{\partial \mathbf{x}} \cdot \mathbf{u}\right) + \boldsymbol{\nabla} P = -\sigma\left(\boldsymbol{\nabla} \cdot \mathbf{n}\right)\boldsymbol{\nabla} c,$$

with $\mathbf{n} = \boldsymbol{\nabla} c / \|\boldsymbol{\nabla} c\|$.

The equation is exactly the same as in Brackbill *et al.* [8] for the one component case. It can be written in conservative form:

$$\frac{\partial \rho\mathbf{u}}{\partial t} + \boldsymbol{\nabla} \cdot \left(\rho\mathbf{u} \otimes \mathbf{u} + P\overline{\overline{I}} + \overline{\overline{\Omega}}\right) = 0,$$

where the capillary tensor $\overline{\overline{\Omega}}$ is given by:

$$\overline{\overline{\Omega}} = -\sigma\|\boldsymbol{\nabla} c\|\left(\overline{\overline{I}} - \mathbf{n} \otimes \mathbf{n}\right).$$

The variation of the Hamilton action with respect to the volume fraction gives as the pressure equilibrium condition:

$$P_1 = P_2 = P = \alpha_1 P_1 + \alpha_2 P_2.$$

resulting to the non-conservative equation (2.2) for α_1 (see Gavrilyuk [22] for details).

Using the constraints on the entropies and mass fractions of each phase, the mixture entropy equation is given by:

$$\frac{\partial s}{\partial t} + \mathbf{u} \cdot \boldsymbol{\nabla}\left(s\right) = 0.$$

The mixture entropy, mass and momentum equations admit the following mixture total energy equation:

$$\frac{\partial \rho E}{\partial t} + \boldsymbol{\nabla} \cdot \left(\left(\rho E + P\right)\mathbf{u}\right) = -\left(\boldsymbol{\nabla} \cdot \overline{\overline{\Omega}}\right) \cdot \mathbf{u}.$$

To transform the previous equation to a fully conservative form, the following relation is used:

$$\left(\boldsymbol{\nabla} \cdot \overline{\overline{\Omega}}\right) \cdot \mathbf{u} = \boldsymbol{\nabla} \cdot \left(\overline{\overline{\Omega}} \cdot \mathbf{u}\right) - \overline{\overline{\Omega}} : \frac{\partial \mathbf{u}}{\partial \mathbf{x}},$$

where the right term still needs to be transformed. It can be developed as:

$$\sigma\left(\|\boldsymbol{\nabla} c\|\overline{\overline{I}} - \frac{\boldsymbol{\nabla} c \otimes \boldsymbol{\nabla} c}{\|\boldsymbol{\nabla} c\|}\right) : \frac{\partial \mathbf{u}}{\partial \mathbf{x}} = \sigma\left(\|\boldsymbol{\nabla} c\|\boldsymbol{\nabla}\cdot\mathbf{u} - \left(\boldsymbol{\nabla} c \cdot \frac{\partial \mathbf{u}}{\partial \mathbf{x}}\right)\cdot\frac{\boldsymbol{\nabla} c}{\|\boldsymbol{\nabla} c\|}\right). \tag{B.3}$$

Using the material derivative equation of $\|\boldsymbol{\nabla} c\|$:

$$\frac{d\|\boldsymbol{\nabla} c\|}{dt} = \frac{d\boldsymbol{\nabla} c}{dt}\cdot\frac{\boldsymbol{\nabla} c}{\|\boldsymbol{\nabla} c\|}, \tag{B.4}$$

with the material derivative operator $d(\cdot)/dt = \partial(\cdot)/\partial t + \mathbf{u}\cdot\boldsymbol{\nabla}(\cdot)$ and the Schwarz theorem, we have:

$$\frac{d\boldsymbol{\nabla} c}{dt} = \boldsymbol{\nabla}\left(\frac{dc}{dt}\right) - \boldsymbol{\nabla} c\cdot\frac{\partial \mathbf{u}}{\partial \mathbf{x}}. \tag{B.5}$$

Hence with equations (B.2) and (B.5), equation (B.4) is rewritten as:

$$\frac{d\|\boldsymbol{\nabla} c\|}{dt} = -\left(\boldsymbol{\nabla} c\cdot\frac{\partial \mathbf{u}}{\partial \mathbf{x}}\right)\cdot\frac{\boldsymbol{\nabla} c}{\|\boldsymbol{\nabla} c\|}.$$

Thus relation (B.3) is now developed as:

$$\begin{aligned}\sigma\left(\|\boldsymbol{\nabla} c\|\overline{\overline{I}} - \frac{\boldsymbol{\nabla} c \otimes \boldsymbol{\nabla} c}{\|\boldsymbol{\nabla} c\|}\right) : \frac{\partial \mathbf{u}}{\partial \mathbf{x}} &= \sigma\left(\|\boldsymbol{\nabla} c\|\boldsymbol{\nabla}\cdot\mathbf{u} + \frac{d\|\boldsymbol{\nabla} c\|}{dt}\right)\\ &= \frac{\partial \sigma\|\boldsymbol{\nabla} c\|}{\partial t} + \boldsymbol{\nabla}\cdot\left(\sigma\|\boldsymbol{\nabla} c\|\mathbf{u}\right).\end{aligned}$$

Finally, the energy conservation law is:

$$\frac{\partial \rho E + \varepsilon_\sigma}{\partial t} + \boldsymbol{\nabla}\cdot\left(\left(\rho E + \varepsilon_\sigma + P\right)\mathbf{u} + \overline{\overline{\Omega}}\cdot\mathbf{u}\right) = 0,$$

with the capillary energy term $\varepsilon_\sigma = \sigma\|\boldsymbol{\nabla} c\|$.

Appendix C

Eigenvectors of model (2.3)

Remind that model (2.3) can be written under a vector form (2.6) with the vector $\mathbf{W}$ and the matrix $\overline{\overline{A}}$ defined by:

$$\mathbf{W} = [\alpha_1, u, v, w, P, w_1, w_2, w_3, s_1, s_2, Y_1, c]^T,$$

$$\overline{\overline{A}}(\mathbf{W}) = \begin{bmatrix} u & -K & 0 & 0 & 0 & 0 & 0 & 0 & 0 & 0 & 0 & 0 \\ 0 & u & 0 & 0 & \frac{1}{\rho} & \frac{1}{\rho}\frac{\partial \Omega_{11}}{\partial w_1} & \frac{1}{\rho}\frac{\partial \Omega_{11}}{\partial w_2} & \frac{1}{\rho}\frac{\partial \Omega_{11}}{\partial w_3} & 0 & 0 & 0 & 0 \\ 0 & 0 & u & 0 & 0 & \frac{1}{\rho}\frac{\partial \Omega_{12}}{\partial w_1} & \frac{1}{\rho}\frac{\partial \Omega_{12}}{\partial w_2} & \frac{1}{\rho}\frac{\partial \Omega_{12}}{\partial w_3} & 0 & 0 & 0 & 0 \\ 0 & 0 & 0 & u & 0 & \frac{1}{\rho}\frac{\partial \Omega_{13}}{\partial w_1} & \frac{1}{\rho}\frac{\partial \Omega_{13}}{\partial w_2} & \frac{1}{\rho}\frac{\partial \Omega_{13}}{\partial w_3} & 0 & 0 & 0 & 0 \\ 0 & \rho a^2 & 0 & 0 & u & 0 & 0 & 0 & 0 & 0 & 0 & 0 \\ 0 & w_1 & w_2 & w_3 & 0 & u & 0 & 0 & 0 & 0 & 0 & 0 \\ 0 & 0 & 0 & 0 & 0 & 0 & u & 0 & 0 & 0 & 0 & 0 \\ 0 & 0 & 0 & 0 & 0 & 0 & 0 & u & 0 & 0 & 0 & 0 \\ 0 & 0 & 0 & 0 & 0 & 0 & 0 & 0 & u & 0 & 0 & 0 \\ 0 & 0 & 0 & 0 & 0 & 0 & 0 & 0 & 0 & u & 0 & 0 \\ 0 & 0 & 0 & 0 & 0 & 0 & 0 & 0 & 0 & 0 & u & 0 \\ 0 & 0 & 0 & 0 & 0 & 0 & 0 & 0 & 0 & 0 & 0 & u \end{bmatrix}$$

The corresponding eigenvalues are real, explicit and given by:

$$\lambda_{1,2,3,4,5,6,7,8} = u,$$

$$\lambda_{9,10} = u \pm a_s,$$

$$\lambda_{11,12} = u \pm a_c,$$

where:

$$a_s^2 = \frac{a^2 + b + \sqrt{(a^2+b)^2 - 4a^2 b\,(n_2^2 + n_3^2)}}{2},$$

$$a_c^2 = \frac{a^2 + b - \sqrt{(a^2+b)^2 - 4a^2 b\,(n_2^2 + n_3^2)}}{2},$$

a is the Wood mixture speed of sound previously defined (2.5) and:

$$b = \frac{\sigma \|\mathbf{w}\|}{\rho} \left(n_2^2 + n_3^2 \right).$$

The system is hyperbolic if the multiple eigenvalues $\lambda = u$ have exactly 8 linearly independent eigenvectors $\mathbf{R}$. 5 of them are straightforward:

$$\mathbf{R}_1 = \begin{bmatrix} 1 \\ 0 \\ 0 \\ 0 \\ 0 \\ 0 \\ 0 \\ 0 \\ 0 \\ 0 \\ 0 \\ 0 \end{bmatrix} \qquad \mathbf{R}_2 = \begin{bmatrix} 0 \\ 0 \\ 0 \\ 0 \\ 0 \\ 0 \\ 0 \\ 0 \\ 1 \\ 0 \\ 0 \\ 0 \end{bmatrix} \qquad \mathbf{R}_3 = \begin{bmatrix} 0 \\ 0 \\ 0 \\ 0 \\ 0 \\ 0 \\ 0 \\ 0 \\ 0 \\ 1 \\ 0 \\ 0 \end{bmatrix}$$

$$\mathbf{R}_4 = \begin{bmatrix} 0 \\ 0 \\ 0 \\ 0 \\ 0 \\ 0 \\ 0 \\ 0 \\ 0 \\ 0 \\ 1 \\ 0 \end{bmatrix} \qquad \mathbf{R}_5 = \begin{bmatrix} 0 \\ 0 \\ 0 \\ 0 \\ 0 \\ 0 \\ 0 \\ 0 \\ 0 \\ 0 \\ 0 \\ 1 \end{bmatrix}$$

And the 3 last eigenvectors for $\lambda = u$ have to be found using the following reduced matrix:

$$\overline{\overline{a}} = \begin{bmatrix} u & 0 & 0 & \frac{1}{\rho} & \frac{1}{\rho}\frac{\partial \Omega_{11}}{\partial w_1} & \frac{1}{\rho}\frac{\partial \Omega_{11}}{\partial w_2} & \frac{1}{\rho}\frac{\partial \Omega_{11}}{\partial w_3} \\ 0 & u & 0 & 0 & \frac{1}{\rho}\frac{\partial \Omega_{12}}{\partial w_1} & \frac{1}{\rho}\frac{\partial \Omega_{12}}{\partial w_2} & \frac{1}{\rho}\frac{\partial \Omega_{12}}{\partial w_3} \\ 0 & 0 & u & 0 & \frac{1}{\rho}\frac{\partial \Omega_{13}}{\partial w_1} & \frac{1}{\rho}\frac{\partial \Omega_{13}}{\partial w_2} & \frac{1}{\rho}\frac{\partial \Omega_{13}}{\partial w_3} \\ \rho a^2 & 0 & 0 & u & 0 & 0 & 0 \\ w_1 & w_2 & w_3 & 0 & u & 0 & 0 \\ 0 & 0 & 0 & 0 & 0 & u & 0 \\ 0 & 0 & 0 & 0 & 0 & 0 & u \end{bmatrix}$$

The corresponding reduced eigenvectors $\mathbf{r}$ are the solutions of $\left(\overline{\overline{a}} - u\overline{\overline{I}} \right) \mathbf{r} = \mathbf{0}$, where $\mathbf{r}$

is written as:

$$\mathbf{r} = [r_1, r_2, r_3, r_4, r_5, r_6, r_7]^T.$$

3 distinct systems of equations results from this equality:

$$\rho a^2 r_1 = 0,$$

$$w_1 r_1 + w_2 r_2 + w_3 r_3 = 0,$$

$$\begin{bmatrix} \frac{1}{\rho} r_4 \\ 0 \\ 0 \end{bmatrix} + \overline{\overline{C}} \begin{bmatrix} r_5 \\ r_6 \\ r_7 \end{bmatrix} = \begin{bmatrix} 0 \\ 0 \\ 0 \end{bmatrix}$$

where $\overline{\overline{C}}$ is the matrix with the only capillary terms:

$$\overline{\overline{C}} = \begin{bmatrix} \frac{1}{\rho}\frac{\partial \Omega_{11}}{\partial w_1} & \frac{1}{\rho}\frac{\partial \Omega_{11}}{\partial w_2} & \frac{1}{\rho}\frac{\partial \Omega_{11}}{\partial w_3} \\ \frac{1}{\rho}\frac{\partial \Omega_{12}}{\partial w_1} & \frac{1}{\rho}\frac{\partial \Omega_{12}}{\partial w_2} & \frac{1}{\rho}\frac{\partial \Omega_{12}}{\partial w_3} \\ \frac{1}{\rho}\frac{\partial \Omega_{13}}{\partial w_1} & \frac{1}{\rho}\frac{\partial \Omega_{13}}{\partial w_2} & \frac{1}{\rho}\frac{\partial \Omega_{13}}{\partial w_3} \end{bmatrix}$$

A solution of the first two equations is: $r_1 = 0$, $r_2 = -\eta w_3$ and $r_3 = \eta w_2$, where η is any real constant. If the matrix $\overline{\overline{C}}$ is invertible, the components r_5, r_6 and r_7 are uniquely defined for a given r_4. First, the derivatives of the capillary tensor terms are:

$$\frac{\partial \Omega_{11}}{\partial w_1} = \frac{\sigma}{\rho} n_1 \left(n_2^2 + n_3^2\right),$$

$$\frac{\partial \Omega_{11}}{\partial w_2} = \frac{\sigma}{\rho} n_2 \left(n_2^2 + n_3^2 - 2\right),$$

$$\frac{\partial \Omega_{11}}{\partial w_3} = \frac{\sigma}{\rho} n_3 \left(n_2^2 + n_3^2 - 2\right),$$

$$\frac{\partial \Omega_{12}}{\partial w_1} = \frac{\sigma}{\rho} n_2 \left(n_2^2 + n_3^2\right),$$

$$\frac{\partial \Omega_{12}}{\partial w_2} = \frac{\sigma}{\rho} n_1 \left(n_1^2 + n_3^2\right),$$

$$\frac{\partial \Omega_{12}}{\partial w_3} = \frac{\sigma}{\rho} n_1 n_2 n_3,$$

$$\frac{\partial \Omega_{13}}{\partial w_1} = \frac{\sigma}{\rho} n_3 \left(n_2^2 + n_3^2\right),$$

$$\frac{\partial \Omega_{13}}{\partial w_2} = \frac{\sigma}{\rho} n_1 n_2 n_3,$$

$$\frac{\partial \Omega_{13}}{\partial w_3} = \frac{\sigma}{\rho} n_1 \left(n_1^2 + n_2^2\right).$$

And then the determinant of the matrix $\overline{\overline{C}}$ is:

$$\det\left(\overline{\overline{\mathrm{C}}}\right) = \left(\frac{\sigma}{\rho}\right)^3 \mathrm{n}_1(\mathrm{n}_2^2(\mathrm{n}_1^2+\mathrm{n}_2^2)^3 + \mathrm{n}_3^2(\mathrm{n}_1^2+\mathrm{n}_3^2)^3$$

$$+6n_1^4n_2^2n_3^2 + 9n_1^2n_2^4n_3^2 + 4n_2^6n_3^2 + 9n_1^2n_2^2n_3^4 + 6n_2^4n_3^4 + 4n_2^2n_3^6).$$

The determinant is non-zero as long as n_1 is non-vanishing, which is numerically always the case. Thus:

$$\begin{bmatrix} r_5 \\ r_6 \\ r_7 \end{bmatrix} = -r_4\overline{\overline{C}}^{-1} \begin{bmatrix} \frac{1}{\rho} \\ 0 \\ 0 \end{bmatrix}$$

Finally the resulting reduced eigenvectors are:

$$\mathbf{r} = \begin{bmatrix} 0 \\ -\eta w_3 \\ \eta w_2 \\ r_4 \\ -r_4\overline{\overline{C}}^{-1} \begin{bmatrix} \frac{1}{\rho} \\ 0 \\ 0 \end{bmatrix} \end{bmatrix}$$

Thus, only a two-parameter family of eigenvectors exists. Linearly independent eigenvectors can be given as:

$$\mathbf{R}_6 = \begin{bmatrix} 0 \\ 0 \\ -w_3 \\ w_2 \\ 0 \\ 0 \\ 0 \\ 0 \\ 0 \\ 0 \\ 0 \\ 0 \end{bmatrix} \qquad \mathbf{R}_7 = \begin{bmatrix} 0 \\ 0 \\ 0 \\ 0 \\ 1 \\ -\overline{\overline{C}}^{-1} \begin{bmatrix} \frac{1}{\rho} \\ 0 \\ 0 \end{bmatrix} \\ 0 \\ 0 \\ 0 \\ 0 \end{bmatrix}$$

and thus 1 eigenvector is missing to have a hyperbolic model. Model (2.3) is then weakly hyperbolic.

Bibliography

[1] C. Aalburg, B. van Leer, and G.M. Faeth. Deformation and drag properties of round drops subjected to shock-wave disturbances. *AIAA journal*, 41(12):2371–2378, 2003.

[2] R. Abgrall and S. Karni. Computations of compressible mutlifluids. *Journal of Computational Physics*, 169(2):594–623, 2001.

[3] M. Aftosmis, J. Melton, and M.J. Berger. Adaptation and surface modeling for cartesian mesh methods. In *AIAA Paper, 12th Computational Fluid Dynamics Conference*, page 1725, 1995.

[4] G. Allaire, S. Clerc, and S. Kokh. A five-equation model for the simulation of interfaces between compressible fluids. *J. Comp. Phys.*, 181:577–616, 2002.

[5] M. Anderson, E.W. Hirschmann, S.L. Liebling, and D. Neilsen. Relativistic mhd with adaptive mesh refinement. *Classical and Quantum Gravity*, 23(22):6503, 2006.

[6] M.J. Berger and P. Colella. Local adaptive mesh refinement for shock hydrodynamics. *Journal of computational Physics*, 82(1):64–84, 1989.

[7] M.J. Berger and J. Oliger. Adaptive mesh refinement for hyperbolic partial differential equations. *Journal of computational Physics*, 53(3):484–512, 1984.

[8] J. Brackbill, D. Kothe, and C. Zemach. A continuum method for modelling surface tension. *Journal of Computational Physics*, 100:335–354, 1992.

[9] A. Chauvin, E. Daniel, A. Chinnayya, J. Massoni, and G. Jourdan. Shock waves in sprays: numerical study of secondary atomization and experimental comparison. *Shock Waves*, pages 1–13, 2015.

[10] A. Chauvin, G. Jourdan, E. Daniel, L. Houas, and R. Tosello. Experimental investigation of the propagation of a planar shock wave through a two-phase gas-liquid medium. *Physics of Fluids (1994-present)*, 23(11):113301, 2011.

[11] H. Chen. Two-dimensional simulation of stripping breakup of a water droplet. *AIAA Journal*, 46(5):1135–1143, 2008.

[12] S. Chen and G.D. Doolen. Lattice boltzmann method for fluid flows. *Annual review of fluid mechanics*, 30(1):329–364, 1998.

[13] X. Chen and V. Yang. Thickness-based adaptive mesh refinement methods for multi-phase flow simulations with thin regions. *Journal of Computational Physics*, 269:22–39, 2014.

[14] W.J. Coirier. An adaptively-refined, cartesian, cell-based scheme for the euler and navier-stokes equations. *Ph.D. thesis, University of Michigan*, 1994.

[15] B.M. Devassy, C. Habchi, and E. Daniel. Atomization modelling of liquid jets using a two-surface-density approach. *Atomization and Sprays*, 25(1):47–80, 2015.

[16] M. Dumbser, O. Zanotti, A. Hidalgo, and D.S. Balsara. Ader-weno finite volume schemes with space–time adaptive mesh refinement. *Journal of Computational Physics*, 248:257–286, 2013.

[17] O.G. Engel. Fragmentation of waterdrops in the zone behind an air shock. *J. Res. Natl. Bur. Stand*, 60(3):245–280, 1958.

[18] N. Favrie and S.L. Gavrilyuk. Diffuse interface model for compressible fluid–compressible elastic–plastic solid interaction. *Journal of Computational Physics*, 231(7):2695–2723, 2012.

[19] N. Favrie and S.L. Gavrilyuk. Dynamic compaction of granular materials. *Proceedings of the Royal Society of London A: Mathematical, Physical and Engineering Sciences*, 469(2160):20130214, 2013.

[20] N. Favrie, S.L. Gavrilyuk, and S. Ndanou. A thermodynamically compatible splitting procedure in hyperelasticity. *Journal of Computational Physics*, 270:300–324, 2014.

[21] R.P. Fedkiw, T. Aslam, B. Merriman, and S. Osher. A non oscillatory Eulerian approach to interfaces in multimaterial flows (The Ghost Fluid Method). *Journal of Computational Physics*, 152:457–492, 1999.

[22] S.L. Gavrilyuk. *Multiphase flow modeling via Hamilton's principle. In the book: F. Dell'Isola and S.L. Gavrilyuk, Eds. Variational models and methods in solid and fluid mechanics, CISM Courses and Lectures*, volume 535. Springer, 2012.

[23] S.L. Gavrilyuk and R. Saurel. Rankine-Hugoniot relations for shocks in heterogeneous mixtures. *Journal of Fluid Mechanics*, 575:495–507, 2007.

[24] S.K. Godunov. A finite difference method for numerical computation of discontinuous solutions of the equations of fluid dynamics. *Math Sb.*, 47:357–393, 1959.

[25] D. Gueyffier, L. Li, A. Nadim, R. Scardovelli, and S. Zaleski. Volume-of-fluid interface tracking with smoothed surface stress methods for three-dimensional flows. *Journal of Computational Physics*, 152:423–456, 1999.

[26] D.R. Guildenbecher, C. López-Rivera, and P.E. Sojka. Secondary atomization. *Experiments in Fluids*, 46(3):371, 2009.

[27] E. Han, M. Hantke, and S. Müller. Efficient and robust relaxation procedures for multi-component mixtures including phase transition. *Journal of Computational Physics*, 338:217–239, 2017.

[28] J. Han and G. Tryggvason. Secondary breakup of axisymmetric liquid drops. II. Impulsive acceleration. *Physics of Fluids*, 13(6):1554–1565, 2001.

[29] L.H. Han, X.Y. Hu, and N.A. Adams. Scale separation for multi-scale modeling of free-surface and two-phase flows with the conservative sharp interface method. *Journal of Computational Physics*, 280:387–403, 2015.

[30] S. Hank, N. Favrie, and J. Massoni. Modeling hyperelasticity in non-equilibrium multiphase flows. *Journal of Computational Physics*, 330:65–91, 2017.

[31] A.R. Hanson, E.G. Domich, and H.S. Adams. Shock tube investigation of the breakup of drops by air blasts. *The Physics of Fluids*, 6(8):1070–1080, 1963.

[32] P.F. Hopkins. A new class of accurate, mesh-free hydrodynamic simulation methods. *Monthly Notices of the Royal Astronomical Society*, 450(1):53–110, 2015.

[33] A. Hosangadi, V. Ahuja, and S. Arunajatesan. Simulations of cavitating flows using hybrid unstructured meshes. *ASME J. Fluids Eng*, 123:331–340, 2001.

[34] L-P. Hsiang and G.M. Faeth. Near-limit drop deformation and secondary breakup. *International Journal of Multiphase Flow*, 18(5):635–652, 1992.

[35] X.Y. Hu, B.C. Khoo, N.A. Adams, and F.L. Huang. A conservative interface method for compressible flows. *Journal of Computational Physics*, 219(2):553–578, 2006.

[36] D. Igra and K. Takayama. Experimental and numerical study of the initial stages in the interaction process between a planar shock wave and a water column. In *Proc. 23rd Int. Symposium on Shock Waves*, volume 5071, 2001.

[37] D. Igra and K. Takayama. Investigation of aerodynamic breakup of a cylindrical water droplet. *Atomization and Sprays*, 11(2):167–185, 2001.

[38] D. Igra and K. Takayama. Numerical simulation of shock wave interaction with a water column. *Shock Waves*, 11(3):219–228, 2001.

[39] D. Igra and K. Takayama. A study of shock wave loading on a cylindrical water column. *Report of the Institute of Fluid Science, Tohoku University*, 13:19–36, 2001.

[40] D. Igra and K. Takayama. Experimental investigation of two cylindrical water columns subjected to planar shock wave loading. *Journal of Fluids Engineering*, 125(2):325–331, 2003.

[41] M. Jalaal and K. Mehravaran. Transient growth of droplet instabilities in a stream. *Physics of Fluids*, 26(1):012101, 2014.

[42] D.D. Joseph, J. Belanger, and G.S. Beavers. Breakup of a liquid drop suddenly exposed to a high-speed airstream. *International Journal of Multiphase Flow*, 25(6):1263–1303, 1999.

[43] A. Kapila, R. Menikoff, J. Bdzil, S. Son, and D. Stewart. Two-phase modeling of DDT in granular materials: Reduced equations. *Physics of Fluids*, 13:3002–3024, 2001.

[44] S. Karni. Multicomponent flow calculations by a consistent primitive algorithm. *Journal of Computational Physics*, 112(1):31–43, 1994.

[45] S. Karni. Hybrid multifluid algorithms. *SIAM Journal on Scientific Computing*, 17(5):1019–1039, 1996.

[46] A.M. Khokhlov. Fully threaded tree algorithms for adaptive refinement fluid dynamics simulations. *Journal of Computational Physics*, 143(2):519–543, 1998.

[47] S. Khosla, C.E. Smith, and R.P. Throckmorton. Detailed understanding of drop atomization by gas crossflow using the volume of fluid method. In *19th Annual Conference on Liquid Atomization and Spray Systems (ILASS-Americas), Toronto, Canada*, 2006.

[48] B. Koren, M.R. Lewis, E.H. van Brummelen, and B. van Leer. Riemann-problem and level-set approaches for homentropic two-fluid computations. *Journal of Computational Physics*, 181:654–674, 2002.

[49] L.D. Landau and E. M. Lifshitz. *Course of theoretical physics*, volume 6. Permagon, 1959.

[50] W.R. Lane. Shatter of drops in streams of air. *Industrial & Engineering Chemistry*, 43(6):1312–1317, 1951.

[51] G. Layes and O. Le Metayer. Quantitative numerical and experimental studies of the shock accelerated heterogeneous bubbles motion. *Physics of Fluids*, 19(042105), 2007.

[52] S. Le Martelot, R. Saurel, and B. Nkonga. Towards the direct numerical simulation of nucleate boiling flows. *International Journal of Multiphase Flow*, 66:62–78, 2014.

[53] O. Le Métayer, J. Massoni, and R. Saurel. Dynamic relaxation processes in compressible multiphase flows. application to evaporation phenomena. In *Esaim: Proceedings*, volume 40, pages 103–123. EDP Sciences, 2013.

[54] T.G. Liu, B.C. Khoo, and K.S. Yeo. Ghost fluid method for strong shock impacting on material interface. *Journal of Computational Physics*, 190(2):651–681, 2003.

[55] J. Luo, X.Y. Hu, and N.A. Adams. A conservative sharp interface method for incompressible multiphase flows. *Journal of Computational Physics*, 284:547–565, 2015.

[56] J. Massoni, R. Saurel, B. Nkonga, and R. Abgrall. Proposition de methodes et modeles Euleriens pour les problemes a interfaces entre fluides compressibles en presence de transfert de chaleur. *Int. J. Heat and Mass Transfer*, 45:1287–1307, 2002.

[57] J. Melton, M.J. Berger, M. Aftosmis, and M. Wong. 3d applications of a cartesian grid euler method. In *AIAA Paper, 33rd Aerospace Sciences Meeting and Exhibit*, page 853, 1995.

[58] J.C. Meng. *Numerical Simulations of Droplet Aerobreakup*. PhD thesis, California Institute of Technology, 2016.

[59] J.C. Meng and T. Colonius. Numerical simulations of the early stages of high-speed droplet breakup. *Shock Waves*, pages 1–16, 2014.

[60] A. Murrone and H. Guillard. Behavior of upwind scheme in the low mach number limit: Iii. preconditioned dissipation for a five equation two phase model. *Computers & Fluids*, 37(10):1209–1224, 2008.

[61] S. Ndanou, N. Favrie, and S.L. Gavrilyuk. Criterion of hyperbolicity in hyperelasticity in the case of the stored energy in separable form. *Journal of Elasticity*, 115(1):1–25, 2014.

[62] S. Osher and R. Fedkiw. Level set methods: An overview and some recent results. *Journal of Computational Physics*, 169:463–502, 2001.

[63] S. Osher and R. Fedkiw. *Level set methods and dynamic implicit surfaces*, volume 153. Springer Science & Business Media, 2006.

[64] S. Osher and J.A. Sethian. Fronts propagating with curvature-dependent speed: algorithms based on hamilton-jacobi formulations. *Journal of computational physics*, 79(1):12–49, 1988.

[65] G.S.H. Pau, J.B. Bell, A.S. Almgren, K.M. Fagnan, and M.J. Lijewski. An adaptive mesh refinement algorithm for compressible two-phase flow in porous media. *Computational Geosciences*, 16(3):577–592, 2012.

[66] G. Périgaud and R. Saurel. A compressible flow model with capillary effects. *J. Comp. Phys.*, 209:139–178, 2005.

[67] F. Petitpas. *Contribution à la théorie des interfaces diffuses: interfaces matérielles, fronts de transition de phase et fronts de détonation*. PhD thesis, Université de Provence, 2008.

[68] F. Petitpas and S. Le Martelot. A discrete method to treat heat conduction in compressible two-phase flows. *Computational Thermal Sciences: An International Journal*, 6(3), 2014.

[69] F. Petitpas, J. Massoni, R. Saurel, E. Lapebie, and L. Munier. Diffuse interface models for high speed cavitating underwater systems. *Int. J. of Multiphase Flows*, 35(8):747–759, 2009.

[70] F. Petitpas, R. Saurel, E. Franquet, and A. Chinnayya. Modelling detonation waves in condensed energetic materials: Multiphase CJ conditions and multidimensional computations. *Shock waves*, 19(5):377–401, 2009.

[71] M. Pilch and C.A. Erdman. Use of breakup time data and velocity history data to predict the maximum size of stable fragments for acceleration-induced breakup of a liquid drop. *International Journal of Multiphase Flow*, 13(6):741–757, 1987.

[72] S. Popinet and G. Rickard. A tree-based solver for adaptive ocean modelling. *Ocean Modelling*, 16(3):224–249, 2007.

[73] S. Quan and D.P. Schmidt. Direct numerical study of a liquid droplet impulsively accelerated by gaseous flow. *Physics of fluids*, 18(10):102103, 2006.

[74] J.J. Quirk and S. Karni. On the dynamics of a shock–bubble interaction. *Journal of Fluid Mechanics*, 318:129–163, 1996.

[75] A.A. Ranger and J.A. Nicholls. Aerodynamic shattering of liquid drops. *AIAA Journal*, 7(2):285–290, 1969.

[76] R. Saurel and R. Abgrall. A simple method for compressible multifluid flows. *SIAM J. Sci. Comp.*, 21(3):1115–1145, 1999.

[77] R. Saurel, S.L. Gavrilyuk, and F. Renaud. A multiphase model with internal degrees of freedom: Application to shock-bubble interaction. *Journal of Fluid Mechanics*, 495:283–321, 2003.

[78] R. Saurel and F. Petitpas. Introduction to diffuse interfaces and transformation fronts modelling in compressible media. In *ESAIM: Proceedings*, volume 40, pages 124–143. EDP Sciences, 2013.

[79] R. Saurel, F. Petitpas, and R. Abgrall. Modelling phase transition in metastable liquids: application to cavitating and flashing flows. *Journal of Fluid Mechanics*, 607:313–350, 2008.

[80] R. Saurel, F. Petitpas, and R.A. Berry. Simple and efficient relaxation methods for interfaces separating compressible fluids, cavitating flows and shocks in multiphase mixtures. *Journal of Computational Physics*, 228(5):1678–1712, 2009.

[81] K. Schmidmayer, F. Petitpas, and E. Daniel. Adaptive Mesh Refinement method based on cells boundaries trees for compressible multiphase flows. *Submitted*, 2017.

[82] K. Schmidmayer, F. Petitpas, E. Daniel, N. Favrie, and S.L. Gavrilyuk. A model and numerical method for compressible flows with capillary effects. *Journal of Computational Physics*, 334:468–496, 2017.

[83] F.S. Schranner, X.Y. Hu, and N.A. Adams. On the convergence of the weakly compressible sharp-interface method for two-phase flows. *Journal of Computational Physics*, 324:94–114, 2016.

[84] K.M. Shyue. An anti-diffusion based eulerian interface-sharpening algorithm for compressible two-phase flow with cavitation. In *Proceedings of the 8th International Symposium on Cavitation, Research Publishing Services*, page 198, 2012.

[85] K.M. Shyue and F. Xiao. An eulerian interface sharpening algorithm for compressible two-phase flow: the algebraic thinc approach. *Journal of Computational Physics*, 268:326–354, 2014.

[86] P.G. Simpkins and E.L. Bales. Water-drop response to sudden accelerations. *Journal of Fluid Mechanics*, 55(04):629–639, 1972.

[87] M. Sussman, P. Smereka, and S. Osher. A level set approach for computing solutions to incompressible two-phase flow. *Journal of Computational Physics*, 114(1):146–159, 1994.

[88] G.I. Taylor. The shape and acceleration of a drop in a high speed air stream. *The scientific papers of G.I. Taylor*, 3:457–464, 1949.

[89] T.G. Theofanous. Aerobreakup of newtonian and viscoelastic liquids. *Annual Review of Fluid Mechanics*, 43:661–690, 2011.

[90] T.G. Theofanous, VV. Mitkin, C.L. Ng, C.H. Chang, X. Deng, and S. Sushchikh. The physics of aerobreakup. II. Viscous liquids. *Physics of Fluids*, 24(2):022104, 2012.

[91] N. Thévand, E. Daniel, and J.C. Loraud. On high-resolution schemes for solving unsteady compressible two-phase dilute viscous flows. *International journal for numerical methods in fluids*, 31(4):681–702, 1999.

[92] A. Tiwari, J.B. Freund, and C. Pantano. A diffuse interface model with immiscibility preservation. *Journal of computational physics*, 252:290–309, 2013.

[93] E.F. Toro. R*iemann solvers and numerical methods for fluid dynamics*. Springer Verlag, Berlin, 1997.

[94] G. Tryggvason, B. Bunner, A. Esmaeeli, D. Juric, N. Al-Rawahi, W. Tauber, J. Han, S. Nas, and Y-J. Jan. A front-tracking method for the computations of multiphase flow. *Journal of Computational Physics*, 169(2):708–759, 2001.

[95] A.R. Wadhwa, V. Magi, and J. Abraham. Transient deformation and drag of decelerating drops in axisymmetric flows. *Physics of Fluids*, 19(11):113301, 2007.

[96] P. Welch and P. Boyle. New turbines to enable efficient geothermal power plants. *Geothermal Resources Council Transactions*, 33:765–772, 2009.

[97] A. Wierzba and K. Takayama. Experimental investigation on liquid droplet breakup in a gas stream. *Rept. Inst. High Speed Mech.(Tohoku Univ.)*, 53(382):1–99, 1987.

[98] A.B. Wood. A textbook of sound. *G. Bell and Sons LTD, London*, 1930.

[99] J. Yang, T. Kubota, and E.E. Zukoski. A model for characterization of a vortex pair formed by shock passage over a light-gas inhomogeneity. *Journal of Fluid Mechanics*, 258:217–244, 1994.

[100] D.P. Young, R.G. Melvin, M.B. Bieterman, F.T. Johnson, S.S. Samant, and J.E. Bussoletti. A locally refined rectangular grid finite element method: application to computational fluid dynamics and computational physics. *Journal of Computational Physics*, 92(1):1–66, 1991.